

Study of Residual Stresses in Selective Laser Melting

Bey Vrancken

Supervisor:
Prof. dr. ir. Jan Van Humbeeck

Dissertation presented in partial
fulfillment of the requirements for the
degree of Doctor in Engineering
Science

June 2016

Study of Residual Stresses in Selective Laser Melting

Bey VRANCKEN

Examination committee:

Prof. dr. ir. Paul Sas, chair

Prof. dr. ir. Jan Van Humbeeck, supervisor

Prof. dr. ir. Jean-Pierre Kruth

Prof. dr. ir. Marc Seefeldt

Prof. dr. ir. Kim Vanmeensel

Dissertation presented in partial
fulfillment of the requirements for
the degree of Doctor
in Engineering Science

Prof. dr. ir. Stéphane Godet
(Université Libre de Bruxelles)

Dr. ir. Marleen Rombouts
(VITO)

June 2016

© 2016 KU Leuven – Faculty of Engineering Science
Uitgegeven in eigen beheer, Bey Vrancken, Kasteelpark Arenberg 44 box 2450, B-3001 Heverlee (Belgium)

Alle rechten voorbehouden. Niets uit deze uitgave mag worden vermenigvuldigd en/of openbaar gemaakt worden door middel van druk, fotokopie, microfilm, elektronisch of op welke andere wijze ook zonder voorafgaande schriftelijke toestemming van de uitgever.

All rights reserved. No part of the publication may be reproduced in any form by print, photoprint, microfilm, electronic or any other means without written permission from the publisher.

ISBN XXX-XX-XXXX-XXX-X
D/XXXX/XXXX/XX

Preface

Beste lezers,

Velen zullen niet veel verder geraken dan dit voorwoord, maar de resterende pagina's zijn het resultaat van net geen 5 jaar werk. Dat is bijna een jaar langer dan de voorgeschreven duur van een doctoraat, en je zou bijna kunnen denken dat dit met opzet is: juni 2006 afgestudeerd van de humaniora, juni 2011 een masterdiploma rijker, en nu juni 2016.

Mijn avontuur in Additive Manufacturing of '3D printen' van metalen begon in 2008-2009, als bachelorstudent. Voor mijn bachelorproef sleet ik vele uren in de metallografielabo's van Paul, waar ook een andere, hardwerkende student vaak aanwezig was. Zij schurend aan haar titaan, ik mijn aluminium. Twee jaar later werd ze mijn thesisbegeleider, dus bedankt Lore voor de kennismaking met SLM! Ik had geen idee waar je het over had toen je destijds uitlegde hoe je monster was geproduceerd, maar ik denk het nu wel door te hebben.

Na mijn thesis kreeg ik van professor Jan Van Humbeeck de kans om een doctoraat te beginnen. Daar sprak ik al van in het begin van mijn carrière als student over, zoals mijn ouders zullen kunnen beamen. Bedankt prof. Van Humbeeck, bedankt Jan. Ik heb veel bijgeleerd van en tijdens onze samenwerking, en ik ben ui-ter-ma-te dankbaar voor je ongezien snelle reacties op mails en drafts. En ik hoop dat je op het einde ook hebt bijgeleerd van mij, want dat is de bedoeling van een doctoraat, zei een wijs man ooit.

Bedankt Jean-Pierre Kruth, door wiens harde werk de AM-groep van de KU Leuven wereldwijd gekend is. Het was steeds verruimend en motiverend om in de door u gecreëerde multidisciplinaire omgeving te mogen werken. Danku Marc Seefeldt, Kim Vanmeensel, Marleen Rombouts en Stéphane Godet voor de tijd en energie gestoken in dit proefschrift, en de suggesties om het werk beter te maken. Ik ben blij dat ik heb kunnen profiteren van jullie ruime ervaring en andere invalshoeken. Bedankt aan de voorzitter van de jury, prof. Paul Sas, voor het bewaken van de nodige protocollen en het modereren van de vragen

tijdens beide verdedigingen.

Financiering voor een groot deel van dit werk kwam van een beurs voor strategisch basisonderzoek No 121186, van het ondertussen ter ziele gegaan Agentschap voor Innovatie door Wetenschap en Technologie in Vlaanderen (IWT-Vlaanderen). Hiervoor ben ik ook dankbaar.

Thank you to my other office colleagues and the multicultural environment that came with them. Thank you Xiebin, Bin and Chen (China), Victoria (South Africa), Maria (Spain/Basque Country) and Akhilesh (India). Our office, 91.47, is envied by others because of its moderate temperatures, amount of windows and our couch, but most of all because of the people that I had the pleasure of spending a lot of time with. I'm also grateful for all the efforts of my thesis students.

Om lokaal 91.47 heen hebben ze ooit nog een heel departement gebouwd, en de hechte sfeer binnen MTM leverde een grote bijdrage aan het werk- en studeerplezier dat ik de afgelopen 10 jaar heb beleefd. Ik ben enorm dankbaar voor de vele *social events*, niet in het minst de voetbal en beachvolleybal (bedankt Stijn voor de organisatie!) and the lunch in the cafeteria-crew.

Zonder het uitstekende technische en administratieve personeel zou er ook geen wetenschappelijk onderzoek zijn. Bedankt aan iedereen die me heeft bijgestaan, in het bijzonder Paul en Louis Depre. De resultaten van jullie expertise en labo's zijn verantwoordelijk voor vele figuren verderop in dit werk.

Ook mede-verantwoordelijk voor vele resultaten is de goede samenwerking met 3DS Layerwise, zij het met Ruben, Lore, of iemand anders. Ik ben blij dat jullie het onderzoek interessant genoeg vonden om vele, honderden, monsters te voorzien!

Met de huidige een voormalige collega's van de AM-groep op PMA was het altijd aangenaam samen te werken. Tom, Jan, Stijn, Karolien, Sam, Mathew, Brecht, Sasan, Raya, Sebastian, Dries, Bavo, Yannis, nog een Stijn, ...: Ik heb van jullie bijgeleerd (ook tijdens mijn masterthesis) en ben zeer dankbaar voor de hulp met de (voor mij) zwarte doos die tegenwoordig de LM-Q heet. A shout out to Maria at the VUB, whose work gave me the opportunity to see a nuclear reactor up close.

Bedankt Bart voor je hulp in het metrologie-labo. And thank you, Pierluigi Pagliaro, whose personal advice and PhD thesis text were invaluable for performing the contour method measurements.

Mama en papa, jullie hebben mij altijd gedreven om de beste versie van mezelf te zijn. Ik ben nooit iets tekort gekomen, en het is de basis die ik van jullie heb meegekregen die dit heeft mogelijk gemaakt.

Ten slotte schreef ik 5 jaar geleden in het dankwoord van mijn masterthesis dat er altijd iemand is geweest die me er aan herinnert dat er belangrijkere zaken in het leven zijn. Nu staan we 5 jaar en vele gedeelde ervaringen verder. Ik heb de vrijheid gekregen om dit doctoraat te maken, maar laten wij nu, samen, nog veel mooiere zaken schrijven.

Bey Vrancken

Juni 2016

Abstract

Additive Manufacturing (AM) is a valid and economically viable technique to produce fully functional, geometrically complex parts. One such AM technique, Selective Laser Melting (SLM), uses a high power laser to selectively melt layers of metal powder. Selective Laser Melting can be compared to a repetitive welding process, stacking thousands of welds next to and on top of each other to produce a 3D geometry. The difference lies in the fact that the purpose of welds is to join two or more separate geometries into one, while in SLM, the welds itself are the geometry. Moreover, the process takes place on a much finer scale compared to commercial welding processes, with melt pool dimensions in the order of 0.1mm^3 .

The localized melt pool and its heat affected zone are small compared to the thermal heat sink effect of the base plate and previously consolidated layers, creating extremely large and directional thermal gradients. In turn, these gradients lead to the build up of residual stresses which have an effect on the mechanical performance and cause deformation, as well as micro- and macrocracks.

Stress is built up locally by the thermal shrinkage of the solidified melt pool, and is larger in the direction of a scan track than perpendicular to it. The shrinkage is impeded in the horizontal direction by the solid material below, causing horizontal tensile stresses at the top surface of SLM produced parts. These horizontal stresses exert a pulling force which would cause the part to curl up if it were not anchored to the base plate. Because the part is anchored, curl up is avoided but vertical tensile stresses are introduced at the side surfaces. Compressive stress in all directions exists in the center of the part.

Different possibilities to induce lower residual stresses were explored in this work, at various stages throughout the SLM process chain. The effects of thermal and other material properties are difficult to isolate from the influence of process parameters during the process, or material specific problems such as ductile

to brittle transitions, solidification cracking, and low temperature allotropic transformations. Overall, using process parameters that increase the heat input reduces macroscopic residual stresses. This includes using thin layers, slow scan speeds, high laser powers and most importantly, base plate preheating. In addition, modified alloy compositions introduce benefits of tailored mechanical properties and, to a certain extent, a tailored microstructure. Finally, the impact of residual stress on the mechanical behavior was highlighted by the overlap of 2D maps of the residual stress with the observed crack growth behavior of Ti6Al4V compact tension specimens produced by SLM.

Base plate preheating, as well as tailored alloy compositions may provide the largest gains. Combining all the favorable procedures described in this work will lower residual stresses, which enables production of bigger parts or processing of new materials.

Beknopte samenvatting

Additieve productietechnieken worden steeds vaker gebruikt om functionele, kritisch belaste onderdelen te maken met een complexe geometrie. In één van deze technieken, genaamd Selectief Laser Smelten (SLM), wordt een laser met een hoog vermogen gebruikt om dunne lagen van metallisch poeder selectief te smelten. SLM kan vergeleken worden met een repetitief lasproces, waarbij duizenden lasnaden naast en op elkaar worden aangebracht om een 3D geometrie op te bouwen. Het grote verschil is dat conventioneel lassen dient om twee of meer verschillende vormen samen te brengen tot 1 geometrie, terwijl de lasnaden zelf de geometrie zijn in het SLM proces. Daarbovenop speelt het SLM proces zich af op een kleinere schaal in vergelijking met commerciële lasprocessen, met dimensies van het smeltbad in de grootteorde van 0.1mm^3 .

Dit gelokaliseerde smeltbad en de bijhorende warmte-beïnvloede zone zijn klein ten opzichte van de basisplaat en reeds gestolde lagen, die functioneren als een groot koellichaam. Hierdoor ontstaan grote, richtingsafhankelijke thermische gradiënten die op hun beurt leiden tot de opbouw van restspanningen. Deze spanningen beïnvloeden de mechanische eigenschappen van stukken geproduceerd met SLM en veroorzaken geometrische vervormingen en scheurvorming tijdens of na het proces.

De spanningen worden lokaal opgebouwd door de thermische krimp van het gestolde smeltbad, en zijn groter in de lengte-richting van het smeltbad dan loodrecht daarop. De krimp wordt in de horizontale richting beperkt door het onderliggend materiaal, waardoor er horizontale trekspanningen aanwezig zijn in het bovenoppervlak van SLM geproduceerde stukken. Deze horizontale spanningen zorgen bovendien voor een opkrullend effect, dat eveneens wordt beperkt door verankering van het stuk aan de basisplaat. Zo leiden de horizontale trekspanningen aan het bovenoppervlak tot verticale trekspanningen aan de zijwanden. In het midden van het stuk heersen drukspanningen in alle richtingen.

In dit werk werden verschillende mogelijkheden onderzocht om de restspanningen

te verminderen. Het effect van de thermische of andere materiaaleigenschappen was moeilijk te isoleren van de invloed van de procesparameters, en materiaal-specifieke fenomenen zoals een bros-ductiel overgang, stollingsscheuren en allotrope transformaties die plaatsvinden bij een lage temperatuur. In het algemeen verlaagt het gebruik van procesparameters die zorgen voor een hogere warmte-invoer ook de macroscopische restspanningen. Dit kan zijn door het gebruik van dünnere lagen, tragere scansnelheden, een hoog laser Vermogen of vooral door voorverwarming van de basisplaat. Daarnaast kan het aanpassen van de samenstelling van de metaallegering tot een betere verwerkbaarheid, maar ook tot betere mechanische eigenschappen leiden. Tot slot werd de invloed van de restspanningen op het mechanisch gedrag aangetoond door de overlap van 2D kaarten van de restspanningen met het scheurpatroon van Ti6Al4V stukken vervaardigd via SLM.

Voorverwarming van de basisplaat en het aanpassen van de metaallegering zijn de krachtigste mechanismen om problemen met restspanningen tijdens SLM tegen te gaan. Een gepaste combinatie van de in dit werk voorgestelde procedures zal leiden tot lagere restspanningen. Dit zorgt ervoor dat grotere stukken gebouwd kunnen worden, en dat meer materialen verwerkt kunnen worden via SLM.

List of abbreviations

bcc	Body Centered Cubic crystal structure
fcc	Face Centered Cubic crystal structure
hcp	Hexagonal Close Packed
α	Hexagonal close packed phase in titanium metal
α'	Hexagonal close packed martensitic phase in titanium metal
α''	orthorhombic martensitic phase in titanium metal
α_2	Ti_3Al precipitate in titanium metal
β	Body centered cubic phase in titanium metal
γ	Face cubic centered matrix phase in nickel based superalloys
γ'	Precipitate in nickel based superalloys
γ''	Precipitate in nickel based superalloys
δ	Precipitate in nickel based superalloys
M_6C	Carbide stoichiometry
$M_{23}C_6$	Carbide stoichiometry
{hkl}	Family of crystal planes
$\langle hkl \rangle$	Family of crystal directions
1D	One Dimensional
2D	Two Dimensional
3D	Three Dimensional
AB	As built
AC	Air Cooling
AM	Additive Manufacturing
AMAVF	Stock ticker for Arcam AB
APT	Atom Probe Tomography
ASTM	American Society for Testing and Materials
at%	atom percent
BCM	Bridge Curvature Method

BD	Building Direction
CAGR	Compound Annual Growth Rate
CMM	Coordinate Measurement Machine
CT	Computer Tomography
DBTT	Ductile-to-Brittle Transition Temperature
DDD	Stock ticker for 3D Systems
DED	Directed Energy Deposition
DIC	Digital Image Correlation
EBM	Electron Beam Melting
EDM	Electric Discharge Machining
EDX	Energy-Dispersive X-ray
FC	Furnace Cooling
FCGR	Fatigue Crack Growth Rate
FE	Finite Elements
FT	Fracture Toughness
GB α	Grain Boundary α
HAZ	Heat Affected Zone
HCF	High Cycle Fatigue
HIP	Hot Isostatic Pressing
Hor.	Horizontal sample orientation (perpendicular to the building direction)
HRC	Rockwell C Hardness
HSS	High Speed Steel
HT	Heat Treated
HV	Vickers Hardness
ICP-AES	Inductively Coupled Plasma - Atomic Emission Spectroscopy
IGA	Interstitial Gas Analysis
IPS	Invariant Plane Strain
ISO	International Organization for Standardization
LC	Laser Cladding
LC	Low carbon
LCF	Low Cycle Fatigue
LEAP	Leading Edge Aviation Propulsion
LENS	Laser Engineered Net Shaping
LLNL	Lawrence Livermore National Laboratory
LMD	Laser Metal Deposition
LM-Q	SLM machine at the PMA division of the Department of Mechanical Engineering, KU Leuven
LOM	Light Optical Microscopy
NP	No Preheating
PSD	Particle Size Distribution

R&D	Research and Development
RS	Residual Stress
S&P500	Stock ticker for Standard&Poor's index
SE Coeff	Standard Error on Coefficients
SEM	Scanning Electron Microscopy
SLM	Selective Laser Melting
SR	Stress Relieved
SSYS	Stock ticker for Stratasy
UK	United Kingdom
UV	Ultra-Violet
Ver.	Vertical sample orientation (parallel to the building direction)
WQ	Water Quench
wt%	weight percent
XEC	X-ray Elastic Constants
XRD	X-Ray Diffraction
Yb:YAG	Ytterbium doped Yttrium Aluminium Garnet Laser

List of Symbols

α	Significance level when determining the confidence interval	-
α_{BCM}	Angle measured for the bridge curvature method	$^{\circ}$
α_{CTE}	Coefficient of thermal expansion	K^{-1}
$[\alpha_{ij}]$	Thermal expansion in tensor form	K^{-1}
ΔK	Difference in stress intensity factors during cyclic loading	$Mpa\sqrt{m}$
ΔK_{max}	Maximum stress intensity difference before failure	$Mpa\sqrt{m}$
ΔK_{th}	Threshold stress intensity difference for which crack growth is detectable	$Mpa\sqrt{m}$
ΔT	Temperature interval	$^{\circ}C$ or K
$\Delta T_{L \rightarrow S}$	Solidification range	$^{\circ}C$
∇T	Temperature gradient, vectorial form	
δ	Deflection	mm
ϵ	Strain	%
$[\epsilon_{ij}]$	Strain tensor	
$\epsilon_{\phi\psi}$	Strain in a direction marked by angle ϕ , for a sample tilt defined by angle ψ	%
ϵ_{frac}	Fracture strain	%
\vec{G}	Directional thermal gradient	K/m
κ	Curvature	m^{-1}
λ	wavelength	μm or Å
μ	Mass attenuation coefficient	cm^2/g
ν_{hkl}	Poisson ratio in the $\langle hkl \rangle$ crystal direction	-
ϕ	Rotation of a sample in XRD around the surface normal	$^{\circ}$

ψ	Angle between the surface normal and the bisector of the incident and diffracted X-rays of a sample in XRD	$^{\circ}$
ρ	Density	kg/m^3
ρ	Relative density	%
σ	Stress	MPa
$[\sigma_{ij}]$	Stress tensor	MPa
σ_{ϕ}	Stress measured via XRD in direction marked by angle ϕ	MPa
$\sigma_{0^{\circ}}$	Stress measured via XRD in direction marked by angle $\phi = 0^{\circ}$	MPa
$\sigma_{90^{\circ}}$	Stress measured via XRD in direction marked by angle $\phi = 90^{\circ}$	MPa
σ_{max}	Maximum stress during cyclic loading	MPa
σ_{min}	Minimum stress during cyclic loading	MPa
σ_1	Largest principal stress	MPa
σ_2	Second largest principal stress	MPa
σ_y	Yield stress	MPa
$\left(\frac{\delta T_L}{\delta C}\right)$	Slope of the liquidus vs component x	$K/wt\%$
$\left(\frac{\delta T}{\delta C}\right)_{crit}$	Critical temperature gradient for a stable planar solidification front	K/m
τ	Thermal shock resistance	-
θ	Angle between the surface and the incident X-rays in XRD	$^{\circ}$
2θ	Diffraction angle in XRD	$^{\circ}$
$2\theta_0$	Unstressed diffraction angle	$^{\circ}$
$2\theta_1$	Stressed diffraction angle	$^{\circ}$
b	Width	cm
C_0	Global concentration	$wt\%$
c_p	Specific heat capacity	$J/(kg \cdot K)$
d_{50}	Particle size for which 50% of particles have a smaller diameter	μm
d_{hkl}	Lattice spacing of $\{hkl\}$ planes	\AA
d_0	Unstressed lattice spacing	\AA
d_1	Stressed lattice spacing	\AA
D_L	Diffusion coefficient in the liquid	m^2/s
D_T	Thermal diffusivity	m^2/s
da/dn	Fatigue Crack Growth Rate	$\mu m/cycle$
E	Energy density	J/mm^3
E	Young's modulus	GPa
E_{hkl}	Young's modulus in the $\langle hkl \rangle$ crystal direction	GPa
$FCGR$	Fatigue Crack Growth Rate	$\mu m/cycle$

h	Hatch spacing (scan spacing)	μm
h	Part height	m
$I(0)$	Energy of incident X-rays	-
$I(x)$	Energy of X-rays at depth x in the material	-
I	Area moment of inertia	m^4
k	Thermal conductivity	$W/(m \cdot K)$
k	Partition coefficient	-
K_{IC}	Mode I fracture toughness	$Mpa\sqrt{m}$
K_{max}	Maximum stress intensity factor during cyclic loading	$Mpa\sqrt{m}$
K_{min}	Minimum stress intensity factor during cyclic loading	$Mpa\sqrt{m}$
K_{res}	Stress intensity factor due to residual stress	$Mpa\sqrt{m}$
L_s	Length of layer	cm
M_f	Finish temperature of the martensitic transformation	$^{\circ}C$ or K
M_s	Start temperature of the martensitic transformation	$^{\circ}C$ or K
P	Laser power	W
P	Probability during statistical testing	-
R	Ratio between minimum and maximum load in cyclic loading	-
\vec{R}	Directional solidification rate	m/s
R	Solidification rate	m/s
R_{app}	Apparent ratio between minimum and maximum load in cyclic loading, including residual stress effects	-
S_1	X-ray Elastic Constant	GPa^{-1}
$S_2/2$	X-ray Elastic Constant	GPa^{-1}
t	Layer thickness	μm
T	Temperature	$^{\circ}C$ or K
T_m	Melting temperature	$^{\circ}C$ or K
T_{base}	Base plate temperature	$^{\circ}C$ or K
T_0	Reference temperature	$^{\circ}C$ or K
UTS	Ultimate Tensile Strength	MPa
v	Scan speed	mm/s
w/t	Width-to-thickness ratio	-
\varnothing	Diameter	m

Contents

Abstract	v
List of abbreviations	ix
List of Symbols	xiii
Contents	xvii
List of Figures	xxiii
List of Tables	xxxvii
1 Introduction	1
1.1 Additive Manufacturing	2
1.1.1 Process categories	2
1.1.2 Economic outlook	5
1.1.3 Applications	8
1.1.4 Standardization	10
1.1.5 Challenges in AM	11
1.2 Residual stress	13
1.3 Research aims and methodology	14

1.4	Outline	16
2	Additive Manufacturing of Metals	19
2.1	Major metal AM processes	19
2.1.1	Electron Beam Melting	19
2.1.2	Laser Metal Deposition	20
2.2	Selective Laser Melting	21
2.2.1	Process Parameters	22
2.3	Materials processed by Selective Laser Melting	30
2.3.1	Titanium alloys	30
2.3.2	Other alloys and materials	45
3	Residual Stress in Additive Manufacturing	57
3.1	Residual Stress	57
3.1.1	Nature and Origins	57
3.1.2	Beneficial Residual Stress	58
3.1.3	Influence of Material Properties	59
3.1.4	Effect on mechanical behavior	62
3.1.5	Material specific behavior	63
3.2	Residual stress in metal AM	66
3.2.1	General residual stress distribution	68
3.2.2	Influence of process parameters	79
3.2.3	Deposition patterns	81
3.2.4	Preheating	84
3.2.5	Summary	86
4	Measurement of Residual Stress	89
4.1	X-ray Diffraction	89

4.2	Contour Method	93
4.2.1	Basic Principle	93
4.2.2	Cutting	95
4.2.3	Surface profile measurement	99
4.2.4	Data Processing	99
4.2.5	Stress calculation	100
4.2.6	Validation	100
4.3	Part deformation	102
4.3.1	Bridge Curvature Method	103
4.3.2	Cantilever specimens	104
5	General Characterization and Influence of the Process Parameters	107
5.1	General characterization of the residual stresses	108
5.1.1	Materials and Methods	108
5.1.2	Results	108
5.1.3	Preliminary conclusions	114
5.2	Influence of 'conventional' parameters	116
5.2.1	Materials and Methods	116
5.2.2	Results	117
5.2.3	Discussion	122
5.2.4	Preliminary conclusions	128
5.3	Preheating	128
5.3.1	Materials and Methods	128
5.3.2	Results	129
5.3.3	Preliminary conclusions	136
5.4	Conclusion	136
6	Influence of material properties	139

6.1	Influence of material properties	140
6.1.1	Materials and Methods	140
6.1.2	Density	142
6.1.3	Microstructure	142
6.1.4	Cracks	143
6.1.5	Residual Stress	148
6.1.6	Correlation between material properties and stress . . .	152
6.1.7	Preliminary conclusions	155
6.2	Ti6Al4V+10Mo	156
6.2.1	Materials and Methods	157
6.2.2	Microstructure	158
6.2.3	Mechanical Properties	165
6.2.4	Preliminary conclusions	167
6.3	Discussion	168
6.3.1	Process parameters and material specific phenomena . .	168
6.3.2	Microstructure modification	168
6.3.3	Alloy modification	169
6.4	Conclusion	172
7	Heat Treatment of SLM Ti6Al4V	175
7.1	Introduction	176
7.2	Materials and methods	176
7.3	Results	177
7.3.1	Microstructure	177
7.3.2	Mechanical Properties	183
7.4	Discussion	187
7.5	Conclusion	189

8	Effect of residual stress on mechanical behavior	193
8.1	Introduction	193
8.2	Materials and Methods	194
8.3	Results	195
8.4	Discussion	198
8.5	Conclusion	199
9	Conclusions and future work	201
A	Appendices	207
A.1	Static mechanical properties of AM Ti6Al4V	207
A.2	$\text{Sin}^2\psi$ -curves for the XRD results discussed in subsection 5.1.2	212
A.3	$\text{Sin}^2\psi$ -curves for the XRD results reported in Table 6.4	213
	Bibliography	217
	Curriculum Vitae	251
	List of Publications	253

List of Figures

1.1	Gartner hype cycle for emerging technologies, published August 2015 [5].	6
1.2	Rise and fall of three major 3D printing stocks, from March 1 2010 until March 1 2016, compared to the S&P500 Index. DDD = 3D Systems, SSYS = Stratasys and AMAVF = Arcam.	7
1.3	Gartner hype cycle for 3D printing, published July 2015 [5].	7
1.4	The AM industry is growing exponentially, and forecasts are good (Data from the 2015 Wohlers report [6]).	8
1.5	Applications of AM: a) dashboard of a prototype car printed in one piece in polymer [7], b) bracket for use in aerospace [10], c) fuel nozzle for the LEAP engine [11], d) Customized acetabular cup [13], e) burner to produce light bulbs [14].	11
1.6	Global structure of AM standards, as devised by ASTM International committee F42 [15].	12
1.7	Illustration of build up of residual stresses. a) via quenching of a hot metal ingot and b) via cold rolling of a metal plate [18].	14
1.8	Prince Rupert's drop: a tadpole shaped, quenched glass droplet that resists hammer blows to the thicker part, but is extremely sensitive to disturbances of the tail. Release of the strain energy (residual stresses) causes the drop to explode.	15
2.1	Schematic representation of the SLM process setup [27].	22
2.2	Schematic representation of the process window for SLM of AlSi10Mg [29].	24

2.3	Morphology of the melt pool on the top surface for (a) 400 W and 2300 mm/s and (b) 400 W and 3500 mm/s (from Qiu <i>et al.</i> [31]).	24
2.4	Relation between the energy density E_V , part density ρ_{rel} and surface roughness P_y for SLM of 316L (from Meier <i>et al.</i> [32]).	25
2.5	Remelting greatly reduces the top surface roughness, which is beneficial for density optimization (from Yasa <i>et al.</i> [34]). . . .	25
2.6	Various types of scan strategies: (a) unidirectional, (b) zig-zag, (c) island scanning with a 90° rotation of the zig-zag pattern within adjacent islands and (d) zig-zag, with indication of the 60° rotation for consecutive layers (from the PhD of L. Thijs [28]).	27
2.7	Intensification of the crystallographic texture by applying a rotation of the zig-zag scan strategy for consecutive layers. (a) Without rotation, SD implies the scan direction in each layer. (b) A 60° rotation and (c) a 90° rotation (from Thijs <i>et al.</i> [39]).	27
2.8	Absorption of bulk material for different laser wavelengths (Adapted from [42]).	29
2.9	Illustration of the effect of different alloy elements on the α - β equilibrium.	32
2.10	Examples of possible microstructures in Ti6Al4V: (a) Equiaxed (b) lamellar and (c) bimodal. The light phase is the α phase [45]).	34
2.11	Comparison of the size of the prior β grains in SLM (a), LMD (b) and EBM (c). Notice that the image for EBM has an approximately 5 times lower magnification. Image (c) adapted from [52].	37
2.12	Comparison of the microstructure inside the prior β grains in SLM (a), LMD (b-c) and EBM (d-e). The inset in image (c) reveals small β particles. The scale for all images is the same. Image (d) and (e) adapted from [57].	38
2.13	Reconstruction of the texture in the original β phase (b,d,f) based on the measured texture of the α phase (a,c,e) [60].	39

2.14	Plot of the ductility-UTS combination for various reported studies on the mechanical properties of AM produced Ti6Al4V. The dashed lines indicate minimum values set forth by the ASTM F2924 standard, and the grey box shows the approximate mechanical properties of an equiaxed material. Values included in this graph are listed in Appendix A1.	41
2.15	FCGR curves for SLM Ti6Al4V in the as built condition, after heat treatment at two different temperatures, and after HIP'ing. In a), the ZX orientation is shown, while b) shows results for the XZ orientation. The scatter band for conventional material is included for comparison (Adapted from [76]).	43
2.16	Precipitation of nanoscale precipitates during aging of SLM produced 18Ni300 maraging steel, determined by APT. (a) Homogeneous distribution of alloy elements in the as built condition, versus (b) clustering of elements in precipitates after aging (Adapted from Ref. [117]).	46
2.17	Carbides form a necklace structure around the cells in SLM produced M2 HSS. Inside the austenitic cells, further precipitation of lath-like martensite is seen [29]).	47
2.18	Cellular Al matrix, with Al-Si eutectic in the intercellular zones, in a top view of SLM AlSi10Mg. The microstructure varies around the melt pool boundary [35]).	48
2.19	Different phases present in the as built microstructure of LMD Inconel718 [53].	50
2.20	Microstructure of EBM copper for (a) a high oxygen concentration, (b) high purity copper and (c) high purity copper processed at a higher preheating temperature (from Frigola <i>et al.</i> [156])	52
2.21	Excessive sintering of Mg powder adjacent to a scan vector [162].	53
2.22	Melting regimes encountered during SLM of gold [168].	54
2.23	Columnar microstructure of SLM pure Ta and strong texture via EBSD mapping. The blue color indicates that the $\langle 100 \rangle$ direction is oriented along the vertical building direction [35].	55
2.24	Small peaks are still visible in the diffraction spectra of SLM produced parts, compared to the smooth curve for a fully amorphous melt spun ribbon [175].	56

3.1	Illustration of the stages of a typical fatigue crack growth rate curve [185].	63
3.2	a) Jagged cracks are formed during high energy regime SLM of CM247LC nickel alloy, which have a dendritic solidification structure at their surface (b). c) Straight grain boundary cracks with brittle fracture surfaces (d) are prevalent in the low energy regime (Adapted from Ref. [188]).	66
3.3	Amount of cracks observed for parts produced with various scan speeds and laser powers [188].	67
3.4	Weld cracking susceptibility of Ni alloys, as a function of the Al and Ti concentration (γ' forming elements) (Adapted from Ref. [140]).	67
3.5	Experimentally measured temperature distribution along the central line spanning from behind the tail of the melt pool ($X=0$) towards just in front of the melt pool ($X=350$). A plateau in temperature near the tail indicates the zone in which solidification takes place [193]).	69
3.6	Realistic modeling of the melt pool shape, melt flow and formation of the scan track [192].	69
3.7	Local residual stresses developed during deposition of a single track. a) longitudinal stresses in the direction of the scan track, scanned from right to left, and b) perpendicular to the scan track. Arrows indicate the tensile stresses inside the solidified melt (2 and 4), the balancing compressive stresses just below (3 and 5), and the compressive stress just in front of the melt pool caused by restricted thermal expansion and plastic yielding due to thermal softening (1). (Adapted from Ref [203]).	70
3.8	Temperature gradients as a function of the normalized wall height and normalized top surface temperature [207].	71
3.9	a) Melt pool area and aspect ratio as a function of the scan speed and laser power for a thin wall produced by LENS. 100 in/min corresponds to 42 mm/s. b) Corresponding solidification map for Ti6Al4V. Note the SLM process area, which typically lies between 600 and 4000 in/min in scan speed, and between 0-500W (Adapted from Ref. [209]).	72

- 3.10 a) Vertical residual stress in a thin, high wall, b) close up of the top region. Stresses are only present near the top because the geometry was assumed stress free, after which the laser passed over the top from left to right and back (Adapted from Ref [204]). 73
- 3.11 Residual stress measured by XRD along the edges of a thin H13 steel wall made by LENS. The values in ksi are for the principal stresses, and the direction of the largest principal stress is indicated. The stress ranges from 80 MPa (12ksi) to 260 MPa (38ksi) [217]. 74
- 3.12 2D plot of the vertical stresses in the cross section of a vertically built 10.9x10.9x100 mm Inconel718 beam, at mid-height. Measurement by the contour method. The dashed line indicates the boundary between tensile and compressive zones [219]. 75
- 3.13 Von Mises stresses are increased near the corner attachments to the base plate. Presence of such stress concentrating features may lead to cracks [220]. 75
- 3.14 Cracks in SLM produced M2 High Speed Steel, using a preheating of 100°C and 90W laser power. From left to right, the scan speed equals 250mm/s, 400mm/s and 550mm/s [221]. 76
- 3.15 Deformation of wedge shaped 316L specimens produced by SLM. (a-c) the deformation in three directions for a sample built horizontally, with d) a schematic representation of the deformation. Equivalent for vertically built samples in images (e-h) (Adapted from Ref. [224]). 76
- 3.16 Residual stress in a H13 steel wedge produced by LENS. The stress distribution is opposite to what is normally found, with compression at the edge and tension in the center, due to dilatation of the martensitic transformation that induces compression [225]. 77
- 3.17 Hardness of M2 HSS, for various preheating temperatures and scan speeds. The hardness increases with increasing preheating temperature, and decreasing scan speed (Adapted from Ref. [227]). 78
- 3.18 Deflection of a steel sheet on which a layer of pure iron was sintered according to a zigzag pattern, with the vectors in the direction of the measured curl. A higher hatch spacing decreased the deflection [235]. 80

3.19	Different scan strategies that lead to different residual stresses. The scan vectors in (a) are oriented, on average, along the long direction of the sample, which could lead to the largest deformation if there was no rotation of the pattern between layers. In (b), the vectors are oriented along the ‘short’ dimension of the part. Island scanning is shown in (c), and striping in (d). . . .	82
3.20	a) Zigzag scanning pattern and b) fractal scanning pattern [244].	83
3.21	Cracks in Ti6Al4V cubes for which each layer was remelted using the same parameters as the first scan. Sample 2 was produced using a high power and high speed, sample 3 with a low power and low speed [246].	84
3.22	Maximum residual stresses, expressed as a ratio with the yield stress, as a function of the temperature gradients. Variation of the laser power (Q) and scan speed (V), along the thick solid line, significantly change the temperature gradient but only moderately affect the stress. For fixed combinations of Q and V (thin lines), increasing preheating temperatures up to 400°C lower the stress by 40% [207].	86
4.1	Schematic representation of the concept behind stress measurement via XRD using the $\sin^2 \psi$ method.	90
4.2	Linear relation between $\sin^2 \psi$ and the strain $\epsilon_{\psi\phi}$. ψ is varied both positively and negatively. The dashed line is the linear fit. Data from a measurement on the top surface of a Ti6Al4V sample.	92
4.3	Principle of the contour method. The residual stresses in the x-direction acting over the middle plane in situation A are released by sectioning along the middle plane, which deforms accordingly in situation B. By forcing the cut surface to the original plane in situation C, the stress in the x-direction along the entire cut plane can be measured (From Ref. [281]).	96
4.4	Clamping only one half of the part during wire EDM cutting allows the part to deform and introduces cutting errors (From Ref. [281]).	97
4.5	Asymmetric errors are averaged out by taking both halves of the cut into account (From Ref. [281]).	98
4.6	Illustration of the bulge error during wire EDM cutting (From Ref. [281]).	98

4.7	Horizontal RS in the beam after the top pins were retracted after plastic bending of the beam. The bend test was modeled using symmetry boundary conditions in the middle plane of the beam, but is mirrored here to show the complete set-up. The color scale ranges from +300MPa (red) to -300MPa (blue), and the black lines in the middle section indicate a stress of 0MPa. The X and Z axes correspond to those of Figure 4.8.	101
4.8	2D stress map in the center of the known residual stress specimen ($X \times Y \times Z = 22 \times 10 \times 100 \text{mm}^3$), obtained using the contour method. The deformations are scaled by a factor of 250. The X-axis corresponds to that of Figure 4.9.	102
4.9	Comparison of the theoretical residual stress profile in a plastically bent beam after 4 point beam testing (dashed line), and that measured via the contour method (black line). The 2D stress profile obtained via the contour method is reduced to a 1D stress profile. The grey lines are different 1D stress profiles measured along the width of the specimen.	103
4.10	a) Dimensions of the BCM specimen. b) bridge shaped part on the base plate and c) removal from the base plate results in curl-up angle α_{BCM} [237].	104
4.11	Dimensions of the cantilever specimen.	105
4.12	Example of the fit of a parabolic curve through the measured deformation.	105
5.1	Schematic representation of the cuts that were used for contour method measurements. The stresses were also measured via XRD on the top surface, indicated in grey, after cut 1 was performed.	109
5.2	Maximum (σ_1 , black markers) and minimum (σ_2 , hollow markers) principal stress on the top surface of the 12 different samples. The grey bands indicate the average of the 12 values ± 1 standard deviation.	109
5.3	Model of the melt pool formation and solidification. In (a) the melt pool is shown 241 μs after the laser is switched on. There is no solidified material yet. The position of the laser is indicated in (b), right on top of the depression it creates. c) 515 μs later, the laser is switched off. At this point, the solidified region shows that the scan track formation is not a deterministic process but depends on local influences (Adapted from Ref. [291]).	111

5.4	Maximum (black markers) and minimum (hollow markers) vertical stress in the base plate-part interface defined by cut 1 in Figure 5.1. The grey bands indicate the average of the 11 values ± 1 standard deviation.	112
5.5	Stress map of the vertical stress in the base plate-part interface, calculated from the average deformations from 11 samples (dimensions are 15x15mm ²). The black line indicates the boundary between the tensile and compressive zone.	113
5.6	Stress map of the horizontal stress in the diagonal area, calculated from the average deformations obtained from 2 samples. The black line indicates the boundary between the tensile and compressive zone. The stress profile along the dashed line is used later on in Figure 5.13b.	115
5.7	Isometric view of the horizontal stress in the diagonal area. The black line indicates the boundary between the tensile and compressive zone.	115
5.8	Indication of all parameter sets used for parts built by 3D Systems Layerwise.	116
5.9	(a-c) Full markers indicate the maximum principal stress (σ_1) for all combinations of P and v shown in (d), as a function of the laser power (a), scan speed (b) and energy density (c). Diamond markers indicate results from parameter sets labeled '1' in (d), while circles are results from group '2'. In addition to the stress, the hollow markers indicate the ratio between the stress in the direction of the scan vectors and perpendicular to the scan vectors.	118
5.10	Maximum principal stress measured via XRD for all parameter combinations, for different layer thicknesses: a) 30 μ m, b) 60 μ m, c) 90 μ m and d) 120 μ m.	120
5.11	Curvature of all process parameter sets, given as combinations of P and v values for different layer thicknesses.	121
5.12	Comparison of the average curvature for each layer thickness between two different batches. There is an overall trend for higher curvatures for thicker layers, but both batches have an anomalous result for one layer thickness value.	121

5.13	Application of the model developed by Mercelis and Kruth [231] to predict the horizontal stresses in a) the base plate ($z=0-0.02\text{m}$) and the part ($z=0.02-0.035$) before the part is removed from the base plate. b) Horizontal stress in the part after the part is removed from the base plate.	126
5.14	The christmas tree step effect (from Ref. [296]).	126
5.15	Diffraction spectra for different preheating temperatures. The $\{200\}$ peak of the β phase becomes visible after using 300°C preheating.	130
5.16	a) Without preheating, the microstructure consists of twinned α' martensite. A collection of twins are indicated by the ellipse. b) Using 400°C leads to a fine, lamellar $\alpha+\beta$ structure. The β phase is present as thin layers between the α plates.	131
5.17	Evolution of the hardness as a function of preheating temperature. Notice the difference between the top and the bottom of the sample. The numbers next to each marker give the exact hardness value.	132
5.18	Influence of the interstitial content on the ductility of pure Ti. The red dashed line indicates the concentration measured in the powder, the blue areas represent the concentrations measured in the parts. (Adapted from Ref. [298]).	134
5.19	Residual stress in the top layer, measured via XRD. There is a 50% decrease by using 400°C preheating.	135
5.20	Deformation of bridge shaped specimens upon removal from the base plate for different preheating temperatures ranging from no preheating (NP) to 400°C	135
5.21	Yield strength of Ti6Al4V as a function of temperature [46]. . .	136
6.1	Columnar microstructure of Ti6Al4V (a,b), Ta (c,d) and W (e,f). a, c and e are side views. b, d and f are top views. The rotation of the scan strategy was 90° for Ti6Al4V causing the appearance of a square pattern. For Ta and W, it was set close to 60° . . .	144
6.2	Side view of the cellular microstructure of a) AlSi10Mg, b) 316L, c) 18Ni300 maraging steel and d) Inconel718. The inset in the top right of each image is a close up of the cells in the top view. The arrows indicate former melt pool boundaries.	145

- 6.3 Microcracking in W (a,b) and Hastelloy C276 viewed from the side and top. The arrow in (c) indicates a jagged, non-vertical crack in Hastelloy C276 which is different from the straight, vertical cracks that are more abundant. 146
- 6.4 Close up of an open crack on the top surface of a Hastelloy C-276 sample, showing the smooth, dendritic surface inside the crack. 148
- 6.5 Top surface of all examined materials. (a) AlSi10Mg, (b) Ti6Al4V-ELI, (c) Ti CP1, (d) 316L, (e) 18Ni300 maraging steel, (f) Inconel718, (g) Hastelloy C-276, (h) W, (i) Ta. The black arrows indicate the scan direction in every track, except for AlSi10Mg where it was not possible to distinguish the scan direction of the tracks. The white arrows indicate the orientation of the maximum principle stress, except for W. 150
- 6.6 Applying the measured curl up α_{BCM} to a stress free bridge yields a stress state identical to a stress state that would lead to that curl up, but of opposite sign. Shown here for Ta. Points A and B mark the locations of the minimum and maximum stress. 152
- 6.7 Plotting the first principal stress σ_1 , measured via XRD, and the BCM curl-up angle α_{BCM} as a function of (a) the thermal diffusivity, (b) the thermal expansion, (c) the melting temperature, (d) the yield stress and (e) the thermal shock resistance. In (f) the first principal stress is plotted versus α_{BCM} , indicating that there is also no clear correlation between the different types of RS measurements. 154
- 6.8 a) Prior β grain columns in Ti6Al4V disappear and melt pool boundaries become visible by addition of 10 wt% Mo in (b). . . 159
- 6.9 a) A top view of the microstructure of Ti6Al4V+10Mo, showing bright, unmolten Mo particles, and fluid lines indicating local variations of Mo concentration due to incomplete mixing in the melt pool. b) Side view, revealing a cellular microstructure, as well as a clear delineation of the melt pool boundaries. The arrows indicate locations where the grains continued growing into a new melt pool. 160
- 6.10 Microstructure of heat treated Ti6Al4V+10Mo, treated and quenched at (a) 650°C, (b) 850°C and (c) 900°C. The arrows indicate Mo rich areas, fully stabilizing the β phase. 160

- 6.11 Diffraction spectra of as built Ti6Al4V+10Mo, as well after quenching from 650°C, 850°C, 900°C and 1050°C. The as built material consists of 100% β phase, and is again so after quenching from 900°C or above. In reality, the magnified peaks are 10 times smaller than depicted. 161
- 6.12 Calculated vertical pseudo-binary phase diagrams of the different compositions. The red line is the liquidus, the blue line the solidus. a) General representation of the partition coefficient k for solute X. b) Ti6Al4V system with varying amount of Al. c) Ti6Al4V system with varying amount of V. d) Ti6Al4V+10Mo system with varying amount of Mo. e) Ti6Al4V+10Mo system with varying amount of Al. f) Ti6Al4V+10Mo system with varying amount of V. 163
- 6.13 Thin region at the melt pool boundary in which planar solidification is stable. Transition (marked by the white striped line) from planar to cellular solidification occurs within 0.5–1.0 μm of the melt pool boundaries, which are indicated by the arrows. 164
- 6.14 Engineering stress-strain curves for Ti6Al4V+10Mo (black) and Ti6Al4V (grey) produced by SLM. 166
- 6.15 Fracture surfaces of Charpy V-notch specimens: a) horizontal specimen, b) vertical specimen. The white arrows indicate the crack propagation direction. The top right inserts show where the images were taken on the fracture surface, and the orientation of the fracture surfaces with respect to the layers. 167
- 6.16 Solidification map for Inconel718, with indication of the expected combinations of \vec{G} and \vec{R} for three different parameter sets [142]. 170
- 6.17 Local variation of the crystal structure in SLM Inconel718 by variation of the scan parameters and use of two different lasers (Adapted from Ref. [142]). 170
- 7.1 Original microstructure of the reference material. The α phase is lighter and the β phase darker. 178
- 7.2 Microstructure of Ti6Al4V produced by SLM after heat treating at different temperatures for two hours, followed by FC. (a) 780°C and (b) 843°C below the β transus, (c) 1015°C above the β transus. Lighter zones are β phase, the dark phase is the α phase. 179

- 7.3 Side view of SLM material (a) after 1h at 940°C and AC followed by 2h at 650°C and AC illustrating the long columnar prior β grains. After heat treatment, a lamellar mixture of α and β is present inside the columnar prior β grains. (b) After 1015°C, 2h, WQ, indicating the extensive growth of the columnar grains. Due to the water quench, the microstructure is fully martensitic. Notice the different scales. 180
- 7.4 Duplex microstructure of the *reference material* consisting of equiaxed α grains and lamellar $\alpha+\beta$. (a) two hours at 780°C, followed by furnace cooling and (b) one hour at 940°C, followed by air cooling to 650°C. The α phase is light, the β phase is dark. Notice the increase in lamellar fraction when treated at a higher maximum temperature. 181
- 7.5 Comparison of the similarity in α plate size after (a) two hours at 940°C and (b) twenty hours at 940°C, followed by furnace cooling. The α phase is light, β is dark. The arrows in (b) indicate globularized α grains. 181
- 7.6 Illustration of the smaller α colony size after (a) two hours at 1020°C compared to after (b) twenty hours at 1040°C, followed by furnace cooling. The α phase is light, β is dark. The arrows indicate grain boundary α 182
- 7.7 Microstructure of the SLM material after two hours at 850°C, followed by (a) furnace cooling, (b) air cooling and (c) water quenching. The α needle size is very similar for all three microstructures, illustrating the minor effect of cooling rate when treated below the β transus. 184
- 7.8 Stress-strain curves for as built SLM material and reference material. 184
- 7.9 a) Fracture strain, and b) yield stress of the reference (full markers) and SLM material (hollow markers) in function of the maximum heat treating temperature. Results of all heat treatments are shown, regardless of cooling rate. All supertransus treatments used either AC or FC from the β range. The dashed line indicates minimum values required to meet ASTM standard F2924 for Ti6Al4V-ELI produced by powder bed fusion. 186

7.10	EBSD orientation maps of a) SLM material after two hours at 850°C, followed by furnace cooling. b) SLM material after half an hour at 1020°C, followed by two hours at 730°C and air cooling. Contrast is provided by the different orientations of the α phase, while the β phase is present as a thin layer between the α phase. Notice the different scale. The build direction for both images is vertical.	189
7.11	$\{10\bar{1}2\}$ pole figures of the hexagonal phase in (a) the as built SLM material and (b) the SLM material heat treated above the β transus, for 20 hours at 1040°C, followed by furnace cooling. In (a), the texture is present in the α' phase which has a similar crystal lattice as the α phase. In (b) the texture in the α phase is shown.	190
8.1	Sample orientations of the XZ, ZX and XY compact tension specimens. The dashed lines indicate the direction in which the crack would normally propagate, but also indicate the plane along which the samples were cut for the contour method. . . .	194
8.2	(a-c) Averaged surface contour for the three samples. d) Fitted quadratic spline of the contour data shown in (c).	196
8.3	Representative fracture surfaces for all three orientations. The surface can be divided in three parts: The notch that was precut using wire EDM and is not an actual part of the fracture surface, the pre-crack (front indicated by dashed red line), and the fast fracture zone. On the right: 2D residual stress plots obtained using the contour method, for a) the XY specimen, b) the XZ specimen and c) the ZX specimen.	197
8.4	FCGR curves for all three orientations in the as built (AB) condition, after stress relief at 650°C (SR) and after heat treatment (HT) at 890°C. Note that in a), the XY orientation shows an increased FCGR after stress relieving, while the XZ and ZX orientation experience a decrease in FCGR after stress relief [72].	199

- A.1 $\text{Sin}^2\psi$ -curves as measured on the Ti6Al4V cubes a) 1 and b) 5, for $\phi=0^\circ$ (top graph), $\phi=45^\circ$ (middle graph) and $\phi=90^\circ$ (bottom graph). Measurement points for negative ψ values are indicated by hollow markers, and those for positive ψ values with full markers. These curves are representative for all curves obtained on Ti6Al4V samples in this work. 212
- A.2 $\text{Sin}^2\psi$ -curves for $\phi=0^\circ$ (top graph), $\phi=45^\circ$ (middle graph) and $\phi=90^\circ$ (bottom graph), as measured on the cubes made of (a) tungsten, (b) tantalum, (c) Inconel 718, (d) Hastelloy C-276, (e) 316L, (f) Ti Grade 1, (g) 18Ni300 maraging steel and (h) AlSi10Mg. Measurement points for negative ψ values are indicated by hollow markers, and those for positive ψ values with full markers. 213

List of Tables

1.1	Categories of AM processes.	3
2.1	Comparison of the three main AM processes for metals: Selective Laser Melting (SLM), Electron Beam Melting (EBM) and Laser Metal Deposition (LMD).	30
2.2	Influence of the various microstructural features on different mechanical properties of Ti6Al4V (From the PhD by E. Brandl [49]).	36
2.3	Fracture toughness of SLM Ti6Al4V reported in literature, for different heat treated conditions. Values for conventional material with a martensitic or lamellar microstructure are also given. . .	42
2.4	Fatigue limit of AM Ti6Al4V reported in literature.	42
3.1	Composition of Inconel718, Inconel625, Inconel738LC and Hastelloy X, four important nickel alloys in AM. All values are maximum values unless intervals are given.	64
4.1	Type of radiation, diffraction angle and associated diffracting crystal planes, and X-ray elastic constants (XEC) of the different materials used in this work.	94
5.1	Regression analysis coefficients based on XRD values for the laser power, scan speed and layer thickness related to Equation (5.1).	119
5.2	Regression analysis coefficients for the laser power, scan speed and layer thickness related to Equation (5.2).	122

5.3	Oxygen and nitrogen content of the powder and of parts produced at different preheating temperatures.	132
5.4	Mechanical properties for the different preheating temperatures. The yield stress goes up, the ductility decreases.	133
6.1	Material properties gathered from literature used to compare all materials [143, 302–304].	141
6.2	Specific etchants used for each alloy.	141
6.3	Composition of Hastelloy C-276. All values are maximum values unless preceded by a ‘~’, indicating approximate values [304].	147
6.4	Overview of density, deformation angle, measured maximum stress and calculated stress to cause the measured deformation for each material. Point A and B refer to the points indicated in Figure 6.6.	149
6.5	The solidification range ΔT and partition coefficient k for the different pseudo-binary sections of Ti6Al4V and Ti6Al4V10Mo shown in Figure 6.12, as calculated by ThermoCalc. The partition coefficient is an average value over the whole solidification range.	164
6.6	Static tensile properties of Ti6Al4V+10Mo compared to regular Ti6Al4V processed by SLM. For reference, standard specifications for two types of β titanium alloys for use in surgical implants are given as well as mechanical properties for Ti15Mo5Zr3Al.	166
7.1	Mechanical properties of as built SLM and reference material.	183
7.2	Mechanical properties of the SLM material after different heat treatments. Treatment six to eight are well known titanium heat treatments [46]. Samples for treatment three were built in a different batch in which building errors are present, which led to premature failure of the components.	185
A.1	Static tensile properties of Ti6Al4V reported in literature, for different AM techniques, heat treatments and build orientations. * = flat. ° = polished	208

Chapter 1

Introduction

Additive Manufacturing or AM is the general term for processes that enable complex 3D parts to be created by adding material where needed rather than subtracting material where it is not. Typically, this is achieved in a layer by layer process, where each layer also consists of line tracks deposited/solidified adjacent to each other. This complex 1D to 2D to 3D approach opens up the field for much more complex designs, but also introduces physical and metallurgical phenomena specific to this type of manufacturing processes, as will be made clear further on. Selective Laser Melting (abbreviated to SLM in the remainder of this work) is one such AM technique, and is also the technique used throughout this research.

The SLM process is compared to other AM processes, and its particularities that are important for the comprehension of this work are highlighted in this introduction. Additionally, the advantages and disadvantages, as well as the current applicability and future outlook of the process are discussed, which will also serve to clarify the need of the research conducted in this project. To conclude, the aim of this research is explained, as well as the methodology followed to achieve the stipulated goals.

1.1 Additive Manufacturing

1.1.1 Process categories

AM has been officially defined by the ASTM F42 committee as *“the process of joining materials to make objects from 3D model data, usually layer upon layer, as opposed to subtractive manufacturing methods”* [1]. It is the mature collective name of processes formerly described as ‘Rapid Prototyping’ or ‘Rapid Tooling’ [2]. It gained traction with the invention of stereolithography by Chuck Hull in 1986 [3]. Stereolithography allows production of polymer parts and was originally intended to serve as a fast way to create prototypes, hence the early name of ‘Rapid Prototyping’. Over time, with the maturation of the technology, new processes were created that also allowed processing of metals or even ceramics. Nowadays, state of the art parts are incorporated in commercial aircraft, inserted into the human body and applied in other safety critical environments, providing the best evidence of the economic viability of AM.

All AM processes share the basic working principle of adding material where needed rather than subtracting it or using molds. However, they differ in the material that is added, the morphology of the material added, the way of supplying this material to where it needs to be and the consolidation mechanism. The International Organisation for Standardization (ISO) has recently defined **7 classes** into which all AM processes can be divided, listed in Table 1.1 [4]. The table details the feedstock type, working mechanism and a qualitative comparison based on cost, speed, resolution and performance.

Table 1.1: Categories of AM processes.

Category Name	Material	Material Form	Working Mechanism	Cost	Speed	Resolution	Performance
Material Extrusion	Polymer	Wire	Warm extrusion of polymer wire fed through a heated nozzle.	+++	0	-	-
Material Jetting	Polymer	Liquid	Material is deposited in droplet form through heated nozzle	0	-	+	-
Binder Jetting	Sand Metal Ceramic	Powder	Binder in droplet form deposited on powder bed, followed by debinding, sintering and infiltration	-	+	-	-
Powder Bed Fusion	Polymer Metal	Powder	Energy source fully melts powder particles in top layer of powder bed	---	--	+++	++
Directed Energy Deposition	Metal	Powder Wire	Powder or wire is fed into the energy source, mounted on a robotic arm	-	++	0	++
Vat Polymerisation	Polymer	Liquid	UV light polymerizes liquid prepolymer layer by layer	+	0	++(+)	+
Sheet Lamination	Paper Metal	Sheet	Sheet cutouts are stacked and bonded	++	-	---	--

- In the first category called **Material Extrusion**, a polymer wire (usually nylon) is fed through a heated nozzle that can move in the X and Y (and Z) direction. If the nozzle cannot move in the Z direction, the base plate onto which the material is deposited can move in the Z direction. The polymer is heated to lower the viscosity and enable smooth deposition of continuous lines. This mechanism is used by most cheap desktop 3D printers.
- During **Material Jetting**, the material is again passed through a heated nozzle, but it emerges as liquid droplets rather than as a semi-viscous continuous line. In a process very similar to 2D inkjet printing, the droplets are deposited first on a base plate and then on top of each other. It is fairly easy to deposit multiple materials during the production of one part. The droplets solidify fast enough to produce a 3D part. This is one of the fewer used categories, with commercial machines and applications still to be announced. Stable droplets need to be produced at a workable temperature, and wax is the go-to material for this category.
- **Binder jetting** is a third category where droplets are deposited through a nozzle. But the droplets themselves are not the material from which the final product is made. Rather, the droplets are deposited on a layer of powder, effectively binding the powder particles together. By repeatedly applying a layer of powder and binding it, fragile ‘green’ 3D parts are built up. This process requires extensive post processing. The binder is first burned away and the powder is sintered together. The sintered part is then infiltrated by a liquid metal, often bronze, to produce a fully dense part. Since the final part usually consists of bronze and a different metal, the resulting mechanical properties are average at most, and these parts are often used for prototypes or sand molds. The advantage however is that it is not a high temperature process that would build up thermal stresses, so large metal parts can be made.
- In **Powder Bed Fusion**, a heat source is directed onto a metal or polymer powder bed, fully melting the powder particles and fusing them together. The energy source is either a laser or an electron beam. The powder is deposited by a scraper, rake or roller moving over the powder bed. Because of the high temperatures during the process, thermal stresses are built up, limiting the maximum size of producible parts. Loose, unmelted powder can act as a support for layers to be deposited on top, but support structures are often needed to conduct heat away and prevent sinking of the melt pool into the powder below. The SLM process belongs to this process category, as does Electron Beam Melting (EBM). Fully dense metal parts are possible, making this the process category with the widest applications in structural or functional applications.

- **Directed Energy Deposition** or DED is similar to powder bed fusion, but the powder is sprayed co-axially into the energy beam, or a wire is fed into the melt pool created by the beam, which is mounted on a robot arm allowing free movement. The process creates a larger melt pool than those commonly found in powder bed fusion, so it cannot attain the high level of detail possible in powder bed fusion. The Laser Engineered Net Shaping or LENS process, also called laser cladding (LC) or laser metal deposition (LMD) is the most prominent technique in this category. The abbreviations LMD, LENS and LC will be used interchangeably in the remainder of this work.
- In **Vat Polymerization** or stereolithography, a liquid bath of prepolymer is illuminated with UV light from above, causing it to polymerize and thus solidify. The parts are attached to a base plate which gradually lowers into the liquid bath as the process continues. Bottom-up approaches exist as well, where a thin liquid layer is illuminated from below, and the base plate is pulled upwards and out of the liquid. This bottom up approach is the one used by an emerging type of desktop 3D printers that have a higher resolution than extruder based designs.
- The last category, called **Sheet Lamination**, is not often used and can only marginally be considered additive manufacturing. A sheet is first cut to the right shape (producing scrap on the way that needs to be processed again) and stacked on top of other cutouts. The layers are bound to each other either via ultrasonic vibrations or glue.

1.1.2 Economic outlook

Figure 1.1 shows the Gartner hype cycle published in 2015 for different emerging technologies [5], including AM or 3D printing as it is called colloquially. These curves have five distinct regions. Moving from left to right, emerging technologies first move up the slope called **technology trigger**. During this period, the technology is still being developed, with scientific breakthroughs still pushing it towards economic viability. The technology then starts receiving widespread media coverage, creating expectations that cannot be met, at the **peak of inflated expectations**. After some time, the public becomes disillusioned with the technology and expectations drop dramatically in the **trough of disillusionment**. From this point onwards, the technology is allowed to mature without the burden of heightened expectations, and will traverse the **slope of enlightenment** to reach the **plateau of productivity**.

3D printing first appeared halfway the technology trigger in 2007, and gradually advanced until it reached the peak in 2012. At this point, it was recognized

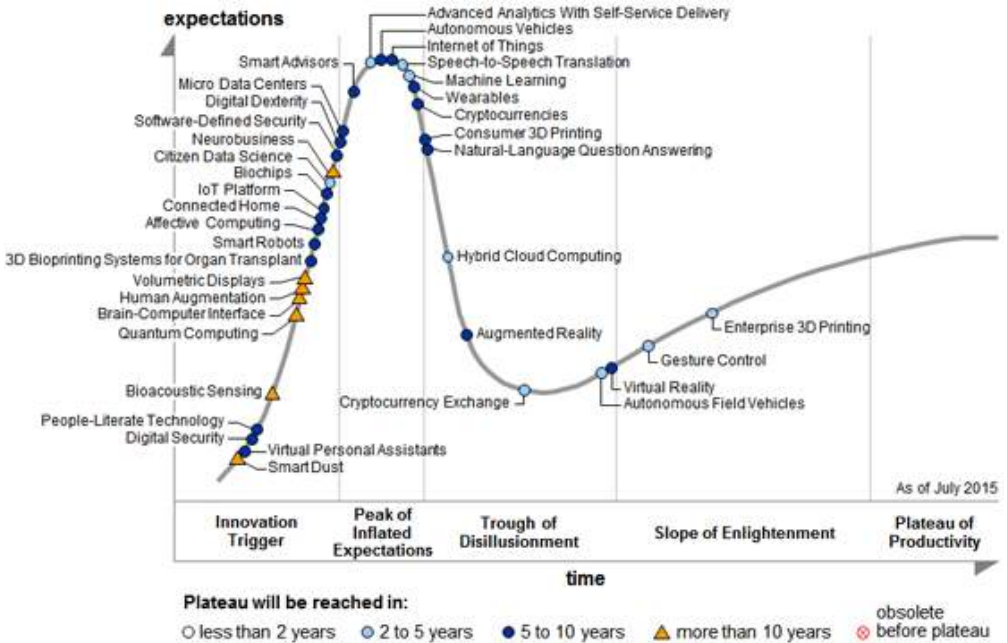


Figure 1.1: Gartner hype cycle for emerging technologies, published August 2015 [5].

that use of 3D printing as an aid in manufacturing was not moving at the same speed as consumer 3D printing. From 2013 onwards, enterprise 3D printing jumped ahead to the slope of enlightenment, while consumer 3D printing is currently still falling down the trough. These evolutions are reflected in the rise and fall of 3D printing stocks as well, shown in Figure 1.2. Peaking around January 2014, they have since lost between 50% and 90% of their maximum value, but are showing signs of bottoming out.

In Figure 1.3, various different technologies within the AM sector are shown along the Gartner hype cycle curve, showing that some parts of the AM sector have already matured, while others are still under development. The sub-sector to which this work would apply most, but not exclusively, is industrial 3D printing. This comprises all uses of AM for industrial applications, where performance is key. This inevitably limits the number of possible AM processes that cater to this subsector, mainly to SLM and EBM, and metal DED.

The growing commercial adaption of AM processes can best be illustrated by the economic revenue of the global AM market shown in Figure 1.4. The curve

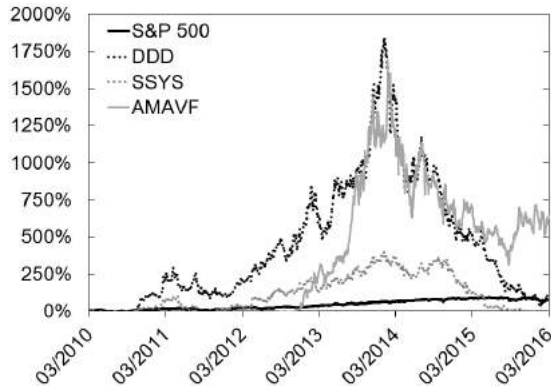


Figure 1.2: Rise and fall of three major 3D printing stocks, from March 1 2010 until March 1 2016, compared to the S&P500 Index. DDD = 3D Systems, SSYS = Stratasys and AMAVF = Arcam.

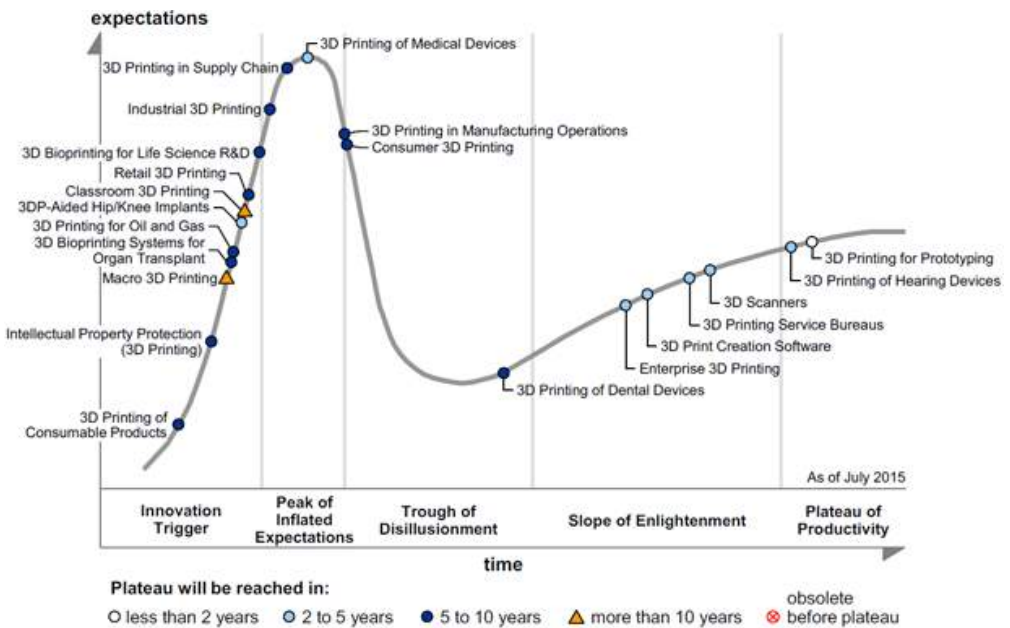


Figure 1.3: Gartner hype cycle for 3D printing, published July 2015 [5].

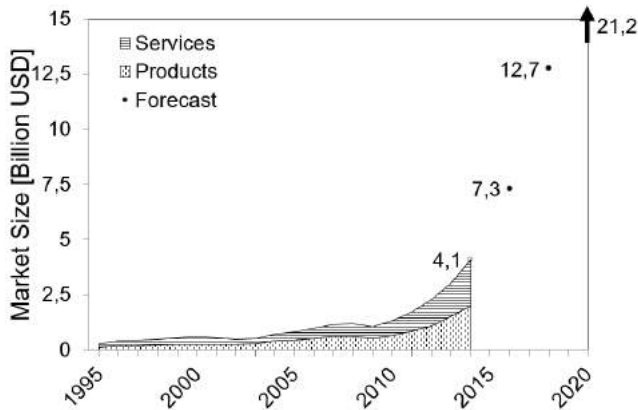


Figure 1.4: The AM industry is growing exponentially, and forecasts are good (Data from the 2015 Wohlers report [6]).

clearly indicates exponential growth over the past 25 years, with a compound annual growth rate (CAGR) of more than 30% for the last three years. Currently valued at \$4.1 billion, the AM market is expected to grow to \$21 billion by 2020. These numbers include all AM related sectors, such as production of AM machines, AM service providers as well as materials sales for use in AM. Based on those materials sales, metal AM is growing at the fastest rate of more than 40% CAGR over the past years [6].

1.1.3 Applications

While AM is a disruptive technology, it by no means has the aspiration to completely replace other manufacturing technologies. To compensate for the additional cost of AM parts, one or more of the advantages that AM offers compared to other technologies need to be exploited. The four main advantages are listed below and all stem from either designing complex structures or the digital nature of the process chain.

- In AM, it costs almost as much to produce the same part 100 times as it does to produce 100 single different parts. This is called **mass customization** and is particularly important for the medical sector. Each patient is unique, and bespoke produced implants increase the durability of the implant as well as the comfort level of the patient.

- Secondly, because material is added rather than removed, part designs can be optimized to have the same functionality with less material. Software can, for a certain load case and boundary conditions, redesign a part to **minimize the weight**. This is called topological optimization and regularly leads to weight savings of 30% or more, which is of major importance in aerospace.
- Weight savings can often be combined with an **improved performance** as well. Parts are currently designed with the limitations of conventional production techniques in mind. Other, optimal designs for a certain application may exist, but can be impossible to produce. For example, in conformal cooling, cooling channels can be placed much closer to the zones that need to be cooled, while the surface of heat exchangers can be maximized.
- Lastly, AM is considered a **fast** manufacturing technique. Ironically, the actual production process is rather slow, but the process chain leading up to the production is fully digital. This means it is a matter of days before a 3D file is printed, as opposed to weeks if molds need to be prepared. Moreover, making molds for unique parts is expensive, while in AM the digital design can quickly be adjusted.

There are additional advantages as well, such as a +90% material usage rate, compared to buy-to-fly ratios as low as 5% for some aerospace parts. Moreover, it allows production of complex parts of high melting point materials such as tungsten or tantalum, or other, hard materials that are difficult to tool.

The Gartner hype cycle specifically for 3D printing shown in Figure 1.3 indicates the wide variety of applications that could benefit from 3D printing. Its original intended use of rapid production of prototypes is already widely adopted, as is the production of patient specific hearing devices. A further selection of applications is given in Figure 1.5.

In Figure 1.5a, a full size polymer model of the dashboard allows car manufacturers to quickly judge the look, functionality but also the feel of the dashboard. Adjustment of the design and printing a second iteration run is a matter of days rather than weeks if molds have to be produced [7].

A different application is found in aerospace, where 1kg of weight reduction translates to \$80,000 in savings in one year of normal operation of an airplane [8]. The bracket shown in Figure 1.5b leads to a weight saving of 10kg for the entire plane, reducing the bracket-related CO_2 emissions by as much as 40% (production+operation), despite the higher input energy during production of the bracket [9]. While this specific design has not been flown yet, the Airbus A350 XWB is fitted with similar metal brackets [10].

Improved performance is also one of the key driving factors for what may be the most ambitious example of industrial application of AM, the fuel nozzle for the Leading Edge Aviation Propulsion or LEAP engine produced by General Electric [11]. The new nozzle shown in Figure 1.5c is five times more durable, 25% lighter and consolidates into one part, what would otherwise be 18 different parts. With around 8000 engines ordered for a total market value of more than \$80 billion, it is the most successful engine ever [12]. Considering that each engine contains 19 fuel nozzles, the production effort is enormous.

Customized hip implants can cater to patients that have a degenerative bone disease, leaving only a small amount of structurally solid bone to fix the implant. The acetabular cup in Figure 1.5d is built with positions of the screw fixations based on CT scans of the hip of a 15 year old girl with a degenerative bone disease. Moreover, the porous structure on the surface of the implant allows the bone to grow into the implant and provide further fixation [13].

Lastly, manufacturing process chains can also benefit from improvements in productivity by taking advantage of the geometrical design flexibility offered by AM processes. An example of this are the Inconel718 burners made by 3D Systems Layerwise and used by Havelis Sylvania to produce light bulbs, shown in Figure 1.5e. The burners' function is to heat the quartz glass to temperatures that allow easy forming. Originally produced in copper because of its excellent heat conductivity, the burner holes regularly clogged, leading to periodic production shutdowns to replace the burner. By optimizing the design and placing the cooling channels closer to the burner holes, the part could be made out of Inconel718, even though it has a lower thermal conductivity. Moreover, none of the AM produced parts have failed to date after more than 18 months, avoiding production shutdowns. These avoided costs easily compensate for the 80% higher primary cost of the part [14].

1.1.4 Standardization

By 2008, the industry had grown to a decent size, but lacked any type of standardization. Therefore, ASTM International founded committee F42 to develop and maintain standards on AM [15]. The decision was made to structure the standards according to Figure 1.6, with top level standards on concepts and requirements that are independent of the material or process, mid-level standards that are valid for material or process categories, and detailed standards on required material properties or other specialized information that would be specific for one material or process. In 2013, ASTM and ISO agreed to cooperate on the development of international standards, and devised a fast-track process for ISO to adopt existing ASTM standards, and vice versa. Not only does this

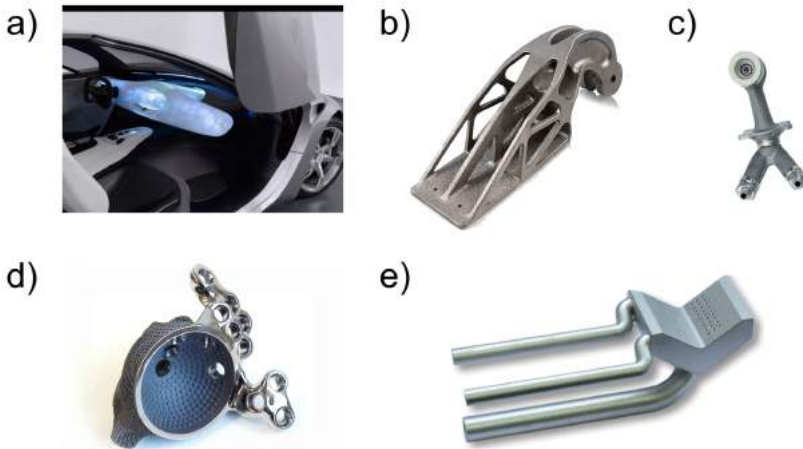


Figure 1.5: Applications of AM: a) dashboard of a prototype car printed in one piece in polymer [7], b) bracket for use in aerospace [10], c) fuel nozzle for the LEAP engine [11], d) Customized acetabular cup [13], e) burner to produce light bulbs [14].

increase the international validity of the developed standards, it also avoids the existence of multiple standards on the same topic, that may or may not provide the exact same information or requirements.

As of March 2016, specialized material properties standards that include requirements for minimal mechanical properties have been published for Ti6Al4V, Ti6Al4V-ELI, Inconel718 and -625, with more standards underway for CoCrMo, 316L, 15-5PH and 17-4PH steel.

1.1.5 Challenges in AM

Despite all of its advantages, several challenges remain for AM to overcome, and aspects of the AM process chain to improve on. One major drawback is that the actual production of parts is slow, with jobs lasting as much as one week or longer. Its reputation as a fast production process comes from the time gained in pre-processing. Improving the build rates will further drive down the cost of AM.

Other, active topics of research in metal AM that need improvement are:

- The **amount of metal alloys** that have been commercialized for metal

Structure of AM Standards

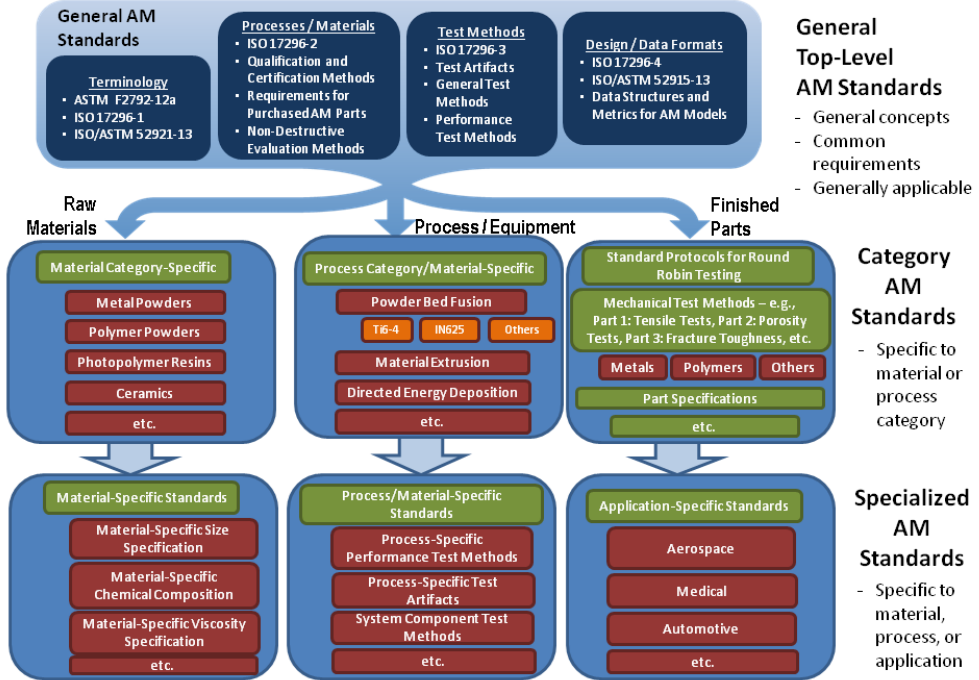


Figure 1.6: Global structure of AM standards, as devised by ASTM International committee F42 [15].

AM is limited, and this limited offer also limits the applicability of AM. There are several reasons for this, including the slow R&D of process parameters.

- **In process quality control.** AM is a prime candidate to produce parts in critical applications. The safety of AM components, however, has not been established. Repeatability is a concern, and therefore every part needs to undergo quality control after the process. Methods employed during this qualification are expensive and time-consuming. Therefore, if part quality could be guaranteed during the process, it would save both time and money.
- High cooling rates during the process create metastable, **unique microstructures** of which the mechanical behavior is not yet completely

documented. Moreover, their response to heat treatment is different than that of cast or forged material.

- Another effect of the high cooling rates are **residual stresses**. The stress limits the part size, causes deformations and can even lead to the formation of cracks. It is also a contributing factor to the limited materials palette that can be produced by AM.
- Non-optimal process parameters lead to **porosity**, and its influence on the mechanical properties, in particular the dynamic properties, is still not fully understood. Too often still, inferior mechanical properties are blamed on the porosity, while the influence of the microstructure or residual stresses are neglected.

1.2 Residual stress

Residual stresses are stresses that remain inside a body that is stationary and at equilibrium with its surroundings.

- Withers, 2001 [16]

Residual stresses (RS) can exist in all solids, be it polymers, metals or even fruit [17]. In metals, residual stresses originate from inhomogeneous plastic deformation. Local differences in plastic strain can be introduced by thermal or mechanical means. A typical example of thermally induced residual stress is quenching of a hot ingot, shown in Figure 1.7a. The outside of the ingot cools and contracts quicker than the inside. This colder, contracted outside compresses the hotter inside, which will yield plastically. The ingot cools down further to room temperature, and because the inside has been compressed plastically previously, it now pulls on the outsides, inducing the final residual stress distribution shown in Figure 1.7 [18]. This final state consists of radial compressive stresses at the surface and tensile stresses in the interior that compensate each other. These typical quenching stresses also exist in quenched glass shapes called Prince Rupert's drops [19]. Shaped like a tadpole, the compressive stresses on the surface are so strong that hitting the head of the tadpole shape with a hammer will not break the glass. However, the long, thin tail is fragile, and any abrupt movement of or kink in the tail will make the residual stress state become unstable, and the object will explode because of the built up strain energy as shown in Figure 1.8.

Another way to induce inhomogeneous plastic strain is by mechanical deformation. Rolling of metal ingots to sheets is one such process. The

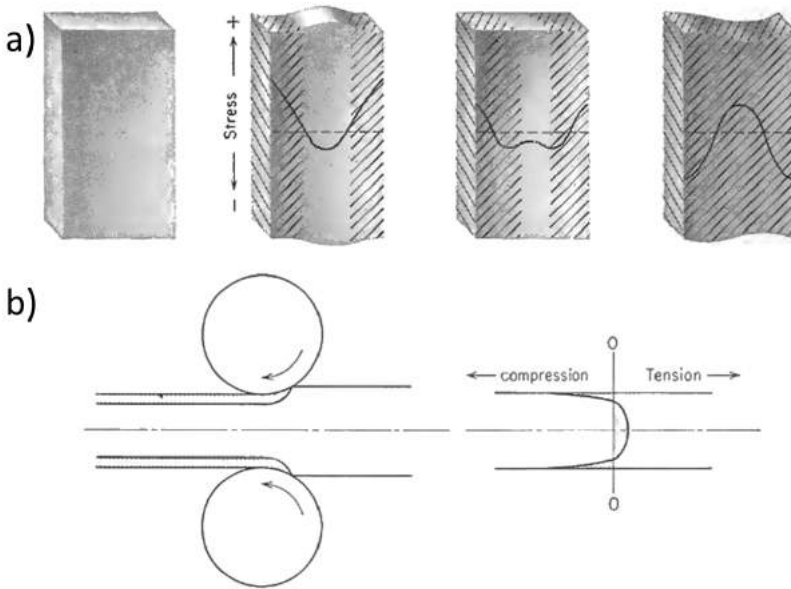


Figure 1.7: Illustration of build up of residual stresses. a) via quenching of a hot metal ingot and b) via cold rolling of a metal plate [18].

outside of the plate tends to plastically stretch more in the rolling direction than the inside. Thus, the outside will exert tensile forces on the inside, while it experiences compensating compressive stresses itself. The final stress state is similar to quenching stress, and is shown in Figure 1.7b.

Residual stresses are sometimes introduced on purpose, mostly to induce high compressive stresses at the surface. For instance, this is often done by a process called shot peening, wherein the surface of a metal object is pelted with small hard balls moving at high speeds. This plastically compresses the outside surface, and the compressive stresses increase the objects resistance to crack initiation. On the other hand, surface tensile stresses need to be avoided at all cost, but unfortunately, as the following chapters will show, SLM induces high tensile stresses at all sides of the parts.

1.3 Research aims and methodology

1. AM of metals is picking up speed, but it has taken years of research to get to the current state of commercialization. Apart from ongoing efforts for



Figure 1.8: Prince Rupert's drop: a tadpole shaped, quenched glass droplet that resists hammer blows to the thicker part, but is extremely sensitive to disturbances of the tail. Release of the strain energy (residual stresses) causes the drop to explode.

hardware improvement and monitoring systems, the current state of the art consists of process parameter windows for various metals, and limited mechanical property data for a smaller subset of that. As the number of unresearched but easily available and processable alloys is reducing, the goal of this research is to provide understanding of and solutions for one of the current major problems, which are **residual stresses**.

2. Conventionally produced parts are almost never used in the state in which they are cast or forged. Heat treatments are applied to change the microstructure and create superior mechanical properties, and for AM produced parts, this is no different. All too much, the heat treatments devised for cast or forged parts are still applied to AM produced parts. In addition to the residual stresses, this research aims to prove that **bespoke heat treatments** for AM produced parts need to be applied to achieve the best results.

The primary aim of this investigation remains to increase overall understanding of the parameters at play during development of residual stresses. This includes both material properties and process parameters. This basic knowledge can then be used to make decisions to deal with, reduce or eliminate residual stress related problems during SLM. It also shows just how much these residual stresses can influence the mechanical behavior of the material, corroborating the need for more knowledge on the matter. As a side effect to studying the residual stresses, this research produced other know-how that increases overall understanding of the SLM process.

Production of test parts, mostly cubes or deformation structures, took place on the LM-Q machine developed at KU Leuven, or by 3D Systems Layerwise [20]. The microstructure was characterized by well known techniques such as Light

Optical Microscopy (LOM), X-Ray Diffraction (XRD) and Scanning Electron Microscopy (SEM). Further determination of the mechanical properties took place by using Vickers hardness measurements and tensile testing. Residual stresses were determined via three distinctly different techniques. In the first method, the deformation of bridge or cantilever shaped structures is measured as an indirect indicator for the residual stress. The second technique employs X-rays and uses the crystal lattice as a strain gage, to determine surface stresses. Lastly, to quantitatively determine the residual stress inside of bulk parts, the contour method was used. Details on the principles and application of these methods are found in Chapter 4.

1.4 Outline

In the initial literature chapters that follow (Chapters 2 and 3), the details of the SLM process are discussed, as well as the state of the art on residual stresses in AM, to familiarize the reader with the basis on which this work is built. After discussing the residual stress measurement techniques employed in this work (Chapter 4), the results are subdivided in four main chapters, 5 to 8, which will each deal with a different aspect of residual stresses and/or improving the properties of the produced material.

In Chapter 5, the general shape, magnitude and directionality of the residual stress distribution are established in section 5.1. This provides necessary starting information to characterize the influence of different **process parameters** on the residual stress, which is discussed in section 5.2 (scan speed, laser power and layer thickness) and 5.3 (preheating).

Next, Chapter 6 looks at the influence of the **material** by comparing the microstructure, deformation of a bridge shaped specimen, and stress measured via XRD of nine different materials, in section 6.1. In section 6.2, the material, i.e. Ti6Al4V, is deliberately modified to change the microstructure and mechanical properties, as a case study for alloy tailoring for the SLM process.

The results from section 6.2 could be considered as measures taken *before* the process to obtain good mechanical properties, by careful alloy design. On the other end of the process chain, Chapter 7 contains results providing a strong case for bespoke *post process heat treatments* for AM produced material, again using Ti6Al4V as the studied material.

Lastly, knowing the general shape of the residual stress distribution from results given in section 5.1, Chapter 8 demonstrates the large influence that residual stresses can have on the mechanical behavior of additively manufactured parts.

The major conclusions drawn from the literature study and each of the results-containing chapters are reiterated in Chapter 9. It identifies the gaps in understanding and questions that have not been answered or were outside the scope of this thesis, but are none the less worthy of further future research.

The vast majority of this work was performed on Ti6Al4V, the material on which most literature exists on processing via SLM, as well as one of the most prevalent material already used for commercial SLM. In Chapter 6, eight other materials are also subjected to research in an attempt to find material related parameters that influence residual stress build-up.

Chapter 2

Additive Manufacturing of Metals

2.1 Major metal AM processes

Additive Manufacturing of metals is largely restricted to three main processes. SLM and EBM make up the process category known as powder bed fusion and have near identical working principles. The third is the LENS process. These three processes are capable of producing dense, functional metal parts that are applicable in demanding, structural applications.

2.1.1 Electron Beam Melting

Using an electron beam as a power source instead of a laser brings about several differences. Firstly, an electron beam cannot be directed using normal mirror optics. Using a magnetic field to guide the electron beam allows the beam to move much faster than a laser beam. The scan speed in laser based systems is limited by the inertia of the rapidly moving mirrors and is capped at around 3 to 5m/s. Being able to move the electron beam almost instantaneously increases productivity and allows creating and maintaining multiple melt pools at the same time.

Secondly, electron beams have a larger power density than laser beams used in AM processes. The higher scan speeds that are made possible by the lack of optics can then also be exploited. At a higher scan speed, the power also

needs to increase to supply enough energy to the powder bed to fully melt the powder particles. It also means that the layers in EBM can be thicker, and consequently, that coarser, cheaper powder can be used. The combination of higher scan speeds and thicker layers leads to EBM being faster and more productive than SLM.

A third consequence of working with an electron beam is that the process needs to take place in a vacuum. If the process chamber were filled with an inert gas, like in SLM, the electrons would collide with the gas molecules instead of interacting with the powder bed. Working in a vacuum also eliminates any problems with contamination of the melt with impurities from the atmosphere, such as oxygen or nitrogen.

Scanning of one layer during the EBM process occurs in two steps. In the first step, the whole powder bed surface is sintered by a fast moving, low power scan. Only in the second step is the powder fully molten and consolidated. This pre-sintering is an absolute necessity, because it avoids that powder particles become charged due to the influx of electrons and repel each other.

The pre-sintering step causes the EBM process to take place at high temperature. For Ti6Al4V, for instance, the temperature of the powder bed is around 600 to 800°C. This *in situ* heat treatment drastically lowers thermal gradients and provides an *in situ* annealing. Consequently, residual stresses are not an issue during EBM. The final product is still encased in the sintered powder volume, and needs to be removed by blasting apart the powder cake with virgin powder, to allow recycling of the powder. Because it works with coarser powder, thicker layers and a pre-sintering step, the surface roughness and precision of EBM parts is inferior compared to SLM.

2.1.2 Laser Metal Deposition

LMD is the main process in the ‘Directed Energy Deposition’ class. Using a robotic arm and spraying powder (or feeding wire) into the melt pool instead of using a powder bed leads to significant differences in process capabilities and limitations compared to SLM and EBM. The laser creates a large melt pool to capture the powder particles, making this process the least accurate of the three, and unable to create fine features possible in SLM and to a lesser extent, in EBM. Even though the scan speed used in LMD is a magnitude 10 times lower than in SLM, the large melt pool means that the overall deposition rate is higher.

The powder is fed through a coaxial nozzle around the laser, and is originally stored in hoppers. Using different hoppers with different powders, varying the

composition of the powder blend is easy, making LMD the optimal process to create functionally graded parts. In theory, this also makes the range of materials processable by LMD bigger than that for SLM and EBM, but in practice, only a limited amount of materials have been processed by LMD. The heat input during LMD is much larger than that in SLM, creating a visible afterglow of the part that becomes larger as the building process progresses (i.e. as the hot zone moves away from the base plate that acts as a heat sink). Although the process is performed at room temperature, this lowers thermal gradients, and creates a moderate amount of residual stresses compared to SLM.

Lastly, the powder bed in SLM and EBM can act as a support for subsequently deposited layers, but this generally leads to a bad surface finish of the down facing surface. Support structures provide extra support, as well as an improved heat conduction compared to the powder. Building of overhang structures via LMD remains impossible, partly because there is no supporting powder bed, but also because it cannot produce support structures that generally consist of a network of thin struts.

2.2 Selective Laser Melting

Figure 2.1 shows a schematic representation of the SLM process setup. A *laser*, typically an Yb:YAG fiber laser with a 1.064 μm wavelength, is directed onto the powder bed surface using a set of optical mirrors. The *optics* can contain additional elements that allow the melt pool shape and intensity to be monitored. Data coming from this monitoring can in a first approach be used to verify the quality of the produced parts after production, or incorporated into an online feedback system to correct any defects occurring during the process [21–25]. In fact, the American National Institute for Standards and Technology recently published a document in which the need for in process qualification and feedback control in AM are stressed [26]. An essential part of the optical system is the *f- θ lens*, that ensures that the focal point of the laser always coincides with the powder bed surface.

The powder is deposited onto the build area by a scraper or roller system moving over the surface. Several types of *deposition systems* exist and some are more suitable to deposit powder that do not flow easily, including irregular shaped particles, small powders or powders with a large spread on the particle size distribution (PSD) .

The powder is delivered to the deposition system either by a hopper mounted on the scraper or roller, or by a separate *powder feed* container, such as shown in Figure 2.1. Before each layer is scanned, this powder container is raised and

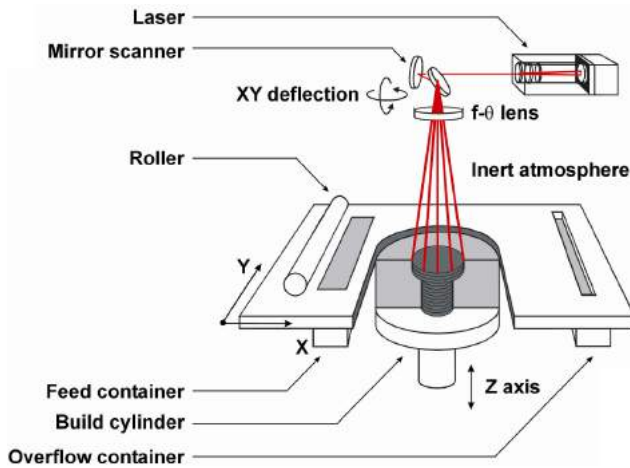


Figure 2.1: Schematic representation of the SLM process setup [27].

powder is then pushed across the powder bed by the deposition system. Before the powder is spread over the powder bed, the **build platform** is lowered by one layer thickness, making room for the new powder layer on top. An excess of powder is usually deposited, and any powder left over ends up in an **overflow container**, to be recycled for further jobs. Lowering the base plate, depositing powder and scanning of the laser over the powder bed are the three steps that are repeated during the SLM process to produce a 3D part.

2.2.1 Process Parameters

Countless parameters influence the final quality of produced parts. For example, the SLM Solutions build processor for the SLM280HL machine contains more than 150 parameter settings that can be changed, including obvious ones such as the laser power and scan speed, but also the laser intensity distribution or recoater speed. The parameters are generally categorized as in-process scan parameters, atmosphere related parameters and the parameters related to working with a laser. Additional to these parameters are the fixed parameters that cannot be changed during the process, such as the laser wave length and the material properties. A full, near-exhaustive list of all parameters affecting the SLM process and a discussion thereof can be found in Ref [28].

Scan parameters

The most important in-process parameters are the *scan speed* v [mm/s], *laser power* P [W], *hatch spacing* or *scan spacing* h [μm], *layer thickness* t [μm] and the *scan strategy* or exposure strategy. These parameters are directly related to how the layers are built up, and are usually the parameters that are varied during initial density optimization runs. Additional to these parameters is the *preheating* temperature of the substrate. As the substrate acts as a large heat sink, preheating lowers thermal gradients and, thus, residual stresses. P , v , h and t are often combined into a single parameter called the energy density E [J/mm^3], given by Equation (2.1). This is an engineering parameter and has no physical meaning, but can be useful to quickly compare parts made with different parameter sets.

$$E = \frac{P}{v \cdot h \cdot t} \quad (2.1)$$

The maximum **power** that can be used during the process is dictated by the laser hardware. For the **scan speed**, inertia of the mirrors in the galvanoscanner provides a practical upper limit. The scan speed and laser power are almost never varied independently, since the primary goal of the SLM process is to always create fully dense parts. In order to do this, sufficient heat must be supplied to a certain volume of material to melt it completely. Figure 2.2 [29] schematically shows the different melting regimes that can be encountered when varying the laser power and scan speed. Using a high power and low speed, excessive amounts of heat are supplied to the material, and the melting enters a keyhole mode regime. In this regime, which is used for laser welding, the melt penetrates deep into the underlying material. This is sustained by substantial vaporization of the material, which creates a recoil pressure that pushes the melt to the side and allows the laser to penetrate deep into the material. This type of melt pool is very unstable and can collapse onto itself, often trapping gas inside. Because this pore is buried so deep, it is unlikely that scanning of the next layer or even remelting the same layer will be able to remove this pore [30].

The low power, high speed zone does not provide enough power to fully melt the powder. When the power in the high speed regime is high enough to fully melt the powder, there is a risk that the heavily elongated melt pool will break up into smaller melts droplets, a phenomenon known as balling.

Balancing appropriate values of the scan speed and laser power, a stable melt pool is obtained. This is possible for various combinations of P and v , and the set of good combinations is called the process window. The influence of using a high or low power is difficult to see when looking at the melt pool, but Figure 2.3 shows that higher scan speeds cause a random variation in width of the

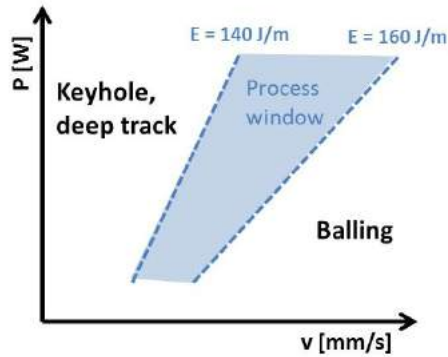


Figure 2.2: Schematic representation of the process window for SLM of AlSi10Mg [29].

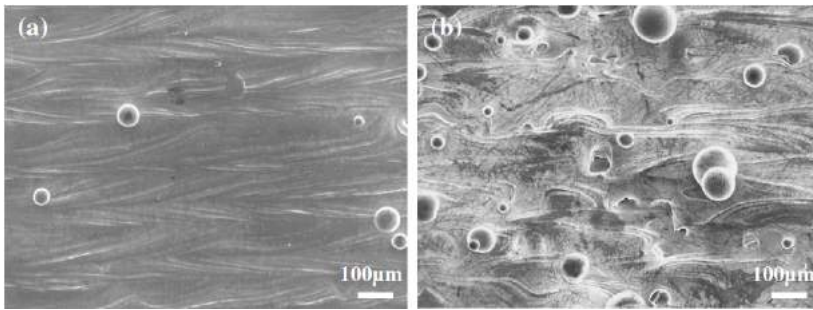


Figure 2.3: Morphology of the melt pool on the top surface for (a) 400 W and 2300 mm/s and (b) 400 W and 3500 mm/s (from Qiu *et al.* [31]).

melt pool, which is a sign of the onset of Plateau-Rayleigh instabilities that ultimately lead to balling [31].

A minimum value in the applied energy density is needed to obtain fully dense parts for SLM, shown in Figure 2.4 for 316L. Moreover, in the range of energy densities for which the part density was high, the surface roughness was minimized when using lower energy densities. Another strategy to increase part density and lower surface roughness is to remelt every layer, or just the top layer for improved top surface roughness only [33]. Remelting eliminates the valleys and peaks, creating a smooth surface, which is beneficial for layers to be added on top (Figure 2.5).

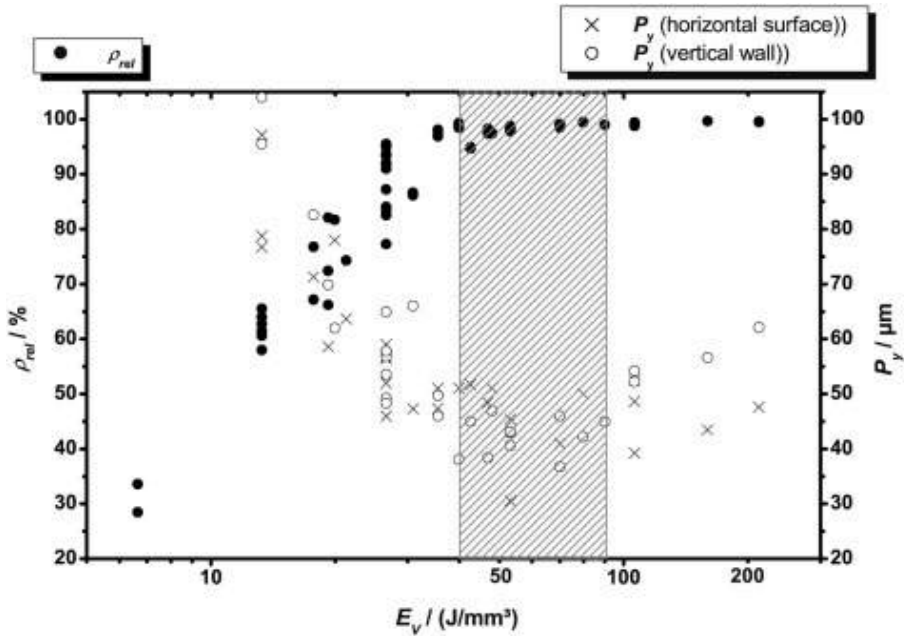


Figure 2.4: Relation between the energy density E_V , part density ρ_{rel} and surface roughness P_y for SLM of 316L (from Meier *et al.* [32]).

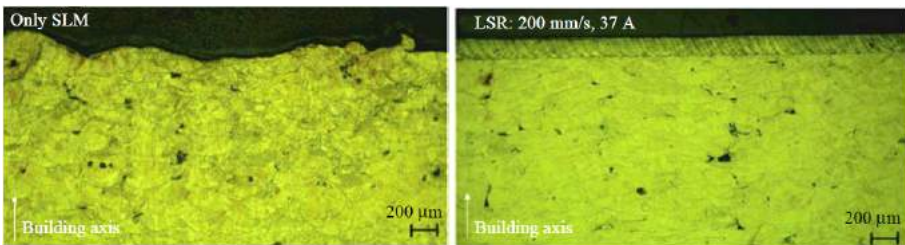


Figure 2.5: Remelting greatly reduces the top surface roughness, which is beneficial for density optimization (from Yasa *et al.* [34]).

The **hatch or scan spacing** is related to and should always be significantly less than the width of the melt pool. This ensures there is enough overlap between adjacent scan vectors. The width of the melt pool is mostly determined by the laser spot size, but also by the laser power and scan speed.

The lower limit of the **layer thickness** is determined by the particle size of the powder, while the upper limit is set by the need for full penetration of the melt pool into the underlying layers. Larger layer thicknesses increase the productivity, but decrease the geometrical resolution and enhance the staircase effect, which increases the surface roughness and deviation from the designed slope of the side surfaces.

One final, important scanning aspect is the **scan strategy** used to melt one layer, and the rotation thereof for consecutive layers. A common scan strategy wherein the laser follows a zig-zag pattern to melt a full layer is shown in Figure 2.6b. When the laser approaches the side of the specimen, it can either slow down, turn around and accelerate again while maintaining power, or switch off once it reaches the edge, perform the turnaround without power and accelerate to the desired scan speed outside the area to be scanned, and switch on the power again at the edge of the specimen. The latter strategy is known as working with ghost vectors, or as skywriting, and was developed because the former turnaround strategy creates local hotspots at the side that caused the formation of keyhole pores [35].

The unidirectional strategy shown in Figure 2.6a is not frequently used, as this tends to lead to lower densities, especially if there is no rotation of the strategy of consecutive layers [36]. In the third strategy, Figure 2.6c, the area to be scanned is divided into smaller ‘islands’ that are scanned sequentially. This subdivision shortens the overall length of the scan vectors, which has been shown to be an effective residual stress mitigating strategy [37]. The scan strategy within one island can still vary, as can the rotation of the scan strategy between adjacent islands. In the next layers, the island pattern can both be rotated by a certain angle, or shifted over a certain distance, to avoid that the island boundaries are at the same location for each layer, which increases the risk of creating aligned porosity due to the local overheating effect described above [38]. The island scan strategy is patented by Concept Laser GmbH, but most commercial systems employ a similar strategy called ‘striping’. This is a variation of the island scan strategy, but where the subdivisions are long stripes instead of square zones.

Finally, the **rotation** of the scan strategy, Figure 2.6d, strongly influences the texture that is developed during the SLM process, by influencing the thermal gradients [39], shown for tantalum (Ta) in Figure 2.7. A non-0° rotation also avoids pile-up of defects at the same location caused by a poorly chosen scan

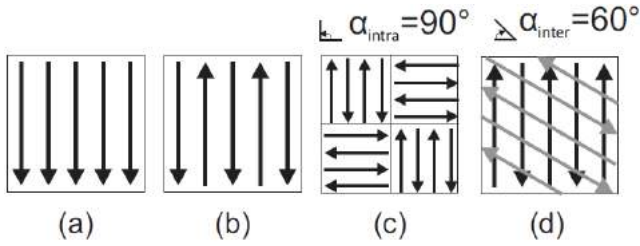


Figure 2.6: Various types of scan strategies: (a) unidirectional, (b) zig-zag, (c) island scanning with a 90° rotation of the zig-zag pattern within adjacent islands and (d) zig-zag, with indication of the 60° rotation for consecutive layers (from the PhD of L. Thijs [28]).

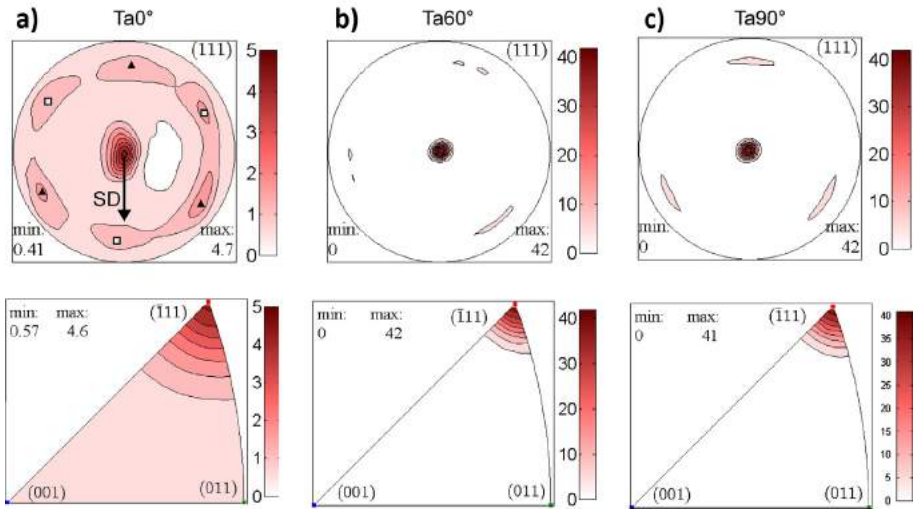


Figure 2.7: Intensification of the crystallographic texture by applying a rotation of the zig-zag scan strategy for consecutive layers. (a) Without rotation, SD implies the scan direction in each layer. (b) A 60° rotation and (c) a 90° rotation (from Thijs *et al.* [39]).

strategy. A seemingly random rotation angle of for example 56° ensures that the exact same orientation of the scan strategy is only repeated every 45 layers. This creates a more (planar) isotropic material.

Atmosphere parameters

The important atmospheric or environment parameters are the pressure and the inert gas that is used, usually nitrogen (N_2) or argon (Ar), and its purity with regards to oxygen (O_2) and moisture (H_2O) content.

The SLM process is almost always performed with a slight **overpressure**. The overpressure ensures that, if there would be a leak in the process chamber, no air will be able to rush in and cause oxidation, fire or an explosion. The surrounding pressure has also been found to have a great effect on the stability of the melt pool. The pressure inside the process chamber exerts a force on the melt pool.

The choice between N_2 and Ar as **inert gas** depends mainly on the material. N_2 cannot be used for all materials, as many metal alloys will interact with nitrogen. Examples are Ti alloys, with a possible formation of TiN, as well as steels, for which nitrogen is a strong austenite stabilizer. A study on SLM of N_2 and Ar gas atomized 17-4PH powder, processed in N_2 and Ar atmospheres, found that the Ar -only route created a martensitic microstructure, while the austenite phase dominated in the N_2 -only route. The N_2 gas atomized powder was fully austenitic, the Ar gas atomized powder was fully martensitic. Mixed modes using one gas for atomization and the other for processing both resulted in 100% martensite [40].

Laser parameters

Apart from the laser power, which was discussed under section 2.2.1, the **scan mode** (pulsed or continuous), the **laser wavelength**, the **intensity distribution**, **laser spot geometry**, **spot size** and **offset** of the focal point with the powder bed are other parameters associated with the use of a laser. The offset has been used to create a larger heated zone, causing in situ aging effect (martensite decomposition) in SLM of Ti6Al4V [41]. Pulsed systems have the advantage that they can deliver higher amounts of power, something that can be used to combine SLM with laser erosion to create a hybrid type of process [34].

Recently, with increasing industrial demand for high thermally conductive materials such as aluminium alloys or copper to be processed by SLM, the wavelength of the laser is becoming a point of discussion again. Currently, SLM systems use Yb:YAG lasers with a wavelength of $\lambda = 1.064\mu\text{m}$. As is visible in Figure 2.8, the absorption of various metal alloys is sufficient at this wavelength. The highly conductive materials however, have a low absorption at that wavelength, and would be more suitably processed with lower wavelength

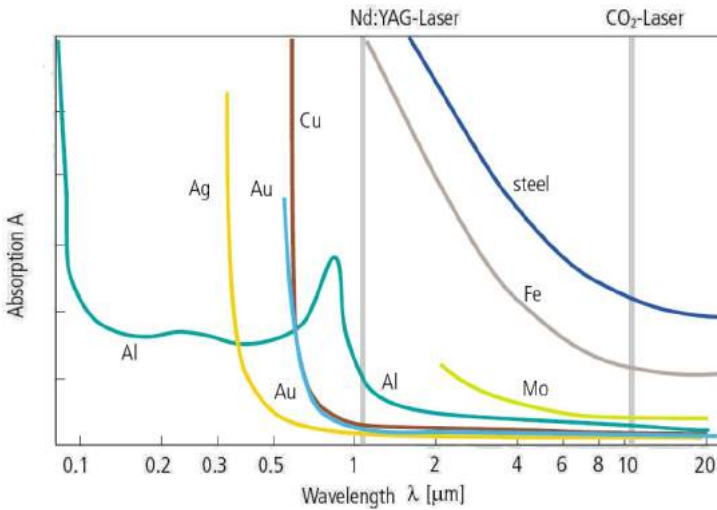


Figure 2.8: Absorption of bulk material for different laser wavelengths (Adapted from [42]).

lasers. One such example is a green laser. However, laser technology has not progressed far enough to make it economically viable to install a powerful green laser in an SLM system. A similar discrepancy between laser technology and SLM process technology occurred when the first SLS machines for metals were installed with CO_2 lasers that have a wavelength of $10.64\mu\text{m}$, because powerful Yb:YAG fiber lasers were not yet available or affordable.

Powders, however, absorb much more laser power than flat, polished surfaces, because the laser light is scattered by the powder particles. Tolochko measured absorptions for powders suitable for AM and measured an absorption of 59% for pure Cu for $\lambda=1.064\mu\text{m}$, while it is less than 5% for a flat surface [43]. Via modeling, Boley, Khairallah and Rubenchik [44] found that a bimodal particle size distribution or PSD can increase the absorption by a further 10% over a powder with a unimodal PSD, but this may reduce flowability.

To summarize, Table 2.1 lists the differences between SLM, EBM and LMD, in terms of their relative strengths and weaknesses for different process aspects discussed above.

Table 2.1: Comparison of the three main AM processes for metals: Selective Laser Melting (SLM), Electron Beam Melting (EBM) and Laser Metal Deposition (LMD).

	SLM	EBM	LMD
Accuracy	+	0	-
Precision	+	0	-
Available materials	+	-	0
Residual stress	-	+	0
Functionally graded materials	-	-	+
Surface roughness	+	0	-
Overhang structures	+	+	0
Production speed	-	0	+

2.3 Materials processed by Selective Laser Melting

At the moment, commercial SLM service bureaus tend to offer between 10 to 15 different alloys, including pure Ti and Ti6Al4V, some steel and nickel alloys, CoCr and AlSi10Mg. Apart from these alloys, numerous research groups are looking into other and sometimes more exotic metals in order to create a suitable process window for these materials. This research typically consists of finding parameters that lead to fully dense parts, characterization of the microstructure and static tensile properties and, in some cases, the influence of heat treatments on the microstructure and properties. These steps have been well documented for the materials mentioned above, and a summary is provided in this section. For a more complete and detailed overview of the origin of AM microstructures and various different materials processed by AM, the reader is referred to the more extensive literature study written by L. Thijs [28].

2.3.1 Titanium alloys

Introduction

Pure titanium is produced through the Kroll process, in which refined rutile ore is first reduced and treated with chlorine gas, forming $TiCl_4$. This gas is reduced to a Ti sponge by interaction with liquid Mg between 800°C and 850°C. The sponge is crushed and processed further into ingots [45].

Pure titanium melts at 1668°C. At temperatures between this melting point and 882°C, the body cubic centered (bcc) β phase is stable. Crossing the β transus, the β phase allotropically transforms into the hexagonally close packed

(hcp) α phase via the crystallographic Burgers relationship given in Equation (2.2).

$$\{110\}_{\beta} // \{0001\}_{\alpha} \text{ and } \langle 111 \rangle_{\beta} // \langle 2\bar{1}10 \rangle_{\alpha} \quad (2.2)$$

Titanium alloys are classified into three categories based on the volume fraction of the α and β phase. **α and near α alloys** have no or less than 10% of a stable β volume fraction at room temperature. These alloys are tough, strong and hard. Due to the limited amount of available slip systems for dislocation glide in the hexagonal α phase, the creep resistance is high as well. However, this also means that α alloys are difficult to form at room temperature, and are often processed in the $\alpha+\beta$ or β range. Unlike bcc materials, there is no ductile to brittle transition, and α alloys are suitable for cryogenic applications [46].

β alloys have a high volume fraction of stable β phase at room temperature. The bcc phase is relatively easy to deform, allowing processing at room temperature. The strength of these alloys can be increased by precipitation of small α precipitates. Addition of β stabilizing elements can lower the martensitic start temperature M_s to temperatures even below room temperature, suppressing the martensitic transformation.

$\alpha+\beta$ alloys have a stable β volume fraction between 10 and 50% and high strength at room temperature. The weldability is bad when the fraction of β exceeds 20%. The volume fractions, size and morphology of the α and β phases can be changed by heat treatment, thereby making it possible to tailor the mechanical properties towards the intended application [45].

Alloying elements can be grouped as α stabilizers, β -isomorphous elements and β -eutectoid elements, and neutral elements that do not influence the α - β volume fractions. Among the **α stabilizing elements**, *Al* is the only substitutional solute element that is commercially used. Oxygen, nitrogen and carbon are other, interstitial solute elements that stabilize the hexagonal phase. These elements push the α to $\alpha+\beta$ transus to higher temperatures, as illustrated in Figure 2.9a. Oxygen is added to pure Ti to create various grades of pure Ti numbered Grade 1 to 4, wherein the yield strength of the high oxygen content (0.4wt%O) Grade 4 is 480 MPa, compared to only 170 MPa for the 0.18wt%O containing Grade 1.

Neutral elements do not significantly influence the α to $\alpha+\beta$ transus as in Figure 2.9b, and are soluble in both the α and β phase. Sn, Zr and Hf are such elements. Although they do not alter the phase equilibrium, they are still added to provide solid solution strengthening.

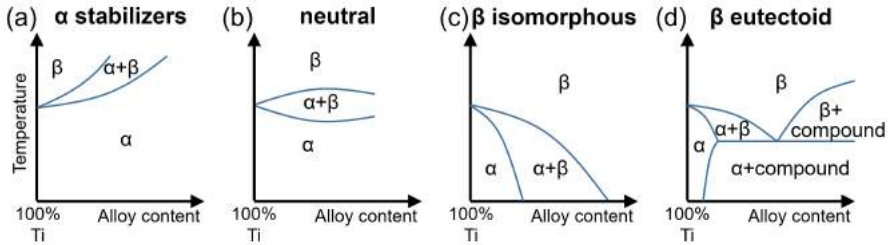


Figure 2.9: Illustration of the effect of different alloy elements on the α - β equilibrium.

Finally, β stabilizers can be divided into β -isomorphous elements and β -eutectoid elements, depending on their solubility in the β phase. If the alloy element is fully soluble over the whole concentration range, as is the case for V and Mo, that element is said to be β isomorphous. Sizeable additions of these elements can lower the β transus temperatures all the way to room temperature, as in Figure 2.9c. β -eutectoid elements, on the other hand, have a limited solubility in the β phase and tend to form an eutectoid reaction, dissociating the β phase into α phase and an intermetallic compound, like in Figure 2.9d. A further distinction can be made between elements for which the intermetallic compound formation is sluggish, like Fe, Mn and Cr, and active compound formers like Cu and Si. For the first category, the compound is formed at such slow rates that it can be neglected to occur during thermomechanical processing, likening the effect of these elements to the β isomorphous elements discussed above. Active compounds formation provide an opportunity for controlled precipitation of the intermetallic to enhance the strength [45, 46].

Ti6Al4V is, by far, the most known and used titanium alloy, particularly for use in aerospace applications, taking up more than 80% of the alloys' use. 50% of the world Ti production goes towards the fabrication of Ti6Al4V [46]. It belongs to the $\alpha+\beta$ alloys, with a stable β phase fraction of around 10% at room temperature. The Al content dominates the V content, pushing the β transus up to 1000°C.

Other phases in Ti alloys

Apart from the equilibrium α and β phase, other metastable, non-equilibrium or undesired phases can form in Ti alloys, the most notable of which is α' hcp

martensite. At high cooling rates from the β rich area above 900°C, the β phase can exhibit a martensitic transformation into an acicular martensite, consisting of α' platelets between 0.5 and 1.0 μm thick. This hexagonal martensite closely resembles the normal α phase, but is supersaturated in β stabilizing elements, which will cause the martensite to transform to $\alpha+\beta$ when heated sufficiently high in the $\alpha+\beta$ temperature range. The M_s temperature can be lowered by addition of β stabilizing elements. For Ti6Al4V, the M_s and martensite finish M_f temperature are 800°C and 500°C, respectively [45].

Other metastable phases include the α'' **orthorhombic martensite**, α_2 (Ti_3Al) and ω , on which more can be found in Ref [45–48].

Microstructures of $\alpha+\beta$ alloys

The microstructure of $\alpha+\beta$ alloys is determined by the thermomechanical history that the material has experienced.

- **Equiaxed:** In a first possible microstructure, the α phase is present as spherical or equiaxed grains, with remnants of β at the grain boundaries and triple points. This type of microstructure can only be achieved by heavy deformation of the material, after which the break-up of the original α lamellae and a dense dislocation structure can lead to recrystallization upon heat treatment in the $\alpha+\beta$ area. Heat treatment at 705°C, known as a mill anneal, can lead to a partial recrystallization, maintaining some lamellar structure as well. A recrystallization anneal at 925°C leads to full recrystallization. An example is shown in Figure 2.10a.
- **Lamellar** Shown in Figure 2.10b, slow cooling from the β area leads to nucleation and growth of a continuous α layer at the β grain boundaries, called grain boundary α or $\text{GB}\alpha$. Upon further cooling, more (secondary) α nucleates at the grain boundaries and grows into the β grains as parallel plates, following the Burgers relation. Groups of parallel, adjacent plates with the exact same Burgers relation are called α colonies, the size of which has a major influence on the mechanical properties. The size of α colonies is limited by the size of the β grain they grow into. Within one colony, the α plates are separated by a thin layer of β . Slow cooling rates such as those obtained during furnace cooling allow the grain boundary α , α plates within one colony and the colony itself to grow to a large size. Air cooling, on the other hand, produces a finer, sharper α phase, less $\text{GB}\alpha$ and smaller colonies, also known as acicular α . Intermediate cooling rates lead to a Widmanstätten or basket weave structure, while quenching

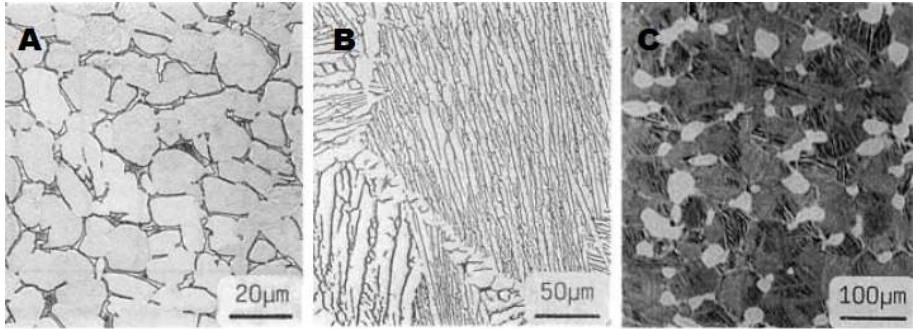


Figure 2.10: Examples of possible microstructures in Ti6Al4V: (a) Equiaxed (b) lamellar and (c) bimodal. The light phase is the α phase [45]).

produces an acicular (or orthorhombic) martensite. There is no time for $GB\alpha$ to form during quenching.

- **Bimodal:** The bimodal structure consists of a combination of equiaxed α grains and transformed β grains, in which a lamellar $\alpha+\beta$ is formed. In Figure 2.10c, the lighter grains are equiaxed α grains, while the dark grains are transformed β grains that under closer inspection consist of a fine lamellar $\alpha+\beta$. This structure can be formed by heat treatment high in the $\alpha+\beta$ area, where there is a large fraction of β , followed by rapid cooling and reheating to a lower temperature.

Mechanical properties

The mechanical properties of Ti6Al4V are strongly dependent on the microstructure. For instance, even the Young's modulus of Ti6Al4V varies between 105 and 120GPa due to the wide range of possible microstructures and the anisotropy of the hexagonal α phase.

For fatigue, both initiation and propagation of a crack are important. For low stress amplitudes (called high cycle fatigue (HCF), because the number of cycles to failure is high), the initiation stage is long and important, as is the growth stage. For higher stresses (low cycle fatigue or LCF), the growth stage is of dominant importance. The LCF limit for lamellar Ti6Al4V is around 880-900MPa for 10^4 cycles and a minimum to maximum stress ratio of $R=0.1$, and the HCF limit with a runout at 10^7 cycles ranges from 500 to 650MPa [46]. For the fracture toughness K_{IC} , crack growth at a microscale is important. K_{IC} values of a lamellar microstructure range between 50 and 100MPa \sqrt{m} ,

higher than that of a martensitic microstructure, which has a K_{IC} between 40 and 60 MPa \sqrt{m} [45, 46]. Equiaxed microstructures are more ductile, while martensitic microstructures are stronger.

Table 2.2 lists the influence of the various microstructural features on the different aspects of the mechanical behavior of Ti6Al4V [49]. At first glance, it is obvious that it is impossible to create a microstructure that optimizes all mechanical properties. Therefore, any applied heat treatment must be chosen with a particular application in mind. The size of the α colonies is one of the major factors, determining the effective slip length of dislocation glide. The colony size is determined mostly by the cooling rate. High cooling rates lead to smaller colonies, and in the extreme case of martensite formation, the colony size is equal to one martensite plate. A smaller colony size increases strength and decreases the ductility because there are more colony boundaries that hinder dislocation movement. An increased presence of boundaries is also beneficial to limit the propagation of microcracks, which is good for LCF.

Resistance against macrocracking, however, increases with increasing colony size, because the cracks need to either branch more often to follow the grain boundaries and thus create more crack surface area, or expedite more energy to cross through a grain. For the same reason, coarse, lamellar structures promote crack branching and a better resistance against crack propagation.

For bimodal microstructures, the segregation of elements into the α phase weakens the lamellar structure in the transformed β grains. This effect gets stronger as the fraction of primary α is larger. This deteriorates the resistance against crack initiation and thus lowers the HCF. The same effect is present for GB α layers on the former β grain boundaries. The strength difference between this layer and the rest of the microstructure increases void formation, lowering the ductility.

As mentioned above, the α colony size is limited by the size of the β grain in which it is formed. In a bimodal structure, the primary formation of some equiaxed α grains leads to smaller β grains, thus leading to a smaller colony size. This creates superior LCF properties compared to fully lamellar structures because the crack growth rate is lower, even though the crack initiation resistance is worse. The fracture toughness, on the other hand, is worse because the extent of crack branching is less.

Microstructure of Additive Manufactured Ti6Al4V

Ti6Al4V is one of the main alloys used in commercial SLM, and still is subject of widespread research. Its success in AM can be ascribed to the relatively

Table 2.2: Influence of the various microstructural features on different mechanical properties of Ti6Al4V (From the PhD by E. Brandl [49]).

	Strength (UTS)	Ductility (ϵ_{frac})	Fracture Toughness (K_{IC})	Crack initiation (HCF)	Crack propagation (HCF+LCF)
Fine	+	+	-	+	-
Coarse	-	-	+	-	+
Lamellar	-	-	+	-	+
Equiaxed	+	+	-	+	-
Widmanstätten α	-	-	+	-	+
Colony α	-	-	+	-	+
Secondary α	+	+	-	+	-
GB α		-	+	-	+

high cost of the base material, favoring high material usage rates such as those in AM, its biocompatibility (for biomedical applications), and high strength combined with low weight (useful in aerospace).

It is generally agreed upon that Ti6Al4V forms a columnar microstructure during AM under most processing conditions, in all three major metal processing techniques (SLM, EBM and LMD) [36, 50]. Representative examples are shown in Figure 2.11 [51, 52]. The elongated grains are oriented along the building direction (BD), or at a slight inclination from the vertical BD, depending on the scan strategy and the rotation thereof [36, 53]. The orientation of these grains is determined by the direction of the largest thermal gradients during solidification [36]. Unlike for other alloys, the planar solidification front is stable for Ti6Al4V, possibly due to the small solidification temperature range of roughly 6 to 10°C [54, 55]. The width of the prior β grains is loosely related with the hatch spacing, and their length to the layer thickness, or in other words, to the melt pool width and depth, illustrated by the different sizes obtained after SLM (Figure 2.11a), LMD (Figure 2.11b), and EBM (Figure 2.11c). Due to the high cooling rates in SLM and LMD, the β phase transforms into acicular α' martensite, although there is a significant gradient in LMD from bottom to top due to heat accumulation, which can cause a fine $\alpha + \beta$ lamellar microstructure at the top (Figure 2.12b). Even at the bottom, small β phase particles shown in the inset of Figure 2.12c can still exist between α' plates. Figure 2.12b was taken at a height of 60mm above the base plate. EBM results in a lamellar $\alpha + \beta$ due to preheating temperatures in excess of 800°C [56], but the scale of

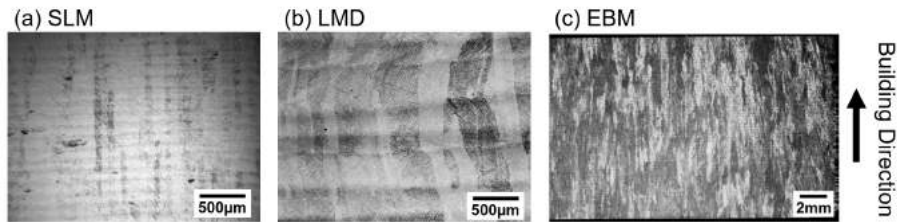


Figure 2.11: Comparison of the size of the prior β grains in SLM (a), LMD (b) and EBM (c). Notice that the image for EBM has an approximately 5 times lower magnification. Image (c) adapted from [52].

the microstructure can still vary, depending on the size of the produced part. Thin sections cool faster and have a finer microstructure than thicker sections, which is evident by comparing Figure 2.12d and 2.12e.

Upon solidification, the β phase in Ti6Al4V forms a $\langle 100 \rangle$ texture, like all other cubic materials processed via SLM. Martensite is formed according to the Burgers relation in Equation (2.2). Because there are a total of 12 possible variants of this relation, the strong texture of the β phase is severely weakened, and consequently, the mechanical properties of AM produced Ti6Al4V are fairly, but not completely isotropic. By reconstructing the parent β grains from α' EBSD maps of additively manufactured Ti6Al4V, several studies have visualized the original β texture [58–60], of which an example is shown in Figure 2.13.

Mechanical Properties of Additive Manufactured Ti6Al4V

Results obtained by different studies on the static mechanical properties of SLM Ti6Al4V are presented graphically in Figure 2.14. The minimum requirements set forth by the ASTM F2924 standard on powder bed fusion of Ti6Al4V are marked by the dashed lines. A grey box marked 'Equiaxed' denotes the typical strength and ductility for conventional Ti6Al4V with an equiaxed microstructure. Orange markers indicate results for EBM, green markers for LMD and blue markers for SLM. Round markers are for material in the as built condition, square markers for stress relieved samples, triangles for heat treated samples and diamond shapes for HIP'ed material. The values marked 'Heat Treatment' indicate samples that were subjected to a heat treatment upwards of 700°C, without the application of pressure. Finally, open markers are horizontal samples, while full markers are vertical samples.

Overall, the strength of SLM material is quite high, due to the fine, acicular

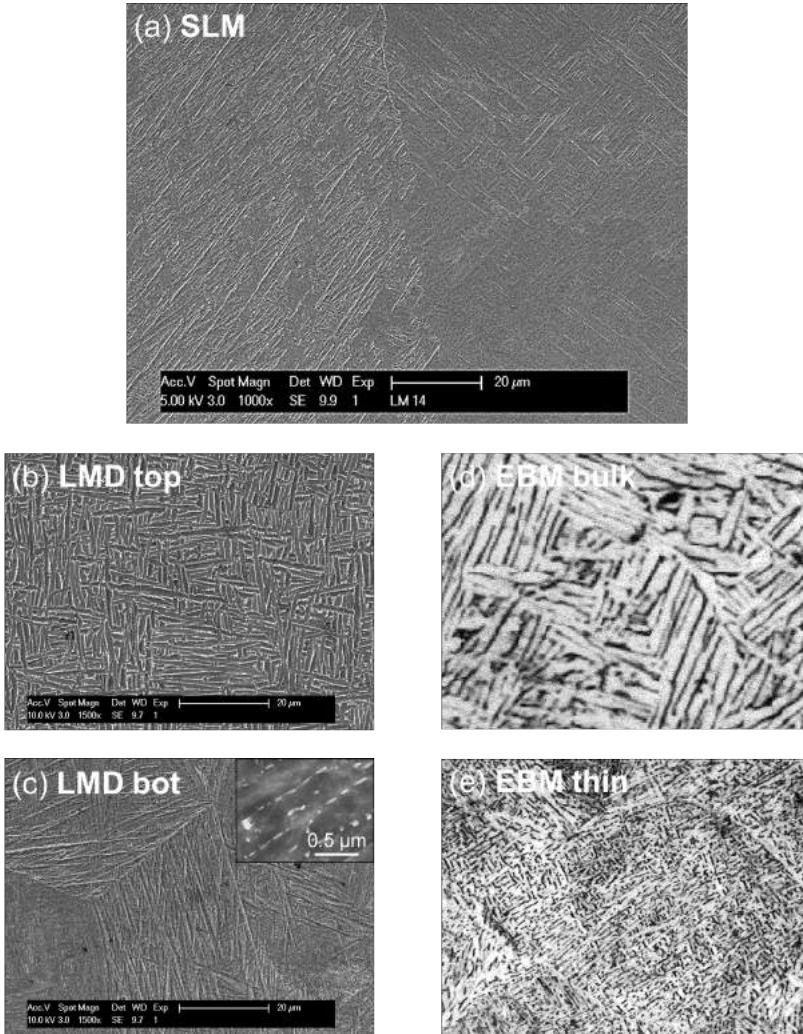


Figure 2.12: Comparison of the microstructure inside the prior β grains in SLM (a), LMD (b-c) and EBm (d-e). The inset in image (c) reveals small β particles. The scale for all images is the same. Image (d) and (e) adapted from [57].

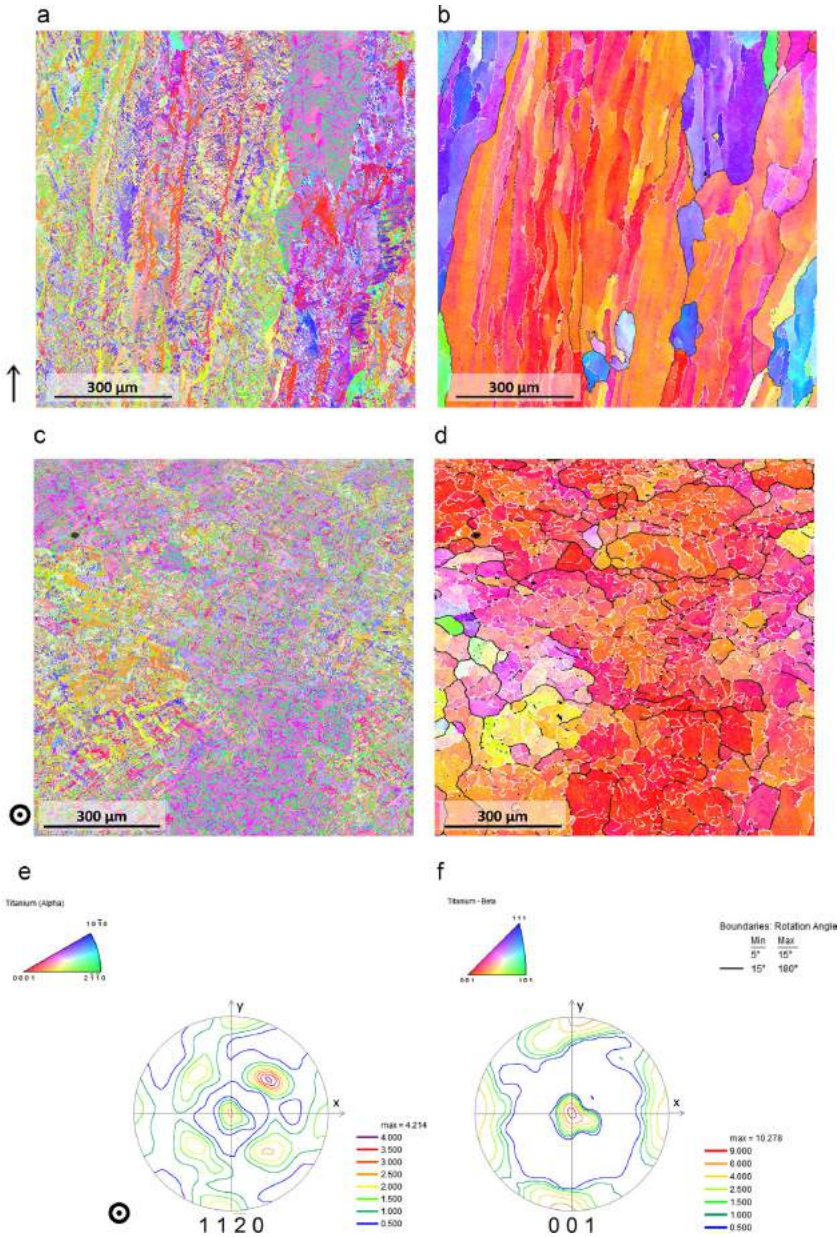


Figure 2.13: Reconstruction of the texture in the original β phase (b,d,f) based on the measured texture of the α phase (a,c,e) [60].

microstructure. Almost all results in Figure 2.14 have a UTS above the minimum required value. In most cases, this is also paired with a low ductility that fails to meet the minimum from ASTM standard F2924 for the most critical applications. Some authors have reported ductilities higher than 10%, achieved through process optimization [61], or by manipulation of the process parameters to obtain martensite decomposition during the process [41]. This created a fine lamellar $\alpha+\alpha'+\beta$ structure, also reported by other authors without analysis of the associated mechanical properties [62]. The ductility for EBM or LMD is generally higher than that for SLM, for a similar reason, being that the microstructure after these processes is coarser. The scatter on all results makes it difficult to distinguish an effect between horizontal and vertical samples. If authors did notice differences, they were attributed to defects between layers if the ductility of vertical samples was lower, or the elongated prior β grains and the crystallographic texture for small differences in strength [51, 52, 63]. HIP increases the ductility [61, 64, 65], indicated by the location of the diamond shaped points in the graph, who are all except one situated to the right of the 10% ductility threshold. Overall, heat treatment improves the ductility as well, but not as much or as consistently as a HIP treatment.

The dynamic properties such as the fracture toughness and fatigue limit are important as well and have received attention from various authors [38, 49, 61, 64, 66–73]. The fracture toughness was found to be dependent on the build orientation of the specimen and the orientation of crack growth [71, 72]. Values for as built SLM samples were reported ranging as low as $18\text{MPa}\sqrt{m}$ [72] up to $67\text{MPa}\sqrt{m}$ [71]. Stress relieving tends to remove unwanted tensile stresses, and a higher temperature heat treatment added a beneficial microstructural shift from the α' martensite to a fine, lamellar $\alpha+\beta$ [72, 73]. From Table 2.2 discussed above, this transition from a fine, acicular microstructure to a slightly coarser, lamellar structure is supposed to increase the fracture toughness, and values as high as $86\text{MPa}\sqrt{m}$ are reported after a recrystallization anneal [73]. Table 2.3 summarizes all results.

The studies on HCF life and fatigue limit for AM Ti6Al4V have produced a wide range of sometimes contradictory results. Overall, the fatigue properties for as built material are worse than heat treated or HIPed material. The fine, acicular microstructure, dense dislocation structure and small defects such as porosities lead to a faster crack initiation. HIP improves the fatigue limit to values above 500MPa, similar to the values for conventional, equiaxed material between 500 and 650MPa [74]. Table 2.4 provides an overview of the fatigue properties published for AM Ti6Al4V. The study on wire AM using either a laser or an electric arc by Brandl *et al.* [49] stands out with extremely high values. They were attributed to the small sample size, namely 26mm long samples, including the clamping area (size effect). A similar size effect was observed by Ref [38].

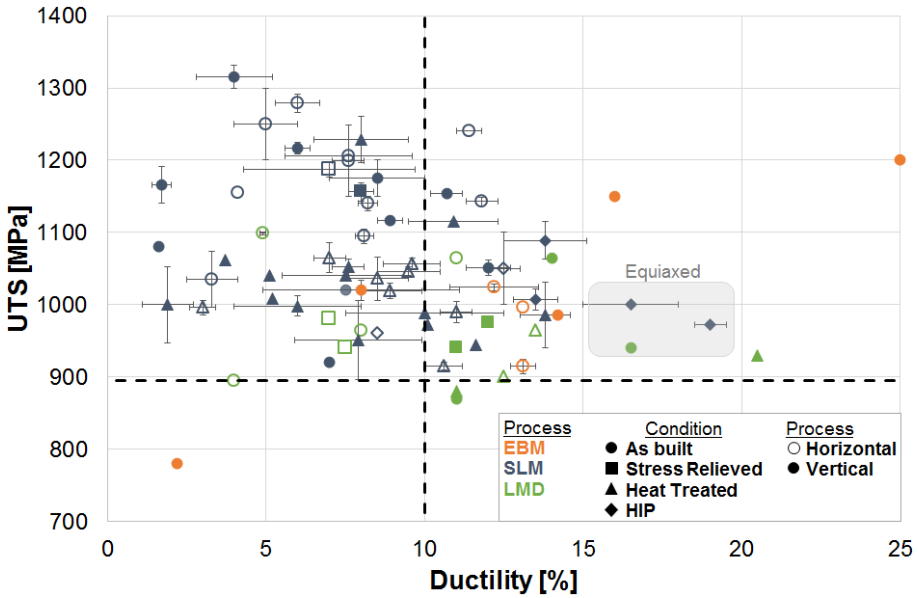


Figure 2.14: Plot of the ductility-UTS combination for various reported studies on the mechanical properties of AM produced Ti6Al4V. The dashed lines indicate minimum values set forth by the ASTM F2924 standard, and the grey box shows the approximate mechanical properties of an equiaxed material. Values included in this graph are listed in Appendix A1.

The increase in fatigue limit by the stress relieve at 600°C was thought to be due to formation of Ti_3Al precipitates during the slow furnace cooling from 600°C.

The fatigue crack growth rate or FCGR is another dynamic property that is important for risk assessment and inspection in aerospace. Figure 2.15 shows the FCGR of SLM produced Ti6Al4V, in different heat treated conditions and for two different specimen orientations (a and b). The expected FCGR of conventionally produced material is also given. The uncertainty on the FCGR of as built Ti6Al4V is big, indicated by the large scattering of the individual measurement points in Figure 2.15a and b. The scattering is attributed to the residual stresses, local defects such as small pores, and the fine acicular microstructure [72, 75, 76]. Moreover, AM samples seemed to have a lower threshold for cracks to start growing, but a slower crack growth rate in the Paris regime (i.e., the slope of the linear part of the curve is less steep for as built material) [71, 72, 76]. The explanation has been given in subsection 2.3.1:

Table 2.3: Fracture toughness of SLM Ti6Al4V reported in literature, for different heat treated conditions. Values for conventional material with a martensitic or lamellar microstructure are also given.

	Fracture Toughness K_{IC}			
	$MPa\sqrt{m}$			
	Condition	XY	XZ	ZX
<i>Donachie [74]</i>	Martensitic	40-60		
	Lamellar	50-100		
<i>Seifi [70]</i>	EBM	72	76	65
<i>Van Hooreweder [69]</i>	AB	50.2±3.5		
<i>Edwards [71]</i>		66.9±2.6	64.8±16.9	41.8±1.7
<i>Cain [72]</i>	AB	28±2	23±1	16±1
	SR650°C	28±2	30±1	31±2
	HT890°C	41±2	49±2	49±1
<i>Dhansay [75]</i>	HT Recryst.	75±1	76±0.5	80±1
<i>Becker [73]</i>	AB	37		
	HT Recryst.	86		
	HIP	58		

Table 2.4: Fatigue limit of AM Ti6Al4V reported in literature.

	Fatigue Limit		
	MPa		
	Condition	Hor.	Ver.
<i>Donachie [74]</i>	Equiaxed	500-650	
	Lamellar	800	
<i>Brandl [49]</i>	LMD, HT	>700	>700
	Arc MD, AB	>700	>700
	Arc MD, HT	>700	>700
<i>Edwards [66]</i>		<200	<100
<i>Gong [67]</i>	AB	500	
<i>Wycisk [68]</i>	AB	210 (45° orientation)	
	Polished	510 (45° orientation)	
	Shot peened	410 (45° orientation)	
<i>Kasperovich [61]</i>	HIP		>200
	HIP+polished		>350
<i>Leuders [64]</i>	HIP		630±5
<i>Vanbuel [38]</i>	SR	252	

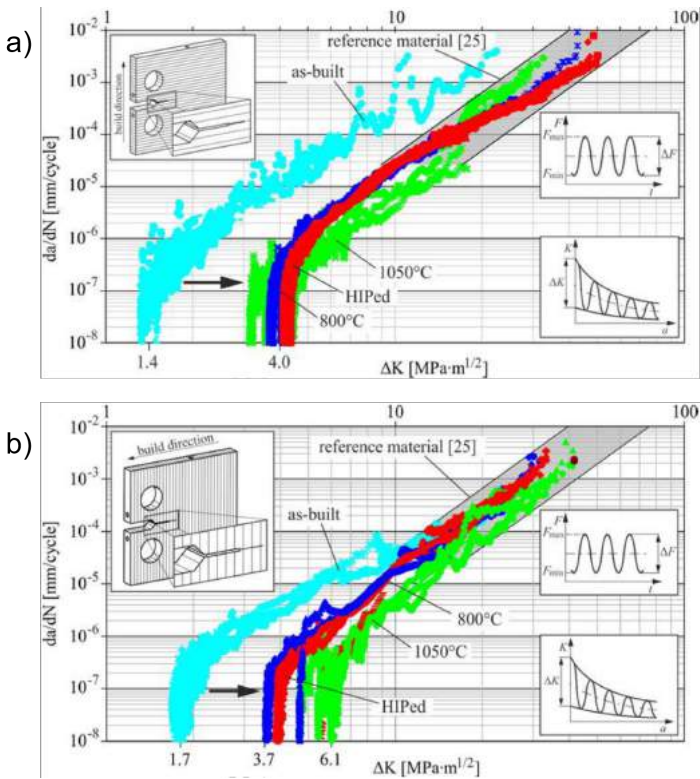


Figure 2.15: FCGR curves for SLM Ti6Al4V in the as built condition, after heat treatment at two different temperatures, and after HIP'ing. In a), the ZX orientation is shown, while b) shows results for the XZ orientation. The scatter band for conventional material is included for comparison (Adapted from [76]).

microstructures that have a multitude of grain boundaries (each individual martensite plate counts as a grain with its boundaries) are more resistant against microcrack propagation. Heat treatment increases the threshold value for crack initiation, but the slope of the Paris regime becomes similar to that for conventional material. It also reduces the scattering, making the fracture behavior more predictable. HIP is not found to have a major influence on the FCGR, as it is already in the same range as conventional material after a normal heat treatment. Nearly all literature on FCGR of AM Ti6Al4V reports a lower threshold and high spread for as built material, and both properties are improved by heat treatments to fall within the range expected for conventional material [70–72, 75, 76].

Porous structures

Several factors have pushed research into porous structures of Ti alloys, apart from the design flexibility offered by AM, the most important being medical scaffolds and the eternal strive to produce parts with a lower weight for aerospace applications. The entire porous or scaffold structure is built based on a particular unit cell that is repeated [77,78]. Studies have focused on the relation between the process parameters, the designed strut thickness and the eventual strut thickness [79–81], use of CT or DIC to analyze and optimize various properties [82–87], FE simulation of local stresses and strains [88, 89], surface finishing [90, 91], mechanical behavior of porous structures [78,82–85,92–96] and obtaining auxetic or specifically designed anisotropic behavior [77,97]. The long, columnar prior β grains were found to grow along the direction of non-vertical oriented thin struts up to a certain misalignment with the vertical direction, rather than vertical [98]. The heat is conducted more efficiently via the dense strut than via the powder bed, so the largest thermal gradients are no longer vertical. This effect disappears for thicker struts or when the strut is considered to be oriented more horizontally.

Other Ti alloys

Apart from Ti6Al4V, pure Ti has also been processed via SLM [88,99]. The microstructure is similar to Ti6Al4V, forming columnar grains that transformed into an acicular α' martensite. Liu *et al.* [100] and Qiu *et al.* [101] both used LMD to process β or near β alloys. Although different alloys were used, they both found that the microstructure consisted of zones wherein the β grains are long and columnar, and zones containing an equiaxed morphology. Lath-like α precipitates were found throughout the part, but the size and quantity differed between top and bottom, and between the zones described above. The tensile properties of SLM Ti-24Nb-4Zr-8Sn (Ti2448) near β alloy are similar to hot forged Ti2448 [102]. The microstructure of SLM Ti45Nb does not display the typical columnar β grains, but a cellular structure in which the Ti microsegregated to the intercellular area [103].

NiTinol

The shape memory alloy NiTiInol has received particular attention and is an interesting subject, as its exotic properties are largely dependent on the microstructure, which is different for SLM compared to conventionally produced NiTiInol. The transformation behavior was found to be linked to the process parameters, with lower overall transformation temperatures for parts produced with a low energy density by Bormann *et al.* [104], but a seemingly contrary

observation was made by Dadbakhsh *et al.* [105], who found that parts made with similar energy densities, but a lower power exhibited higher transformation temperatures. Bormann *et al.* attributed the behavior to Ni losses when applying higher energy densities. However, the behavior of high power and low power samples after annealing was identical in the work by Dadbakhsh *et al.*, disproving the Ni loss hypothesis. The different transformation temperatures and thermal behavior were then linked to the microstructure, which was mainly martensitic for the low power samples, but austenitic for the high power samples. In a follow up study, Bormann *et al.* [89] discussed the microstructure and texture in greater detail, as did Dadbakhsh *et al.* [106]. Both found a strong $\langle 100 \rangle$ texture of the austenite phase in the building direction.

The damping capabilities [107] and biocompatibility of NiTi scaffold structures [108] have also been investigated. Lastly, *in situ* formation during SLM of the NiTi intermetallic bond was investigated by blending precise amounts of Ti and Ni powder. No pure Ti or Ni remain after processing, but parts produced with a high scan speed have a significant concentration of Ti_2Ni [109].

2.3.2 Other alloys and materials

Steel alloys

The variety of steel alloys that have been processed via AM is large. The most notable are 316L stainless steel [30, 32, 33, 110–115], 18Ni300 maraging steel [35, 116–120] and H13 tool steel [121–126]. A common denominator of these materials is their low carbon content, a crucial factor in their processability.

The microstructure after SLM of 18Ni300 maraging steel has been found to be martensitic with some retained austenite but without precipitates [118]. The associated hardness was 40HRC. An aging treatment at an optimal temperature of 480°C increased the hardness to 58HRC [118]. A multitude of true nano-scale precipitates were found to be the reason [117], shown in Figure 2.16b using atom probe tomography (APT) data [117]. The UTS of 2220MPa of the material in the aged condition is 70% higher than that in the as-built condition (1300MPa), but the ductility is also reduced from 13.3% to 1.6% [116, 119]. 18Ni300 maraging steel also contains a lot of elements with a high affinity for oxygen, of which Al and Ti are the strongest oxide formers. Consequently, an oxide layer has been found to cover almost the entire top surface of SLM produced parts, and several Al_2O_3 and TiN particles were trapped inside the microstructure as well [35].

As with all AM produced materials, the fine microstructure of AM 316L is strong,

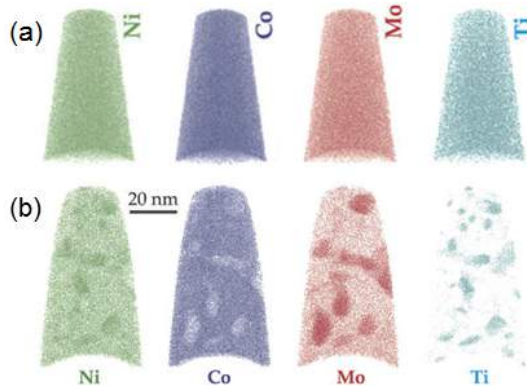


Figure 2.16: Precipitation of nanoscale precipitates during aging of SLM produced 18Ni300 maraging steel, determined by APT. (a) Homogeneous distribution of alloy elements in the as built condition, versus (b) clustering of elements in precipitates after aging (Adapted from Ref. [117]).

but not as ductile. The orientation of the laser and powder feed with respect to the deposited track was found to have a major influence on the ductility of LMD parts, which were attributed to a light increase in overall porosity (still lower than or around 1%), but also the larger size of the pores [110]. The mechanical properties are anisotropic because of the crystallographic texture [113]. The Charpy impact toughness is around 60J, far below the 160J of cast and annealed material [115], a low value attributed to porosity, but undoubtedly also related to the lower ductility.

H13 tool steel is a popular material to explore the production of functionally graded materials or metal matrix composites (MMCs), having been used in combination with tungsten carbide (WC) [121], copper [127–130] and nanosized Ni [123]. Hardnesses after LMD vary from 450-550HV [123, 124] to 550-650HV [121]. Surprisingly, addition of hard WC particles, which raises the cracking susceptibility, did not raise the hardness but lowered it to 450-550HV by partial dissolution of the WC into the H13 matrix [121]. The hardness of pure H13 steel processed by EBM was reported to be around 500HV. EBM processing suffered from vaporization of certain alloy elements, which was countered by using a starting powder of which the composition was enriched in the most volatile elements. A few cracks were observed in the produced parts [125]. Microstructure, mechanical properties and tempering heat treatment were later optimized by Telasang *et al.* [131].

Contrary to the alloys discussed above, M2 high speed steel has a carbon

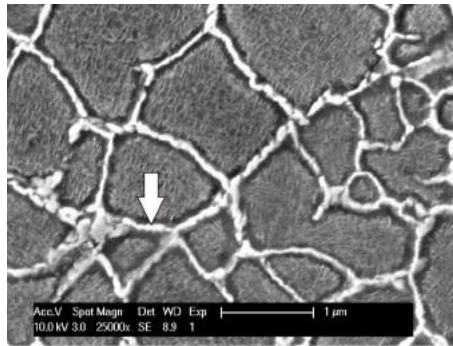


Figure 2.17: Carbides form a necklace structure around the cells in SLM produced M2 HSS. Inside the austenitic cells, further precipitation of lath-like martensite is seen [29]).

content of around 1%. This makes the material significantly stronger both through solid solution strengthening as well as through the formation of carbides, shown to decorate the intercellular area in SLM M2 HSS in Figure 2.17 [29]. It also lowers the ductility, and attempts at processing M2 HSS by SLM have resulted in the creation of macroscopic cracks, which could be remedied by using preheating [132, 133].

Aluminium alloys

AM of aluminium alloys is largely restricted to AlSi10Mg and AlSi12, a hypoeutectic and eutectic alloy respectively, widely used in casting. Other, wrought alloys have been gaining attraction for AM processing, particularly for use in aerospace. Most notable are Al6061 and Al7075. However, these alloys are more complex, precipitation hardened and in the case of Al7075, non-weldable.

Apart from the high reflectivity and thermal conductivity, another challenge in processing Al via AM is its high affinity for oxygen, both at room temperature and at elevated temperatures. Room temperature oxidation creates a thin but stable Al_2O_3 oxide layer on the powder particles. In EBM, the powder is presintered by a low energy density scan first to fixate the powder. However, it is very difficult to sinter the Al powder without applying external forces, because of the oxide layer. Further complications can arise from vaporization of high vapor pressure elements such as Mg and Zn, present in significant quantities in Al7075. In the 10^{-3} mbar vacuum of the EBM process, Zn and Mg vaporize at 300°C and 375°C, well below the vapor point of Al around 1200°C [134].

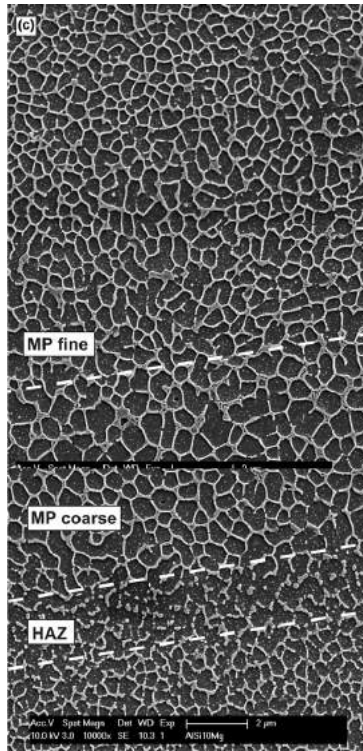


Figure 2.18: Cellular Al matrix, with Al-Si eutectic in the intercellular zones, in a top view of SLM AlSi10Mg. The microstructure varies around the melt pool boundary [35]).

AlSi10Mg and AlSi12 both have similar microstructures after SLM, consisting of primary Al cells growing towards the center of the melt pool, with a fine, nanoscale Al+Si eutectic interspersed in between, as shown in Figure 2.18 [35]. Porosity in these Al alloys is often referred to as hydrogen porosity, because the solubility of hydrogen is high in the melt but drops rapidly during solidification and cooldown. It can be kept to a minimum by applying a fast, low power pre-scan to remove the moisture from the powder, and using faster scanning speeds. Higher speeds create higher solidification rates, prohibiting the hydrogen porosity to form and trapping it in a supersaturated Al matrix [135].

The fine and homogeneous dispersion of Si in the Al matrix leads to excellent mechanical properties of SLM parts. Measured values for the hardness in the as-built condition of around 125 to 135HV are comparable with those of high

pressure die cast *and* aged material, 130-135HV [132, 136]. The Al matrix is supersaturated with Si [137], and further aging between 120°C and 170°C causes precipitation of small Si particles inside the Al cells, increasing the hardness to 150HV or higher [138]. Preheating temperatures above 150°C lower cooling rates and produce coarser microstructures. But the 90HV hardness when using 250°C preheating is still higher than the minimum requirements for conventionally cast and aged material [136].

While the strength of SLM produced AlSi10Mg and AlSi12 is high, the ductility in tensile testing is good as well, ranging between 3.5 and 5.5% [132], compared to 3-5% for cast and aged AlSi10Mg [132]. The fatigue life was found to be influenced by the building orientation, preheating temperature and porosity [139].

Nickel based superalloys

Nickel based superalloys are mainly of interest for the aerospace industry, for turbine blades and other components susceptible to creep. These alloys find additional use in the oil and gas industry, for their ability to retain good mechanical properties at high temperature and a good corrosive resistance. Inconel718, Inconel625, Hastelloy X and Inconel738LC have received particular interest from the AM sector.

The microstructure of nickel based superalloys mainly consists of an fcc matrix called the γ phase. Depending on the composition, different kinds of precipitates (γ' , γ'' , δ), carbides (M_6C or $M_{23}C_6$) or second phases can form. Alloy elements can be classified as γ' , γ'' or carbide formers, or as segregating to the grain boundaries. Elements from group V, VI and VII such as Co, Cr, Mo, W and Fe stabilize the γ phase, as their atomic radius is similar to that of Ni. Group III and IV elements like Al, Ti, Nb and Ta tend to create γ' precipitates, and carbides are mainly formed by Cr, Mo, W, Ta, Nb and Ti [140, 141].

Segregation of elements such as Cr, Mo or W to grain boundaries can also create different intermetallic phases, of which the Laves phase is the most important. This is an undesired, brittle, low melting point eutectic phase. Large amounts of Laves-phase, along with γ' and δ precipitates were found in the as built microstructure of LMD Inconel718, shown in Figure 2.19 [53].

Both Dehoff *et al.* [142], working with EBM, and Parimi *et al.* [53], working with LMD, independently showed that the texture of Inconel718 could be altered by variation of the process parameters. A high heat input gave rise to a columnar microstructure, while use of lower laser or electron beam power created finer grains, and a weakened texture. Through variation of the process parameters,

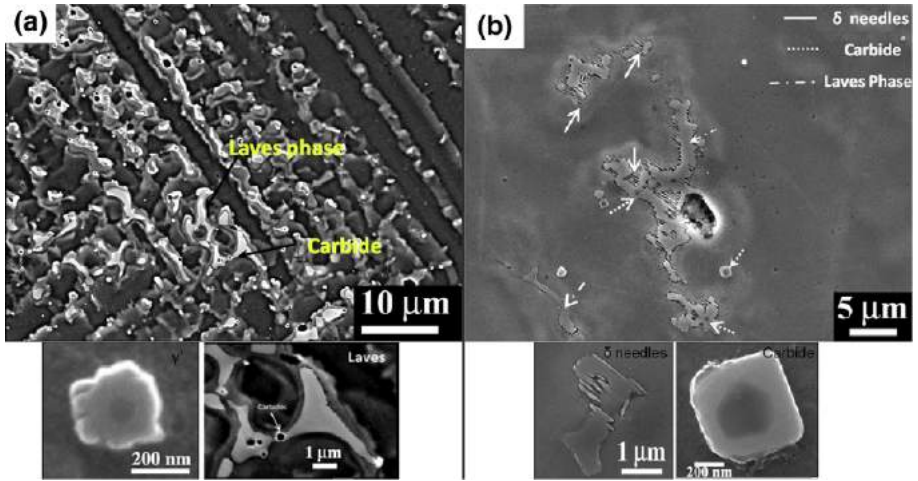


Figure 2.19: Different phases present in the as built microstructure of LMD Inconel718 [53].

the thermal gradient \vec{G} and solidification rate \vec{R} can be altered and different solidification regimes can be used.

For all nickel alloys, the high cooling rates during AM processing limit the formation of the various precipitates by limiting the diffusion distances and kinetics of nucleation and growth. In Inconel625, a single phase microstructure was found after SLM, but vertical rows of γ'' precipitates were observed after EBM [57].

For Inconel718, several authors have observed the presence of γ'' phase in the as built microstructure [143–146]. Additionally, $(Ni, Cr, Fe)_2(Nb, Mo, Ti)$ Laves-phase was found at the grain boundaries [53,144,145], as well as carbides [53,144]. Moreover, the carbides, δ precipitates and Laves-phase were larger in high power, high speed samples produced by LMD, and almost absent for low heat input samples [53]. During a conventional two step heat treatment, γ' precipitates are formed that further strengthen the material, achieving a tensile yield strength σ_y of 1000-1200MPa, UTS of 1300-1400MPa and elongation between 10 and 20%. These values are consistent over all studies and comparable to values for wrought Inconel718, even though the specific heat treatment temperatures differed [143–145,147].

Hastelloy X is a solid solution strengthened alloy, in which precipitation should not occur. However, microstructures observed by Wang *et al.* [148] clearly show the presence of a second phase in the intercellular regions, but these were not

discussed. Opinions differ on the precipitation behavior of Hastelloy X during SLM processing. Tomus *et al.* [149] produced two sets of parts, with a differing Mn and Si content and claimed that a lower Mn and Si content would limit the formation of undesirable phases at the grain boundaries, thereby reducing crack formation. Via EDX line measurements crossing over cracks, Harrison *et al.* [150] showed that there are no compositional variations. Furthermore, calculated diffusion distances indicate it is impossible for alloy elements to segregate to the grain boundaries. On the other hand, the diffusion distances in Hastelloy X are comparable to those in Inconel718, for which precipitates *are* present after SLM.

Copper and copper alloys

The industrial pull for complex copper parts made by AM has always been strong, in a large part due to its excellent thermal conductivity and consequent use as thermal heat exchangers. Early research into AM of copper found that major problems were encountered with oxygen pickup and the high reflectivity [151–154].

Via EBM, Ramirez *et al.* [155] produced fully dense, impure copper (98.5%) parts. Cu_2O precipitates were found to decorate the Cu cell boundaries. The powder bed was preheated by a 550°C base plate preheating, as well as 10 preheating passes by the electron beam before each layer was scanned. No problems related to the high heat conductivity of copper were mentioned, and microcracks appearing along grain boundaries were shown but not discussed. Frigola *et al.* [156] were the first to report production of fully dense, high purity copper parts, and they did so by using EBM. Problems encountered with the high heat conductivity were solved by limiting the heat conduction via the base plate by mounting stainless steel plates underneath the copper base plate. Use of a high vacuum during production avoids too much oxygen contamination. The thermal and electrical conductivity as well as the tensile yield strength were excellent and comparable to wrought (99.99% pure) copper. The microstructure was highly dependent on the oxygen content and preheating temperature, as shown in Figure 2.20. In Figure 2.20a, oxides decorate the cell boundaries for high oxygen parts. High purity copper displays a columnar microstructure (Figure 2.20b), while higher preheating leads to recrystallization (Figure 2.20c). These images show how much of an influence the material composition and process parameters can have on the final microstructure. A demo part of a cathode containing internal cooling channels was produced and successfully tested. Lastly, the UK based company *3tRPD* reported that they were able to produce pure copper parts by SLM [157], but there are no related scientific publications.

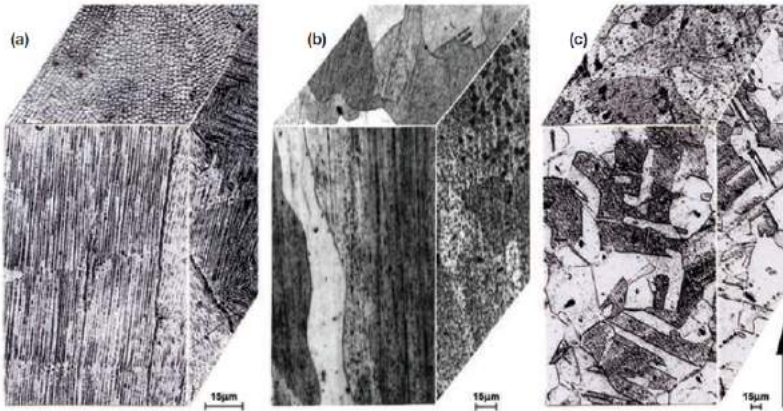


Figure 2.20: Microstructure of EBM copper for (a) a high oxygen concentration, (b) high purity copper and (c) high purity copper processed at a higher preheating temperature (from Frigola *et al.* [156])

SLM of copper alloys, more specifically of Hovadur K220, has been more successful. The Fraunhofer ILT used a 1kW laser to supply enough power to form and maintain a stable melt pool [158]. Also at the Fraunhofer ILT, Weisheit *et al.* [159] used a 1kW laser in LMD to produce graded structures of K220 copper alloy and W, Mo and Cr. AeroJet RocketDyne [160] used SLM to produce rocket parts of a proprietary copper alloy. The produced parts were still in excellent shape after 19 hot-fire tests.

Magnesium

Since magnesium is biocompatible, complex magnesium structures could serve as implants that are completely resorbed by the body. Unfortunately, Mg has a very high affinity for oxygen, and working with Mg powders is dangerous. The first published study on SLM of Mg uses a small working chamber that allowed better atmospheric control [161]. The single tracks that were produced displayed excessive sintering of powder particles in the heat affected zone, see Figure 2.21. Microstructures of these optimized single tracks showed a fine grain distribution, but magnesium oxides were formed at the grain boundaries [162]. Zhang, Liao and Coddet [163] blended elemental Mg and Al powder to a Mg-9wt%Al mixture. They found that the surface of the produced parts showed a uniform distribution of small, dendritic-type grains, which were attributed to the evaporation and subsequent redeposition of Mg onto the solidified melt pool.

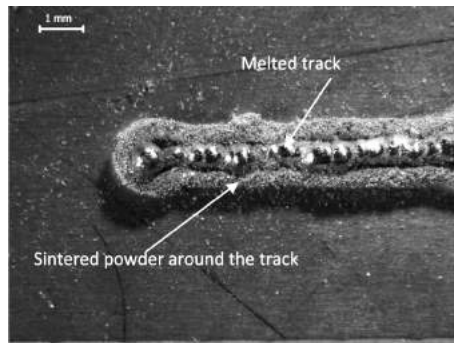


Figure 2.21: Excessive sintering of Mg powder adjacent to a scan vector [162].

The Al was dispersed homogeneously in the final microstructure, and parts were up to 82% dense. The elemental blend used by Zhang is in fact known as the AZ91D Mg alloy. Wei *et al.* [164] used prealloyed AZ91D powder and produced parts with +99% density. The microstructure consists of α -Mg grains, with interspersed β - $Mg_{17}Al_{12}$. The as-built hardness of 85 to 100HV is much higher than that of a die-cast ingot (58HV), due to the finer microstructure. Lastly, Gieseke *et al.* [165] produced coarse single tracks and 3D parts out of MgCa0.8. Excessive powder sintering along the single tracks was again observed.

Precious alloys

Precious metals are most commonly processed by AM by first 3D printing a lost wax model to produce a mold for casting. However, metals such as silver [166], gold [167–169] and platinum [169] have also been used in direct SLM. Great care must be taken during powder handling to avoid material loss. This has led to smaller machines that hold less powder and are adapted to minimize material losses. Given the high conductivity and reflectivity of gold, the process window for which good melting is obtained is very narrow, as determined by Khan *et al.* [168] and shown in Figure 2.22.

High melting point metals

AM is a very suitable process for the otherwise difficult to process high melting point metals such as tantalum [35, 98, 170] and tungsten [171] or tungsten heavy alloys [102]. Tantalum was surprisingly easy to process and resulted in fully dense parts with excellent mechanical properties. Because Ta is a

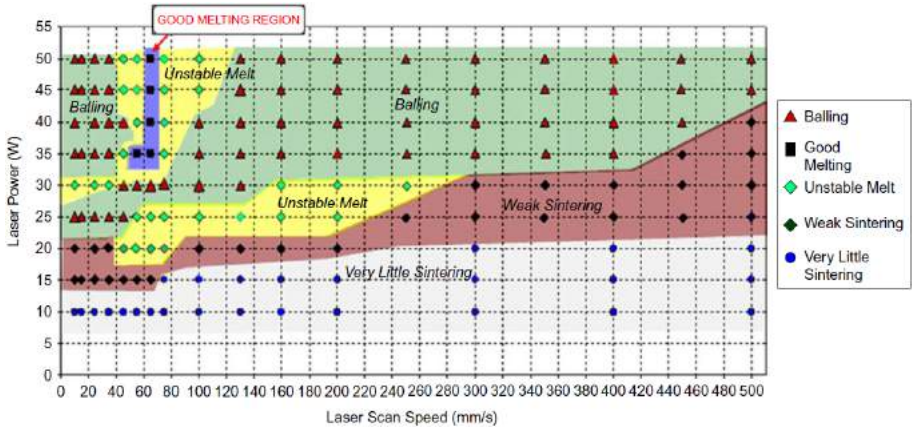


Figure 2.22: Melting regimes encountered during SLM of gold [168].

pure metal, the microstructure consists of vertical, columnar grains with an extremely strong texture, as is evident from Figure 2.23. Tungsten, however, has been difficult to process, with a maximum reported density of 98% with the presence of microcracks. However, it is still suitable for non-mechanically loaded applications such as collimators [172] or wave band guides [173].

High Entropy Alloys

Brif *et al.* [174] produced fully dense parts of a high-entropy alloy using two different layer thicknesses. High-entropy alloys are alloys with more than four elements, of which none is present in much higher quantities than the others. The results indicated that strong and ductile parts could be created, but the ductility still fell short of conventional material, as is often the case for SLM produced material.

Glass and Metallic Glass

Another novel type of metal alloys are the metallic glasses. They have a composition for which the crystallization kinetics are slower than other alloys. Using non-equilibrium processing, this allows the microstructure to remain fully amorphous. High cooling rate processes such as melt spinning, atomization or copper mold casting enable the production of amorphous material, but the maximum size of parts is very limited to keep cooling rates high enough

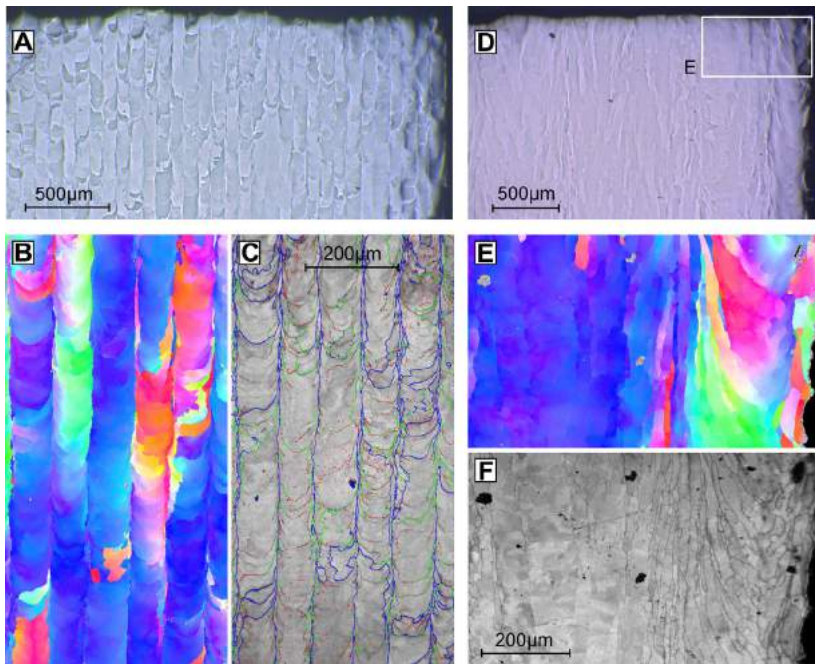


Figure 2.23: Columnar microstructure of SLM pure Ta and strong texture via EBSD mapping. The blue color indicates that the $\langle 100 \rangle$ direction is oriented along the vertical building direction [35].

throughout the part. Selective Laser Melting is a non-equilibrium processing technique in which the high cooling rates are localized, which in theory removes dimensional limitations and as such is considered a promising technique to produce large, amorphous metal components. Using an iron based alloy, Pauly *et al.* [175] successfully demonstrated that amorphous, or at least nanocrystalline parts can be produced by SLM, as diffraction spectra in Figure 2.24 still contain small peaks in comparison to the spectra of a melt spun ribbon. Prasanth *et al.* [176] studied SLM of Al85Nd8Ni5Co2, a potential metallic glass under the right circumstances. However, they did not succeed in making it fully amorphous, but rather obtained a multi-phase material with a nano-sized grain structure consisting of an Al matrix with high melting point, hard intermetallic phases. The intermetallics caused the material to have a high, 500MPa ultimate compressive stress at 300°C, 50% of its room temperature strength. Luo *et al.* [177] managed to produce single layers of actual glass via SLM, but the opacity was too high and mechanical properties were poor due to internal porosity. Markus Kayser [178], as a proof of concept and work of art, used

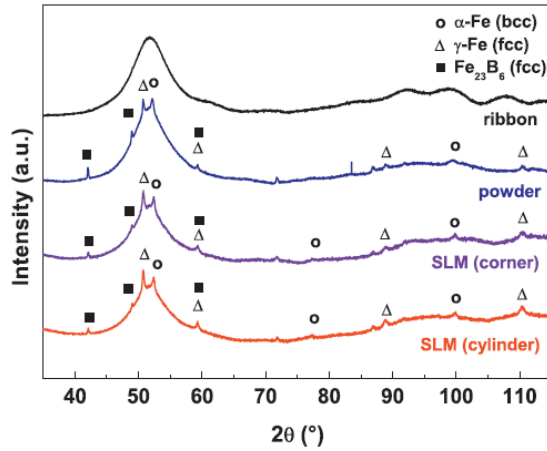


Figure 2.24: Small peaks are still visible in the diffraction spectra of SLM produced parts, compared to the smooth curve for a fully amorphous melt spun ribbon [175].

mirrors to focus sunlight in the desert to sinter silica (desert) sand. Kayser later took part in research by Klein *et al.* [179], in which they produced transparent, large and dense glass parts with a gravity based extrusion nozzle, keeping the part above the glass transition temperature ($>500^{\circ}\text{C}$) for the duration of the build. Both the mechanical and optical properties were excellent.

Chapter 3

Residual Stress in Additive Manufacturing

3.1 Residual Stress

3.1.1 Nature and Origins

There are different ways to classify residual stresses. One common way is to define residual stresses based on the length scale l_0 over which they self-equilibrate. *Type I* residual stresses act on the whole body, and would cause a deformation of the part if boundary conditions are changed. These stresses are also called macroscopic residual stresses and equilibrate over the length of the entire structure $l_{0,I}$. Residual stresses that originate from local, intergranular phenomena that are averaged out over the range of a couple of grains $l_{0,II}$ are *Type II* stresses. Type II residual stresses are nearly always present in a polycrystalline material because of the different orientations of grains and the inherent anisotropy of a crystal structure [16]. *Type III* stresses act on an even smaller scale and are caused by intragranular defects in the crystal structure, such as dislocations, vacancies or alien atoms distorting the crystal lattice, and have an even smaller range $l_{0,III}$. Generally, Type II and III stresses are considered microscopic residual stresses [180].

Residual stresses can have many origins, all of which essentially cause inhomogeneous plastic deformations. Different plastic behavior in a multi-phase material, or different crystal orientations of neighboring grains are the

major microscopic phenomena that contribute to the development of local residual stresses. Hexagonal crystals display a greater anisotropy than cubic crystals, and are therefore more prone to develop local mismatches between grains. Macroscopic or microscopic stress concentrators during application of a uniform load, or simply applying non-uniform loads are further mechanical means by which inhomogeneous deformation can occur.

Thermal residual stresses originate from temperature gradients, but can even occur during equilibrium cooling because of local differences in thermal expansion between neighboring grains or in a multi-phase material. The temperature gradients divide the material into a softer hot zone and stronger cold zone. Contraction of the cold zone causes the hot zone to yield, as was illustrated in the introductory chapter. A typical process that introduces temperature gradients is welding, a form of a local heat treatment.

3.1.2 Beneficial Residual Stress

Residual stresses are not always unwanted. Beneficial residual stresses are sometimes introduced, and most techniques revolve around creating a layer of compressive residual stress at the surface by mechanical, chemical or thermal means.

Via shot peening, the surface layer is plastically stretched upon impingement of the high velocity balls, which turns into compressive residual stresses because stretching is prohibited by the non-deformed material below. Another mechanical example is prestressed concrete, which ultimately allows the concrete to be loaded in tension. By subjecting the metal reinforcements to elastic tensile stresses during casting and setting of the concrete, and removing the applied stress afterwards, compressive stresses are introduced inside the concrete, balanced by residual tensile stresses in the metal reinforcements. Contrary to other beneficial residual stress distributions, this places the entire matrix under compression rather than only the surface layer.

During nitriding of steel, diffusion of nitrogen into the surface causes the formation of nitrides. The incorporation of these nitrides into the matrix compresses the material around it.

A final example was already given in the general introductory chapter 1. Thermally toughened glass benefits from rapid quenching from high temperatures. The outer layer cools down and shrinks faster than the hotter inside, which yields to the compression it experiences. Upon further cooling, the inside has gone through the normal amount of shrinkage + the plastic compression, and it compresses the outer layer to shrink to the same amount.

When the compressive outer layer is breached, the inner tensile stresses are released and the glass shatters into numerous pieces. The magnitude of the inner tensile stresses can even be deduced from the size of the broken pieces [181].

3.1.3 Influence of Material Properties

The tendency of a metal alloy to build up residual stress, and its response to the presence of residual stress, are dependent on a multitude of material properties. The influence of general material aspects, such as the presence of an allotropic transformation and the nature thereof, the thermal and the mechanical properties, are valid for all metal alloys. Moreover, there are other material properties that affect the build up of, and in particular the response to, residual stresses. These are mostly specific to one alloy or alloy class.

Thermal and mechanical properties

The general description of the strain tensor, $[\epsilon_{ij}]$, that originates from thermal shrinkage due to a uniform temperature difference ΔT , is given by Equation (3.1). In this equation, the tensor $[\alpha_{ij}]$ contains the coefficients of thermal expansion α_{ij} . For a polycrystalline material without texture, the thermal expansion is isotropic, and thermal strains in one direction are often given by $\epsilon = \alpha_{CTE} \cdot \Delta T$, where α_{CTE} is the *linear* coefficient of thermal expansion.

$$\begin{bmatrix} \epsilon_{11} & \epsilon_{12} & \epsilon_{13} \\ \epsilon_{21} & \epsilon_{22} & \epsilon_{23} \\ \epsilon_{31} & \epsilon_{32} & \epsilon_{33} \end{bmatrix} = \begin{bmatrix} \alpha_{11} & \alpha_{12} & \alpha_{13} \\ \alpha_{21} & \alpha_{22} & \alpha_{23} \\ \alpha_{31} & \alpha_{32} & \alpha_{33} \end{bmatrix} \cdot \Delta T \quad (3.1)$$

Residual thermal strain in an unconstrained material, however, is never the consequence of a uniform temperature change ΔT , but that of thermal gradients ∇T inside the material. These thermal gradients are vectorial, so apart from the possible anisotropy contained in $[\alpha_{ij}]$, this contributes to the heterogeneity and directionality of the thermal strains $[\epsilon_{ij}]$. In turn, $[\epsilon_{ij}]$ will lead to anisotropic residual thermal stress with another possible introduction of anisotropy via the stiffness matrix $[C]$: $[\sigma] = [C] [\epsilon]$. For ease of argumentation, this subsection continues using the simplified, scalar relation $\epsilon = \alpha_{CTE} \cdot \Delta T$, but the reader should keep in mind the tensorial nature of the thermal strains and thermal stresses, and the vectorial nature of the temperature gradient.

While the realistic situation is much more complex due to plastic yielding, the influence of several material parameters can be discussed based on Equation (3.2). In this simplified equation, the residual stress σ (function of temperature)

at an arbitrary temperature T during quenching of a perfect elastic, fully constrained material is given. It is a variant of Hooke's law $\sigma = E\epsilon$, where the strain has been substituted for the linear shrinkage strain as described above.

$$\sigma(T) = E(T) \cdot \alpha_{CTE}(T) \cdot [T_m - T] \quad (3.2)$$

First of all, the temperature interval over which residual stresses can build up is limited by the melting temperature. A lower melting point therefore lowers that range. Next, the rate at which strain is built up while cooling down is determined by the thermal expansion α_{CTE} . Lastly, conversion of these strains to stress is governed by the stiffness, E . α_{CTE} and especially E are both dependent on temperature, with α_{CTE} typically increasing with increasing temperature, and E reducing to 0 at the melting temperature.

The assumption of full constraint is not realistic. The material is constrained by colder material adjacent to it. Therefore, it is not only the temperature range over which the solid cools that is important, but more so the temperature gradients ∇T . Any variation of a material property that increases temperature gradients, also leads to larger strain misfits and thus larger residual stresses. A low thermal conductivity $k \left[\frac{W}{m \cdot K} \right]$, high specific heat capacity $c_p \left[\frac{kJ}{kg \cdot K} \right]$, a high coefficient of thermal expansion $\alpha_{CTE} \left[K^{-1} \right]$ and a high density $\rho \left[\frac{kg}{m^3} \right]$ all lead to high strain mismatches upon quenching. These parameters can be combined into the thermal diffusivity D_T , given in Equation (3.3). A low thermal diffusivity will increase the temperature gradients and the mismatch strains [18].

$$D_T = \frac{k}{\rho \cdot c_p} \quad (3.3)$$

Introducing plastic yielding into the discussion, the yield stress acts as an upper limit for the magnitude of residual stresses. As briefly mentioned in section 1.2, internal stresses are only retained as residual stresses if plastic deformation has occurred. If mismatch strains are too large, the material will accommodate these by plastic relaxation of the thermoelastic stresses. Therefore, a higher yield stress allows higher residual stresses. However, it is the dependence of the yield stress on the temperature that is of major importance. If a material maintains a high yield stress at high temperatures, like Ni superalloys do, residual stresses can already reach high values at high temperatures, and mismatch strains are large. Conversely, a rapid decrease of the yield stress with increasing temperature keeps mismatch strains small.

Overall, the thermal properties dictate the temperature gradients and therefore the mismatch strains. The magnitude of the resulting residual stress is dictated by the stress-strain relationship (i.e. yield stress and stiffness) and the variation thereof with temperature.

Temperature gradients $|\nabla T|$ become larger for higher cooling rates, as this promotes non-equilibrium cooling. The ability of the material to withstand crack formation for high cooling rates is given by the thermal shock resistance τ in Equation (3.4) [182]. The formula conventionally contains the yield stress σ_y , but since plastic yielding is unavoidable during AM processes, it is replaced by the ultimate tensile strength UTS. For a material to withstand thermal shocks, a high strength is obviously beneficial. Upon closer inspection, the denominator of Equation (3.4) is proportional to the right hand side of Equation (3.2), with $\Delta T \sim 1/k$ and ΔT more representative of a temperature gradient rather than a temperature range. The thermal shock resistance can thus be seen as a ratio between the materials strength and the possible value of residual stress build up by quenching.

$$\tau = \frac{UTS \cdot k}{E \cdot \alpha_{CTE}} \quad (3.4)$$

Allotropic transformations

Two types of solid phase transformations exist, and the interaction of both with the residual stress is different. Displacive or martensitic transformations encompass a rapid distortion of the crystal into a new crystal structure, without diffusion or long-range rearrangement of solute elements. Reconstructive transformations feature the uncoordinated diffusion of all solute and host matrix elements. The latter introduces an isotropic volume change that, if the material is constrained, may introduce residual stresses. Displacive transformations, on the other hand, are accompanied by both a dilatational strain as well as shear along a certain habit plane. The strain associated with such transformations is called Invariant Plane Strain or IPS, because the habit plane remains undistorted and unrotated [180].

When a displacive transformation is taking place, existing residual stresses inside a component tend to favor the formation of selected variants. Variants for which the IPS is oriented in such a way that it partially cancels out the existing strains will be favored. By this mechanism, phase transformations can be a mechanism by which residual stresses are lowered. Moreover, if the phase transformation occurs at a lower temperature, the built up residual stresses are partially relieved, and the remaining temperature range over which thermal stresses can build up is small. Lower transformation temperatures therefore lead to lower residual stresses, as the end of the transformation marks the beginning

of residual stress build up [16, 181]. A side effect of the variant selection due to the presence of residual stress is that the final microstructure is textured, and the material displays a degree of anisotropy [183].

3.1.4 Effect on mechanical behavior

The influence of residual stresses on the mechanical behavior can be summarized as the following three different phenomena:

- Superposition of residual stresses onto applied stresses may lead to unexpected failure.
- Unwanted deformation of a component, if the boundary conditions are changed. The residual stresses redistribute to find a new equilibrium.
- Stress-corrosion cracking can take place if Type I or II tensile stresses are present at exposed surfaces. These types of stresses act over grain boundaries, and stress-corrosion cracking is mostly an intergranular phenomenon [18, 181].

The first point in particular is of interest for static loading, but also for fatigue behavior. Residual stress has little effect on low cycle fatigue, for which the applied loads are high and often induce significant plasticity near the crack tip that washes out the residual stress after the first cycles. High cycle fatigue, on the other hand, is very sensitive to residual stress. Crack initiation is mostly governed by local defects inside the material, but the FCGR is susceptible to residual stress.

The FCGR during cycling loading is typically illustrated by a $\log(da/dn)$ vs $\log(\Delta K)$ curve as shown in Figure 3.1, with a the crack length, n the number of cycles and K the stress intensity factor. This curve consists of three different regions. Crack growth is absent or below the detection limits in the first region for low ΔK . For a certain threshold value ΔK_{th} , crack growth starts and the crack growth rate expressed as $\log(da/dn)$ vs $\log(\Delta K)$ is linear in the second region, the so called Paris regime. Finally, at ΔK_{max} , the crack growth rate rapidly increases and the material fails. A parameter not shown on this graph is the ratio between the minimum and maximum applied stress, $R = \frac{\sigma_{min}}{\sigma_{max}}$. Superposition of residual stresses onto the applied dynamic loads does not change ΔK values, since $\Delta K = (K_{max} + K_{res}) - (K_{min} + K_{res}) = K_{max} - K_{min}$. It does, however, change the mean applied stress, and the stress ratio R : $R_{app} = \frac{K_{min} + K_{res}}{K_{max} + K_{res}}$ [184]. Residual stresses therefore, have little influence on the Paris regime. The exception is when the residual stresses lead to crack closure, and therefore

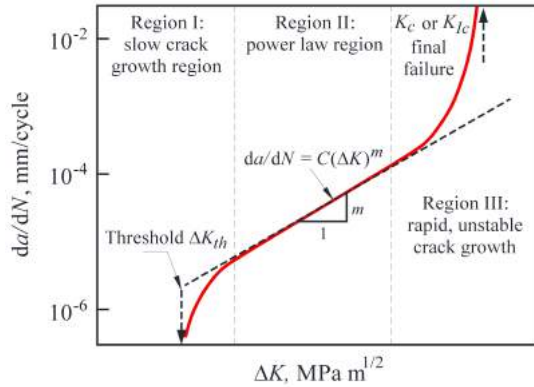


Figure 3.1: Illustration of the stages of a typical fatigue crack growth rate curve [185].

introduce compressive effects at the crack tip. The threshold and rupture values, ΔK_{th} and ΔK_{max} , are greatly affected by the mean stress [180], and thus also by residual stresses. Only Type I macroscopic residual stress influences the FCGR, since Type II and III stresses typically act on a scale smaller than the plastic zone at the crack tip, and have no effect on FCGR.

3.1.5 Material specific behavior

It has long been known that the weldability of steels decreases with increasing carbon content. A high carbon content not only strengthens the martensite, but will also cause formation of carbides in the HAZ. These carbides cause a local depletion of the matrix in certain alloy elements that can change corrosion properties, or embrittle the material such that cracks may occur. It is therefore no surprise that SLM of an ultra-high carbon steel (2.1% C) leads to numerous cracks, as does SLM of the 1% C containing M2 HSS [186, 187], while the low carbon content 18Ni300 maraging steel does not [118].

A specific group of alloys prone to cracking, that is receiving widespread attention from the AM community, are the nickel based superalloys. As was mentioned in the previous chapter, many of these alloys rely on the precipitation of either γ' or γ'' precipitates or carbides, but can also form other phases like a Laves phase or δ precipitates that have no beneficial effect. Table 3.1 illustrates the complexity and diversity of nickel based superalloys. Important to highlight are the high Nb content in Inconel718 and associated tendency to form γ'' , and

Table 3.1: Composition of Inconel718, Inconel625, Inconel738LC and Hastelloy X, four important nickel alloys in AM. All values are maximum values unless intervals are given.

	Ni	Cr	Fe	Mo	Nb	Co	Mn
<i>Inconel718</i>	<i>min</i> 50 <i>max</i> 55	<i>min</i> 17 <i>max</i> 21	balance	<i>min</i> 2.8 <i>max</i> 3.3	<i>min</i> 4.75 <i>max</i> 5.5	1.0	0.35
<i>Inconel625</i>	balance	<i>min</i> 20 <i>max</i> 23	5.0	<i>min</i> 8 <i>max</i> 10	<i>min</i> 3.15 <i>max</i> 4.15	1.0	0.5
<i>Inconel738LC</i>	balance	<i>min</i> 15.7 <i>max</i> 16.3	0.5	<i>min</i> 1.5 <i>max</i> 2.0	2.0	<i>min</i> 8 <i>max</i> 9	0.2
<i>Hastelloy X</i>	balance	22	18	9		1.5	1
<i>continued</i>	Cu	Al	Ti	Si	C	S	P
<i>Inconel718</i>	<i>min</i> 0.2 <i>max</i> 0.8	<i>min</i> 0.65 <i>max</i> 1.15	0.3	0.35	0.08	0.015	0.015
<i>Inconel625</i>		0.4	0.4	0.5	0.1	0.015	0.015
<i>Inconel738LC</i>		<i>min</i> 3.2 <i>max</i> 3.7	<i>min</i> 3.2 <i>max</i> 3.7	0.3	<i>min</i> 0.09 <i>max</i> 0.13	0.015	
<i>Hastelloy X</i>	0.5	0.5	0.15	1.0	0.1	0.03	0.04

high amount of Al and Ti in Inconel738LC, that lead to increased formation of γ' precipitates.

Carter and Attalah [188] summarized the four main possible hot cracking mechanisms in nickel based alloys as follows:

1. **Solidification cracking:** Also known as hot tearing, these types of cracks originate in the mushy zone of the not yet fully solidified melt pool. Liquid flow between recently solidified dendrites may be difficult, creating pores. These pores and the liquid zones cannot sustain any stress and can act as crack nucleators due to solidification shrinkage.
2. **Liquation cracking:** This type of cracking is most prevalent in low energy regime welding. Rapid heating of the material in the HAZ liquifies low melting point phases at the grain boundaries, such as the Laves phase or certain carbides. These liquified regions are soft and are nucleation points for further grain boundary cracking.
3. **Strain-age cracking:** This type of cracking does not occur during the process, but happens during post-process heat treatments. Relaxation of stresses during slow heating occurs slowly compared to further precipitation of γ' precipitates, in addition to the already formed precipitates. This additional aging reduces ductility, and precipitation may even cause extra stress because of coherency strains, so the material may actually fail before any stress relieving can take place.

- 4. Ductility dip cracking:** The exact metallurgical mechanism behind ductility dip cracking is subject of debate. One hypothesis states that it is a creep like mechanism, occurring in a temperature range high enough for grain boundary sliding but too low for recrystallization. This would lead to strain concentrations and voids that can initiate cracks. Adding fine particles on the grain boundaries reduces the risk of the formation of voids at grain boundary triple points but causes voids to form around the particles themselves. More tortuous grain boundaries provide a higher resistance against this type of cracking, as well as reducing the amount of high angle grain boundaries. The second hypothesis, on the other hand, states that it works via a mechanism much like strain age cracking, with carbide precipitation to blame.

Using the CM247LC alloy, which has a very high Al content as seen from Figure 3.4, the type of cracking during SLM was found to be dependent on the process parameters [188]. Using a low energy input regime, cracks are straight and vertically oriented, while a high energy regime resulted in jagged cracks with a random orientation. A close up of both types of cracks, shown in Figure 3.2, reveals that the jagged cracks of the high energy regime show a smooth, dendritic solidification structure on the inside, while the straight, low energy regime cracks display the features of a typical brittle fracture. This indicates that the main crack mode in the high energy regime is solidification cracking, while grain boundary cracking (liquation cracking) is dominant in the low energy regime. Overall, the amount of cracking is reduced when the dominant cracking mechanism is grain boundary cracking, which happens at higher scan speeds and lower laser powers, visible in Figure 3.3. The exact values of the process parameters were not stated in Ref. [188], but from the process window, the optimum parameters are probably close to the following: laser power of 100W, scan speed of 1600mm/s or higher, and a layer thickness of 20 μ m. The spot size of the laser used was 150 μ m and smaller hatch spacings provided better results, so the hatch spacing is assumed to be around 100 μ m.

Simply put, the cracking susceptibility of nickel based alloys can be visualized by Figure 3.4. The dashed line marks the compositional boundary for Al and Ti, above which extensive formation of γ' precipitates embrittles the HAZ too much. One material that stands out is Inconel738LC. The LC stands for low carbon, as the formation of carbides provides additional unwanted embrittlement. Kunze *et al.* [189] reported that processing via SLM leads to microcracking, which could be eliminated by post-process HIPing. They were unable to detect γ' precipitates or carbides in the as built microstructure, which was attributed to their small size. Precipitates and carbides were introduced by applying a standard heat treatment, which resulted in a finer distribution than the same treatment applied to cast material. The high temperature creep behavior tested

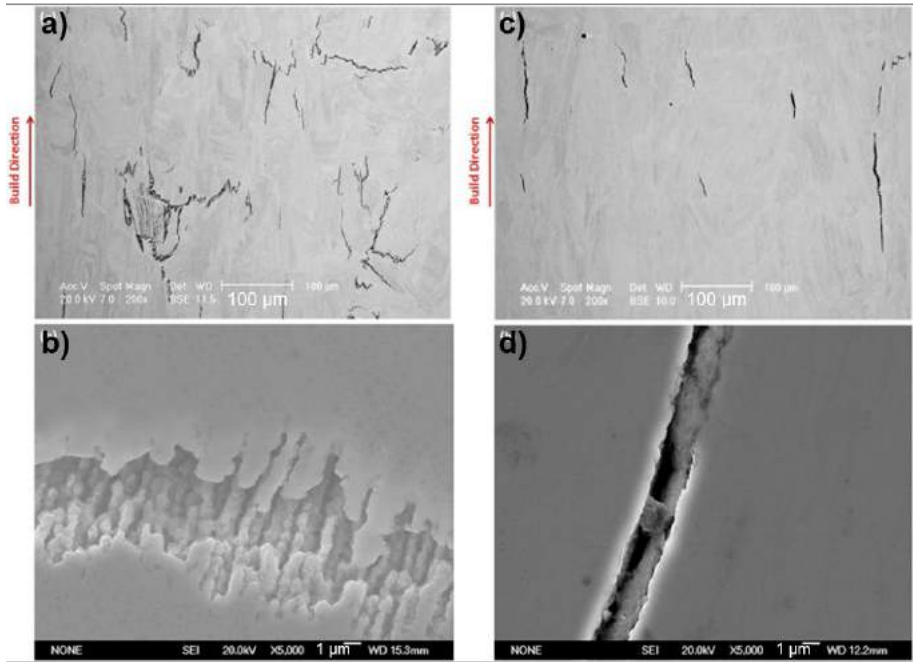


Figure 3.2: a) Jagged cracks are formed during high energy regime SLM of CM247LC nickel alloy, which have a dendritic solidification structure at their surface (b). c) Straight grain boundary cracks with brittle fracture surfaces (d) are prevalent in the low energy regime (Adapted from Ref. [188]).

in the vertical direction was within the lower boundaries of what is expected for conventional material, while it was inferior when tested in the horizontal direction. This was attributed to the lack of grain boundaries perpendicular to the loading direction as a result of the columnar microstructure.

3.2 Residual stress in metal AM

Selective Laser Melting can be compared to a repetitive welding process, stacking thousands of welds next and on top of each other to produce a 3D geometry. The difference lies in the fact that the purpose of welds is to join two or more separate geometries into one, while in SLM, the welds themselves are the geometry. Moreover, the process takes place on a much finer scale compared to commercial welding processes, with melt pool dimensions in the order of

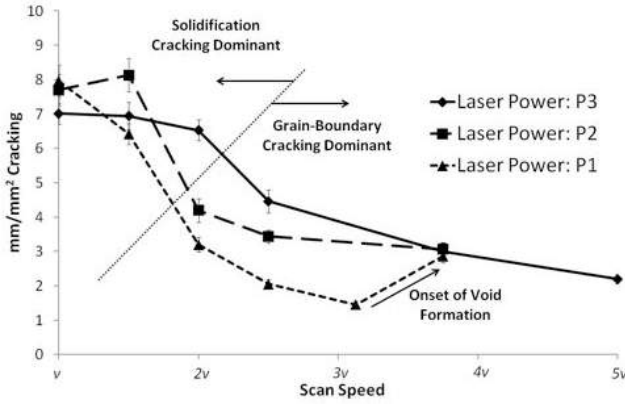


Figure 3.3: Amount of cracks observed for parts produced with various scan speeds and laser powers [188].

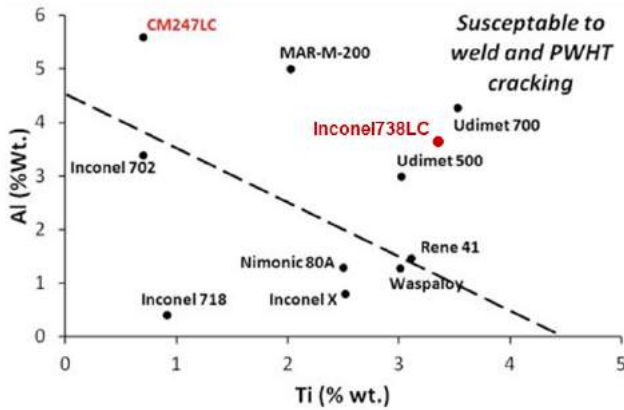


Figure 3.4: Weld cracking susceptibility of Ni alloys, as a function of the Al and Ti concentration (γ' forming elements) (Adapted from Ref. [140]).

10^{-1}mm^3 . In addition to the solidification and shrinkage of the melt pool, metallurgical effects in the HAZ provide an extra mechanism through which residual stresses influence the final structural integrity. As early as 1993, with metal AM in its infancy, residual stresses were tagged as one of the major problems that would be encountered [190]. The influence of various process parameters are discussed below, as well as the specific problems certain materials are faced with.

3.2.1 General residual stress distribution

As the introduction states, stresses in AM are repetitively built up on a small scale, and superposition of all locally induced stresses finally yields the macroscopic residual stress state. Extensive modeling effort has gone into the formation of the melt pool, and the temperature field around it [54, 191–198] sometimes even predicting the formation of porosity [199]. Increasing the scan speed elongates the melt pool and lowers the maximum temperature of the melt [191, 194, 195, 197, 198]. Increasing the laser power causes the melt pool size to grow, and increases the maximum temperature [194–199]. The experimentally measured temperature distribution along a line from the center of the melt pool towards its tail in Figure 3.5 shows a plateau at the tail where solidification takes place, both for SLM [193] and EBM [200].

Most models show the melt pool as a hot zone on a flat FE model, where the individual elements are given properties based on the type of material they represent (powder, solid or liquid). Evaporation is often not taken into account. It has been taken into account, together with numerous other effects such as melt flow and individual powder particles, in the work performed at Lawrence Livermore National Laboratory (LLNL) [192]. This extremely detailed model, of which a resulting side-view cross section of the melt pool is shown in Figure 3.6, shows that the laser penetrates deeply into the material, almost forming a keyhole weld type melt pool. The melt is pushed back by the recoil pressure due to evaporation, and surface tension causes the melt bead to rise above the level of the layer below. The model was detailed enough to show the effect of individual powder particles being drawn into the melt pool and the unstabilities this created.

Figure 3.7 shows the modeled local stress distribution that develops in front of and behind the melt pool. Vertical stresses are not shown, but (a) shows the longitudinal stress along the scan track and (b) the transversal component. Arrow 1 indicates a compressive zone in front of the melt pool, caused by its rapid thermal expansion, which additionally lowers its yield and leads to plastic deformation. The stress in this zone is greatly reduced when the melt pool

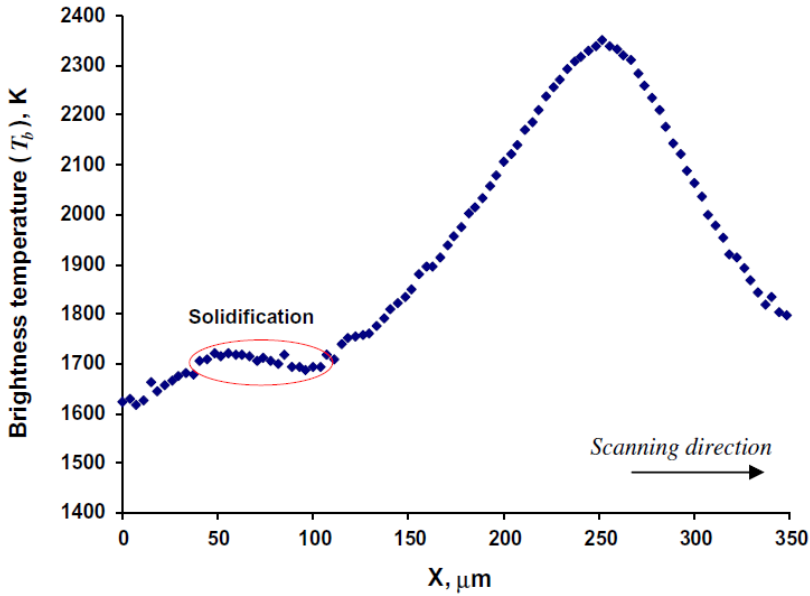


Figure 3.5: Experimentally measured temperature distribution along the central line spanning from behind the tail of the melt pool ($X=0$) towards just in front of the melt pool ($X=350$). A plateau in temperature near the tail indicates the zone in which solidification takes place [193]).

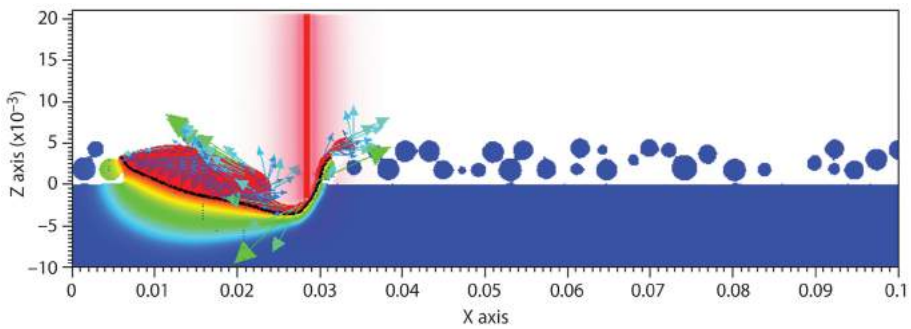


Figure 3.6: Realistic modeling of the melt pool shape, melt flow and formation of the scan track [192].

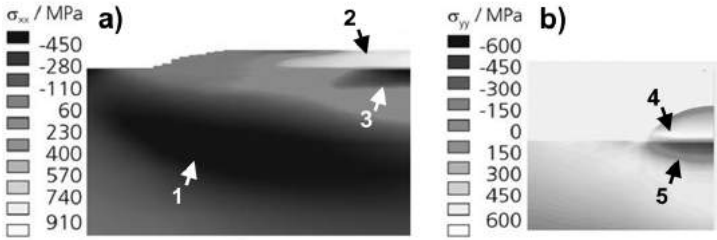


Figure 3.7: Local residual stresses developed during deposition of a single track. a) longitudinal stresses in the direction of the scan track, scanned from right to left, and b) perpendicular to the scan track. Arrows indicate the tensile stresses inside the solidified melt (2 and 4), the balancing compressive stresses just below (3 and 5), and the compressive stress just in front of the melt pool caused by restricted thermal expansion and plastic yielding due to thermal softening (1). (Adapted from Ref [203]).

passes over it by raising the temperature even higher. The melt pool itself cannot sustain any stresses, but the solidified material just behind the molten melt pool (arrows 2 and 4) exhibits high tensile stresses, both in the direction of the scan track and perpendicular to it. The tensile stress in this zone is a result of the restricted thermal shrinkage. The material just below the melt, indicated by arrows 3 and 5, was originally cold and was rapidly heated to high temperatures. Just like the zone in front of the melt, this imposed thermal expansion creates compressive yielding. The temperature of this zone is so high, however, that this effect is negligible. Instead, it is the contraction of the solidified material above that compresses the non-molten material. Notice that the maximum values in the scale bar of Figure 3.7a are larger than those in Figure 3.7b. The stresses in the direction of the scan track are therefore higher than those perpendicular to it, and were found to be about two [201] to three [202] times higher.

An interesting approach by the research groups of J. Beuth at Carnegie Mellon and N. Klingbeil at Wright State University has been to convert the process parameters into dimensionless equivalents [204–210]. Thermal simulations allowed them to create process maps for stable melt pool formations during LENS production of thin walls. Temperature gradients were also extracted, and a mapping of the normalized temperature gradients as a function of the dimensionless wall height \bar{h} and normalized temperature of the top surface \bar{T}_{Top} is shown in Figure 3.8. Apart from material parameters, \bar{h} contains the part height h and scan speed V , while \bar{T}_{Top} contains the preheating temperature T_{Base} and laser power equivalent αQ , where α represents an absorption factor.

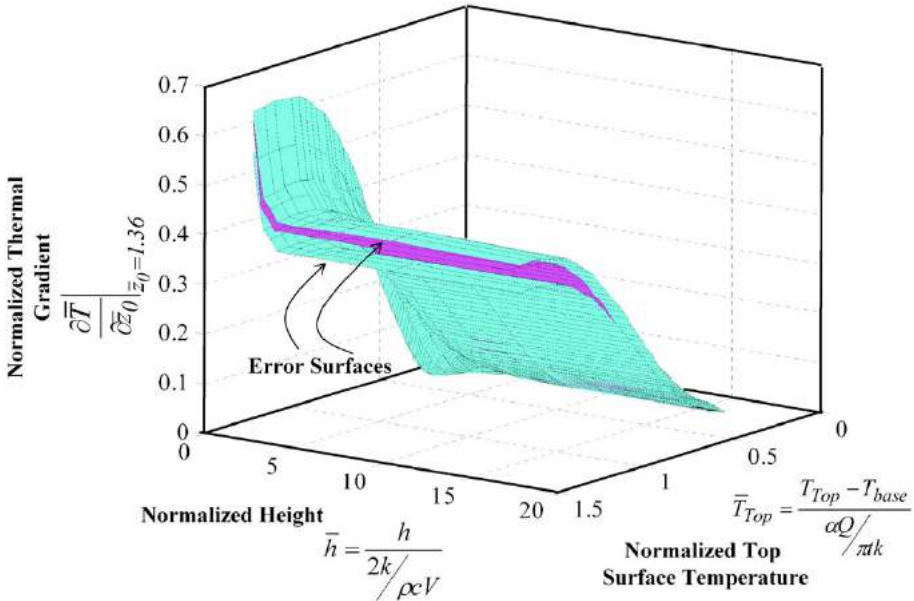


Figure 3.8: Temperature gradients as a function of the normalized wall height and normalized top surface temperature [207].

This map indicates that temperature gradients are reduced for increasing part height, as well as increasing preheating or increasing the laser power. A decrease in scan speed seemingly increases thermal gradients, but the increase in thermal gradients for small values of \bar{h} is predominantly due to small values of h . Additionally, the normalization equation for the thermal gradients includes the scan speed, via which it is made clear that the *actual* thermal gradients are increased with increasing scan speeds for a given *normalized* thermal gradient. Moreover, cooling rates during the LENS process are found to be in the order of 10^5 K/s. Contrary to the discussion in Section 3.1.3, a low thermal conductivity in this model reduces the thermal gradients and associated strain mismatches, but this contradiction with other literature was not discussed.

Costa *et al.* [211] and later, Crespo, Rui and Vilar [212] coupled the thermal simulations of the production of a thin wall by LENS with detailed material models. They were able to accurately predict hardness and phases present at different locations in the wall for a martensitic stainless steel [211] and Ti6Al4V [212]. Cross-referencing thermal models that can simulate the effect of different process parameters with material solidification maps, as is shown in Figure 3.9 [209], it is furthermore possible to link the process parameters with

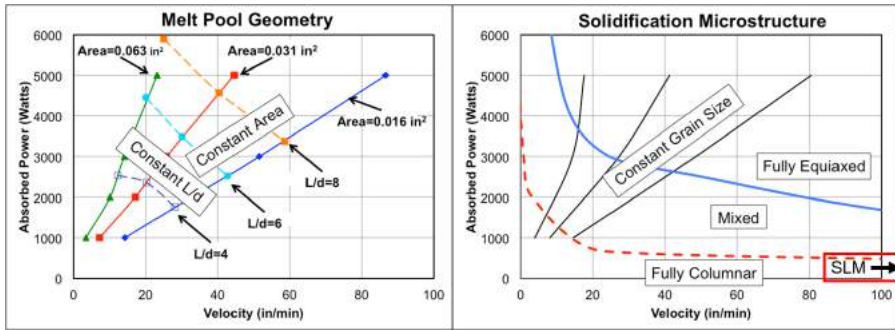


Figure 3.9: a) Melt pool area and aspect ratio as a function of the scan speed and laser power for a thin wall produced by LENS. 100 in/min corresponds to 42 mm/s. b) Corresponding solidification map for Ti6Al4V. Note the SLM process area, which typically lies between 600 and 4000 in/min in scan speed, and between 0-500W (Adapted from Ref. [209]).

the obtained microstructure, in this case for Ti6Al4V.

On the part scale, Figure 3.10 illustrates the effect of two laser passes (left to right, then right to left) on the top of an originally stress-free thin wall. Due to the constraints of the solid material below, only a limited amount of shrinkage of the hot, molten zone is possible. This induces a bending effect, with large vertical tensile stresses at the outer edges that are balanced by a large compressive zone in the center. Because the tensile stresses are confined to a smaller zone, the maximum tensile stress is larger than the maximum compressive stress. The situation depicted in Figure 3.10 is unrealistic, in that residual stresses are only created by the last two layers. In reality, similar stress states are introduced and superposed on top of each other during deposition of the entire part. For a thin wall, this results in large vertical stresses along the entire side of the part, as is shown in Figure 3.11, balanced by compression in the center [213]. The maximum principal stress in this H13 tool steel thin wall produced by LENS, as measured by XRD at various locations along the edges, is oriented vertically and ranges from 80 to 260 MPa. Large vertical stresses compared to the horizontal stresses in thin walls are measured by neutron diffraction in Ref. [214] and Ref. [215], but the latter only measures compressive stresses throughout the part, questioning the stress balance. The predictions in Ref. [216] confirm the dominance of vertical stresses as well, although the model shows a thin layer of compression at the sides which is unaccounted for.

It is of course no surprise that the maximum stress near the edges of a thin wall is oriented vertically, as the horizontal stress in the direction of the wall length

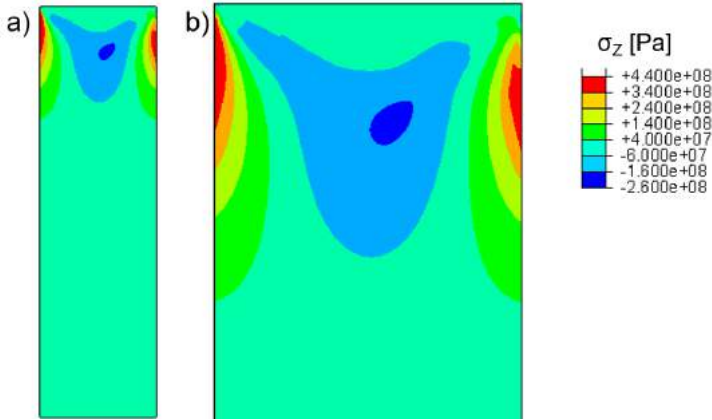


Figure 3.10: a) Vertical residual stress in a thin, high wall, b) close up of the top region. Stresses are only present near the top because the geometry was assumed stress free, after which the laser passed over the top from left to right and back (Adapted from Ref [204]).

approaches zero near the free edge, and the limited thickness also limits stresses in the other horizontal direction. However, similar arguments are valid for the 3D case, and stresses are again tensile at the outer surfaces and compressive in the center [218]. Evidence of similar stress states in 3D parts is given in Figure 3.12 [219]. The contour plot was taken at mid-height of a vertically built $10.9 \times 10.9 \times 100 \text{ mm}^3$ Inconel718 beam made by the LENS process. The vertical stresses shown in this map are tensile at the outer edges, balanced by a compressive zone in the center, and the dashed line marks the boundary between the two zones. The maximum tensile stresses occur at the four corners of the cross-section. Extension of these vertical tensile stresses towards the connection with the base plate creates local stress concentrations, as shown in Figure 3.13 [220]. Such stress concentrations at corners or other stress concentrating features near the base plate can locally lead to stresses higher than the strength of the material and cause cracks. An example of such cracks is shown in Figure 3.14 [221].

A less severe but none the less still detrimental consequence of the residual stress is deformation of the produced parts. The bending moment that is created by the stresses causes parts to curl upwards, regardless of the part shape itself. This is illustrated in Figure 3.15, where the corners of the horizontally built wedge have a large positive deformation in the Z direction. The flat orientation of the part provides little resistance to the bending stresses, and the total deviation in the Z direction after removal from the base plate is $130 \mu\text{m}$. When the same

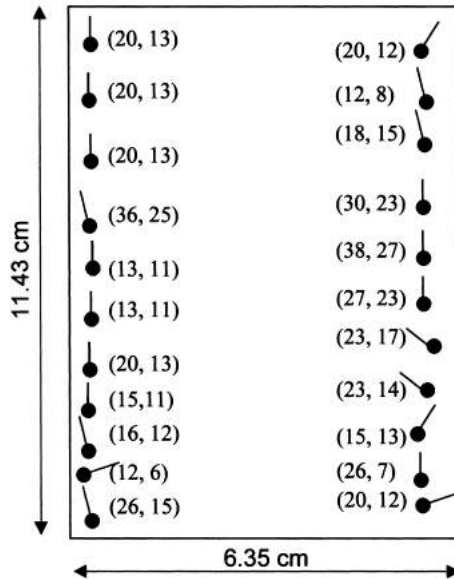


Figure 3.11: Residual stress measured by XRD along the edges of a thin H13 steel wall made by LENS. The values in ksi are for the principal stresses, and the direction of the largest principal stress is indicated. The stress ranges from 80 MPa (12ksi) to 260 MPa (38ksi) [217].

geometry is built vertically, the bottom corners still tend to curl upwards, but the geometry is now better equipped to handle the bending stresses. The difference between the maximum negative and positive deviation is now only 50 μ m, indicating that part orientation can be a crucial parameter during the SLM process. This tendency of parts to curl upwards after removal from the base plate is often exploited as a way to study the residual stress [136, 222, 223].

Cottam *et al.* [225] found that the residual stress distribution in a wedge shaped H13 specimen produced by LENS contained a residual stress distribution that was completely opposite to that found in most other sources. The direction of the stresses that are mapped in Figure 3.16 was not indicated, but from the distribution it is safe to assume it is the stress in the ‘L’ direction. Compressive zones (maximum value around -250MPa) at the top and bottom and tensile stresses in the center region (maximum value around 150MPa) contradict the ‘*tensile on the outside and compression in the center*’ consensus established in literature. The compressive zone at the top of the specimen was attributed to a martensitic transformation, and the low M_s temperature. As discussed in subsection 3.1.3, martensitic transformations possess a dilatational and shear

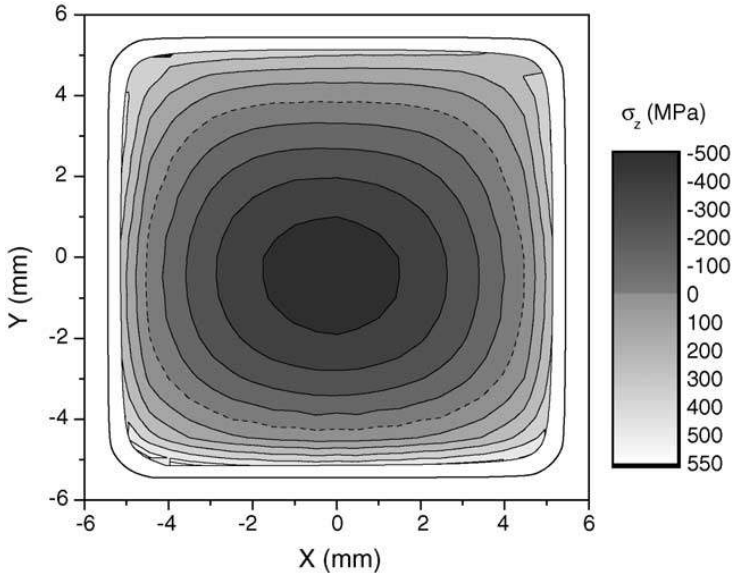


Figure 3.12: 2D plot of the vertical stresses in the cross section of a vertically built 10.9x10.9x100 mm Inconel718 beam, at mid-height. Measurement by the contour method. The dashed line indicates the boundary between tensile and compressive zones [219].

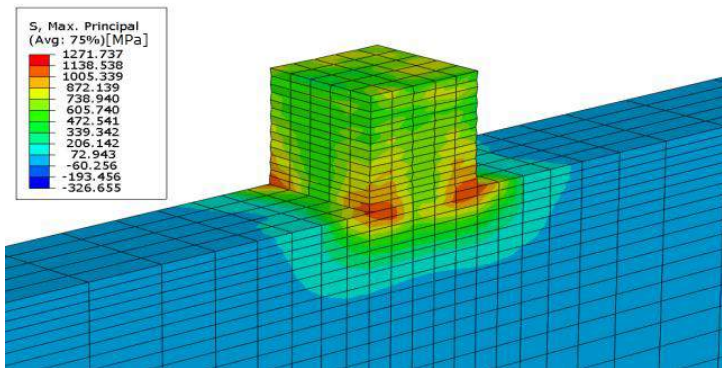


Figure 3.13: Von Mises stresses are increased near the corner attachments to the base plate. Presence of such stress concentrating features may lead to cracks [220].



Figure 3.14: Cracks in SLM produced M2 High Speed Steel, using a preheating of 100°C and 90W laser power. From left to right, the scan speed equals 250mm/s, 400mm/s and 550mm/s [221].

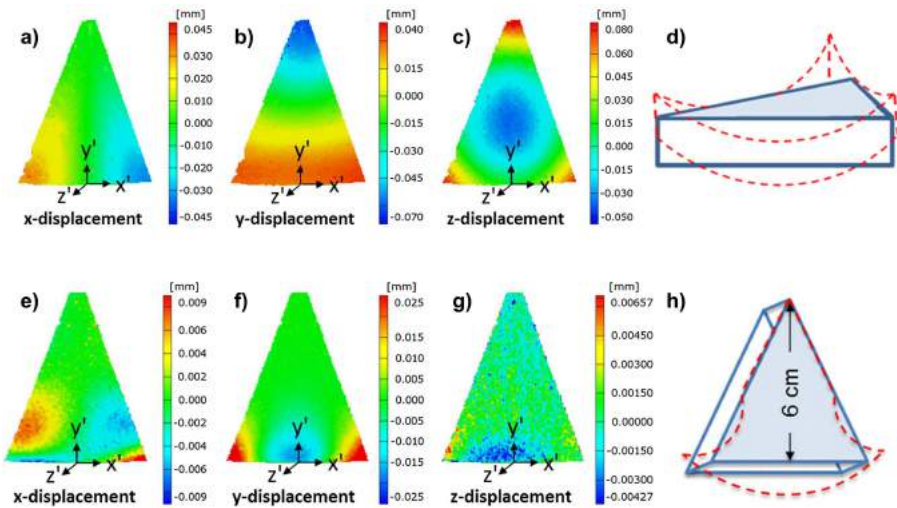


Figure 3.15: Deformation of wedge shaped 316L specimens produced by SLM. (a-c) the deformation in three directions for a sample built horizontally, with d) a schematic representation of the deformation. Equivalent for vertically built samples in images (e-h) (Adapted from Ref. [224]).

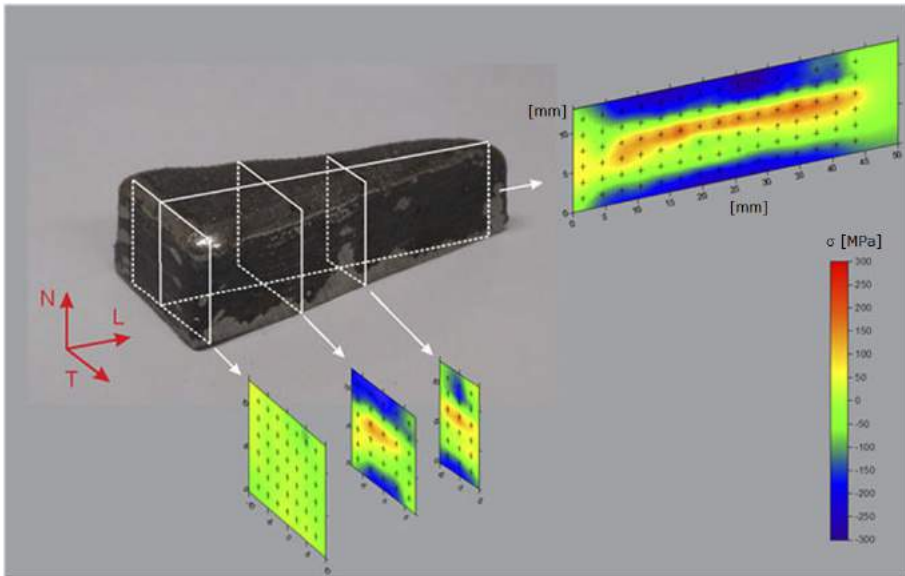


Figure 3.16: Residual stress in a H13 steel wedge produced by LENS. The stress distribution is opposite to what is normally found, with compression at the edge and tension in the center, due to dilatation of the martensitic transformation that induces compression [225].

component, and the transformation interacts with existing residual stresses. Before the transformation took place, the residual stress at the top of the wedge was tensile. Because the martensite formation is accompanied by a volume expansion, the tensile stresses are reduced to compressive stresses. For H13, this transformation takes place at a low temperature. This means tensile stresses don't have a large temperature window below the transformation temperature to build up again, and the final stresses at the top are compressive. The tensile zone in the center corresponds to a local increase in hardness, caused by tempering of the martensite to form ferrite and carbides. The lower compressive zone was said to exist to balance the tensile stresses in the center. Modeling by Ghosh and Choi [226] proved that the residual stresses, tensile in nature without the phase transformation, were converted to compressive stresses by including the phase transformation in a model of LENS of H13 steel, with stress reductions up to 300MPa.

An observation from Figure 3.14 is the increase in cracking intensity for lower scan speeds. This is contrary to the observations of Bruckner *et al.* [203], who found that local stresses inside the solidified melt pool are smaller for lower

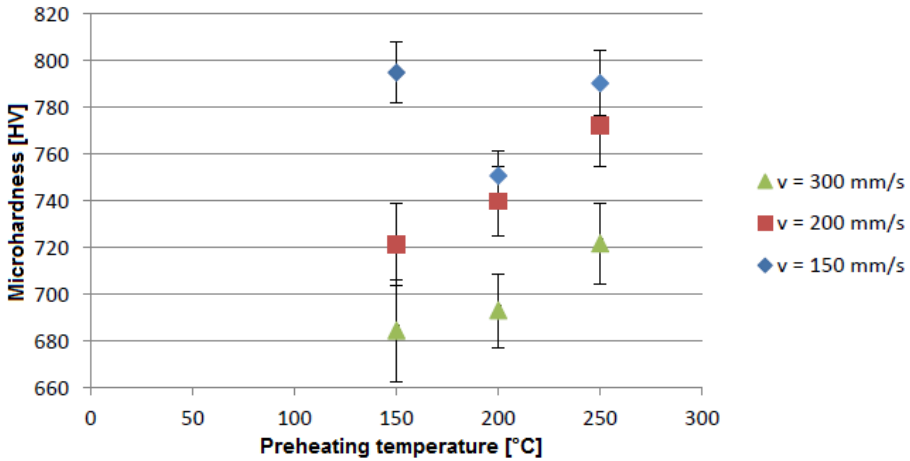


Figure 3.17: Hardness of M2 HSS, for various preheating temperatures and scan speeds. The hardness increases with increasing preheating temperature, and decreasing scan speed (Adapted from Ref. [227]).

scan speeds, and Vasinonta *et al.* [207], who found through modeling that temperature gradients are reduced for lower scan speeds. This indicates that the cracking mechanism does not purely rely on the magnitude of the residual stress. Instead, lower scan speeds cause the material to respond *differently* to the residual stress. In the case of M2 HSS, lower scan speeds do in fact lower the temperature gradients, which increases the retained austenite at room temperature, but also leads to an increased amount of carbide formation. These carbides strengthen, as is evident from Figure 3.17, but embrittle the material, making it more susceptible to cracking.

Lastly, there is good agreement between different models on the temperature gradients that exist in the LENS and SLM process. For LENS, the temperature gradients (and cooling rates) are always found to be on the order of 10^5K/m (K/s for the cooling rate) [207, 217, 228], while they are an order of magnitude larger in SLM, at 10^6K/m (and K/s) or higher [35, 193, 195, 197]. In terms of the maximum values of the residual stress that is present in SLM produced samples, several authors have experimentally measured values close to the yield stress of the material [219, 229], while others have assumed that the tensile stress in the upper layer is equal to the yield stress in their models [230, 231].

3.2.2 Influence of process parameters

The scan speed and laser power, and by extension the layer thickness and hatch spacing, cannot be varied independently, as a high final part density always needs to be achieved. It is therefore difficult to distinguish the influence of the individual process parameters on the development of residual stresses during the process. One solution is the use of thermomechanical models that neglect the influence of the parameters on the formation of a stable melt pool, but are none the less detailed enough to allow variation of the process parameters. Another is to explore the limits of the experimental process window to find upper and lower values for the parameters to compare. The list below summarizes the influence of the scan speed, laser power, hatch spacing and layer thickness, as reported in literature.

- **Scan speed:** Lowering the scan speed reduces the residual stresses in the one track model in Ref. [203], reduces temperature gradients according to Ref. [207] and also decreases the cooling rate according to Ref. [232]. It also reduced deformation of bridge shaped specimens [233]. These are all similar conclusions. Additionally, higher cooling rates for higher speeds increased the amount of martensite in a high carbon steel, which increased the amount of cracks even though the porosity was also higher [234]. Only one author reported opposite results, where the deformation seemed to be lower for higher scan speeds [235].
- **Laser power:** A first consequence of lowering the laser power is that the maximum temperature of the melt pool is reduced [232,236]. This also reduces the melt pool size, but increases the cooling rates [232]. Similar to a lower scan speed, a higher laser power lowers the deformation [224,233]. Contradictory results were reported in Ref. [236], in which the model predicted slightly lower stresses for lower laser powers.
- **Hatch spacing:** In Ref. [235], the deflection of a steel sheet, onto which a couple of layers of pure iron were sintered measuring 60mm by 14mm, was measured. The laser passed over the powder in the long direction. Increasing the hatch spacing from 100 μ m to 300 μ m reduced the deflection by more than half, see Figure 3.18. The author associated this to more localized heating if lower hatch spacings were used, creating larger temperature gradients and thus larger deflections. The study failed to take into account that tripling the hatch spacing also greatly reduces the number of tracks that are deposited, and no mention was made of the densities of the sintered layers. The influence of the hatch spacing is therefore not known.

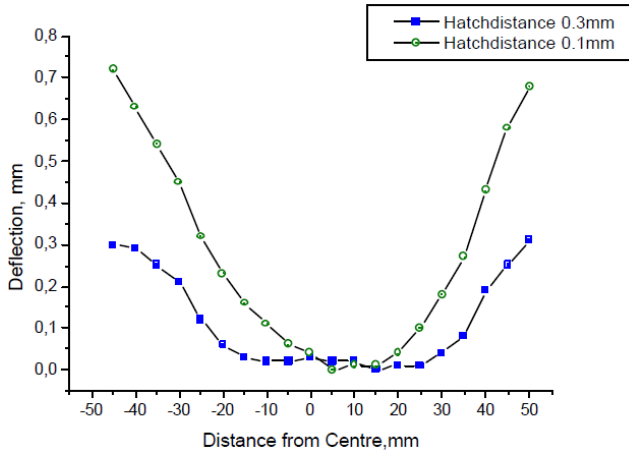


Figure 3.18: Deflection of a steel sheet on which a layer of pure iron was sintered according to a zigzag pattern, with the vectors in the direction of the measured curl. A higher hatch spacing decreased the deflection [235].

- **Layer thickness:** The deformation of bridge shaped specimens [237], thin plates onto which layers were deposited [238] and cantilever specimens [222] were all reduced by increasing the layer thickness, all citing decreased cooling rates due to the increased energy input when working with thicker layers.

The four parameters above are all found in the energy density $E = \frac{P}{v \cdot h \cdot t}$. An increase in the laser power and decrease of the laser speed increase the energy density and are reported to lower the residual stress. On the other hand, thicker layers lower the energy density, and are also reported to lower residual stress. Elambasseril *et al.* [223] failed to distinguish the effect of the individual parameters, but compared four different parameter sets applied to Ti6Al4V for which the energy density was identical and equal to 84 J/mm^3 . The hatch spacing and layer thickness were equal to $74 \mu\text{m}$ and $30 \mu\text{m}$, respectively, and the scan speed and laser power were varied from 225 to 1875 mm/s and from 42 to 350 W . Even though the ‘slow’ parameter sets used a low power, they led to a lower deformation than using a high power, but also high scan speed.

Another, less conventional process parameter that has been investigated is the downtime between layers. Van Belle, Vansteenkiste and Boyer [238] found, through modeling, that increasing the downtime between scanning of subsequent layers allows the complete structure to come to thermal equilibrium. Keeping the downtime low allows some heat to be built up inside the part, which lowers

temperature gradients and thus, residual stress. Denlinger *et al.* [239] found that the response to varying the downtime was different for Ti6Al4V than for Inconel625. Shorter downtimes lead to heat buildup up to temperatures in the stress-relieving regime of Ti6Al4V, lowering the final residual stress. For Inconel625, increasing dwell times lowered the residual stress, which contradicts the other results.

3.2.3 Deposition patterns

In the previous section, it was established that the stresses in the direction of the scan tracks are larger than those developed perpendicular to it. When determining the pattern that the laser will follow to scan one layer, this can be used to mitigate residual stress buildup.

Independent of the model work predicting that the longitudinal stresses dominate the transverse stresses, several authors found that the deformation of the part, or that of a thin substrate onto which one or more layers were deposited, was larger in the direction of the scan tracks [37, 222, 233, 235, 237, 240]. The number of possible ways to scan one layer is immense, and various scan strategies have been tested with regards to the resulting residual stresses. The overall conclusion from these works is that limiting the length of the scan vectors is beneficial, and that varying this length has the greatest possible impact on deformations and residual stresses compared to other process variables, excluding preheating [233].

The most popular of these adapted scan strategies has been to divide the area to be scanned into subsectors that are scanned one by one. If these subsectors are square or rectangular in shape, this strategy is known as **island scanning**. If one dimension of the island is larger than the part dimensions, the area is divided into stripes and the strategy is aptly called '**striping**'. These two alternative scan strategies have been widely adopted in commercial SLM. In Figure 3.19, these strategies are illustrated, and the black lines represent the path that the laser follows. The direction in which it scans each line is neglected for clarity of the image, and because this has not been investigated yet for its significance in residual stress creation.

The mechanism behind the beneficial effect of using shorter scan vectors is unclear, and it is probably a combination of several favorable phenomena, listed below:

- Less time passes between the deposition of two adjacent tracks. The heat input of the first track has therefore not been fully dissipated, and the second track is deposited onto and next to warmer material. This local

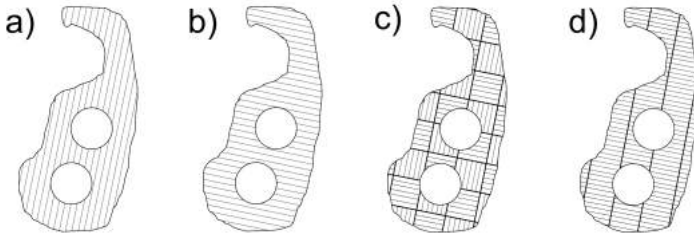


Figure 3.19: Different scan strategies that lead to different residual stresses. The scan vectors in (a) are oriented, on average, along the long direction of the sample, which could lead to the largest deformation if there was no rotation of the pattern between layers. In (b), the vectors are oriented along the ‘short’ dimension of the part. Island scanning is shown in (c), and striping in (d).

preheating effect reduces thermal gradients, and also the yield stress of the material, which reduces residual stress by plastic flow.

- Similar to the stress build up in the fibers in short fiber composites, residual stresses in the direction of the scan tracks are, by definition, zero at the start and end of the scan track. This argument was also made by Mercelis and Kruth [231], who explained the reduction in stress found for island scanning by the stress-free boundaries of every island, as long as the neighboring islands have not been scanned yet.

In island scanning, each subsector can be regarded as an area for which the scan strategy can be chosen independently of other islands. In the example shown in Figure 3.19c, the scan vectors of adjacent islands are perpendicular to each other. An advantage of having differently oriented scan tracks within one layer is that there is no major stress buildup in one particular direction. Instead, a more planar isotropic stress state is obtained. Another way to achieve this on a slightly larger scale is to apply a suitable rotation of the scan pattern between subsequent layers. Neutron diffraction measurements performed by Zaeh *et al.* [222] have shown that residual stresses throughout the part built with island scanning are reduced compared to full-layer zigzag scanning. Replacing the zigzag pattern by islands leads to a large decrease in stresses, but the reduction reaches a maximum value after which reducing the island size does not matter anymore [233, 241]. It is unclear why smaller islands are not better, since both arguments given above should also decrease the stress for reduced island sizes.

Another scan strategy, wherein the laser follows a spiral path, is known as the **helix scan strategy**. The laser can either start scanning from the outside and

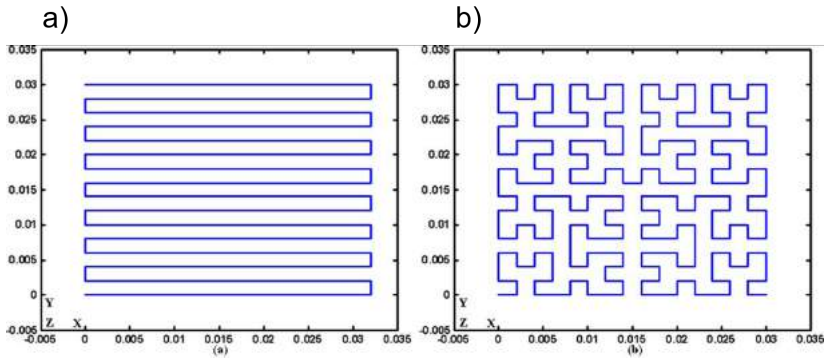


Figure 3.20: a) Zigzag scanning pattern and b) fractal scanning pattern [244].

move inwards, or the other way around. This strategy also shortens the average scan vector length, and scan vectors are oriented in different directions within one layer. Though the average length of the vectors may be lower than regular full layer zigzag scanning, it still contains full length vectors at the outside of the spiral. Nickel, Barnett and Prinz [37] found no difference between full zigzag scanning and helix scanning in the magnitude of the deformation of a thin sheet onto which a single layer was deposited. These strategies did differ in the final deformed shape. Later, Qian *et al.* [242] used the helix scan strategy to produce a complex shaped part. The scan vectors followed the curvature of the contour of the part. While they were unable to produce the part using a full layer zigzag pattern, production was successful when the helix scan strategy was applied. Having the scan tracks follow the smooth contours of the part actually creates one long track, but the direction changes constantly.

A last noteworthy deposition pattern is obtained when the laser follows a **fractal scanning pattern**. The software problems associated with the implementation of fractal scanning patterns were discussed in Ref. [243], and modeling of the deformation after deposition of one layer was performed by Ma and Bin [244]. Fractal scanning patterns, an example of which is shown in Figure 3.20b, also create a layer of short scan tracks with varying orientation. In the modeling work by Ma and Bin, the deformation for the fractal scanning pattern was only half as large as that resulting from the zigzag pattern. No further studies were reported on the use of fractal scanning patterns in AM, possibly due to the complexity in hatching every layer for geometries that are more complex than simple cuboids.

Lastly, it is still unclear whether or not **rescanning** each layer a second time will be beneficial. Rescanning with a low energy density, so that the material

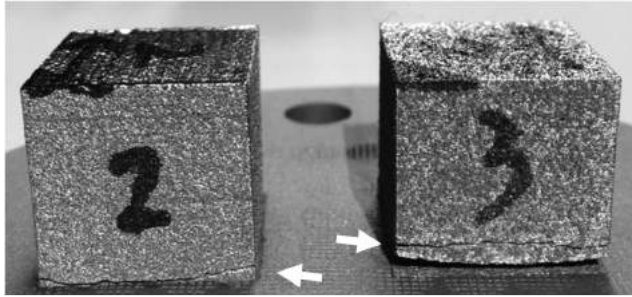


Figure 3.21: Cracks in Ti6Al4V cubes for which each layer was remelted using the same parameters as the first scan. Sample 2 was produced using a high power and high speed, sample 3 with a low power and low speed [246].

was not molten but just locally heated, reduced cracking in glassy components in SLM [194] and in TiAl in EBM [245]. The positive effect of using moderate values for the scan parameters was also confirmed by Ref. [231] and [233], in which it was also reported that rescanning with the same parameters as the first scan actually increases the residual stresses. Figure 3.21 illustrates that using the same parameters for remelting induces cracks, that were absent without remelting. The only contradictory study on using a high energy remelting was performed by Shiomi *et al.* [230], who found that full remelting of every layer lowers stresses, even when the hatch spacing is decreased to such an extent that the energy input during rescanning is 150% of that during the initial scan.

3.2.4 Preheating

Use of preheating in Selective Laser Melting was proposed as a solution to thermal stress buildup as early as 1998 [247]. Abe *et al.* [248] proposed that it could be in the form of a second laser that would locally preheat the area just in front of the melt pool. A similar proposal was examined by Aggarangsi *et al.* [205] by FE modeling of laser cladding, but found that it was not nearly as effective as a uniform preheating, which has become increasingly common during metal AM.

Taking an unconventional approach, Vora *et al.* [249] applied concepts borrowed from Selective Laser Sintering of polymers in SLM. The base plate was heated up to temperatures at which the material being processed was in the semi-solid or mushy state, thereby completely eliminating the rapid solidification that causes residual stresses and metastable microstructures to form. To prevent the powder

from melting as well at these preheating temperatures, this technique can only be used with elemental powders of elements that form an eutectic when mixed, in this case Al with 12wt% Si. Highly probable issues such as powder sintering or sinking of the mushy material into the powder bed could not be encountered and discussed because the preheating system only allowed preheating up to 380°C, well below the eutectic temperature of 577°C. Using this preheating did lower warpage of unsupported overhang structures, but Buchbinder *et al.* [136] have shown that using a preheating of 250°C is already enough to eliminate stress induced deformations of large cantilever specimens for an almost identical Al alloy, AlSi10Mg. The microstructure was significantly coarser for higher preheating temperatures, which led to a lower, but still acceptable hardness.

And, although the case was made earlier that the EBM does not suffer from thermal stresses, the response of the system to the thermal loading may still result in deformations. Understanding these effects is critical to correctly predict the final, cooled-down shape of the produced parts [250]. Stresses may not reach large magnitudes during deposition, as the material is very soft due to the high temperatures and thus will also yield and deform easily. Tang *et al.* [245] found that a very high preheating temperature, high power input and reheating (but not melting) of each layer eliminated cracks in a Nb rich TiAl processed by EBM. Moreover, the top part of the sample was found to contain a lot of dislocations, while the center did not, further confirming the stress relieving and annealing effect of preheating.

Residual stresses were calculated from uncoupled mechanical simulations, using the temperature input from the thermal models using dimensionless parameters developed by Vasinonta *et al.* and Aggarangsi *et al.* [204,206], the result of which is shown in Figure 3.22 [207]. While Figure 3.22 shows that decreasing temperature gradients also decrease residual stress, the relation is not linear and depends on the specific combination of process parameters. Moreover, use of preheating only slightly shifts the temperature gradients to lower values, but still leads to a significantly lower value for the maximum residual stress. The beneficial effect of preheating therefore needs to be considered twofold: the first is the reduction of temperature gradients, but the second and more important mechanism is reduction of the yield stress at higher temperatures [207].

It is unanimously agreed upon by all literature sources that preheating reduces residual stresses [136, 203, 205, 207, 222, 236, 248, 251]. However, one can imagine the case presented by Cottam *et al.* [225], who found that residual stresses were compressive on the outside, and tensile in the center. This is a beneficial residual stress distribution, and could only exist because of the martensitic transformation that occurred due to fast cooling rates, and because this transformation took place at a relatively low temperature. From a certain temperature upwards, preheating would stop these metallurgical

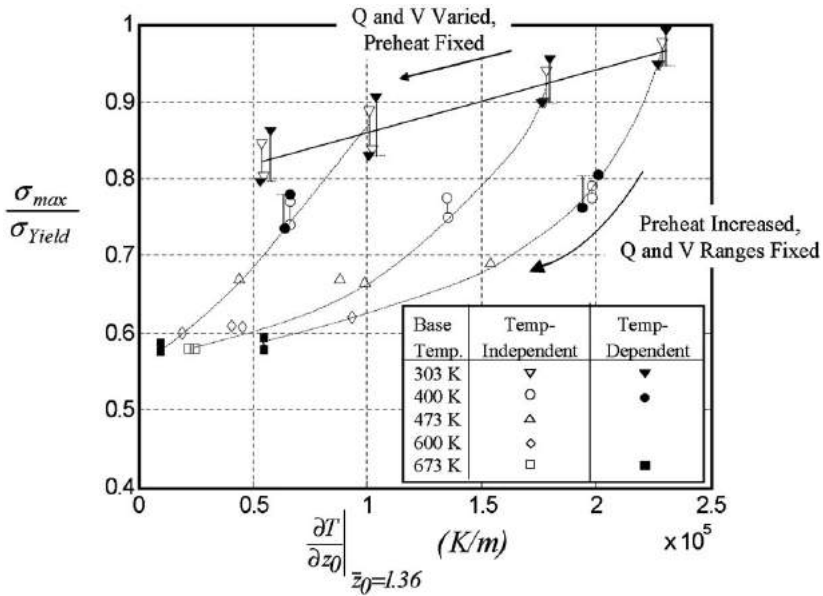


Figure 3.22: Maximum residual stresses, expressed as a ratio with the yield stress, as a function of the temperature gradients. Variation of the laser power (Q) and scan speed (V), along the thick solid line, significantly change the temperature gradient but only moderately affect the stress. For fixed combinations of Q and V (thin lines), increasing preheating temperatures up to 400°C lower the stress by 40% [207].

phenomena from taking place. In the absence of such phenomena, the preheating temperature must be set sufficiently high, as temperatures during the process are easily above 100°C due to the heat input of the laser alone [252]. For instance, preheating of 304SS was only effective above 100°C [222]. The autonomous temperature increase due to the process itself is dependent on the material, the scan parameters and the area to be scanned for each layer.

3.2.5 Summary

- The stresses in the newly deposited track are tensile in all directions, and are larger along the direction of the track than perpendicular to it. These tensile stresses compress the non-molten material directly below it.

- The tensile stresses at the top create a bending effect, which introduces large vertical stresses. Residual stresses in SLM are tensile along the side surfaces, balanced by compression in the center.

Residual stresses, deformation, temperature gradients and/or cooling rates are reduced by:

- A high laser power,
- Low scan speed,
- Thicker layers,
- Shorter scan vectors,
- Use of preheating.

In terms of the material properties, a high thermal diffusivity, low thermal expansion, low yield stress, low Young's modulus and low melting point also leads to lower residual stress, in the absence of allotropic transformations or other metallurgical phenomena.

Chapter 4

Measurement of Residual Stress

Different techniques can be used to measure residual stress, and they vary in sampling volume, accuracy and destructiveness. Out of all possible techniques, three were chosen and used in this thesis, namely X-ray diffraction, the contour method and a semi-quantitative method based on the deformation of specific geometries.

4.1 X-ray Diffraction

Diffraction is a non-destructive method to measure residual stresses. Destructive methods work by removing material or sectioning the part to release residual stresses and induce deformations from which these stresses can be measured. Diffraction, on the other hand, uses the crystal lattice as a strain gage.

In this work, X-rays were used, which have a low energy and limited penetration depth, and are therefore only suited to measure RS at the surface. The penetration depth can be calculated using the Beer-Lambert law given in Equation (4.1), in which $I(x)$ is the intensity at depth x , $I(0)$ the original intensity of the incoming rays and μ the mass attenuation coefficient. μ depends on the energy of the incoming rays, which itself depends on the wavelength λ .

The energy of $K\alpha_1$ rays generated by a Cu tube is 8.047 keV [253]. Additionally, μ is often given as μ/ρ , and for Ti this ratio equals $202.3 \text{ cm}^2/\text{g}$ for waves with

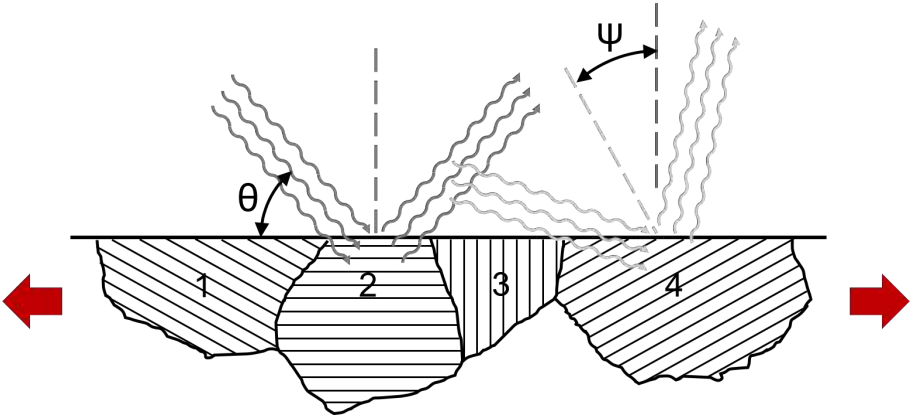


Figure 4.1: Schematic representation of the concept behind stress measurement via XRD using the $\sin^2 \psi$ method.

an energy of 8 keV [254]. For Ti6Al4V, the penetration depth or attenuation length to which $I(x)$ falls to $1/e$ of the incoming intensity $I(0)$ is then around $11\mu\text{m}$.

$$I(x) = I(0)e^{-\mu x} \quad (4.1)$$

$$n\lambda = 2d_{hkl} \sin \theta \quad (4.2)$$

Incoming X-rays at an angle θ with the surface are diffracted by a specific family of crystal planes for which Bragg's law, Equation (4.2), is obeyed. In a stress free material, the lattice spacing would equal d_0 , which translates to a stress-free diffraction angle $2\theta_0$. The presence of RS affects the lattice spacing, which changes to a new value d_1 , causing a shift of the diffraction peak to $2\theta_1$. In theory, this information is enough to determine the residual stress, since the shift in lattice spacing can be translated into a lattice strain $(d_1 - d_0)/d_0$. This method relies heavily on knowing the correct value for d_0 , which is sometimes difficult to determine.

Alternatively, the $\sin^2 \psi$ method is often used, and the mechanism behind the $\sin^2 \psi$ method is schematically shown in Figure 4.1. The influence of the d_0 value is minimized by comparing the reaction of different groups of grains that have different orientations with respect to the RS component being measured, rather than comparing the reaction of one group of grains with a stress free

reference. Moreover, it is capable of determining the full 3D stress state, as described below.

In Figure 4.1, assume that tensile residual stresses are present, as pictured by the red arrows. In this situation, the lattice spacing in grain 2 is *decreased* by the Poisson contraction. The lattice spacing in grain 3, however, is *increased*. It is practically impossible to measure the specific lattice spacing shown in grain 3, since the normal to the lattice planes deviates too much from the normal of the free surface. For more moderate misalignments, such as that of grains 1 and 4, the sample can be tilted by an angle ψ so that the bisector of the incident and diffracted X-rays is parallel to the normal to the lattice planes, which enables the measurement of their d value. Measuring the peak shift for different values of ψ , both positive and negative, therefore allows sampling different groups of grains. From this information, the residual stress in any direction defined by a rotation ϕ around the surface normal with respect to the direction of the first principal stress σ_1 can be calculated using Equation (4.3). The mathematical deduction of this equation can be found in Ref. [255]. σ_1 and σ_2 are the principal stresses. Remembering from subsection 3.1.3 that the strain is a tensor $[\epsilon_{ij}]$, measuring the linear strain in three different directions (usually $\phi=0^\circ$, 45° and 90°) provides enough information to determine the full stress tensor and thus the principal stresses which are the eigenvalues of the stress tensor, given the following assumptions:

- The normal stress (σ_{33}) perpendicular to the surface is equal to zero, which is a feasible assumption given the limited penetration depth of the X-rays.
- The shear strain components ϵ_{13} and ϵ_{23} are equal to zero. Practically, this means that ψ -splitting is absent, i.e. the measurement points in the $\sin^2 \psi$ curve are identical for negative and positive values of ψ . In this case, the $\sin^2 \psi$ curve is linear, whereas it would form an open ended ellipse if ψ -splitting is present. Figure 4.1 provides evidence of the validity of the second assumption for Ti6Al4V samples used in this work, for which the two data points for a certain $\sin^2 \psi$ value coincide. Further evidence for Ti6Al4V and other materials used in this work is provided in Appendix A2 and A3.
- The reference coordinate system is that of the principal stresses σ_1 and σ_2 .

In the end, this equation describes a linear relation between $\sin^2 \psi$ and the strain $\epsilon_{\psi\phi}$ in a certain direction ϕ , which can be plotted as in Figure 4.2. The presence of texture or shear stresses cause deviations away from the linear

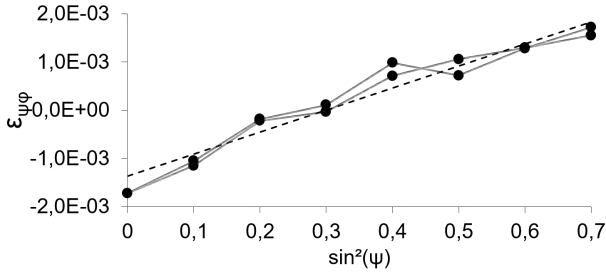


Figure 4.2: Linear relation between $\sin^2 \psi$ and the strain $\epsilon_{\psi\phi}$. ψ is varied both positively and negatively. The dashed line is the linear fit. Data from a measurement on the top surface of a Ti6Al4V sample.

relation and can be handled accordingly. High diffraction angles 2θ are more susceptible to changes induced by RS, and a rule of thumb is that 2θ should be higher than 120° [256].

$$\epsilon_{\psi\phi} = \left(\frac{1 + \nu_{hkl}}{E_{hkl}} \sigma_\phi \sin^2 \psi \right) - \left[\frac{\nu_{hkl}}{E_{hkl}} (\sigma_1 + \sigma_2) \right] \quad (4.3)$$

In Equation (4.3), E_{hkl} and ν_{hkl} are the stiffness and Poisson ratio associated with the chosen $\{hkl\}$ family of crystal planes. The multiplier to the slope, $\frac{1+\nu_{hkl}}{E_{hkl}}$, is also called $S_2/2$, and $-\frac{\nu_{hkl}}{E_{hkl}}$ is labeled S_1 . $S_2/2$ and S_1 are the X-ray elastic constants or XEC. They can be calculated based on the single crystal elastic constants of the material, for cubic [257] and hexagonal [258] crystals. Using the Voigt approximation, all grains are assumed to experience the same average strain. The Reuss approximation assumes that all grains experience the same average stress. These approximations are the upper and lower bound for the real XEC. The Neerfeldt-Hill limit is to take the average of the results obtained when using the Voigt and Reuss approximation. A more detailed explanation can be found in Ref. [256].

In this work, the Neerfeldt-Hill limit was used, and the XEC as well as other diffraction parameters for all materials investigated in this work are given in Table 4.1. If the XEC for a particular alloy were not readily available from literature, they were calculated from single crystal elastic constants of the pure base metal, as mentioned above. This may cause the used XEC to differ slightly from the actual, but unknown values.

RS determination by XRD was always performed on the as-built top surface of SLM parts without any surface modification. While this avoided the introduction of extra RS, the rough surface lowered the intensity of the diffraction peaks.

A Siemens D500 with Cu radiation with a wavelength of $\lambda_{Cu} = 1.542\text{\AA}$ or a Seifert MZ4 with Cr radiation with a wavelength of $\lambda_{Cr} = 2.29\text{\AA}$ were used for the measurements. The incoming beam width was $5 \times 5 \text{mm}^2$, which, for $\phi = -45^\circ$ and $2\theta = 142^\circ$ as for Ti6Al4V, leads to a maximum interaction area of $5 \times 11.4 \text{mm}^2$.

4.2 Contour Method

4.2.1 Basic Principle

The contour method was invented by Michael Prime at Los Alamos National Laboratory and described for the first time in Ref. [259]. It has since been expanded to allow multiple cuts on one part [260, 261], superposition of stress measured by other means [262, 263], or the measurement of multiple stress components from one cut [264]. The method requires that the part be sectioned completely. The principle of the method is schematically illustrated in Figure 4.3.

The stresses to be measured are the horizontal stresses perpendicular to the middle plane, indicated in situation A. By cutting the part in half, stress perpendicular to the middle plane is completely relaxed since it is zero by definition for the newly created free surface. This relaxation causes the cut surface to deviate from planarity. Tensile stress will pull the material back, while compressive stresses push the material outwards, as in situation B. Lastly, by returning the deformed cut surface back to the original cut plane, the stresses that were released and that were responsible for the deformation can be calculated. The method is better suited for material with a high σ_y/E ratio, since this leads to higher deformations.

Table 4.1: Type of radiation, diffraction angle and associated diffracting crystal planes, and X-ray elastic constants (XEC) of the different materials used in this work.

	λ	2θ	$\{hkl\}$	$-\frac{S_1}{\nu/E}$	$\frac{S_2/2}{(1+\nu)/E}$	E_{hkl}	ν_{hkl}	Source
		[$^\circ$]		[10^{-3} GPa $^{-1}$]	[10^{-3} GPa $^{-1}$]	[GPa]		
Ti Grade 1	Cu	141.5	{1233}	2.864	11.694	113.24	0.3243	[258, 265, 266]
Ti6Al4V	Cu	141.5	{1233}	2.864	11.694	113.24	0.3243	[258, 265, 266]
316L	Cu	145	{331}	1.588	6.691	195.98	0.3113	[267]
18Ni300 Steel	Cr	155.5	{211}	1.500	6.179	213.72	0.3210	[268]
Ta	Cu	137.5	{400}	2.642	9.664	142.42	0.3763	[269–271]
W	Cu	155	{400}	0.688	3.137	408.31	0.2810	[269, 270, 272]
Inconel718	Cu	145	{331}	1.746	7.039	188.92	0.3298	[273–276]
AlSi10Mg	Cu	162.5	{333} + ^{551}	5.086	19.657	68.63	0.3490	[277–279]
Hastelloy C-276	Cu	145	{331}	1.336	5.866	220.76	0.2950	[280]

The assumptions and consequences of the implementation of the contour method are:

1. The deformation is the result of *elastic* relaxation of residual stress.
2. The slot width created by the cut is infinitely *thin*.
3. The original cut is *flat* and has a *constant width*.
4. The cut is *symmetric*. Asymmetric cuts can be accounted for by assigning different weights to the measured cut surfaces during averaging, but should be avoided if possible.
5. Modeling the cut surface as flat and applying the measured surface profile (with opposite sign) as a displacement boundary condition yields the same results as modeling the deformed surface and forcing it back to planarity. Since deformations are small compared to the part size, this is reasonable.
6. Shear stresses are averaged out by using both halves of the cut, so the average profile is the result of the normal stresses only.
7. Components of the deformation other than that normal to the cut surface are not taken into account.
8. Antisymmetric defects are averaged out by averaging both halves of the cut surface.

4.2.2 Cutting

The accuracy of the contour method and the validity of some of the assumptions depend on the cut. While it is impossible to cut a component in half with an infinitely thin cut (assumption 2), using wire Electro-Discharge Machining (EDM) and a thin wire ($\varnothing 100\mu\text{m}$) has been proven to be the best approximation of this assumption [282]. Moreover, adequate clamping of both halves of the specimen during cutting is the best assurance of a planar cut. If only one half of the part is clamped, as in Figure 4.4, relaxation of the stresses causes the part to deform and the cut to deviate from the original plane (assumption 3). Clamping both halves also serves to minimize other cutting errors, which are discussed below.

The errors that arise during cutting can be classified as either symmetric errors or antisymmetric errors. Anti-symmetric errors are errors that introduce defects of opposite sign or direction on the two cut surfaces. They include shear stresses,

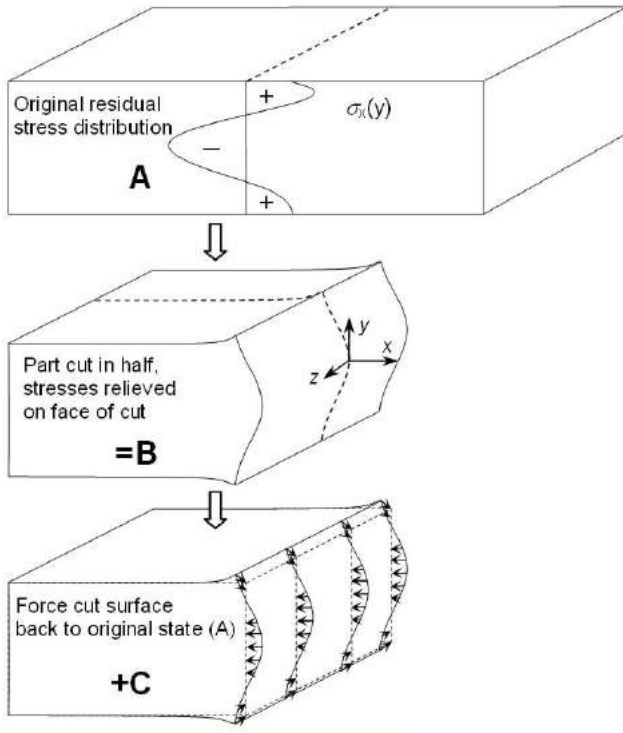


Figure 4.3: Principle of the contour method. The residual stresses in the x-direction acting over the middle plane in situation A are released by sectioning along the middle plane, which deforms accordingly in situation B. By forcing the cut surface to the original plane in situation C, the stress in the x-direction along the entire cut plane can be measured (From Ref. [281]).

crooked cut paths and even movement of the part during cutting. Averaging the two surface profiles cancels out these errors, as is illustrated in Figure 4.5.

Symmetric errors, on the other hand, are not averaged out. They include:

- Deviation from a planar cut by wire vibrations (barreling effect),
- changes in cut width due to changes in the material composition or part thickness,
- wire breakage,
- stress induced by the cutting itself,

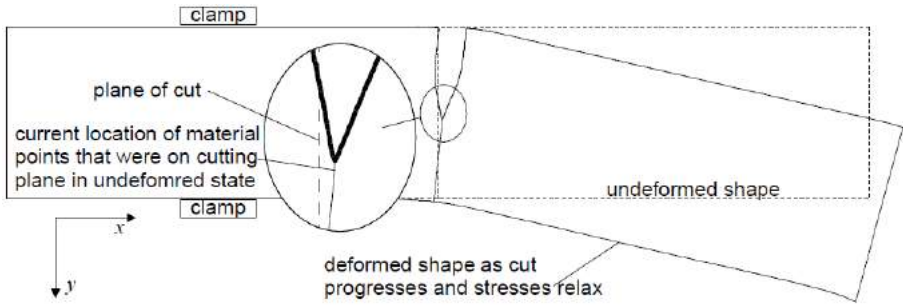


Figure 4.4: Clamping only one half of the part during wire EDM cutting allows the part to deform and introduces cutting errors (From Ref. [281]).

- flaring of the top and bottom edge of the cut, where the wire feed enters and leaves during cutting and
- the bulge error.

Most of these errors are mitigated by using a strong, thin wire, and by using so called ‘*skim cut*’ settings. This is a low power setting that is normally used to pass over a previously cut surface to lower the surface roughness. The stress that is introduced by wire EDM does not depend on the stress magnitude in the part. Apart from using skim cut settings, another solution therefore is to use a reference cut on an identical, stress free geometry and to subtract the induced surface profile from the profile measured on the part containing RS. Since a duplicate, stress free part is often not available, this is also possible by cutting a thin layer after performing the first cut. Since the first cut released all normal stresses, the material just below the cut surface can be assumed to be stress free.

A specific type of symmetric error is the bulge error, illustrated in Figure 4.6. Stress relaxation causes deformation at the cut tip near the wire, so the cut width is not constant. The effect is proportional to the stress intensity factor at the cut tip, and thus proportional to the magnitude of the residual stress [282]. The bulge error causes the location of peak stresses to be misjudged slightly, and also lowers the measured peak values. Additionally, it can cause a large deviation at the end of the cut. Clamping on both sides, close to the cut is the best means to minimize the bulge error. In Ref. [282], the bulge error was seen to triple by increasing the slot width to part thickness ratio w/t from 1% to 5%. In this work, w/t is around 1 to 2%.

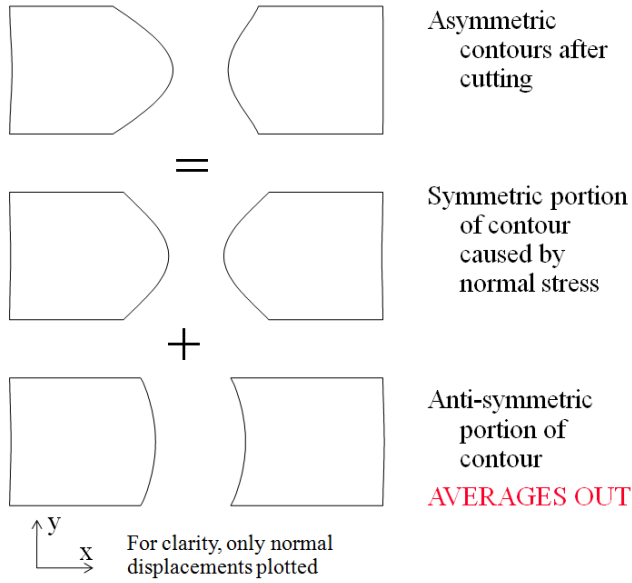


Figure 4.5: Asymmetric errors are averaged out by taking both halves of the cut into account (From Ref. [281]).

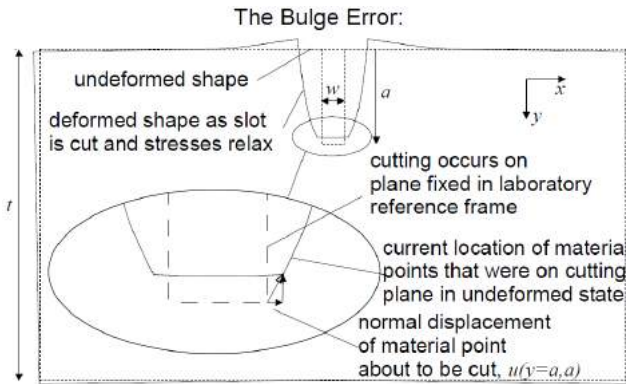


Figure 4.6: Illustration of the bulge error during wire EDM cutting (From Ref. [281]).

4.2.3 Surface profile measurement

The deviation from a planar cut can be measured with a touch probe coordinate measurement machine (CMM), typically with a ruby tipped stylus with a diameter of 2-4mm. A non-contact confocal laser probe has also been used and was found to be more accurate for small parts and/or lower stress levels [283]. Using a laser probe is also faster and creates more data points, but this does not contribute to the accuracy of the contour method [283]. A laser triangulation probe, that can often be mounted onto a CMM, experiences difficulties with optical surface variations (change in color/reflectivity) that are present on EDM'ed surfaces, and is therefore less suitable [283]. The point spacing reported in literature when using a touch probe varies between 130 μ m in earlier work [259], to anywhere between 0.3mm and 1.0mm in later work when it was found that this was sufficient to capture the surface profile [283,284]. The point spacing in this work was 0.4mm for results reported in chapter 5, and 0.3mm in chapter 8. Roughness variation, measurement error and any kind of cutting error are superposed on the smooth variations in height that are caused by the RS, and need to be taken care of during further data processing.

4.2.4 Data Processing

In this work, outliers in the point clouds obtained from the previous step are removed by a MATLAB routine that compares each data point to its neighbors. If the point deviates too much, it is given a new value that is the average of the surrounding points. This clean-up routine can be repeated if necessary. Surface defects that cannot be smoothed out this way, such as wire breakage, are manually removed. The point cloud is leveled and a zero plane is defined and subtracted.

Next, the point cloud is interpolated onto a predefined grid, and the edges are removed, and replaced by extrapolation from the inner values. The interpolation onto a predefined, common grid is also necessary to average the two measured surface profiles of both halves of the cut. Extrapolation is needed to be able to apply a deformation boundary condition on the entire surface in the FE model.

Lastly, a bivariate spline surface is fitted through the averaged surface profile. If the rough point cloud itself were applied as a boundary condition to an FE model, the remaining roughness would create unrealistic stress peaks. The knot spacing of the spline needs to be low enough (i.e. high spacing) to smooth out random surface roughness, but high enough (i.e. low spacing) to avoid losing information about the RS distribution. In Ref. [283], the knot spacing was varied and the optimum was defined to be 0.4 knots per mm, or a knot spacing

of 2.5mm. This value can change slightly depending on the RS distribution. In this work, the knot spacing was chosen between 2.5 and 3mm.

4.2.5 Stress calculation

To convert the measured deformations to stresses, the measured contour is applied as a deformation boundary condition to an FE model of a half of the original part by evaluating the spline at the node coordinates. In theory, the part should be modeled with the deformed surface, which would then be returned to planarity. However, because deformations are small, it is also acceptable to apply the measured deformation to a flat surface, given that the sign of the deformation is flipped.

Because the deformations have been centered around an arbitrary zero plane in the previous step, they lead to stresses that obey force and moment balance. The FE model therefore only needs constraints that prohibit free body movement, which is done by constraining the in-plane movement of one corner of the cut surface, and a further constraint of the movement in one in-plane movement of another corner point [259]. These constraints are shown in Figure 4.8 by the small pyramid shapes. The ABAQUS model node spacing at the cut plane equals 0.3mm in chapter 8 to 1.0mm for the validation below and chapter 5, and consists of brick elements with reduced integration (type C3D8R in chapter 8 and 5, type C3D20R in the validation below).

4.2.6 Validation

To validate the contour method procedure used in this work, an M2 HSS beam measuring 22x10x100mm³ was plastically bent up to 1% plastic strain using four point bending. This introduced a known, unidirectional residual stress profile, which was simulated by an FE model shown in Figure 4.7. The material hardening behavior was based on tensile tests performed on material obtained from the same plate.

The beam was symmetrically cut in the middle by wire EDM using a 100 μ m thick brass wire, and skim cut settings while it was clamped in a custom-made clamping rig. This rig was designed to allow clamping of a wide variety of geometries, including a cylindrical base plate and a cubic part.

After cutting, the deformation of both halves of the cut surface was measured using a Coord3 CMM equipped with a 3mm diameter ruby tipped stylus. Measurement points were spaced 0.4mm apart in both X and Y direction, creating a 55x25 point cloud. The accuracy (total systematic and random error)

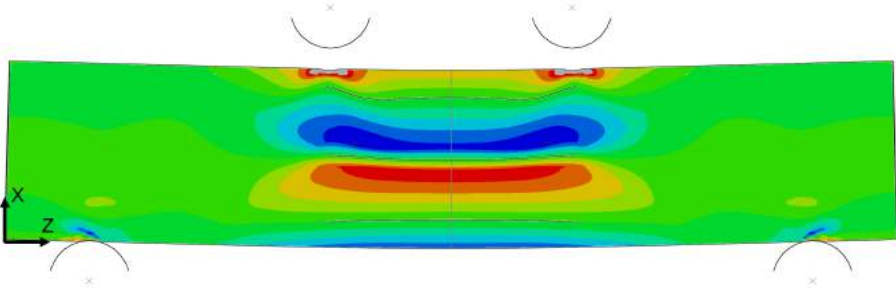


Figure 4.7: Horizontal RS in the beam after the top pins were retracted after plastic bending of the beam. The bend test was modeled using symmetry boundary conditions in the middle plane of the beam, but is mirrored here to show the complete set-up. The color scale ranges from +300MPa (red) to -300MPa (blue), and the black lines in the middle section indicate a stress of 0MPa. The X and Z axes correspond to those of Figure 4.8.

and precision (single point repeatability) of the machine are $5\mu\text{m}$ and $1\mu\text{m}$, respectively.

The 2D map of the RS in the beam measured via the contour method is shown in Figure 4.8, using an E-modulus of 220GPa (measured via impuls excitation) and a Poisson ratio of 0.3. Although the stress profile in this example is supposed to be identical over the width (Y-direction) of the beam, the advantage of the contour method over other sectioning methods such as the crack compliance method [285] is that it is capable of measuring stresses over an entire 2D plane. For this validation, however, the stresses over the width are averaged to produce a 1D stress profile that can be compared with a theoretical profile.

The results in Figure 4.9 show the theoretical RS profile extracted from Figure 4.7 (dashed line) and the profile measured by the contour method (solid black line). The shape of the RS profile is replicated well, although the locations of the maximum and minimum stress are shifted over a small distance, and the maximum and minimum value of the stress are also slightly underestimated. The shift of the peaks and slight underestimation of the values was expected and are caused by the bulge error.

In hindsight, the material that was used for the validation was not optimal. M2 tool steel has a high σ_y/E ratio only after a hardening heat treatment, but such a heat treatment also limits plastic flow. The M2 steel bars used for the validation were in the unhardened condition, with a yield stress of only 300 MPa. As a result, the peak-to-valley distance of the deformed surface was only $10\mu\text{m}$. Nevertheless, Figure 4.9 shows that the stress values and shape were

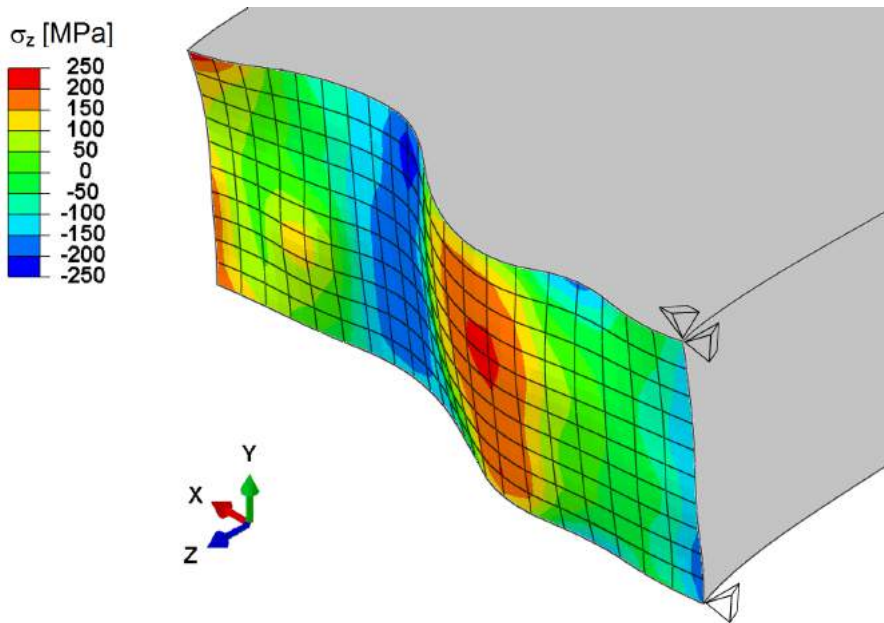


Figure 4.8: 2D stress map in the center of the known residual stress specimen ($XxYxZ = 22 \times 10 \times 100 \text{mm}^3$), obtained using the contour method. The deformations are scaled by a factor of 250. The X-axis corresponds to that of Figure 4.9.

captured adequately. It would have been better to use Ti6Al4V, to which the contour method has been applied in the remainder of this work. The σ_y/E ratio for Ti6Al4V is six times higher than that of the M2 steel bars, which improves the accuracy.

4.3 Part deformation

Because RS during SLM is built up in the base plate-part *system*, separating the part from the base plate causes a redistribution of the stresses, and a deformation of the part. By designing the part geometry so that this deformation results in a measurable quantity, the residual stress can be studied.

Two different specimen geometries were used in this work. In chapter 6, a bridge shaped specimen was used as described below in subsection 4.3.1, while other

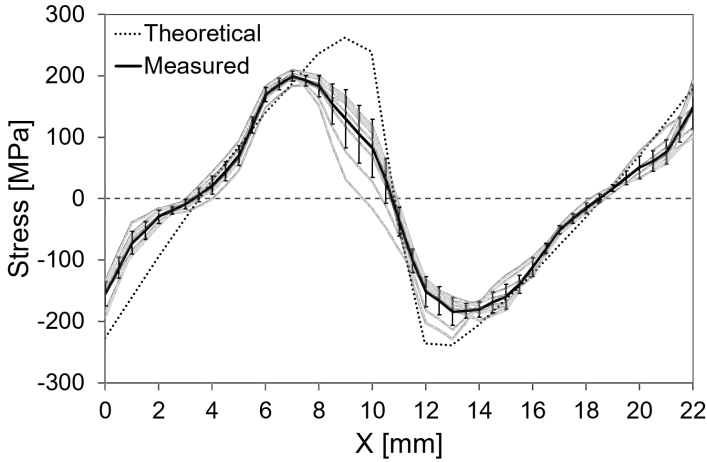


Figure 4.9: Comparison of the theoretical residual stress profile in a plastically bent beam after 4 point beam testing (dashed line), and that measured via the contour method (black line). The 2D stress profile obtained via the contour method is reduced to a 1D stress profile. The grey lines are different 1D stress profiles measured along the width of the specimen.

chapters used the cantilever specimen and associated procedure described in subsection 4.3.2.

4.3.1 Bridge Curvature Method

The Bridge Curvature Method or BCM has been described in detail in Ref. [237]. The small bridges, of which the dimensions are given in Figure 4.10a, curl up after removal from the base plate. In the absence of residual stress, the cut surface of both ends of the bridge remain coplanar. the curl-up results in an angle between the two cut planes as indicated in Figure 4.10b, which can be measured with relative ease.

The angle of deformation α_{BCM} is measured using a Mitutoyo Quick Vision Pro 202 optical coordinate measuring machine. The bridges were placed on their side with backlighting, and a line was fitted trough the edge of the bottom of each end. The same software then calculated the angle between the two lines. For each bridge, this was repeated 5 times, after which the bridge was placed on its other side and the measurements were repeated. Three bridges were produced per material.

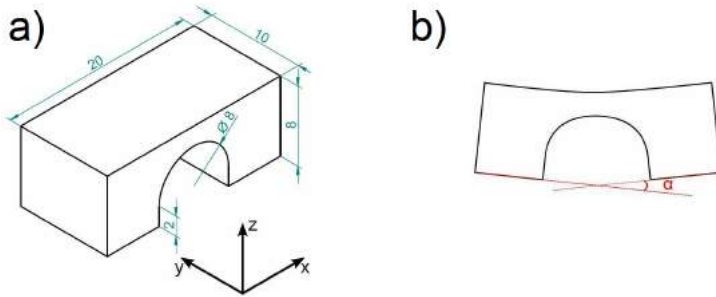


Figure 4.10: a) Dimensions of the BCM specimen. b) bridge shaped part on the base plate and c) removal from the base plate results in curl-up angle α_{BCM} [237].

In an effort to convert α_{BCM} to actual stress values that could be compared between materials, the deformation was applied as a boundary condition to an FE model of the bridge shape using the commercially available ABAQUS FE package. This will be discussed in chapter 6, subsection 6.1.5.

4.3.2 Cantilever specimens

The disadvantage of the BCM geometry is that the main source of the deformation is the thin region of the overhanging section of the bridge. The measured curl-up angles, therefore, are small which decreases the accuracy with which they can be determined. Therefore, an improved design was used for other work packages, shown in Figure 4.11. The T-shaped cantilever specimen consists of two, large overhanging regions on both sides of a central, solid support. The overhang structure is supported by thin pillars. The end of the overhang structure is rigidly fixed with solid end blocks to avoid cracking problems and form deviation encountered in Ref. [136]. This type of geometry has also been used elsewhere to study RS in SLM [136, 222, 223, 286, 287], as early as 1994 [288].

The relaxation of stress along the entire length of the specimen now contributes to the deformation, which was measured with a Coord3 touch probe coordinate measurement machine with a 3mm diameter ruby tipped stylus. Along the long direction of the cantilever, the deformation was measured every 2mm, resulting in 24 measurement locations along the 50mm length. Four measurements were taken along the width and averaged to minimize the effect of surface roughness. These averages are shown for one sample by the black markers in Figure 4.12.

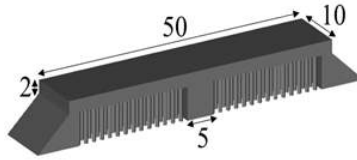


Figure 4.11: Dimensions of the cantilever specimen.

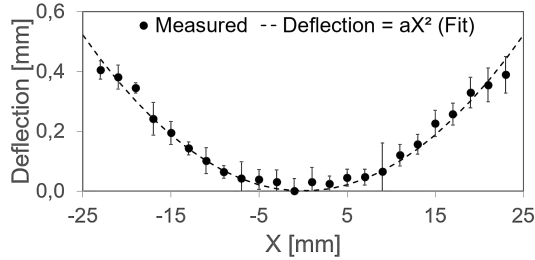


Figure 4.12: Example of the fit of a parabolic curve through the measured deformation.

Next, a parabolic curve was fitted through the data points in an attempt to further minimize the influence of surface roughness. The bottom (vertex) of the parabola was set in the center of the cantilever specimen and assigned a value of zero. The parabolic fit then has an equation in the form of $y = ax^2$. The value of a was optimized using a least-squares fit. The curvature at the vertex of a parabola with function $y = ax^2$ is given by $\kappa = 2a$ [289]. It is this curvature that is used in this work to characterize the magnitude of the RS (comparative method).

Chapter 5

General Characterization and Influence of the Process Parameters

Before the influence of any variable on the residual stresses can be assessed, it is necessary to understand the overall residual stress state in SLM parts. Focusing on Ti6Al4V, this chapter first characterizes the magnitude and shape of the residual stresses, after which the influence of several process parameters is discussed, in particular the laser power, scan speed, layer thickness and preheating temperature. The overall shape of the RS distribution and expected influence of these process parameters were already discussed in the literature study in section 3.2, and the results in this chapter therefore go without introduction.

The results in this chapter have been partially published in the conference papers below.

- Vrancken, B., Buls, S., Kruth, J., Van Humbeeck, J. (2015). Influence of preheating and oxygen content on Selective Laser Melting of Ti6Al4V. Proceedings of the 16th RAPDASA Conference. RAPDASA, Annual International Conference on Rapid Product Development Association of South Africa. Pretoria, South Africa, 4-6 November 2015.
- Vrancken, B., Buls, S., Kruth, J., Van Humbeeck, J. (2015). Preheating of Selective Laser Melted Ti6Al4V - Microstructure and mechanical

properties. Proceedings of the World Conference on Titanium. World Conference on Titanium. San Diego, CA, US, 16-20 August 2015 TMS.

5.1 General characterization of the residual stresses

5.1.1 Materials and Methods

12 identical cubes measuring $15 \times 15 \times 15 \text{mm}^3$ were built on the LM-Q machine of the PMA Division of the department of mechanical engineering, KU Leuven. More details on this machine can be found in Ref. [290]. They were built in 12 separate jobs to avoid possible differences caused by location of the part on the base plate. Process parameters were set at $P=250\text{W}$, $v=1600\text{mm/s}$, $h=60\mu\text{m}$, $t=30\mu\text{m}$ and a zigzag scan strategy was employed that was rotated 90° every layer. In theory, these 12 cubes should be identical.

Residual stresses were determined by two different methods for all cubes. First, the parts were removed from the base plate using wire EDM performed with a thin, $100\mu\text{m}$ diameter brass wire using skim cut settings, rather than the normal, fast cutting using a $250\mu\text{m}$ diameter wire (labeled *Cut 1* in Figure 5.1). This allowed the cut surface to be used for contour method stress calculations. Unfortunately, cut 1 is not a symmetric cut, and therefore averaging the deformations from both cut surfaces is not possible (see chapter 4, section 4.2). Only the deformation of the cut surface of the cube was measured and used, so anti-symmetric errors are not averaged out and the accuracy is reduced. Wire breakage during removal of sample 12 caused too many artifacts to deal with during data post-processing, so contour results from sample 12 were not taken into account.

After removal from the base plate, the stress on the top surface, colored grey in Figure 5.1, was measured using XRD. Finally, for sample 1 and 2, a second cut, labeled *Cut 2* was made to expose the blue diagonal surface shown in Figure 5.1. This cut reveals the horizontal stress inside the sample.

5.1.2 Results

XRD

The principal stresses in the top surface, measured by XRD, are shown in Figure 5.2. Averaged over all samples, the maximum principal stress σ_1 equals $409 \pm 66 \text{MPa}$, and the minimum principal stress $125 \pm 43 \text{MPa}$. The direction of

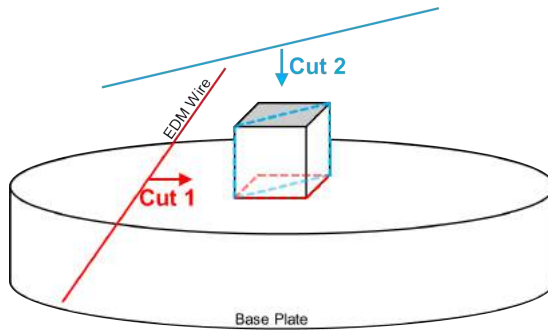


Figure 5.1: Schematic representation of the cuts that were used for contour method measurements. The stresses were also measured via XRD on the top surface, indicated in grey, after cut 1 was performed.

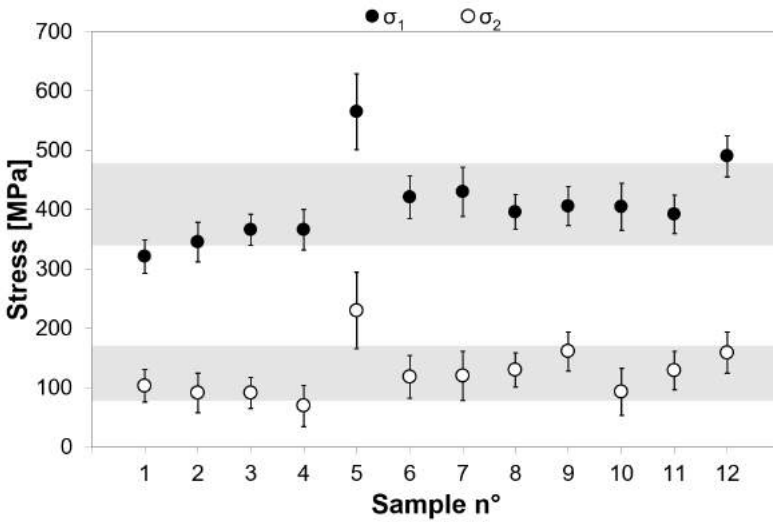


Figure 5.2: Maximum (σ_1 , black markers) and minimum (σ_2 , hollow markers) principal stress on the top surface of the 12 different samples. The grey bands indicate the average of the 12 values ± 1 standard deviation.

the maximum principal stress with respect to the direction of the scan tracks in the top layer is $5 \pm 10^\circ$, which is a confirmation of results in literature that indicate that RS in the direction of the scan track is the largest.

Rather than the average value, what's most interesting about Figure 5.2 is the spread on the results. Although the production parameters for all 12 samples were identical, there is a large spread on the measured stresses. The lowest σ_1 , $321 \pm 28 \text{MPa}$ for cube 1, is only 57% of the maximum measured stress, equal to $565 \pm 64 \text{MPa}$ for cube 5.

A combination of factors can be responsible for the large spread, all of which eventually cause a variation in melt pool dimensions, cooling rates and thermal gradients:

- Powder packing: With layer thicknesses equal to the average particle size, only a handful of powder particles are irradiated at a given time, causing a large variation of material going into the melt pool. Additionally, powder particles that are adjacent to the melt pool can get pulled into the melt, which causes disturbances.
- Variation of power and speed: At a speed of 1600mm/s and vector length of 15mm, the time to scan one scan track is less than a hundredth of a second. In that time, the laser needs to be accelerated, turned on, decelerated and turned off again. The speed and power, therefore, are not constant either.
- Plateau-Rayleigh instabilities. As the melt pool becomes more elongated for high scan speeds, surface tension will drive the melt pool to break up into smaller droplets to minimize the surface area. This is known as balling, and the onset of this phenomenon creates melt pools for which the width fluctuates.

The SLM process is not a deterministic process, but a process that depends on a combination of stochastic variables. Many thermal simulations that model the powder layer as a homogeneous material, and are only interested in the steady state, do not capture these variations. Recent work at Lawrence Livermore National Laboratory does model the powder particles as individual entities [291]. Moreover, the Marangoni flows inside the melt pool, surface tension and recoil pressure from vaporized material were captured as well. The results, shown in Figure 5.3, are strong evidence of the violent nature of the SLM process. In Figure 5.3a to c, the final stage of track scanning and subsequent solidification of the melt pool are given at various time intervals. From Figure 5.3a to c, the laser moves to the right and creates a depression that allows the laser to melt deep into the powder layer and the solid substrate below. The solidified part of the scan track in Figure 5.3c shows that the width of the track varies, as does the depth (not shown here). Powder particles that have been pulled into the melt pool create denudated zones next to the melt pool. The shape of the

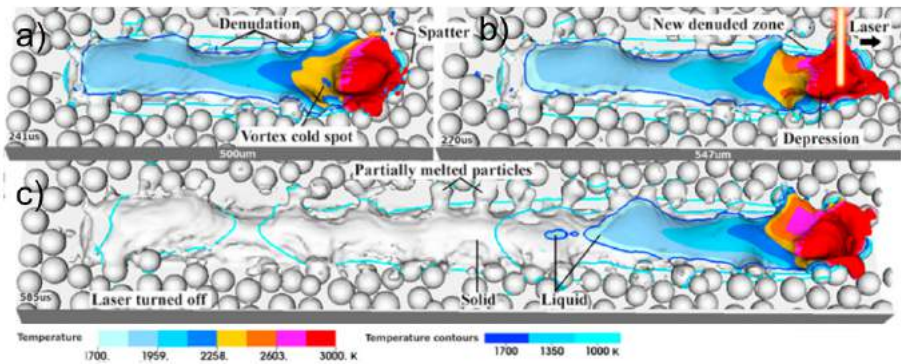


Figure 5.3: Model of the melt pool formation and solidification. In (a) the melt pool is shown $241\mu\text{s}$ after the laser is switched on. There is no solidified material yet. The position of the laser is indicated in (b), right on top of the depression it creates. c) $515\mu\text{s}$ later, the laser is switched off. At this point, the solidified region shows that the scan track formation is not a deterministic process but depends on local influences (Adapted from Ref. [291]).

solidified track varies, and depends on the combination of the three phenomena given above.

An unfortunate consequence is that residual stresses will vary between different parts that have been built with identical production parameters. This greatly complicates research into the effect of different process parameters on the residual stresses, and makes it impossible to determine quantitative relations. Instead, this chapter and those that will follow focus on distinguishing qualitative trends.

Contour Method

The results of the contour method residual stress measurements from the base plate-part interface (*cut 1*) are summarized in Figure 5.4. The maximum tensile stresses are higher than the maximum compressive stresses, because the region experiencing residual tensile stress is smaller, and because the corners act as stress concentrators. The spread on the results originates from the contour method itself rather than the stochastic nature of the SLM process, as was the cause of the spread in the previous subsection. The variations that exist inside and between individual scan tracks are assumed to be of smaller significance over the part scale, which consists of tens of thousands of scan tracks.

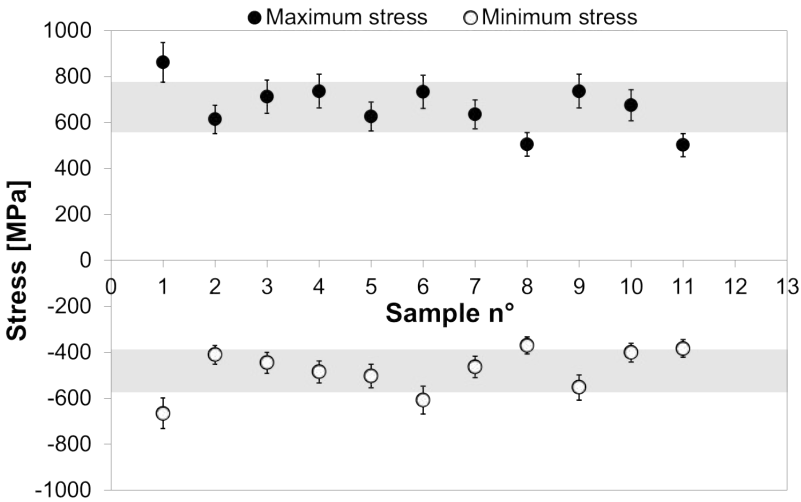


Figure 5.4: Maximum (black markers) and minimum (hollow markers) vertical stress in the base plate-part interface defined by cut 1 in Figure 5.1. The grey bands indicate the average of the 11 values ± 1 standard deviation.

An averaged map, calculated from the averaged deformations from 11 cut surfaces exposed by *cut 1* (excluding sample 12), is shown in Figure 5.5. The stresses in this map are the vertical residual stresses that exist in the interface between the base plate and the part. The stress distribution along the X direction is different than that along the Y direction, caused by a slightly wider cut near the top and bottom [292]. For all cuts, the wire was parallel to the Y axis, so the entry and exit points of the wire into the cut were located at the edges parallel to the X axis. At these locations, wire EDM is known to cause flaring of the edges [292]. Unfortunately, this effect is present in all the measured contour maps. Given that these mappings were based on only one of the cut surfaces and that anti-symmetric errors were not averaged out, the results still match well with the overall shape of the vertical RS distribution reported in literature [219].

In chapter 3, vertical tensile stresses at the side surfaces were described to cause cracks at stress concentrations, such as corners. Figure 5.5 reveals these stress concentrations at the corners. The overall stress distribution consists of a tension zone along the outer surfaces, and compression in the center. After averaging all the deformed surfaces, the maximum tensile stress is found at the corners, at 580 ± 67 MPa. Caution is advised, however, when interpreting this value,

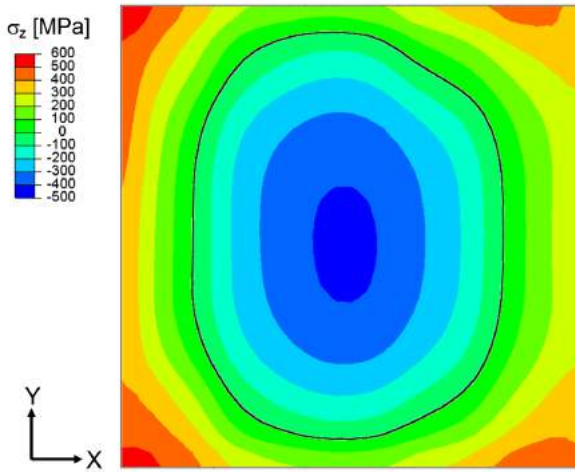


Figure 5.5: Stress map of the vertical stress in the base plate-part interface, calculated from the average deformations from 11 samples (dimensions are $15 \times 15 \text{ mm}^2$). The black line indicates the boundary between the tensile and compressive zone.

since the contour method inaccuracies are largest at the edges. In the center, compressive stresses reach values around $-419 \pm 45 \text{ MPa}$. These values are lower than the maximum and minimum stress obtained by averaging the maximum and minimum values after evaluating each surface individually. Averaging the surface deformations *before* calculating the resulting stresses also averages away local extreme values that are still present in the individual maps, mostly at the corners. These extremes result in higher tensile stresses, and higher offsetting compressive stresses.

The origin of these vertical stresses are the horizontal stresses that are introduced by successive melting and subsequent contraction of every layer. Because the horizontal contraction is constrained, the deposition introduces vertical tensile stresses along the side surfaces, and compressive stresses in the bulk. After removal from the base plate, stresses along all outer surfaces are tensile, and compressive in the center, as will be demonstrated below. If the part width-to-height ratio is large, removal from the base plate results in significant deformation or curl-up. However, for smaller width-to-height ratios, the resistance to curl-up is large (scales with the cube of the height), and stresses that were introduced can no longer be substantially relieved by deformation of the sample, but are stored inside the sample as residual stress.

Apart from the vertical stresses in the base plate-part interface measured by *cut 1*, sample 1 and 2 were also sectioned along the diagonal plane shown in Figure 5.1, labeled by '*Cut 2*'. *Cut 2* reveals the horizontal RS inside the part. There is no particular reason why a diagonal cut was chosen over a cut parallel to the side surfaces. On the part scale, the horizontal stresses are assumed to be the same in the X and Y direction, as the scan strategy is rotated 90° every layer, and the parts consist of 500 layers. Information obtained from a diagonal cut is therefore equivalent to that of a cut parallel to a side surface.

The stress map in Figure 5.6 is an average of the two diagonal maps. The horizontal stress in the corners of the vertical sides of the cubes (left and right edge of the map) are low, as the geometry becomes thin near this edge and stresses perpendicular to a surface are zero by definition, something which is more obvious from Figure 5.7. This map is identical to Figure 5.6, but with smooth contouring. Stress near the top surface is tensile, which transitions to a large zone of compressive horizontal stresses in the center. Near the bottom, horizontal stresses are thought to be near zero or compressive *before* removal from the base plate. Removing the part results in a redistribution of the RS, and causes the tensile stresses at the bottom that are shown in Figure 5.6. The maximum tensile stress in this map is equal to $270\pm 35\text{MPa}$, and compressive stresses peak at $-162\pm 18\text{MPa}$. Compared to the maximum vertical stresses obtained from *cut 1*, the horizontal maxima are less than 50% of the vertical maxima. Moreover, this distribution corresponds to the profile predicted by the simple 1D model developed by Mercelis and Kruth [231], discussed in more detail in subsection 5.2.2.

It would be incorrect to compare the horizontal stresses near the top surface obtained via the contour method with the stresses in the top layer measured by XRD. Besides from measuring different stress components (the contour method measured macroscopic, Type I stress, while XRD measures both Type I and II stress), the location of the stress measurement itself is different. XRD measures stress in the top 10-15 μm , while inaccuracy of the contour method is the highest near the edges.

5.1.3 Preliminary conclusions

- There is a large spread on the RS inside SLM produced Ti6Al4V, caused by the stochastic nature of the SLM process.
- The stress in the direction of the scan vectors is larger than the stress perpendicular to the scan vectors.

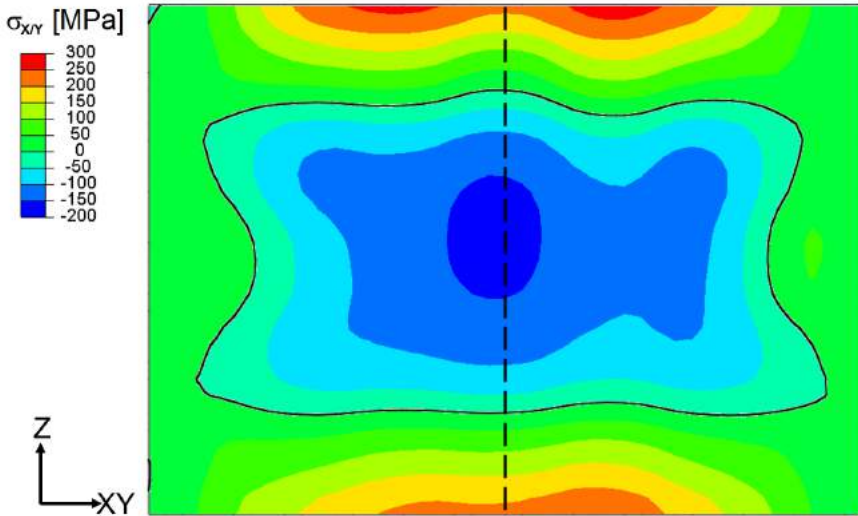


Figure 5.6: Stress map of the horizontal stress in the diagonal area, calculated from the average deformations obtained from 2 samples. The black line indicates the boundary between the tensile and compressive zone. The stress profile along the dashed line is used later on in Figure 5.13b.

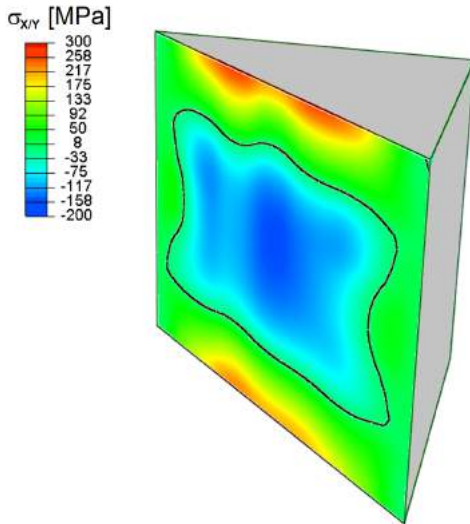


Figure 5.7: Isometric view of the horizontal stress in the diagonal area. The black line indicates the boundary between the tensile and compressive zone.

- The overall RS distribution inside cubic parts after removal from the base plate is tensile along all outer surfaces, balanced by compressive stresses in the center.

5.2 Influence of ‘conventional’ parameters

5.2.1 Materials and Methods

These results are a compilation of several different batches of samples produced throughout the duration of this PhD. All results were obtained on samples produced by 3D Systems Layerwise, except for the results given in Figure 5.9, which are based on samples produced on the LM-Q machine. Cuboid samples were used for XRD stress determination and density measurements, and cantilever shaped specimens for an indication of the macroscopic RS.

Parameters sets of the parts produced by 3D Systems Layerwise are given in Figure 5.8. These sets can be clustered, for each layer thickness (30-60-90-120 μm), as combinations of three laser powers (P1, P2 and P3), and four scan speed intervals (v1, v2, v3 and v4). Note that the scan speed may differ within one interval for different layer thicknesses).

The hatch spacing was kept constant. Some parameter sets led to low density, and these parameter sets have a cross drawn over them in Figure 5.8. There were 7 parameter sets that led to high densities above 99% (two of the 28

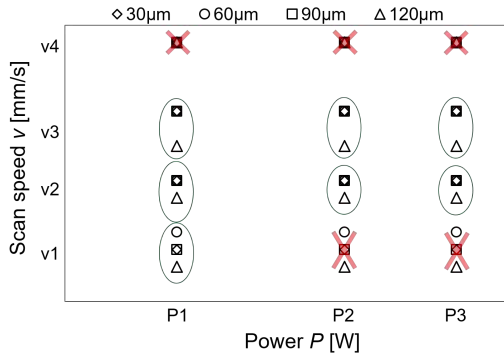


Figure 5.8: Indication of all parameter sets used for parts built by 3D Systems Layerwise.

combinations only 98%) of the cuboid samples. These are circled in Figure 5.8. Cantilevers were made using these parameter sets.

Each batch consisted of 28 cantilevers (7 combinations of P and v for four different layer thicknesses). Unfortunately, the identity of the cantilevers was lost for a first batch of 28 cantilever specimens. Therefore, results from batch 1 are only suitable to compare the layer thicknesses (since the scan pattern on the top layer was different for the different layer thicknesses, and could therefore be distinguished), and a second batch was produced.

5.2.2 Results

XRD

LM-Q samples

A first set of experiments was based on the collection of parameter sets that resulted in good density, determined by D. Van Buel and O. Raeymaekers [38, 293]. A wide range of scan speeds (189-1600mm/s) and laser powers (42-250W) were used. All parameter sets can be divided into two groups, based on the measured residual stress. In Figure 5.9, results for parameter sets with low laser power and scan speed are marked as diamonds (also circled and labeled '1' in Figure 5.9d), whereas results for high speeds and powers are marked as circles (labeled '2' in Figure 5.9d). The stress for group one is lower than the stress for group two, even though they may have similar energy densities (Figure 5.9c). The residual stress, indicated with the full markers, is larger for higher powers/speeds.

Using only the stress values, it is not possible to distinguish if the scan speed or the laser power is causing this effect from this data, since they are not independent of each other (Figure 5.9d).

In addition to the stress, the hollow markers in Figure 5.9 also show the ratio of residual stress parallel to the scan vectors and that perpendicular to it. Like the residual stress magnitude, this ratio also increases with increasing scan power and scan speed, and this may be used to determine whether it is the laser power or the scan speed that is responsible for increasing the RS. Increasing the laser power will slightly enlarge the melt pool dimensions in all directions, but increasing the scan speed will cause the melt pool to elongate. A high scan speed therefore leads to a higher anisotropy, whereas a high laser power would have little effect, or may even act to reduce anisotropic effects.

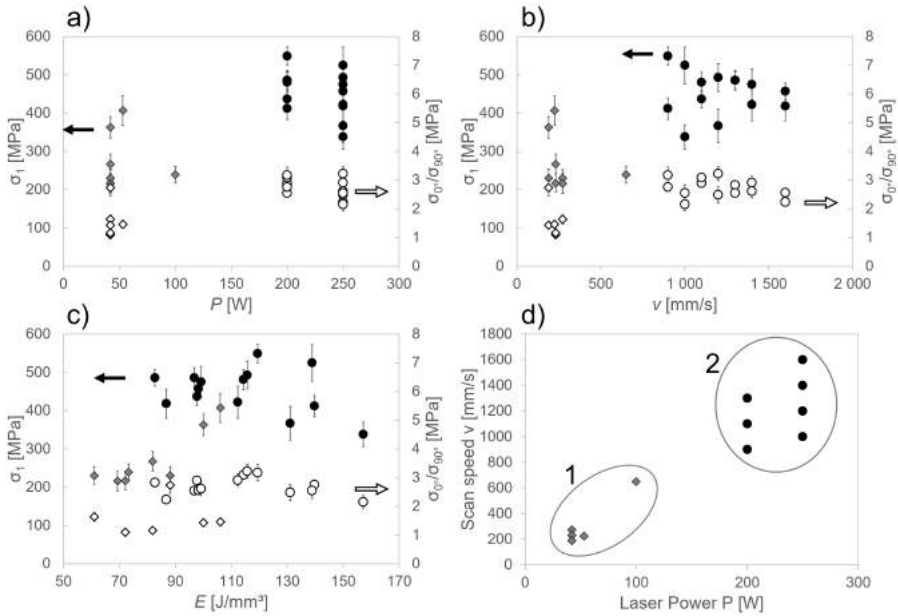


Figure 5.9: (a-c) Full markers indicate the maximum principal stress (σ_1) for all combinations of P and v shown in (d), as a function of the laser power (a), scan speed (b) and energy density (c). Diamond markers indicate results from parameter sets labeled '1' in (d), while circles are results from group '2'. In addition to the stress, the hollow markers indicate the ratio between the stress in the direction of the scan vectors and perpendicular to the scan vectors.

3D Systems Layerwise samples

Results for a second set of experiments using the parameter sets shown in Figure 5.8 are summarized in Figure 5.10. The values in these surface plots are the maximum principle stresses σ_1 , and the scale is identical for all four subplots. These measurements seem to indicate that a thicker layer leads to much lower stresses. Additionally, a less obvious but still visible trend is that low scan speeds and high laser powers, i.e. high energy densities (front corner of the plots in Figure 5.10), also lead to lower stresses.

To capture these trends in numbers, a linear regression model was fitted through the data. Interactions were not taken into account, as these terms would possibly obscure the influence of the individual parameters. Because the exact form of the correlation between the parameters and the stress is unknown, and interactions

Table 5.1: Regression analysis coefficients based on XRD values for the laser power, scan speed and layer thickness related to Equation (5.1).

Term	Coef	SE Coef	P-Value
Constant	525.3	98.4	0.000
P [W]	-0.705	0.260	0.009
v [mm/s]	0.0895	0.0298	0.004
t [μm]	-3.130	0.398	0.000

are ignored, the resulting regression equation is not realistic and should not be used to predict the RS. A testament to this is that the difference between the predicted stress value and measured stress value is up to 200MPa for some data points, as well as the large standard error on the predicted coefficients (column 3 of Table 5.1). The adjusted R^2 -value of the regression is equal to 63%.

In the regression equation given in Equation (5.1), the sign of the coefficients indicates whether the stress and the parameters P, v and t are positively or negatively correlated. The minus signs for P and t indicate that higher values for these parameters will lower residual stresses, while a higher scan speed v increases the residual stress. The values of the coefficients in Equation (5.1) are not a direct indication of the magnitude of the effect of the associated parameter, since the parameters themselves vary between different ranges. Instead, the P-values, given in column 4 of Table 5.1, provide insight into the relative importance of each parameter. All P-values are smaller than $\alpha=0.05$, so the influence of all parameters is significant, and the influence of the layer thickness ($P=0.000$) is stronger than that of the scan speed ($P=0.004$), which is in turn stronger than that of the laser power ($P=0.009$).

$$\sigma_1[MPa] = 525.3 - 0.705P[W] + 0.0895v[mm/s] - 3.130t[\mu m] \quad (5.1)$$

Cantilever deformation

The curvatures for all parameter sets of the samples in batch 2 are shown in Figure 5.11. Although lines connect the data points, there is no ranking order between the data points. The line is only present to visualize that the layer thickness has a big influence, but that influence is not 100% clear. The curvature increases from 30 μm up to 90 μm layer thickness, but is lower again for samples built with a 120 μm layer thickness.

In Figure 5.12, the data points for one layer thickness are averaged, so that a comparison can be made for batch 1 and batch 2. This shows that the results for both batches are different. In batch 1, a 30 μm layer thickness seems to be

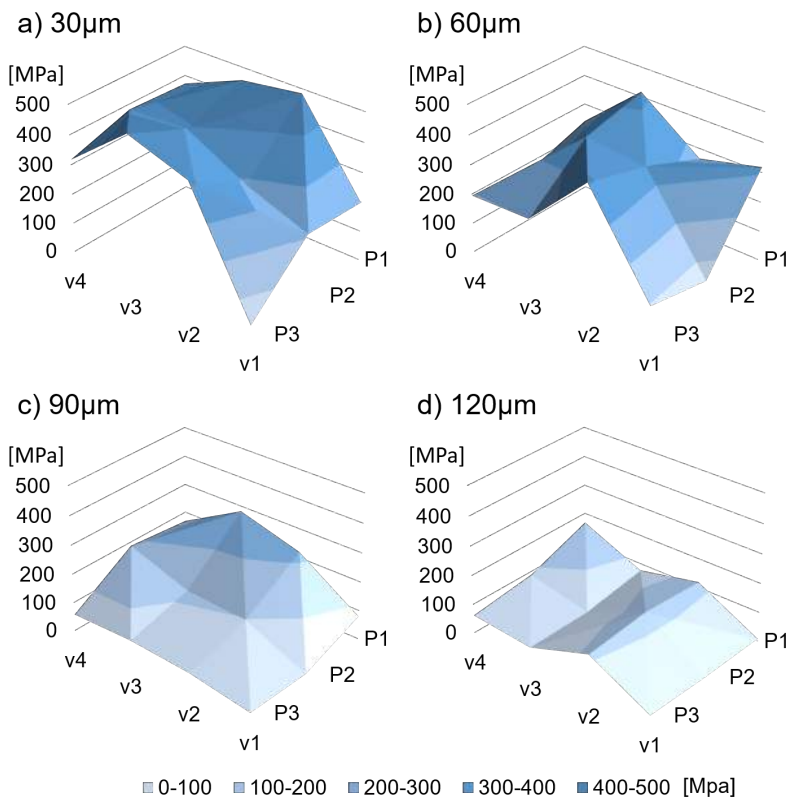


Figure 5.10: Maximum principal stress measured via XRD for all parameter combinations, for different layer thicknesses: a) 30µm, b) 60µm, c) 90µm and d) 120µm.

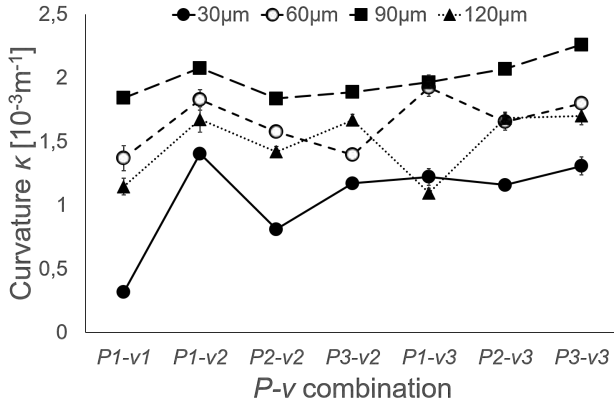


Figure 5.11: Curvature of all process parameter sets, given as combinations of *P* and *v* values for different layer thicknesses.

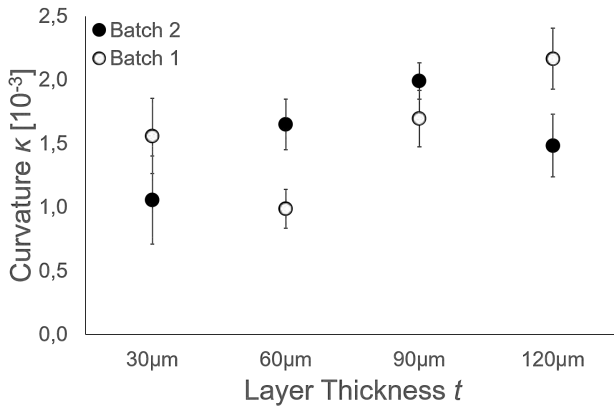


Figure 5.12: Comparison of the average curvature for each layer thickness between two different batches. There is an overall trend for higher curvatures for thicker layers, but both batches have an anomalous result for one layer thickness value.

anomalous compared to the trend of increasing curvature for increasing layer thickness, while the 120μm layer thickness is anomalous in batch 2. Moreover, the curvatures for the same layer thickness, but measured on samples produced in different batches, do not overlap.

Table 5.2: Regression analysis coefficients for the laser power, scan speed and layer thickness related to Equation (5.2).

Term	Coef	SE Coef	P-Value
Constant	0.161	0.470	0.734
P [W]	-0.00008	0.00132	0.954
v [mm/s]	0.000727	0.000262	0.011
t [μm]	0.00632	0.00198	0.004

Regression analysis of the results of batch 2 indicates that laser power does not have a significant influence ($P=0.954$), and that increasing the scan speed ($P=0.011$) and layer thickness ($P=0.004$) increases the curvature. The influence is captured in Equation (5.2), and the relevant statistical numbers summarized in Table 5.2. For this regression, the adjusted R^2 -value is only 33%, which can barely be considered a relevant fit. The curvature of the cantilever specimens seems to respond differently to the various process parameters than the stress measured by XRD on the top surface of cuboid specimens. These XRD measurements resulted in lower stresses for high layer thickness, while the deformation of cantilever specimens with thicker layers seems to be slightly larger than that of thinner layers.

$$\kappa[10^{-3}m^{-1}] = 0.161 - 0.00008P[W] + 0.000727v[mm/s] + 0.00632t[\mu m] \quad (5.2)$$

The parameter sets used for this set of experiments (i.e. combinations of v1-v4 and P1-P3 of samples produced by 3D Systems Layerwise, shown in Figure 5.8) are all located in the v-P region 2 of Figure 5.9d (i.e. combinations of v and P used on the LM-Q). Although there was a difference in stress measured by XRD between low and high scan speeds and laser power between region 1 and 2 of Figure 5.9d for the LM-Q samples, there was little variation within region 2 itself. This may possibly explain why the XRD results and the deformation of the cantilevers of the samples produced by 3D Systems Layerwise indicate a smaller effect of the laser power and scan speed compared to the XRD results of samples produced on the LM-Q machine.

5.2.3 Discussion

Timoshenko developed an analytical equation for the deformation of bimetal strips during uniform heating, given in Equation (5.3) [294]. In this equation, α_1 is the thermal expansion of the upper layer, h_1 its thickness, E_1 its stiffness and I_1 the area moment of inertia, given by $I = bh^3/12$ with b equal to the

width of the strip. α_2 , h_2 , E_2 and I_2 are the same properties for the bottom layer. T is the temperature to which the bimetal strip is uniformly heated, and T_0 the reference temperature. Material behavior is assumed isotropic.

$$\kappa = \frac{(\alpha_2 - \alpha_1)(T - T_0)}{\frac{(h_1 + h_2)}{2} + \frac{2(E_1 I_1^3 + E_2 I_2^3)}{(h_1 + h_2)} \left(\frac{1}{E_1 h_1} + \frac{1}{E_2 h_2} \right)} \quad (5.3)$$

This equation can be converted for use in AM, which was already proposed to a certain extent by Amon *et al.* [190]. By setting the thermal expansion of the bottom layer to zero, applying cooling rather than heating (negative ΔT), and assuming the width b to be unity, Amon proposed Equation (5.4) to predict the curvature when a hot layer is applied to a cold substrate.

$$\kappa = \frac{-\alpha \Delta T}{\frac{(h_1 + h_2)}{2} + \frac{(E_1 h_1^3 + E_2 h_2^3)}{6(h_1 + h_2)} \left(\frac{1}{E_1 h_1} + \frac{1}{E_2 h_2} \right)} \quad (5.4)$$

Based on the same principles of force and moment balance, Zhu *et al.* [295] deduced Equation (5.5) to describe the deflection δ of a part made of N layers with a thickness t , when n more layers are added. Since they were dealing with polymer parts, $T_g - T_r$ indicates the temperature interval between the glass temperature and room temperature, which is the temperature interval over which stresses can build up. L_s is the length of the layer. This deflection can be converted to a curvature using Equation (5.6) [294], valid when the deflection δ is small compared to the radius of curvature $1/\kappa$. Lastly, a third, independent derivation of a similar formula based on the same principles was deduced by Nickel [296], and is given in Equation (5.7). The combined base plate and part height or thickness is $2h$, and the (re)melted region or layer is $(h - r)$ thick.

$$\delta = \frac{(N + n)^3 t}{6\alpha N (T_g - T_r)} \left[1 - \cos \left(\frac{3\alpha N L_s}{(N + n)^3 t} (T_g - T_r) \right) \right] \quad (5.5)$$

$$= \kappa \frac{L_s^2}{8} \quad (5.6)$$

$$\kappa = \frac{3\alpha \Delta T}{4h} \left(1 - \left(\frac{r}{h} \right)^2 \right) \quad (5.7)$$

Although these equations all seem to be different, they can be reduced to the exact same equation when using assumptions appropriate for AM, or SLM to

be more specific. The two assumptions are that the material of the new layer and substrate are the same, and that the layer thickness is small compared to the substrate thickness. When adding one layer (important for Equation (5.5)), using these simplifications results in Equation (5.8). The simplification is shown in full starting from Equation (5.4) only, but is analogous for Equation (5.5) and (5.7). Keep in mind that ΔT is negative, so the curvature is positive.

$$\begin{aligned}
 \kappa &= \frac{-\alpha\Delta T}{\frac{(h_1+h_2)}{2} + \frac{E(h_1+h_2)(h_1^2-h_1h_2+h_2^2)}{6(h_1+h_2)} \left(\frac{h_1+h_2}{Eh_1h_2}\right)} \\
 &= \frac{-\alpha\Delta T}{\frac{(h_1+h_2)}{2} + \frac{(h_1^2-h_1h_2+h_2^2)}{6} \left(\frac{h_1+h_2}{h_1h_2}\right)} \\
 &= \frac{-\alpha\Delta T}{\frac{h_2}{2} + \frac{h_2^2}{6} \frac{1}{h_1}} \\
 &= \frac{-\alpha\Delta T}{h_2 \frac{(3h_1+h_2)}{6h_1}} \\
 &= \frac{-6h_1\alpha\Delta T}{h_2^2} \tag{5.8}
 \end{aligned}$$

By including perfect elastic-plastic material behavior, Nickel [296] proposed a slight modification of Equation (5.8), given in Equation (5.9). Practically, this corresponds to substituting $\alpha\Delta T$ in Equation (5.8) with σ_y/E (thermal stress: $\sigma = E\alpha\Delta T$). The layer thickness is given by h_1 and substrate thickness by h_2 . This lowers the curvature, but still fails to take temperature dependent behavior into account, or yielding of the substrate.

$$\begin{aligned}
 \kappa &= \frac{12\sigma_y}{E} \frac{h(h-r)}{(r+h)^3} \\
 &= \frac{6\sigma_y h_1}{Eh_2^2} \tag{5.9}
 \end{aligned}$$

In Equation (5.9), the curvature is linearly dependent on the layer thickness, as a thicker layer can exert a larger force. Quadrupling the layer thickness from 30 μm to 120 μm therefore quadruples the introduced curvature. On the other

hand, the number of layers needed to built a part of the same height is four times less, so there are less layer depositions through which curvature can be accumulated. Assuming only elastic stresses exist, the principle of superposition can be applied and the curvature introduced by each consecutive layer can be summed up.

Since the analyses by Timoshenko, Nickel and Zhu are purely mechanical, the larger force by the thicker layers is canceled out by the reduced number of layers, and the predicted accumulated curvature is the same for any layer thickness. The problem of these analyses is illustrated in Figure 5.13. The model developed by Mercelis and Kruth [231] is based on the same equilibrium boundary conditions, and describes the horizontal stress inside the base plate and part. To obtain the exact stress distributions shown in Figure 5.13, the base plate width was chosen to be 100mm, and the part width 15mm. The base plate height was 20mm, the part height was 15mm. These conditions are representative of the conditions used to build the 12 cubic parts discussed in the beginning of this chapter.

Moving from the right (top of the part) to the left in Figure 5.13a, the tensile stresses in the upper layers slightly compress the layers below, reducing the tensile stresses in the lower section of the part. At the base plate-part interface, a sharp stress jump exist since there were no original stresses in the base plate, the top of which is now being compressed by the tensile stress in the part. A difference in width between the part and base plate further contributes to the discontinuity. At the bottom of the base plate, tensile stresses ensure the moment balance.

The horizontal residual stress inside the part after removal from the base plate, shown in Figure 5.13b, features tensile stress near the top and bottom of the part, and compressive near the center. For reference, the experimentally measured horizontal stress profile in the central axis of the part is extracted from the contour map shown in Figure 5.6 and plotted alongside the model results in Figure 5.13b. Although the mechanical models cannot be used to study the effect of layer thickness, they are fairly accurate in predicting the shape of the stress distribution in the part. Notice however that the magnitude of the RS is underestimated by a factor 20.

The mechanical analysis cannot be compared to the results obtained by XRD on the top surface. There is a large difference between the stresses obtained via XRD on the top surface, and macroscopic residual stress as characterized using cantilever specimens. The difference is the location over which stresses are measured. X-rays only penetrate Ti6Al4V 11 μ m deep. Therefore, only the stress in the top of the top layer is measured. For the 30 μ m layer, this top section is 37% of the layer thickness, for 120 μ m only 9%. In addition, the top

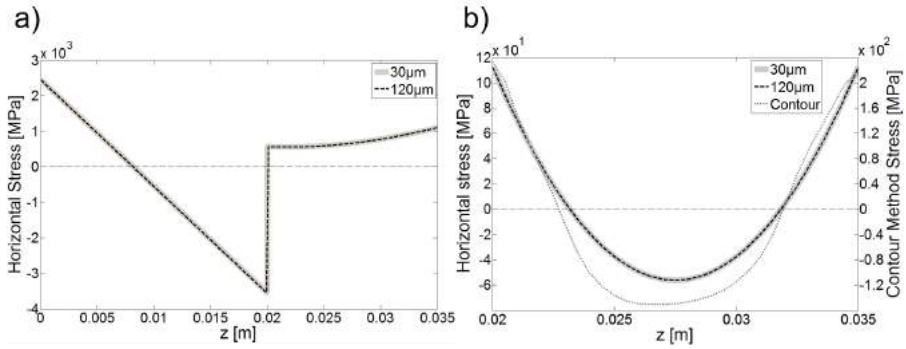


Figure 5.13: Application of the model developed by Mercelis and Kruth [231] to predict the horizontal stresses in a) the base plate ($z=0-0.02\text{m}$) and the part ($z=0.02-0.035$) before the part is removed from the base plate. b) Horizontal stress in the part after the part is removed from the base plate.

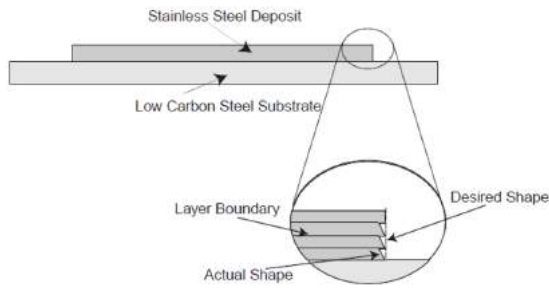


Figure 5.14: The christmas tree step effect (from Ref. [296]).

of the melt pool is far away from the constraining effect of the solid material below, even more so for thicker layers. Consequently, the top of thick layers is able to contract more than that of thin layers. This effect was called the ‘Christmas tree step’ effect by Nickel [296], and is illustrated in Figure 5.14.

A large discrepancy between the discussion so far and realistic conditions during SLM is that the actual melt pool depth is not equal to the layer thickness. Large parts of previously deposited layers are remolten. A $30\mu\text{m}$ layer thickness is therefore not equivalent to the addition of a hot layer $30\mu\text{m}$ thick, but to a thicker one. The amount of layers that are molten, however, remains the same. Using a layer thickness of $120\mu\text{m}$ does not actually produce a melted zone four times as deep as $30\mu\text{m}$. Unfortunately, the melt pools are not visible

in the microstructure of Ti6Al4V after SLM, so it is not possible to discern the actual melt pool depth. 316L samples produced with different layer thicknesses, courtesy of M. Montero, do not indicate a large difference in melt pool size when using a 30 μm layer thickness versus using a 120 μm layer thickness. Given that in the mechanical model, each layer introduces stress related to its thickness, using more realistic values for the melt pool depth rather than using the powder layer thickness would predict that using thinner powder layers would result in higher stresses, because the number of layers is higher.

The results obtained on the cantilever specimens, however, predict an opposite trend than that predicted by a mechanical model. Although the correlation is not strong, Figure 5.12 shows a weak upward trend in residual stress magnitude when using thicker layers. The main reason thereof is that the mechanical models fail to incorporate the effect of temperature.

SLM is a thermal process, and the most likely explanation for the observed correlation between layer thickness and curvature of the cantilever specimens is accumulated heat. Keep in mind that the laser powers and scan speeds used are of the same magnitude for all layer thicknesses (slightly lower speed for a 120 μm layer thickness). The total heat input for a part made of N layers 30 μm thick is therefore four times as large as the heat input for the same part built with $N/4$ layers of 120 μm . Moreover, for thin layers, a larger fraction of the applied heat is directed towards remelting/reheating the material below. Two different scenarios with similar outcomes can then be considered:

1. Parts with different layer thicknesses are built in one job (as was the case for the cantilever specimens). In this scenario, parts with the 30 μm layers are scanned every layer, and experience a temperature increase every layer. After a layer is scanned of the parts with 120 μm thick layers, they do not receive any heat input for three subsequent layers and the downtime is therefore longer. This means there is more time for the heat to be conducted away from these parts compared to parts with 30 μm layers. Van Belle, Vansteenkiste and Boyer [220] investigated the effect on downtime for Ti6Al4V, and found that short downtimes allow the temperature to increase substantially compared to longer downtimes, which decreased the deformation.
2. Parts with different layer thicknesses are built in different jobs. In this case, the 30 μm layer job will take four times as long to finish than the 120 μm layer job. The time during which heat can be accumulated is four times longer, and temperatures during the job have more time to increase.

In both scenarios, the thin layer part reaches a higher temperature during the process than the thick layer part. This effect is then identical to using

preheating, which will be discussed in the following section.

5.2.4 Preliminary conclusions

Although each individual data set lacks the information to paint the complete picture, combination of the XRD results obtained on the samples produced on the LM-Q, XRD results of 3D Systems Layerwise samples and the cantilevers provides substantial evidence to support the following conclusions:

- Increasing the layer thickness will increase the macroscopic residual stress by limiting the heat accumulation inside the part.
- Increasing the scan speed also increases the residual stress by increasing the thermal gradients, and leads to a higher anisotropy of the stress in one layer.
- Compared to the previous two parameters, the laser power has the smallest effect. Overall, high laser powers increase the heat input and lower thermal gradients, which will act to lower the residual stress.

5.3 Preheating

The motivation to use preheating during SLM is twofold. On the one hand, preheating will create a different thermal history of the part, which may change the microstructure and consequently, positively affect the mechanical properties. As an example, Xu *et al.* [41] were able to induce decomposition of the martensite to a fine lamellar $\alpha+\beta$ during the SLM process. By varying the layer thickness but also by offsetting the focal point of the laser with the powder bed and using 200°C base plate preheating, they were able to maintain the heat affected zone above a critical temperature for long enough to decompose the martensite. This resulted in an increased ductility around 13% without any loss in strength.

On the other hand, preheating lowers thermal gradients and is expected to lower the residual stress, which is the main intent of the results discussed in this section.

5.3.1 Materials and Methods

The jobs were built chronologically with increasing preheating temperature, and the same powder was recycled each time for use in the next job. 10x10x10

($X \times Y \times Z$) mm^3 cubic samples were built for density and microstructure analysis, $20 \times 20 \times 20 \text{mm}^3$ cubic samples for stress analysis and $3 \times 90 \times 15 \text{mm}^3$ samples from which the dogbone shape was milled for tensile testing. Cantilever specimens were produced to measure the curl up caused by residual stress.

All parts were produced on the LM-Q machine, using $P=250\text{W}$, $v=1600\text{mm/s}$, $h=60\mu\text{m}$ and $t=30\mu\text{m}$, a zigzag scan strategy and 90° rotation between layers.

The density was measured using the Archimedes method. For microstructural examination, samples were ground using a 1200 grit SiC grinding paper, and polished using a $\text{SiO}_2\text{-H}_2\text{O}_2$ suspension. Etching with a solution of 50 ml H_2O , 25 ml HNO_3 and 5 ml HF for 5 to 10 seconds revealed the microstructure. An Axioskop 40 Pol/40 A Pol microscope was used to examine the microstructure with relatively small magnifications, while a FEI Nova nanoSEM allowed high magnification images. A Siemens D500 diffractometer with Cu radiation was used to determine diffraction spectra based on polished cross sections parallel to the building direction, and residual stress on the as-built top surface.

Oxygen and nitrogen content was determined by Evans Analytical Group using Interstitial Gas Analysis (IGA). The Vickers microhardness tests were performed on a Leitz-Durimet tester using a weight of 500g. Values in the text are an average of 10 measurements per specimen. Four tensile specimens per preheating temperature were tested according to ASTM E 8M at a strain rate of 1mm/min using an INSTRON 4505 machine. Yield stress and Young's modulus were determined according to ASTM E111. The loading direction was perpendicular to the building direction during SLM.

5.3.2 Results

Microstructure

The XRD spectra shown in Figure 5.15 indicate that the parts made without preheating (NP) and 200°C preheating are fully martensitic. The spectrum corresponding to 100°C is omitted because of redundancy. The strongest β peak that does not overlap with α/α' peaks is located at a diffraction angle around $57^\circ 2\theta$, and belongs to the $\{200\}$ crystal planes. At 300°C preheating, the $\beta_{\{200\}}$ peak is starting to become apparent, though the β fraction remains very small. However, its presence indicates that the thermal history the material experiences changes significantly. It means that either the thermal gradients are low enough to result in an incomplete transformation of the material to martensite, or that the HAZ remains above a critical temperature long enough to allow decomposition of the martensite. At 400°C , the $\beta_{\{200\}}$ peak is even

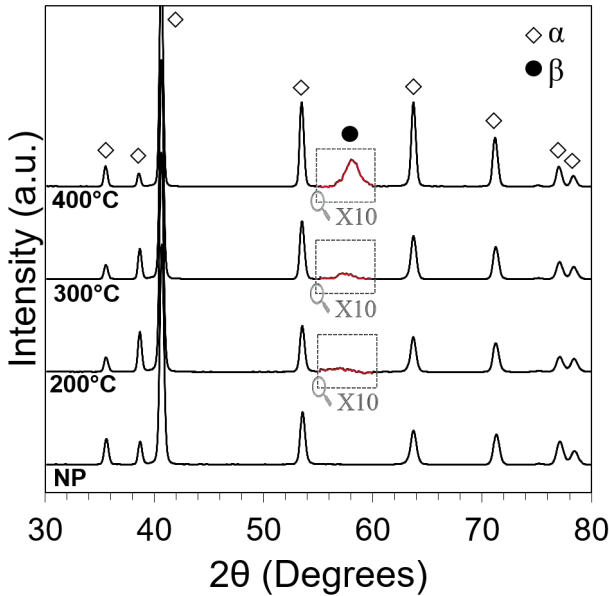


Figure 5.15: Diffraction spectra for different preheating temperatures. The $\{200\}$ peak of the β phase becomes visible after using 300°C preheating.

more visible. Concerning the α/α' peaks, it is impossible to distinguish if they belong to the martensitic α' phase or the α phase, since both crystal structures are nearly identical.

The microstructure differs significantly for the samples built without preheating and those built with 400°C preheating, shown in Figure 5.16. Without preheating, acicular α' martensite is visible, of which the individual plate edges are straight and jagged. Moreover, many plates seem to be riddled with twin structures. These twins accommodate the dimensional changes that accompany the β to α' transformation. Using 400°C preheating, the microstructure is not only coarser, but it can no longer be called acicular. This lamellar structure shows fine α/α' plates, in between which a thin layer of β phase exists. The equilibrium β phase fraction in Ti6Al4V is around 10%. The β fraction in the current microstructure is significantly lower than 10%. This indicates that some α' must still be present. The mechanism behind these transformed microstructures is the decomposition of the martensite in the heat affected zone (HAZ) in lower layers, when a new layer is added. According to Xu *et al.* [41], this mechanism takes place for regions in the HAZ that experience temperatures

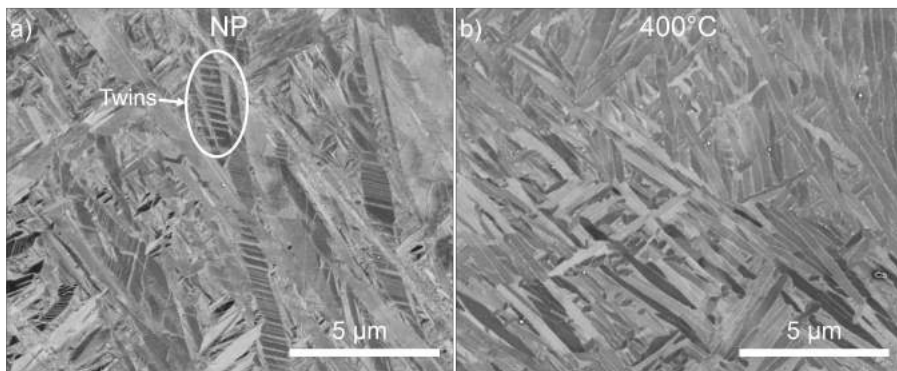


Figure 5.16: a) Without preheating, the microstructure consists of twinned α' martensite. A collection of twins are indicated by the ellipse. b) Using 400°C leads to a fine, lamellar $\alpha+\beta$ structure. The β phase is present as thin layers between the α plates.

above 400°C , which is the maximum preheating temperature used in this study.

The evolution of the hardness as a function of the preheating temperature, shown in Figure 5.17, shows the opposite trend than that expected based on the microstructure. The hardness at the top of the sample rises from 414 ± 4 to $459\pm 6\text{HV}_{0.5;10s}$, and there is a difference between the top and bottom of the part that increases with increasing preheating temperature. The first phenomenon is unfortunately caused by a drastic increase in the oxygen and nitrogen concentration inside the material, see Table 5.3. The oxygen and nitrogen content in the (recycled) powder remain well below specifications for Grade 23, even though the powder visibly changes from a metallic grey to a grey-brown color after the 400°C preheating job. This indicates that only the outer shells of the powder particles oxidize but that the insides are unaffected. Meanwhile, the molten and resolidified material that makes up the parts does pick up a significant amount of oxygen and nitrogen, even without preheating, and can no longer be classified as Grade 23, but as Grade 5 Ti6Al4V. Even though the builds occur in an argon atmosphere (generated from liquid argon), trace oxygen and nitrogen are easily picked up by the hot melt pool. With increasing preheating temperature, it is thought that the temperature of the melt pool increases, thereby also increasing the oxygen and nitrogen concentration in the final parts. Additionally, unpublished results on preheating of other materials have shown that the melt pool size increases for increasing preheating temperatures, so a certain location will remain liquid for a longer time, which also contributes to increasing the oxygen and nitrogen pickup.

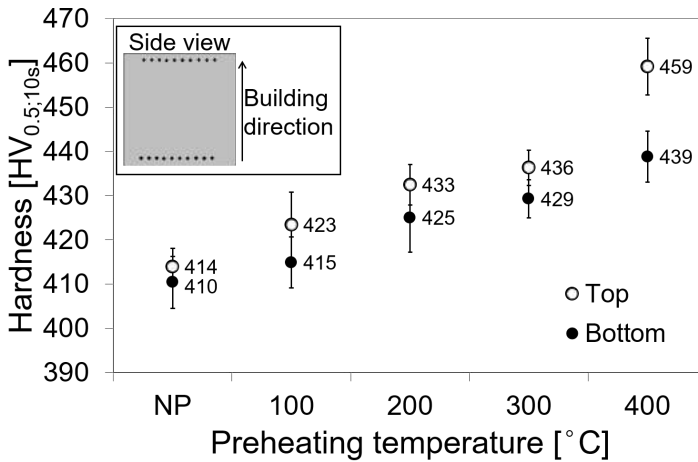


Figure 5.17: Evolution of the hardness as a function of preheating temperature. Notice the difference between the top and the bottom of the sample. The numbers next to each marker give the exact hardness value.

Table 5.3: Oxygen and nitrogen content of the powder and of parts produced at different preheating temperatures.

	O [ppm]	N [ppm]
<i>Ti6Al4V Grade 5</i>	Max. 2000	Max. 500
<i>Powder</i>	1170±180	92±26
<i>Powder 400°C</i>	1180±130	139±63
<i>Part NP</i>	1660±35	384±20
<i>Part 200°C</i>	1940±53	594±65
<i>Part 400°C</i>	2380±42	552±36

The difference between the top and bottom part is caused by the same phenomenon that leads to a different microstructure after preheating. The bottom of the parts has been part of the HAZ of overlying layers more than the top, and has had more opportunity to transform to the softer, lamellar structure. Consequently, the top presumably still consists of harder acicular martensite. Using a 60µm layer thickness (double that used in this study), Xu *et al.* [41] deposited at least eight layers without occurrence of martensite decomposition. This translates to a fully martensitic zone near the top of roughly 500µm deep.

The effect of the oxygen and nitrogen is also visible on the tensile properties, which are summarized in Table 5.4. The material yields around 1100MPa for preheating temperatures up to 100°C. For higher preheating temperatures, the

Table 5.4: Mechanical properties for the different preheating temperatures. The yield stress goes up, the ductility decreases.

	E [GPa]	σ_y [MPa]	UTS [MPa]	ϵ_f [%]
NP	113±2	1088±14	1221±15	6.9±1.9
100°C	113±1	1092±22	1234±26	6.4±1.2
200°C	115±1	1135±11	1234±7	3.7±1.2
300°C	118±1	1147±7	1230±7	4.5±0.8
400°C	118±1	1215±13	1280±11	3.9±1.4

yield stress rises to above 1200MPa when using 400°C preheating. Another noticeable effect is that the material becomes stiffer, but unfortunately, also less ductile. In general, the effect of interstitial nitrogen is more important than that of oxygen in HCP Ti [297]. For low N concentrations (<1000ppm) in particular, a small increase in concentration leads to a dramatic reduction in ductility [298], as shown in Figure 5.18. The red dashed line indicates the concentrations measured in the powder. The blue areas represent the range of concentration measured in the parts. This range is bounded on the left by concentrations in parts built without preheating, and on the right by concentrations in parts built with 400°C preheating. Yu *et al.* [299] found that the core structure of edge dislocations in HCP pure Ti was not significantly affected by oxygen content, but that of screw dislocations was. The strong pinning effect of the oxygen interstitials on screw dislocations leads to a significant increase in yield strength. While their analysis focused on oxygen, it is also valid for other interstitial solutes such as nitrogen and carbon.

Residual Stress

By preheating the base plate to 400°C, the residual stress was decreased by 50%, illustrated in Figure 5.19, as measured on the top layer of 20x20x20mm³ cubes via XRD measurements. The top layer has never been part of the HAZ of layers deposited on top of it, and thus has not received any short in-situ heat treatment. As mentioned above, the hardness measurements indicate that the top still consists of α' martensite. Lower thermal gradients are not the only mechanism by which preheating reduces residual stress.

The deformation of the cantilever specimens matched the reductions in stress measured by XRD. Shown in Figure 5.20, the curvature of the bridges produced without preheating is double that of bridges produced with 400 °C preheating. There is no apparent difference for the samples produced without preheating, 100°C, and 200°C preheating, since temperatures during the process are known to rise well above 100°C from heat input of the laser alone. There is, however,

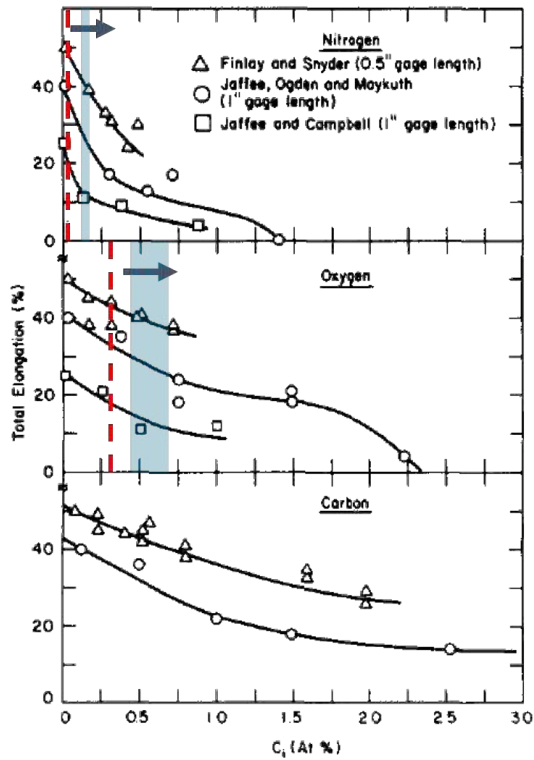


Figure 5.18: Influence of the interstitial content on the ductility of pure Ti. The red dashed line indicates the concentration measured in the powder, the blue areas represent the concentrations measured in the parts. (Adapted from Ref. [298]).

a significant drop in curvature for the 300 °C and 400 °C specimens. The large decrease in curvature between using 300 °C and 400 °C preheating furthermore suggests that a moderate further increase in preheating temperature may lead to a large beneficial decrease of residual stress.

The beneficial effect of preheating on the reduction of the residual stress is only partly caused by a decrease of the thermal gradients. As proposed by Vasinonta *et al.* [207], it is the reduction of the materials yield strength at higher temperatures that limits the residual stress build-up. The temperature dependence of the yield strength of Ti6Al4V is shown in Figure 5.21. In this figure, the yield strength at 400 °C is only 60 to 65% of the room temperature value, while the yield strength at 100 °C is still 90% of the RT value.

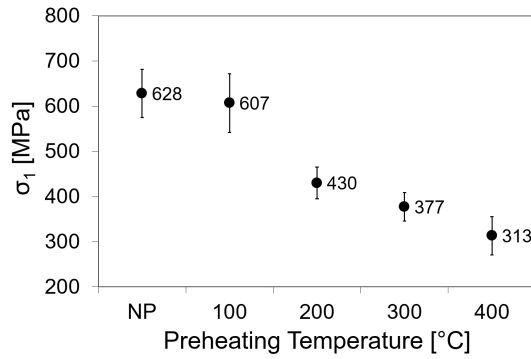


Figure 5.19: Residual stress in the top layer, measured via XRD. There is a 50% decrease by using 400°C preheating.

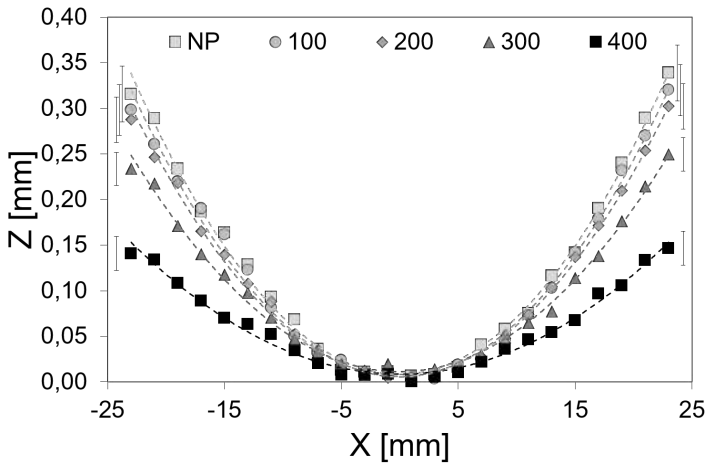


Figure 5.20: Deformation of bridge shaped specimens upon removal from the base plate for different preheating temperatures ranging from no preheating (NP) to 400°C.

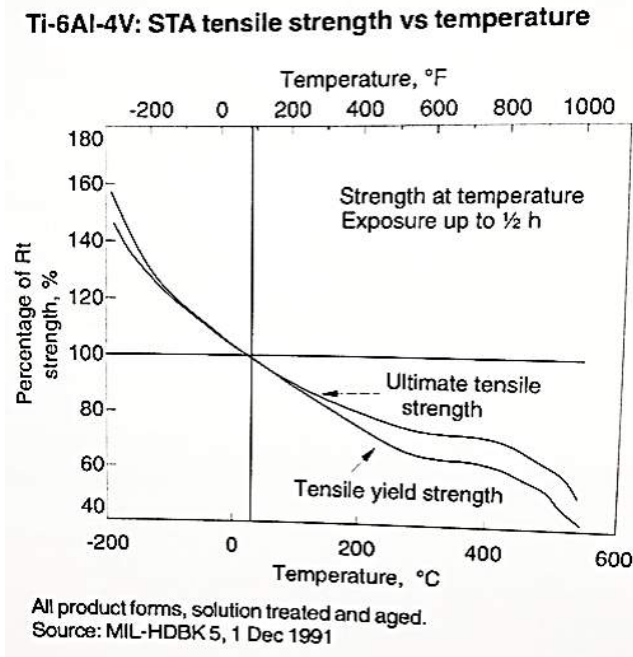


Figure 5.21: Yield strength of Ti6Al4V as a function of temperature [46].

5.3.3 Preliminary conclusions

By using a preheating of 400°C, the microstructure changed from acicular α' to lamellar $\alpha + \alpha' + \beta$ due to partial decomposition of the martensite in the heat affected zone caused by deposition of overlying layers. Moreover, a lower yield strength of the material at higher temperature reduces the residual stress by 50% when using 400°C preheating. Lastly, increased oxygen and nitrogen pickup by the hot melt pool caused embrittlement, increasing the hardness but reducing the ductility.

5.4 Conclusion

This chapter first tracked the development of residual stresses in SLM Ti6Al4V from the melt pool all the way up to the part scale by using XRD to measure stress in the top layer, and the contour method to visualize the overall stress

distribution in SLM produced cuboid shapes. Afterwards, the influence of four main process parameters on the RS was discussed.

- During SLM, residual stress is introduced by the contraction of the top layer, which itself consists of many individual scan tracks. The formation and solidification of the melt pool in these tracks is subjected to stochastic variations in the process parameters, the inhomogeneity of the powder layer and Plateau-Rayleigh instabilities. As a result, there is a large spread on the RS in the top layer.
- Because the contraction of the top layer is constrained, the horizontal stresses introduce vertical stresses. These vertical stresses are tensile at the side, and compressive in the center. After removal from the base plate and associated stress redistribution, the horizontal stress inside the part is tensile near the top and bottom surface, and compressive in the center. Furthermore, the shape of the RS distribution matches well with that predicted by the 1D model developed by Mercelis and Kruth, but the magnitude does not [231].
- While high laser powers increase the melt pool dimensions in all directions, the higher scan speeds elongate the melt pool, which increases the anisotropy of the RS in one layer, and increases thermal gradients. The residual stress therefore increases for higher scan speeds, but the effect is not linear. Instead, above a certain scan speed, the effect becomes indistinguishable. Higher laser powers on the other hand increase the heat input, which acts to lower the stresses, although the magnitude of this effect is inferior to that of the scan speed.
- The layer thickness has the largest effect on the macroscopic RS, although it is still relatively unclear whether there is a positive or negative correlation. The positive correlation in this chapter is explained by the heat accumulation. Parts with thicker layers take less time to build. When built simultaneously with other parts with thinner layers, they have longer downtimes between subsequent layers. This limits the rise of the temperature of the part.
- Lastly, preheating the base plate up to 400°C changes the acicular α' martensite to a lamellar mix of α' , α and β . RS is lowered by 50% mainly because the yield stress, which limits the RS build-up, is lower at higher temperatures. Preheating is therefore the most effective process parameter in reducing RS, but brings about other practical issues that have to be dealt with.

Chapter 6

Influence of material properties

This chapter consists of two parts that discuss different aspects of the interaction of the material with the SLM process. First in section 6.1, the general behavior of various materials during the SLM process is observed and discussed, both in terms of the developed microstructure as well as the material specific response to the residual stresses. Second, the possibility of creating a novel material with superior properties was explored by addition of Mo powder to Ti6Al4V powder (section 6.2).

The results in this chapter have been published in the following conference and journal publications:

- Vrancken, B., Wauthlé, R., Kruth, J., Van Humbeeck, J. (2013). Study of the influence of material properties on residual stress in selective laser melting. Proceedings of the Solid Freeform Fabrication Symposium. Solid Freeform Fabrication Symposium. Austin, Texas, USA, 12-14 August 2013 (pp. 1-15).
- Vrancken, B., Thijs, L., Kruth, J., Van Humbeeck, J. (2014). Microstructure and mechanical properties of a novel β titanium metallic composite by selective laser melting. Acta Materialia, 68, 150-158.

6.1 Influence of material properties

Slow R&D of SLM process parameter sets for new materials was identified as a major drawback in several roadmaps for AM [300, 301]. If knowledge could be transferred from the R&D of one material to another, these development times could be reduced. More often than not, residual stress is an issue that is encountered during the R&D process. A correlation between material properties and residual stresses developed during SLM could improve the knowledge transfer.

SLM is a thermal process, in the sense that no mechanical force is applied. In chapter 3, section 3.1.3, the influence of material properties on the development of thermal residual stresses was discussed in general. In addition to the general discussion, section 3.1.5 also highlighted that material specific phenomena can occur. This was discussed in more depth for nickel based superalloys, but is not limited to those alloys.

6.1.1 Materials and Methods

Table 6.1 lists all investigated materials together with all the relevant room temperature material properties that are used for the comparison. All parts except those made of 316L, 18Ni300 maraging steel, Inconel 718 and Hastelloy C-276 were produced with an identical scanning strategy and layer thickness, but different process parameters. 316L, 18Ni300 maraging steel, Inconel 718 and Hastelloy C-276 parts were produced with identical scanning strategy, layer thickness and process parameters. All samples were produced by 3D Systems Layerwise, except those made of AlSi10Mg. For each material, one 1cm³ cube, used for XRD stress measurement on the top surface and microstructural analysis, and three BCM specimens were produced.

Stress was characterized by the BCM method (see subsection 4.3.1) and via XRD measurements. Density was measured using the Archimedes method. An Axioskop 40 Pol/40 A Pol light optical microscope and Philips XL30 FEG scanning electron microscope (SEM) were used to investigate microstructure, as built top surfaces and fracture surfaces. Vickers microhardness was measured using a Leitz-Durimet microhardness tester using a weight of 300g for 10 seconds. Table 6.2 lists the etchants used for all investigated materials.

Table 6.1: Material properties gathered from literature used to compare all materials [143, 302–304].

	α_{CTE}	Thermal expansion	k	Thermal conductivity	c_p	Specific heat capacity	D_f	Thermal diffusivity	ρ	Density	T_m	Melting point	HV	Hardness	σ_y	Yield stress	UTS	Ultimate Tensile Strength	E	Young's modulus	ν	Poisson ratio
	$10^{-6} K^{-1}$		W/(m.K)		J/(kg.K)		$10^{-6} m^2/s$		kg/m ³		K		HV _{0.3;10s}		MPa		MPa		GPa			
<i>Ti Grade 1</i>	9.4		16		520		6.82		4510		1943		225		572		629		96			0.320
<i>Ti6Al4V-ELI</i>	10.1		6.7		930		1.63		4430		1933		399		1050		1140		111			0.320
<i>316L</i>	18.6		21.5		500		5.41		7950		1648		230		500		635		170			0.285
<i>18Ni300 Steel</i>	11.3		15		450		4.12		8100		1686		388		1000		1100		180			0.300
<i>Ta</i>	6.5		54.4		139.1		23.45		16680		3269		225		463		513		185			0.360
<i>W</i>	4.5		173		130		69.13		19250		3695		395		1600		1725		400			0.280
<i>Inconel718</i>	16		11.4		450		3.08		8220		1533		347		634		980		170			0.284
<i>AlSi10Mg</i>	23		113		963		43.95		2670		868		138		275		445		70			0.330
<i>Hastelloy C-276</i>	13.4		19		427		5.03		8840		1644		295		351		620		205			0.320

Table 6.2: Specific etchants used for each alloy.

	Etchant solution	Time [s]
<i>Ti Grade 1</i>	50ml H ₂ O, 25ml HNO ₃ , 5ml HF	5-10
<i>Ti6Al4V-ELI</i>	50ml H ₂ O, 25ml HNO ₃ , 5ml HF	5-10
<i>316L</i>	50ml H ₂ O, 50gr oxalic acid, electrolytic	20-30
<i>18Ni300 Steel</i>	95ml H ₂ O, 5ml HNO ₃ (5% Nital)	10-30
<i>Ta</i>	20ml HNO ₃ , 20ml HF, 60ml H ₂ SO ₄	60
<i>W</i>	H ₂ O ₂ , boiling	30
<i>Inconel718</i>	50ml H ₂ O, 50gr oxalic acid, electrolytic	10-30
<i>AlSi10Mg</i>	190ml H ₂ O, 5ml HNO ₃ , 3ml HCl, 2ml HF (Keller's etchant)	10-30
<i>Hastelloy C-276*</i>	50ml H ₂ O, 50ml HCl, 10gr CuSO ₄ (Marble's reagent)	5-60

*Not effective.

6.1.2 Density

The relative densities for all materials have been summarized in the first column of Table 6.4. All relative densities are higher than 99%, except for 18Ni300 maraging steel, W, AlSi10Mg and Hastelloy C-276. Porosity is an important factor in the final residual stress state, as the pores are stress free zones in a highly stressed material, causing relaxation in the direct vicinity of the pores. For W and Hastelloy C-276, the lower density values can be explained by microcracking and in the case of W also by large irregular pores, visible in Figure 6.1e,f and 6.3a,b. These pores and cracks are also the cause of the relatively low Vickers hardness of the W samples. Improper build conditions during the AlSi10Mg build led to large irregularly shaped pores. These conditions were likely caused by an unacceptable concentration of oxygen during the build. In addition, fairly spherical, large keyhole pores are also present. Other than the low density, the bad build conditions for AlSi10Mg resulted in a poor surface quality, shown in Figure 6.5a. Lastly, oxide particles were trapped inside the 18Ni300 maraging steel parts. These oxides have a lower density than the metal itself, lowering the apparent density.

6.1.3 Microstructure

Two different types of microstructures are generally obtained after SLM, as discussed in great detail in Ref. [28]. Most alloys form a cellular structure, while pure metals and Ti6Al4V form a columnar microstructure. The three materials for which an elongated microstructure were obtained in this work are Ti6Al4V, Ta and W, and their microstructures are shown in Figure 6.1.

Of particular note in Figure 6.1 are the straight columns in Ti6Al4V and Ta versus the ‘flame-like’ appearance of the grains in W samples. W is a pure metal, and as such is also expected to form a columnar microstructure. While the grains are still longer than those observed in alloys which solidify in a cellular-dendritic way, they are clearly more tortuous than those in Ti6Al4V and Ta. One reason may be that the W sample contains around 2% porosity, which interrupts the columnar growth. Viewed from the top, the microstructure of Ti6Al4V displays a square pattern due to the 90° scan strategy rotation (Figure 6.1b), while the rotation of around 60° for Ta and W likewise created a distinguishable pattern (Figure 6.1d and f).

In Figure 6.1f, the W grains have an ‘S’ shape, for which the extremities point along the orientation of the scan track but in opposite directions, but the inner part is fairly perpendicular to the scan track. The origin of these S-shaped grains is the local temperature gradient across the scan track. Along the midline

of the scan tracks and at the back of the moving melt pool (where the material solidifies), the thermal gradient is the largest in the scan direction, so grains will tend to grow in this direction. Moving from the midline to the edge of the melt pool, the maximum thermal gradient rotates and at the edge, is perpendicular to it. However, due to the overlap of scan tracks, part of the scan track is remelted, and the grain is partially remelted. Due to the fast cooling conditions, the grains grow epitaxially towards the center of the new melt pool, where thermal gradients are again parallel to the scan direction, which is rotated 180° compared to the adjacent scan track due to the zigzag scanning strategy. The final outcome is an S-shaped grain spanning the centers of adjacent tracks. The ends point along the center lines, in the opposite direction of the laser movement. Therefore, what seems to be the outlines of the edges of the scan tracks in Figure 6.1f, are actually the centers of the scan tracks. Ta is known to form a similar grain shape when viewed from the top. This is not visible in Figure 6.1d, but has been reported in Ref. [39] and was shown in chapter 2 in Figure 2.23. A more detailed discussion on the origin of the S shaped grains can be found in Ref. [39].

All other examined materials developed a cellular microstructure, examples of which are shown in Figure 6.2. For AlSi10Mg in Figure 6.2a, this is a two-phase microstructure consisting of primary Al cells (dark), and eutectic Al-Si in the intercellular regions. High cooling rates mean that the Al cells are supersaturated in Si. SLM of 316L, 18Ni300 maraging steel and Inconel718 on the other hand creates monophase microstructures, austenitic for 316L and Inconel718, martensitic for 18Ni300 maraging steel, although the latter contains about 5% of retained austenite. The contrast between the cells is provided by microsegregation. A close up of the cells, in the top right corner of each image, reveals that the intercellular spacing for each material is remarkably similar, varying around 0.5 μm . These cells are not individual grains but constitute a substructure inside one grain. Grains are defined by a group of adjacent cells that grew in the same crystallographic direction. The arrows indicate the melt pool boundaries in the side views. While this is a fine, well defined line for 316L, Inconel718 and maraging steel, it is a somewhat diffuse zone for AlSi10Mg in which the microstructure is slightly coarser in the HAZ.

6.1.4 Cracks

W (Tungsten)

In Figure 6.3a and b, the microcracks in W parts are shown. The cracks form a linked network and are all located on the grain boundaries, which is evident by comparing the crack pattern in Figure 6.3b with the S-shaped grains in

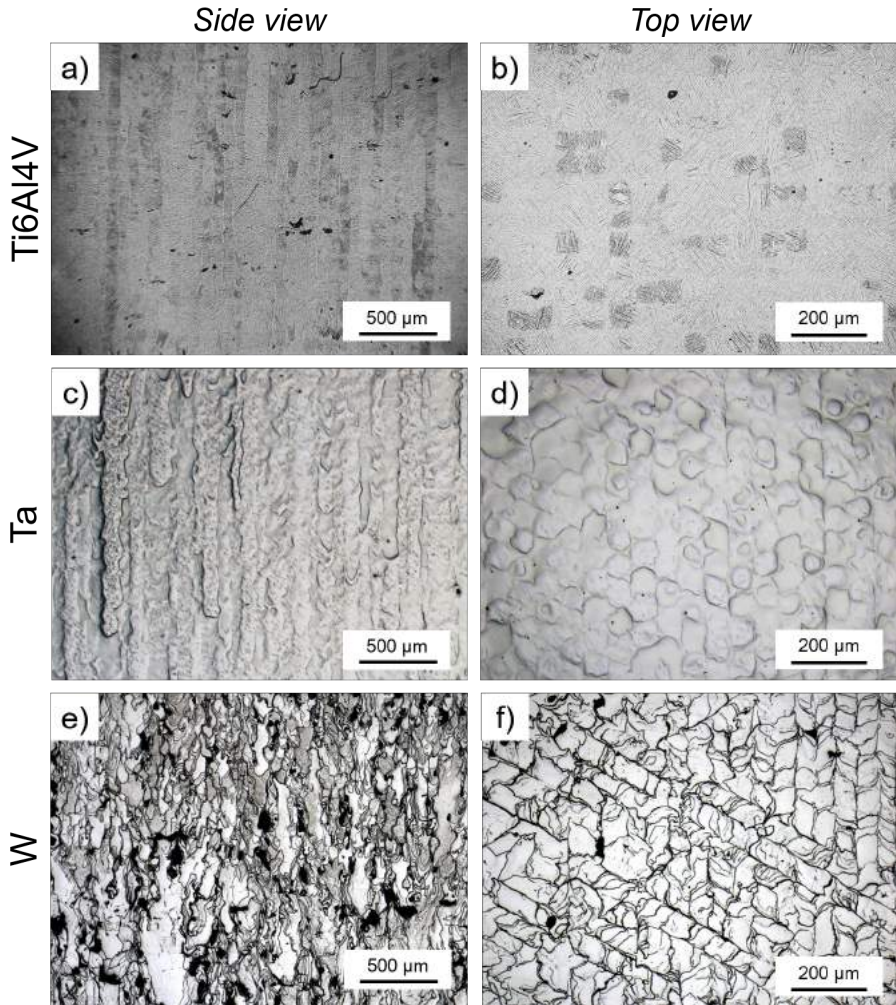


Figure 6.1: Columnar microstructure of Ti6Al4V (a,b), Ta (c,d) and W (e,f). a, c and e are side views. b, d and f are top views. The rotation of the scan strategy was 90° for Ti6Al4V causing the appearance of a square pattern. For Ta and W, it was set close to 60° .

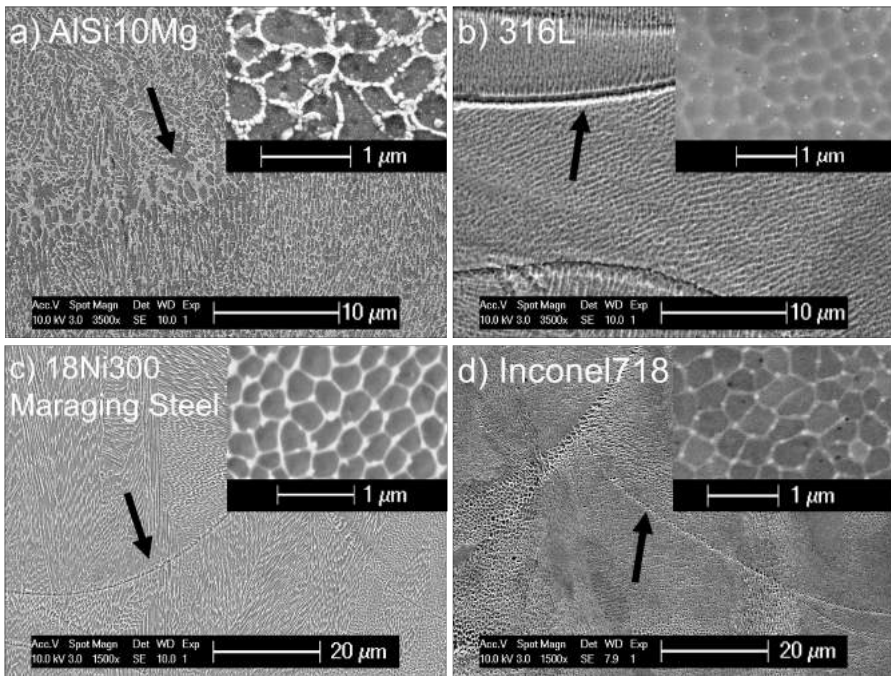


Figure 6.2: Side view of the cellular microstructure of a) AlSi10Mg, b) 316L, c) 18Ni300 maraging steel and d) Inconel718. The inset in the top right of each image is a close up of the cells in the top view. The arrows indicate former melt pool boundaries.

Figure 6.1f. The majority of the cracks are oriented along the scan direction in the center of the scan track, which is best seen on the top surface in Figure 6.5h. In this research, the relative density of the tungsten parts was around 98%, contrary to previous reports in which the density reached a maximum of 90% [172]. Even for a density as low as 83%, microcracks were found in W samples produced by SLM [171]. A porosity level of 17% greatly reduces macroscopic residual stresses, as each pore is a stress free zone that reduces the residual stress around it. This is an indication that it is not just the overall build up of residual stress that leads to cracks in W parts, and that other phenomena contribute as well.

Because W is a bcc material, it has a ductile to brittle transition temperature (DBTT). The high melting point of tungsten ($>3400^{\circ}\text{C}$) means that the DBTT is above room temperature. Plastic deformation is almost non-existent for

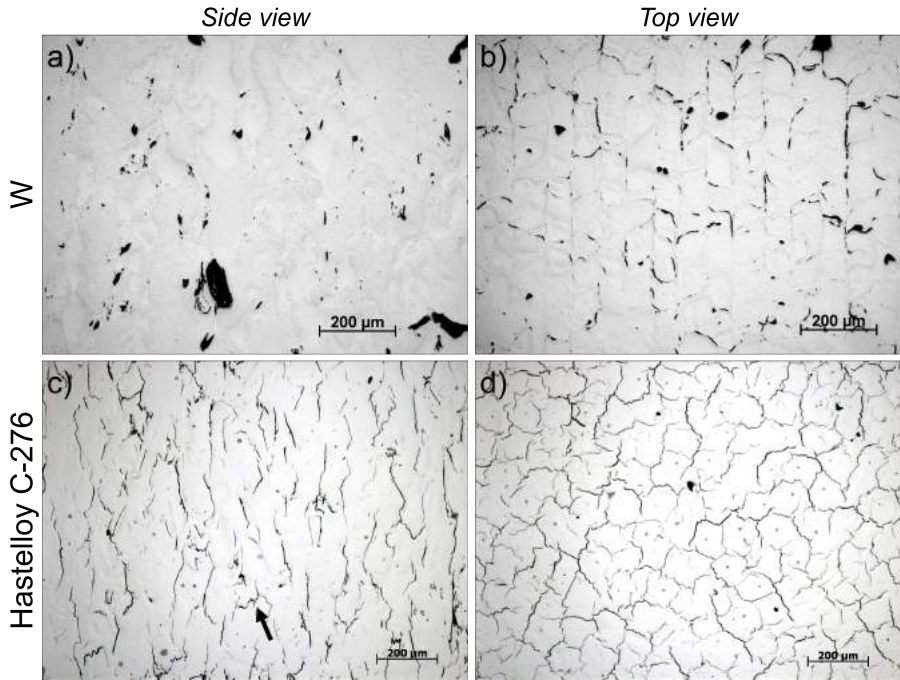


Figure 6.3: Microcracking in W (a,b) and Hastelloy C276 viewed from the side and top. The arrow in (c) indicates a jagged, non-vertical crack in Hastelloy C276 which is different from the straight, vertical cracks that are more abundant.

temperatures below 200°C, while good ductile behavior usually only starts at temperatures above 400°C [272]. A study on the weldability of tungsten showed that pre-heating to above the DBTT is needed to eliminate cracking in pure tungsten parts [305]. It also showed that multiple passes can greatly increase the extent of the cracking. Unfortunately, multiple passes are a necessary feature of the SLM process. The similarity between welding and SLM leads to the belief that the above-room temperature DBTT is the origin of microcracking in W.

Assuming the DBTT is the main origin of cracks, the extensive residual stresses that are built up by cooling from 3400°C to around 400°C are relieved by the formation of microcracks in the brittle regime below the DBTT. This means there is only a small temperature range left over which residual stresses can build up again. Thus, the W parts are relatively stress free after removal from the base plate, indicated by the low stress in the top layer measured by XRD, and low curl-up angle of the bridge specimen, see Table 6.4.

Table 6.3: Composition of Hastelloy C-276. All values are maximum values unless preceded by a ‘~’, indicating approximate values [304].

Ni	Cr	Mo	Fe	Nb	W	Co	Mn	Cu	Al	Ti	Si	C
bal.	~16	~16	~5	/	~4	~2.5	1	/	/	/	0.08	0.02

Hastelloy C-276

By contrast, in the Hastelloy C-276 sample, the grain boundaries are not clearly discernible from the crack pattern and the cracks seem to resemble the scan strategy, as seen in the top view in Figure 6.3d. This results in a roughly hexagonal crack pattern. In the side view, the vertical cracks are a mix of straight cracks with sharp corners, resembling a lightning shape, and tortuous cracks that have no clear orientation, as indicated by the arrow in Figure 6.3c. The straight cracks are not oriented perfectly parallel with the build direction but under a slight angle.

Carter and Attalah [188] observed both types of cracks in CM247LC, noting that the straight cracks are caused by liquation of low-melting point phases in the HAZ, and that the tortuous cracks are solidification cracks, originating at the end stage of the melt solidification. Both types of cracks have been discussed in subsection 3.1.5 in chapter 3. Cloots *et al.* [306], however, also classified the vertical microcracks in Inconel738LC as solidification cracks, observing a smooth, dendritic surface inside the cracks.

The composition of Hastelloy C276 is indicated in Table 6.3. It does not contain any of the γ' precipitate formers, which were discussed in subsection 2.3.2 in chapter 2 to be Al, Ti, Nb and Ta. It does, however, contain generous amounts of Cr, Co, Mo and W, which stabilize the γ phase, but Cr, Mo and W are also strong carbide formers. None of these carbides, however, have a lower melting point than the alloy itself (melting range 1323°-1371°C). Segregation of Cr, Mo and W towards grain boundaries does allow formation of Laves phase.

A closer view of the cracks on the top surface, shown in Figure 6.4, reveals that the inside surface of the crack is smooth, and is a continuation of the dendritic structure also visible on the top surface itself. Given that this crack is open to the top surface, it is unlikely that it was formed as part of the HAZ, since there are no layers deposited on top of it. The microcracks in Hastelloy C-276 are therefore solidification cracks. As the cracks are already formed upon solidification, stresses can build up over the entire temperature range between the melting point and room temperature. The residual stress at room temperature and the curl-up are thus considerably higher for Hastelloy C-276 than for tungsten, seen in Table 6.4.

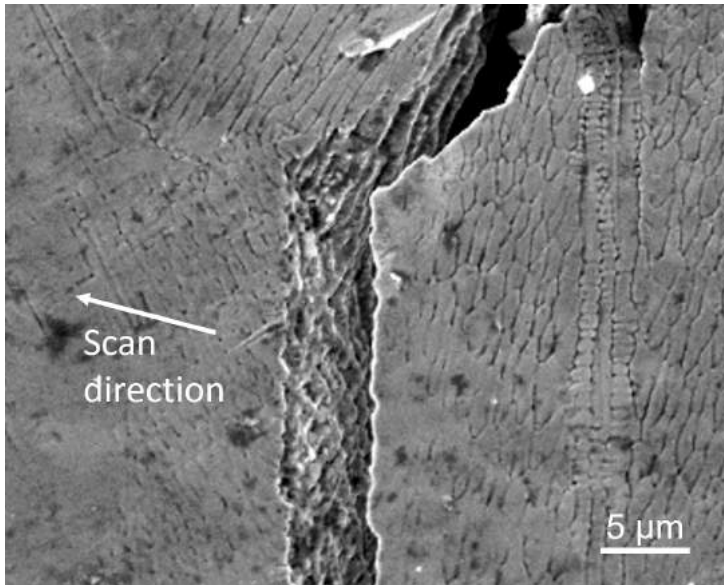


Figure 6.4: Close up of an open crack on the top surface of a Hastelloy C-276 sample, showing the smooth, dendritic surface inside the crack.

6.1.5 Residual Stress

XRD: Direction of the principal stress

Figure 6.5 shows a close up of the scan tracks on all the as built top surfaces of the cube samples. The black arrows with white edges indicate the scan direction in every track, except for AlSi10Mg where it was not possible to distinguish the scan direction of the tracks. The white arrows indicate the orientation of the maximum principle stress, except for W, for which the stress was too low to give accurate results in terms of the principal stress direction. $\text{Sin}^2\psi$ -curves for all measurements are shown in Figure A.2 in Appendix A.3.

Because the penetration depth of X-rays into the material typically ranges between 5 and 20 μm , only the stress in the last scanned layer is measured. Due to the plane stress assumption, only two principal stresses are nonzero. σ_1 is the upper limit of the stress and σ_2 the lower limit. Both stresses are perpendicular to each other and are reported in Table 6.4.

The difference between σ_1 and σ_2 is large and clearly illustrates the anisotropic nature of the residual stress build up. The white double arrow in the right

Table 6.4: Overview of density, deformation angle, measured maximum stress and calculated stress to cause the measured deformation for each material. Point A and B refer to the points indicated in Figure 6.6.

Sample geometry	All	Cube	Cube	Bridge	Bridge Point A	Bridge Gradient A-B
	Density [%]	σ_1 [MPa]	σ_2 [MPa]	α_{BCM} [°]	[MPa]	[MPa]
<i>Ti Grade 1</i>	99.7±0.3	222±10	101±10	0.87±0.06	216	445
<i>Ti6Al4V-ELI</i>	99.3±0.2	406±25	119±20	1.29±0.07	351	723
<i>316L</i>	99.6±0.1	-68± 3	-15±3	0.77±0.04	352	724
<i>18Ni300 Steel</i>	98.0±0.4	-263±13	-138±13	0.23±0.11	98	202
<i>Ta</i>	99.6±0.1	197±24	85±24	0.34±0.08	149	306
<i>W</i>	98.0±1.7	-34±15	24±15	0.15±0.06	144	296
<i>Inconel718</i>	99.3±0.2	419±15	296±15	1.53±0.11	615	1267
<i>AlSi10Mg</i>	98.2±0.6	64± 3	55± 3	0.78±0.07	129	266
<i>Hastelloy C-276</i>	97.6±0.6	358±14	98±14	0.90±0.19	436	899

upper corner of each image in Figure 6.5 indicates the direction of the largest principal stress (σ_1) in the top layer. Remarkably, this direction almost perfectly coincides with the direction of the scan vectors of the last layer for all materials. In chapter 5, it was already established that the residual stress in the direction of the scan vectors is larger than perpendicular to it, typically between two to three times larger. In this research, the σ_1/σ_2 ratio varies between 1.4 for Inconel718, to 3.4 for Ti6Al4V-ELI.

BCM Method

The BCM method provides a qualitative measurement of the residual stress, in the form of the curl up angle α_{BCM} , shown in Figure 6.6. The average curl-up angle α_{BCM} is given in Table 6.4. The values range from $0.15\pm0.06^\circ$ for W to $1.53\pm0.11^\circ$ for Inconel718. In an effort to convert this angle to actual stress values, the curl up can be applied to a stress-free, undeformed FE model of the bridge. Because α_{BCM} is small, the resulting deformation creates a stress distribution inside the part that is identical but of opposite sign to one would lead to the measured deformation α_{BCM} . This is more convenient than modeling the deformed shape, and applying a deformation that would bring it back to the undeformed shape. The resulting stresses are of opposite sign, and are based on identical tensile and compressive mechanical behavior.

The residual stress distribution obtained as such is not unique for the measured deformation. Many residual stress distributions would lead to the measured α_{BCM} . The result, shown for Ta in Figure 6.6, is not realistic since all stress is concentrated in the thin part of the bridge, but converts the angle to a stress

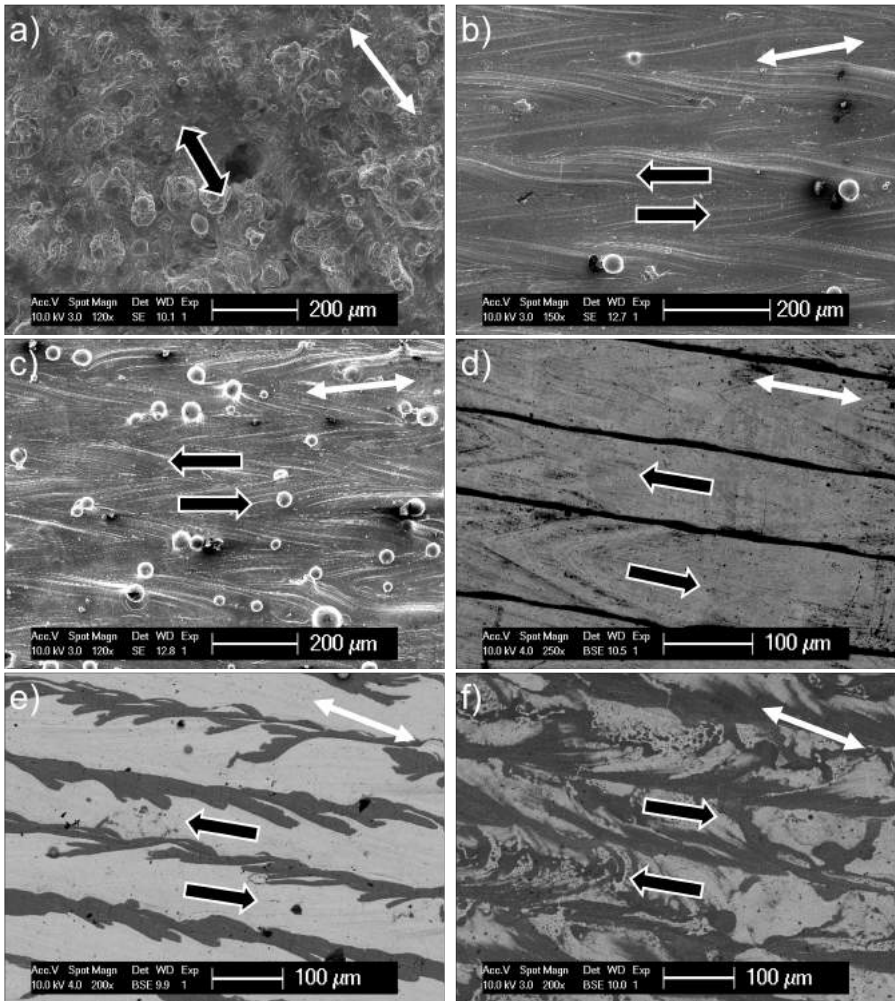


Figure 6.5: Top surface of all examined materials. (a) AlSi10Mg, (b) Ti6Al4V-ELI, (c) Ti CP1, (d) 316L, (e) 18Ni300 maraging steel, (f) Inconel718, (g) Hastelloy C-276, (h) W, (i) Ta. The black arrows indicate the scan direction in every track, except for AlSi10Mg where it was not possible to distinguish the scan direction of the tracks. The white arrows indicate the orientation of the maximum principle stress, except for W.

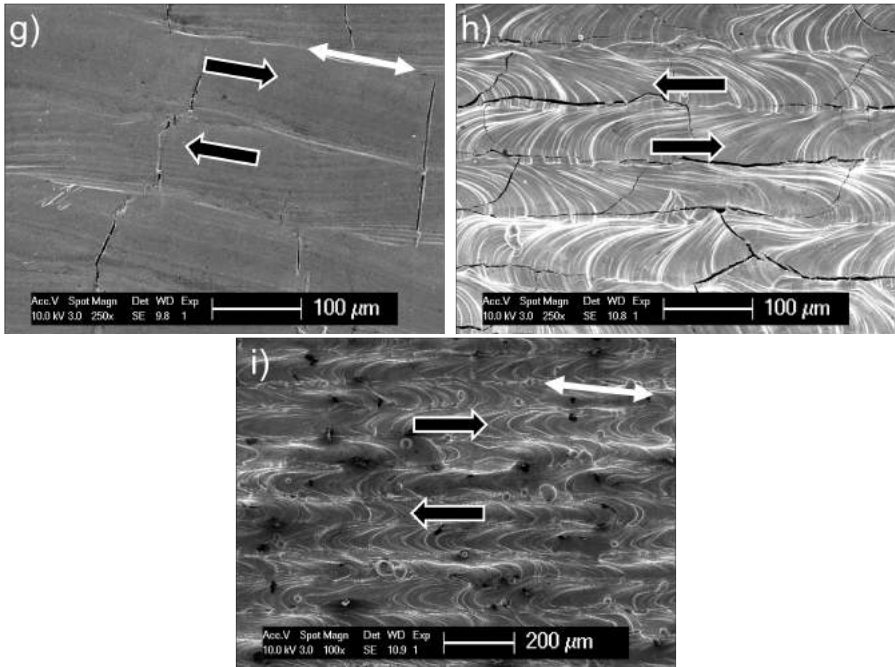


Figure 6.5 (cont.)

value that can be compared to the material properties, more specifically the yield stress.

While the model is too simple to take the resulting local stress values as correct, it is more likely that the model gives a semi-accurate estimate of the stress gradient between the top of the part, at point A, and the top of the underside of the bridge, at point B two millimeters lower (see Figure 6.6). After all, it is mainly the stress gradient between these two locations that makes the bridge curl up to the measured angle, since this is the smallest cross section. Values for this gradient are given in the last column of Table 6.4. The gradients are very large and vary between 101MPa/mm for 18Ni300 maraging steel to 634MPa/mm for Inconel718.

The stress gradient is the lowest for 18Ni300 maraging steel, due to the very limited curl-up of the BCM specimens. Moreover, XRD measurements of the cube specimen show compressive stresses at the top. This is contradictory to the consensus in literature that residual stresses in SLM parts are tensile on the outer surfaces and compressive in the bulk. The origin of the compressive

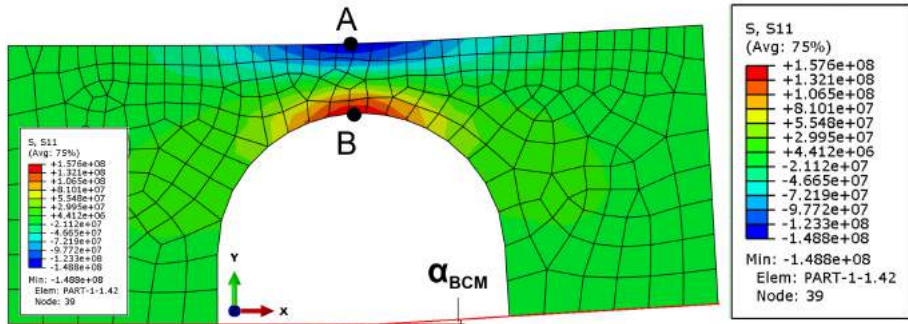


Figure 6.6: Applying the measured curl up α_{BCM} to a stress free bridge yields a stress state identical to a stress state that would lead to that curl up, but of opposite sign. Shown here for Ta. Points A and B mark the locations of the minimum and maximum stress.

stresses is similar to that of the compressive stresses in H13 steel, described in section 3.2.1 in chapter 3, and is the dilatation accompanying the martensitic transformation. Additionally, 18Ni300 maraging steel was the only material for which the shear stress measured via XRD was significant, at values around -40MPa. Again, the phase transformation is thought to be the cause.

6.1.6 Correlation between material properties and stress

The overall, expected influence of material properties was discussed in subsection 3.1.3 in chapter 3. Materials with a small thermal diffusivity D_f are more prone to develop large thermal residual stresses. These materials retain a lot of heat due to their high specific heat capacity C_p and do not conduct the heat away effectively due to their low thermal conductivity k . Paired with a high thermal expansion α_{CTE} , this leads to large thermal gradients inside the part, and consequently to large strain gradients and large residual stresses. However, when plotting the maximum principal stress and curl-up angle against the thermal diffusivity in Figure 6.7a, it is impossible to distinguish this trend from the data.

Because the shrinkage during cooling is constrained by previously deposited material, larger shrinkage should lead to larger stresses. As a simplistic example, consider the shrinkage in the longitudinal direction of a scan track of $L = 1\text{cm}$ length of 316L and of 18Ni300 maraging steel. Assume the thermal expansion to be constant and equal to the value at room temperature. Both materials have a

similar melting temperature. The total unconstrained shrinkage of 316L would be equal to $\Delta L_{316L} = \alpha_{CTE,316L} \cdot L \cdot \Delta T_{316L} = 221\mu\text{m}$, where ΔT_{316L} is the difference between the melting temperature and room temperature. For 18Ni300 maraging steel, the shrinkage is $\Delta L_{Mar} = \alpha_{CTE,Mar} \cdot L \cdot \Delta T_{Mar} = 157\mu\text{m}$. This demonstrates the theoretical effect of the thermal expansion on residual stress build up. Because the thermal expansion coefficient is not constant and goes up with rising temperature, these absolute values for the unconstrained shrinkage are an underestimation.

The same formula also describes the effect of the melting temperature. Comparing AlSi10Mg and Ti6Al4V, the unconstrained shrinkage of the Al alloy would be equal to $\Delta L_{AlSi10Mg} = 120\mu\text{m}$, while that of Ti6Al4V would be $\Delta L_{Ti6Al4V} = 132\mu\text{m}$, even though the thermal expansion coefficient of AlSi10Mg is much larger than that of Ti6Al4V. Because Ti6Al4V solidifies at much higher temperatures, shrinkage occurs over a larger temperature range and stresses can develop to a larger extent during cooling.

However, the shrinkage is constrained and assumed to be small in a real SLM part. The theoretical shrinkage can then be converted to strains and, using the Young's modulus, to stresses, assuming all deformations are elastic. Performing this calculation for all materials, this would mean that the final stress in one scan track is much higher than the yield stress at room temperature, which is unrealistic. For instance, the stress inside a Ti6Al4V track would amount to 1.49GPa. This means that the material will yield due to the residual stress at some point during cooling. The temperature at which the material yields depends on the total amount of virtual shrinkage that has already taken place, and the value of the yield stress at that temperature. Thus, the value of the yield stress at high temperature is also important, as was demonstrated in section 5.3.

Plotting the largest principal stress measured via XRD and α_{BCM} against various material parameters in Figure 6.7, no clear trends could be distinguished. Using combinations of material properties listed in Table 6.1 or scaling the measured stress with the yield stress does not result in better correlations. Various phenomena obscure the influence of the material parameters, such as microcracking, the formation of oxides and porosity. Furthermore, because all samples were built with different parameters to obtain high density, a wide range of parameters and energy densities were used in this research, which also influences the RS as demonstrated in the previous chapter.

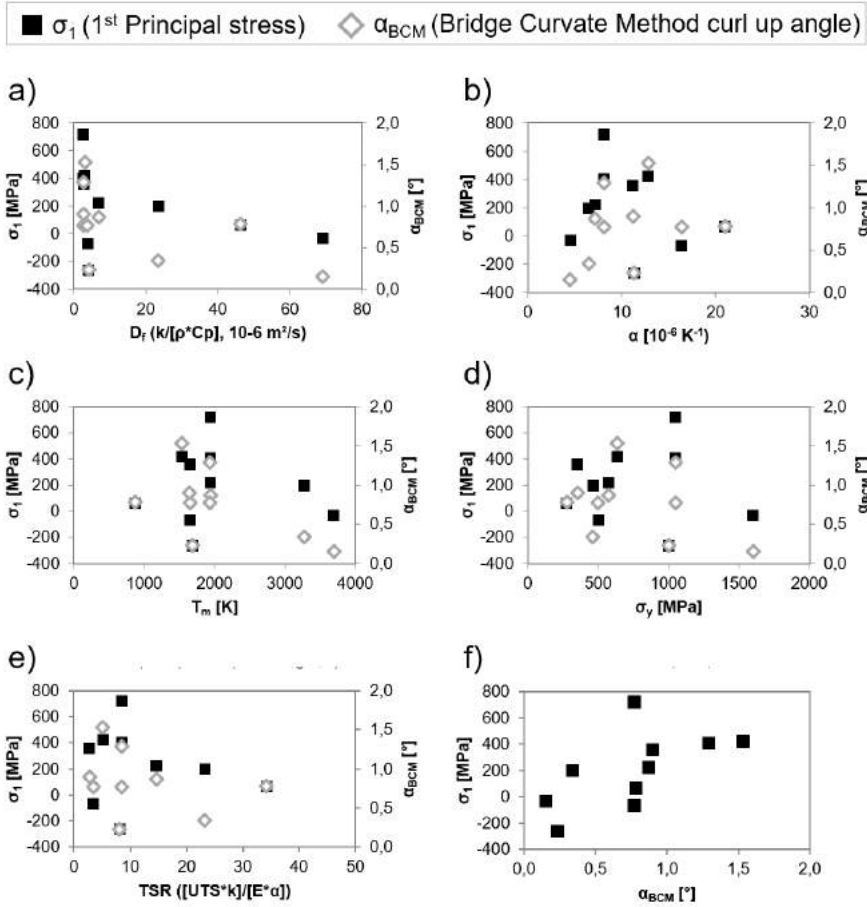


Figure 6.7: Plotting the first principal stress σ_1 , measured via XRD, and the BCM curl-up angle α_{BCM} as a function of (a) the thermal diffusivity, (b) the thermal expansion, (c) the melting temperature, (d) the yield stress and (e) the thermal shock resistance. In (f) the first principal stress is plotted versus α_{BCM} , indicating that there is also no clear correlation between the different types of RS measurements.

6.1.7 Preliminary conclusions

W and Hastelloy C-276 both develop microcracks, while the other materials do not. In Table 6.1, there are no material properties that set them apart from all the other materials studied in this research. Material specific phenomena, such as a DBTT (W), sensitivity to solidification cracking (Hastelloy C-276), phase transformations (18Ni300 Maraging steel) and formation of precipitates are not captured in values of traditional material properties. Moreover, the process parameters are different for every material to obtain a high density part. This means that it is unlikely to find strong correlations between material properties and residual stresses. Possible solutions to eliminate cracking are preheating or alloying the material with suitable elements. These elements could, for example, raise the toughness or high temperature material properties, lower the DBTT or lower the thermal expansion coefficient, much like Si does in Al alloys.

6.2 Ti6Al4V+10Mo

For a long time, the development of suitable SLM process parameters focused on existing alloys, alloys that were historically developed to be processed by casting, forging or optimized for machinability or property-enhancing heat treatments. Ti6Al4V is one of those alloys, designed to be heat treatable by changing the α and β phase morphology. However, work with blended elemental powders of Ti, Al and V showed that in SLM, the best composition to obtain high strength and ductility in the as built condition contained slightly less alloy elements than 6wt% Al and 4wt% V [307]. Rapid cooling rates in SLM create a fine microstructure that leads to high strength. Using this feature reduces the necessary amount of alloy elements, and thus enables a higher ductility. In Ref. [307], no comments were made regarding the further heat treatability of this alloy or the effect of a stress relief.

The full potential of AM lies not only in the *design* flexibility it offers, but also in the *material* flexibility. The thermomechanical history that the material goes through during the process is different from that in casting or forging, and material properties should be tailored initially to improve the processability. Because the process is powder based, specific alloys can be made by simply mixing different powders together. This, however, does raise the question of homogeneity of the distribution of all different alloy elements in the final microstructure.

On the other hand, changing the alloy composition can serve a second purpose, which is to create a material which has better properties than other materials, be it mechanical, functional or other. As an example of alloy modification, Stenlund *et al.* [308] added 0.04wt% Zr to CoCrMo F75, in order to improve osseointegration. Simply mixing the base CoCrMo powder with Zr powder was not an option, as such a small weight percentage would mean the Zr would be too in-homogeneously distributed. Therefore, Zr was added to the alloy before gas atomization. The powder was then processed by EBM to create dense bone implants, and compared to implants without Zr. The results indicate that osseointegration was improved.

Microalloying addition of up to 0.13wt% boron to Ti6Al4V led to much finer prior β grains, elimination of GB α , and led to a more rounded shape of the α grains after LMD processing [55]. The boron addition greatly increased the solidification range from 5°C to 130°C, causing a significantly larger solute redistribution between dendrites and the interdendritic zones, which allowed platelike TiB to form in the interdendritic regions.

A final example of the effect of small additions of a high melting point powder to pure Ti is provided in Ref. [144]. Rhenium has a melting point of 3186°C and a

maximum of 1.5 at% was added to increase the high temperature properties of Ti. It is a strong β stabilizer, but the microstructure was still fully martensitic after SLM. The particles were partially dissolved, more so when lower scan speeds were used. The ductility was lowered from $21\pm 3\%$ for pure Ti to $2\pm 0.4\%$ for Ti+1.5at%Re, but the yield strength was more than doubled, from $461\pm 34\text{MPa}$ to $1038\pm 43\text{MPa}$.

In Ref. [309] and [310], the aim was not to create a multiphase material, but simply to explore the differences in microstructure and properties by varying the amount of β stabilizers in Ti via LMD. By creating parts with a graded V or Mo content across the layers, the minimum composition to retain 100% of the β phase after processing could be determined by analysis of a single part. A minimum of 10wt% Mo or 17wt% V was needed to retain the β phase, but the hardness reached a maximum for compositions just below these minima, caused by the homogeneous distribution of small α grains inside the β matrix.

6.2.1 Materials and Methods

Extra-low interstitial Ti6Al4V (Grade 23) powder with a d_{50} of 34 μm was mixed with smaller sized irregularly shaped Mo powder. All samples were produced on the LM-Q machine using a scan speed v of 1600mm/s, a laser power P of 250W, 60 μm hatch spacing h , and a 30 μm layer thickness t . Layers were scanned using a continuous laser mode according to a zigzag pattern, rotated 90° between each layer.

The exact amount of Mo in the final parts was determined by inductively coupled plasma atomic emission spectroscopy (ICP-AES). HNO_3 was added after dissolving the majority of the sample in HCl to dissolve leftover Mo. The average composition was determined to be 5.89 wt% Al, 3.35 wt% V and 10.5 wt% Mo, remainder Ti.

To reveal the microstructure, an etchant containing 50ml distilled water, 25ml HNO_3 and 5ml HF was used. X-ray measurements were performed on a Siemens D500 diffractometer on polished cross sections perpendicular to the building direction.

Heat treatments were performed in a vertical tube furnace under pure argon atmosphere with a heating rate of 10°C/min, 30 minute residence time and subsequent water quench with a delay of less than 1 second. Four tensile test samples were built as rectangular beams from which the final shape was milled. Tensile tests were performed according to ASTM E 8M at a strain rate of 1mm/min. Yield stress and Young's modulus were determined according to ASTM E 111. The tensile test loading direction was perpendicular to the

building direction. Charpy V-notch samples were built with the long axis parallel (vertically) and perpendicular (horizontally) to the building direction. The notch was included in the design instead of EDM'ed afterwards, as this reduces labor time and does not have a significant effect on the results [115]. Charpy V-notch impact testing was performed using an Instron Wolpert PW5. Specimen dimensions were those of the standard sub-size specimen as defined in ASTM E 23.

Lastly, thermodynamic calculations of the Ti-Al-V-Mo system were performed using the ThermoCalc software and the commercially available TCFE7 database, courtesy of Dr. S. Huang.

6.2.2 Microstructure

The columnar prior β grains of the macrostructure of Ti6Al4V processed via SLM have already been discussed in subsection 6.1.3, and are repeated in Figure 6.8a for comparison with Figure 6.8b. In this latter figure, columns are absent after the addition of 10wt% Mo to Ti6Al4V. Instead, the melt pool shape is revealed by local concentration variations of Mo in the material. Unmolten Mo particles are randomly distributed in the titanium matrix and are present in various sizes but are generally smaller than 10 μ m. These particles are indicated by the arrows in Figure 6.8b, but can be better distinguished in Figure 6.9. The applied energy density of the SLM process, $E=86.8$ J/mm³, is sufficient to fully melt the Ti6Al4V powder, which has a melting temperature of 1668°C. However, Mo has a melting temperature of 2623°C and the Mo particles only melt partially. The volume fraction of remaining Mo particles was calculated via pixelcount of SEM images taken with BSE contrast, such as Figure 6.9a. In these images, the Mo particles are lighter than the surrounding matrix due to the larger atomic number of Mo compared to Ti. At 0.8%, the Mo particle content is too low to be measured via XRD and no Mo peaks are present in the diffraction spectra discussed below and shown in Figure 6.11.

The Mo particles are distributed homogeneously in the matrix. Furthermore, the local variations in color of the matrix, visible in Figure 6.9a, indicate Mo rich and Mo poor bands due to an incomplete mixing of Mo in the melt pool or diffusion of Mo around the Mo particles. The lighter bands are richer in Mo, and the bands outline the elliptical shape of the melt pool.

In Figure 6.9b, the melt pool boundaries are prominently delineated and sometimes act as nucleation sites for new grains. However, most grains grow epitaxially across the melt pool boundaries, indicated by the arrows, and form elongated grains. These grains grow towards the top center of the melt pool, in the opposite direction of the maximum thermal gradient. Contrary to Ti6Al4V,

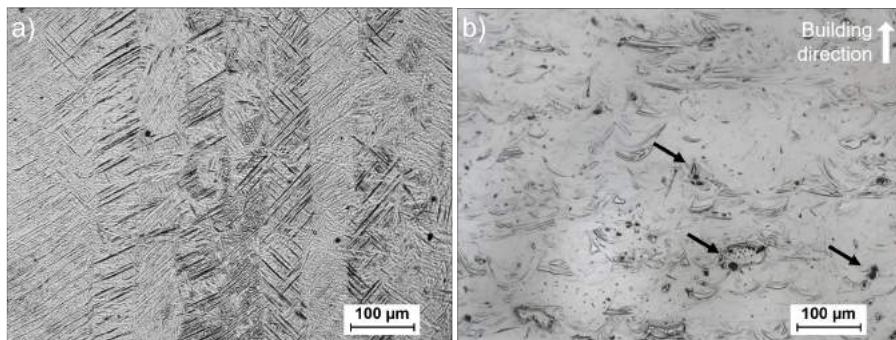


Figure 6.8: a) Prior β grain columns in Ti6Al4V disappear and melt pool boundaries become visible by addition of 10 wt% Mo in (b).

the melt pool boundary is still visible. The grains are typically 5 to 15 μm wide, which is much smaller than the columnar grains in Ti6Al4V, which range from 50 to 150 μm in width. Within each grain, a cellular substructure with an intercellular spacing of less than 1 μm is present, also directed towards the melt pool center. The prevalence of the β phase rather than the α' phase leads to a slightly lower hardness of $338 \pm 5 HV_{0.3;10s}$, compared to $399 HV_{0.3;10s}$ for Ti6Al4V. Combined with the results above, microsegregation of alloying elements occurs at two different scales. On the larger scale, Mo bands delineate the melt pool shape. On the smaller scale, Mo, Al and V are segregated due to the formation of the cellular solidification structure.

In Ti6Al4V, the β phase transforms to α' martensite during fast cooling. In agreement with literature [310–313], the addition of 10 wt% Mo completely suppresses this transformation and the β phase is fully retained. The effect of Mo on the martensitic transformation is twofold: firstly, the critical cooling rate to retain β is decreased. Secondly and more importantly, by adding β stabilizers, the M_s temperature is lowered drastically. The different microstructures translate into different hardness values.

In a review of Ti-Mo alloys, Murray [314] summarized results from several independent studies, concluding that the β transus temperature lowers around 9° to 10°C per wt% Mo added. Given that the β transus of Ti6Al4V is 995°C, the new β transus is expected to be around 900°C. To examine the stability of the β phase and validate this assumption, four samples were respectively subjected to an annealing temperature of 650°C, 850°C, 900°C and 1050°C for 30 minutes, followed by water quenching.

Microstructural examination showed that the sample treated at 650°C contained

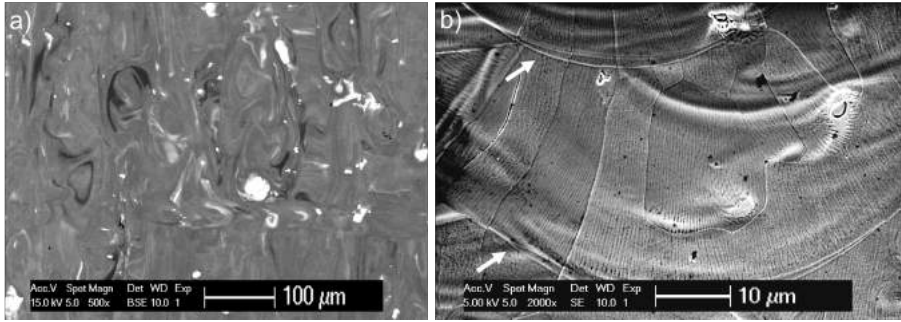


Figure 6.9: a) A top view of the microstructure of Ti6Al4V+10Mo, showing bright, unmolten Mo particles, and fluid lines indicating local variations of Mo concentration due to incomplete mixing in the melt pool. b) Side view, revealing a cellular microstructure, as well as a clear delineation of the melt pool boundaries. The arrows indicate locations where the grains continued growing into a new melt pool.

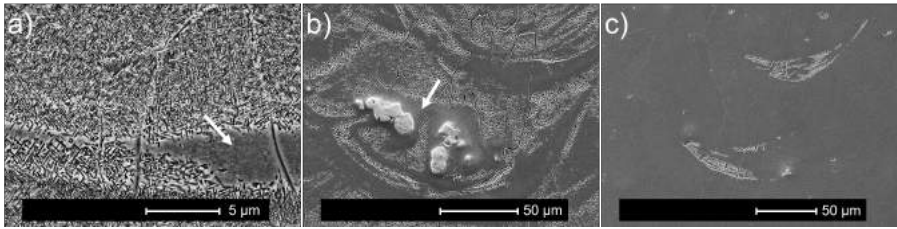


Figure 6.10: Microstructure of heat treated Ti6Al4V+10Mo, treated and quenched at (a) 650°C, (b) 850°C and (c) 900°C. The arrows indicate Mo rich areas, fully stabilizing the β phase.

an extremely fine distribution of α platelets, as shown in Figure 6.10a. XRD confirmed that α phase was present, as clear α peaks appear in the diffraction spectrum in Figure 6.11. The Mo is still heterogeneously distributed in the matrix, which is evident from Mo enriched, full β phase regions, indicated by the black arrow. Due to the presence of the α phase, solute redistribution causes the β peaks to shift slightly to the right compared to the as built specimen. Furthermore, this also causes the microsegregation linked with the cellular substructure to disappear. The extremely fine two phase microstructure leads to a higher hardness of $468 \pm 7HV_{0.3;10s}$, which is remarkably higher than that of the Ti6Al4V material processed via SLM ($399HV_{0.3;10s}$).

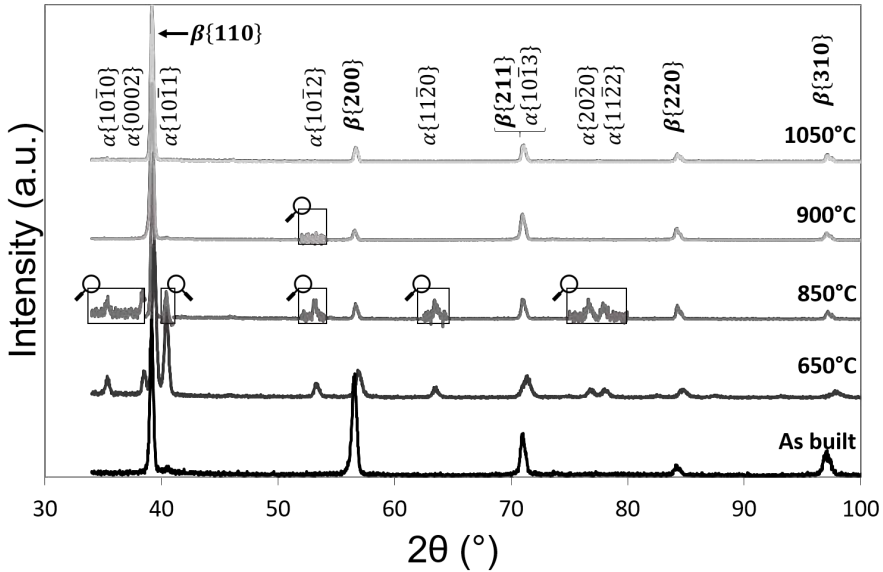


Figure 6.11: Diffraction spectra of as built Ti6Al4V+10Mo, as well after quenching from 650°C, 850°C, 900°C and 1050°C. The as built material consists of 100% β phase, and is again so after quenching from 900°C or above. In reality, the magnified peaks are 10 times smaller than depicted.

Micrographs of the sample treated at 850°C in Figure 6.10b show slightly etched regions at β grain boundaries and along the contours of the melt pools. The arrow indicates the Mo enriched zones around the Mo particles, consisting fully of β phase. The α phase volume fraction is too small to cause any hardening. After heat treatment at 850 °C, the microhardness now equals $338 \pm 6 HV_{0.3;10s}$, the same as in the as built condition ($338 HV_{0.3;10s}$). The α peaks in the diffraction spectrum are almost invisible relative to the β phase peaks, but are still present under closer inspection, indicated in the diffraction spectrum in Figure 6.11. At 900°C, there is almost no α phase left, as shown in Figure 6.10c. Additionally, α peaks in the diffraction spectrum in Figure 6 are indistinguishable from background noise. At $331 \pm 8 HV_{0.3;10s}$, the hardness is again identical to that of the as built condition. Because of the limited amount of α phase present after quenching from 900°C, the β transus is likely located just above 900°C, corresponding well to the expected transus temperature. After heat treatment at 1050°C, the microstructure is again fully β . The β grains did not grow significantly, and the hardness is $336 \pm 4 HV_{0.3;10s}$.

Solidification Structure

In a binary alloy system, the conditions for a stable planar solidification front is given as Equation (6.1) [315]. In this equation, the critical temperature gradient $\left(\frac{\delta T}{\delta x}\right)_{crit}$ for a stable planar solidification front is given as a function of the overall solute concentration C_0 , the solute diffusion coefficient D_L in the liquid phase, the solute partition coefficient k , the solidification rate R and the gradient of the equilibrium melting point $\frac{\delta T_L}{\delta C}$, which is the slope of the liquidus in the phase diagram.

$$\left(\frac{\delta T}{\delta x}\right)_{crit} = \left(\frac{C_0 R}{D_L}\right) \left(\frac{1-k}{k}\right) \left(\frac{\delta T_L}{\delta C}\right) \quad (6.1)$$

Planar solidification is rare for alloys and usually requires slow solidification. Consequently, it is remarkable that the planar front is stable in Ti6Al4V processed via SLM, even though it contains 10wt% alloying elements, and solidification rates are extremely high. This is caused by the narrow solidification range $\Delta T_{L \rightarrow S}$ of Ti6Al4V of only 5°C. This range influences the partition coefficients, as a larger range usually leads to values of k further away from the ideal value of $k = 1$ (no partitioning between liquid and solid). The limited extent of solute partitioning lowers the critical gradient, thereby favoring planar solidification.

Adding 10 wt% Mo to Ti6Al4V disturbs this equilibrium. Most importantly, it expands the solidification range to 17 °C, more than 3 times the value without Mo, as is clear from the pseudo-binary phase diagrams in Figure 6.12d-f and the calculated values in Table 6.5. The Mo itself has an average partition coefficient k_{Mo} of 1.41 over the whole solidification range. Furthermore, the calculations indicate that the increased solidification range decreases k_V to 0.33, less than half of its original value of 0.71. Additionally, Figure 6.12e shows that the effect of Al is reversed and the first solid to form will contain little Al, leading to an average k_{Al} of 0.27 over the whole solidification range. While Equation (6.1) has been analytically derived for a binary system, the impact of the different material parameters is similar in more complex alloys. The new partition coefficients of both Al and V lead to an increase of the second factor on the right side in Equation (6.1), thereby increasing the critical temperature gradient and promoting the destabilization of the solidification front. The addition of an extra alloying element with a large partition coefficient additionally increases the critical gradient.

Figure 6.13 shows the transition from planar to cellular solidification at the melt pool boundary (boundaries are indicated by the black arrows). The white striped line delineates the transition from the initial planar zone to the

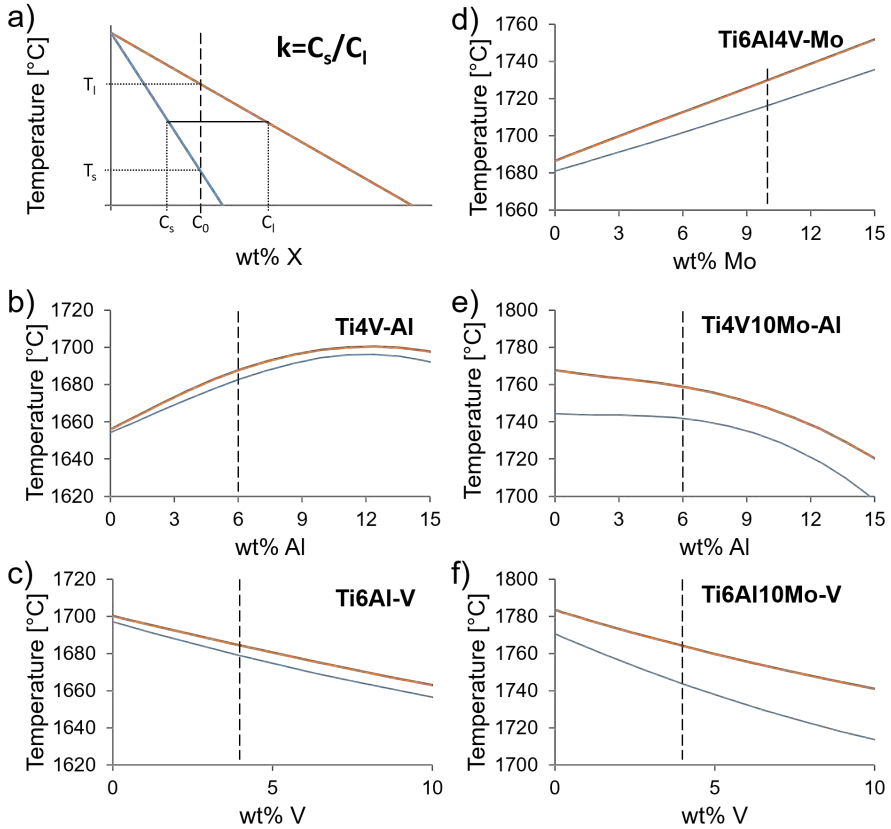


Figure 6.12: Calculated vertical pseudo-binary phase diagrams of the different compositions. The red line is the liquidus, the blue line the solidus. a) General representation of the partition coefficient k for solute X. b) Ti6Al4V system with varying amount of Al. c) Ti6Al4V system with varying amount of V. d) Ti6Al4V+10Mo system with varying amount of Mo. e) Ti6Al4V+10Mo system with varying amount of Al. f) Ti6Al4V+10Mo system with varying amount of V.

Table 6.5: The solidification range ΔT and partition coefficient k for the different pseudo-binary sections of Ti6Al4V and Ti6Al4V10Mo shown in Figure 6.12, as calculated by ThermoCalc. The partition coefficient is an average value over the whole solidification range.

ΔT [°C]	Ti6Al4V		Ti6Al4V10Mo		
	Ti_4V-xAl	Ti_6Al-xV	$Ti_4V10Mo-xAl$	$Ti_6Al10Mo-xV$	Ti_6Al_4V-xMo
	5			17	
k	1.24	0.71	0.27	0.33	1.41

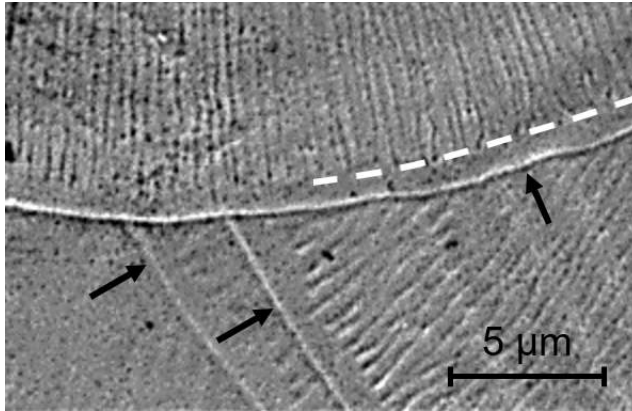


Figure 6.13: Thin region at the melt pool boundary in which planar solidification is stable. Transition (marked by the white striped line) from planar to cellular solidification occurs within 0.5–1.0 μm of the melt pool boundaries, which are indicated by the arrows.

dendritic zone in the top melt pool. During the first stage of solidification, the concentration gradients at the liquid-solid interface are still increasing and have not reached a steady state. Consequently, the critical thermal gradient for planar solidification is low and a planar front is stable. At a certain moment, enough solute distribution will have taken place to increase the critical thermal gradient above the actual thermal gradient, at which point the solidification switches from a planar to a cellular mode. This transition can occur before a steady state is reached.

6.2.3 Mechanical Properties

Tensile testing

Stress-strain curves for Ti6Al4V and Ti6Al4V+10Mo are shown in Figure 6.14. The lower Young's modulus of the fully β Ti6Al4V+10Mo is apparent from the more gradual slope of the elastic regime. The Young's modulus equals 73 ± 1 GPa, and is much lower than conventional Ti6Al4V which has a modulus of 105-120 GPa. Secondly, at an average of $20.1\pm 2.0\%$, the elongation of Ti6Al4V+10Mo is much higher than that of Ti6Al4V, which is only $7.3\pm 1.1\%$, even though both were produced using identical parameter sets. The trade-off for a higher elongation is a lower yield stress. Ti6Al4V+10Mo yields at 858 ± 16 MPa, while the stronger martensitic Ti6Al4V yields at 1110 ± 9 MPa.

The stress-strain curve of Ti6Al4V+10Mo displays no strain hardening. The UTS is quickly reached after the onset of plastic deformation, after which a constant stress plateau extends up to failure. By comparison, Ti6Al4V processed via SLM but using slower scan parameters ($P = 42$ W, $v = 225$ mm/s and $h = 74$ μ m) led to a yield stress similar to that of Ti6Al4V+10Mo, namely 827 ± 17 MPa. The elongation, which was equal to $11.3\pm 1.1\%$, was still significantly lower than that of Ti6Al4V+10Mo reported here. This indicates that the increase in elongation can be attributed to a microstructural change to the more ductile β phase rather than the reduced strength.

The results are summarized in Table 6.6, and minimum values for three typical β -Ti alloys are given as a reference, namely wrought Ti15Mo (ASTM F2066), Ti12Mo6Zr2Fe (ASTM F1813) and Ti15Mo5Zr3Al. Ti6Al4V+10Mo combines high strength with excellent ductility and has a low Young's modulus. Moreover, it meets the elongation requirements set for Ti15Mo and exceeds its strength requirements by several 100 MPa. In addition, it only just falls below the strength requirements for Ti12Mo6Zr2Fe, but is considerably more ductile. The tensile properties are comparable mostly with Ti15Mo5Zr3Al, in which the UTS after solution treatment in the β field ranges between 900 and 1000 MPa, the Young's modulus about 80 GPa and elongation around 20% [46]. This alloy is mostly used in corrosive environments due to its high Mo content.

Charpy V-notch impact testing

Yasa et al. [115] investigated the energy absorption during Charpy V-notch impact testing of Ti6Al4V specimens fabricated by SLM. The energy absorption was found to be independent of building direction and equaled 11.5 ± 0.5 J. Ti6Al4V+10Mo absorbed much less energy upon impact, at only 3.8 ± 0.1 J for

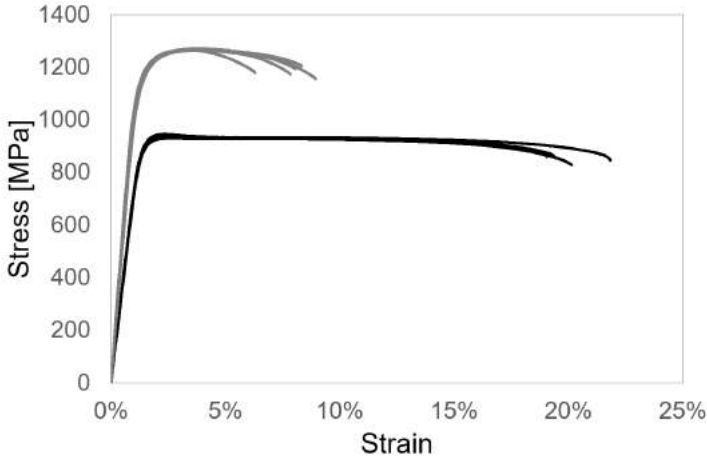


Figure 6.14: Engineering stress-strain curves for Ti6Al4V+10Mo (black) and Ti6Al4V (grey) produced by SLM.

Table 6.6: Static tensile properties of Ti6Al4V+10Mo compared to regular Ti6Al4V processed by SLM. For reference, standard specifications for two types of β titanium alloys for use in surgical implants are given as well as mechanical properties for Ti15Mo5Zr3Al.

	E [GPa]	σ_y [MPa]	UTS [MPa]	ϵ_{frac} [%]	Source
<i>Ti6Al4V+10Mo</i>	73 ± 1	858 ± 16	919 ± 10	20.1 ± 2.0	This work
<i>Ti6Al4V</i>	109 ± 3	1110 ± 9	1267 ± 5	7.3 ± 1.1	[316]
<i>Ti15Mo</i>		483	690	20	ASTM F2066 ^a
<i>Ti12Mo6Zr2Fe</i>		897	932	12	ASTM F1813 ^b
<i>Ti15Mo5Zr3Al</i>	80		900–1000	20	[46]

^a Bar, beta annealed. ^b Solution treated.

horizontally built specimens and 1.4 ± 0.5 J for specimens built parallel to the vertical axis. The difference between both directions is the direction of crack growth. In the horizontal specimens, the crack front is parallel to the building direction, but crack growth is in the horizontal direction. For the vertical specimens, the crack grows in between the layers. The fracture surface of a representative horizontal sample is rougher than that of a representative vertical sample, as shown in Figure 6.15. This means that the crack path is deflected more in the horizontal sample, through which more energy is absorbed. Strain rate during tensile testing is around $5 \times 10^{-3} \text{s}^{-1}$, while the strain rate during Charpy V-notch impact testing is 10^2 to 10^3s^{-1} . Additionally, in contrast to α' Ti6Al4V, β Ti6Al4V+10Mo possesses a ductile to brittle transition, which is

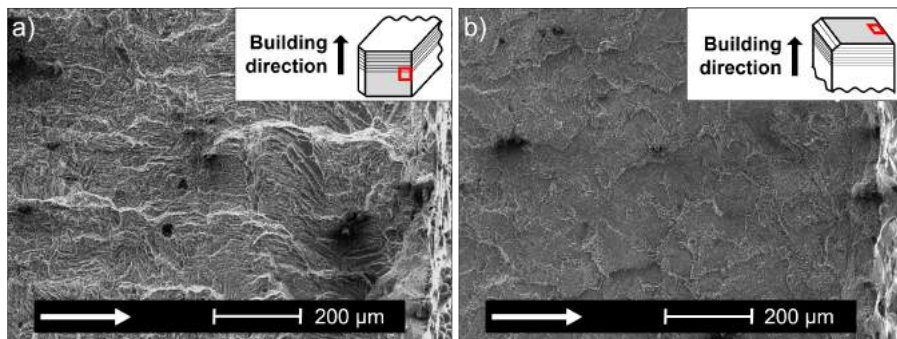


Figure 6.15: Fracture surfaces of Charpy V-notch specimens: a) horizontal specimen, b) vertical specimen. The white arrows indicate the crack propagation direction. The top right inserts show where the images were taken on the fracture surface, and the orientation of the fracture surfaces with respect to the layers.

both temperature and strain rate sensitive.

6.2.4 Preliminary conclusions

10 wt% Mo powder was mixed with Ti6Al4V-ELI powder and processed via SLM, which led to a lower β transus temperature of around 900°C and the stabilization of the β phase at room temperature after rapid solidification. Moreover, the solidification mechanism changed from planar to cellular due to severe solute distribution between liquid and solid, which is a direct result of tripling the solidification temperature range. The resulting microstructure consists of homogeneously dispersed Mo particles in a fully β titanium matrix. In addition, static tensile properties show a combination of high strength ($\sigma_y=858$ MPa) and excellent ductility ($\epsilon_{frac}=20.1$ %).

6.3 Discussion

6.3.1 Process parameters and material specific phenomena

The work in chapter 5 was performed using Ti6Al4V as the subject material. This alloy does not have any specific behavior apart from a displacive allotropic transformation, but this occurs at higher temperatures, as high as 800°C. Overall, this allowed to study the influence of the process parameter in the absence of any interfering material specific behavior.

The conclusions that were drawn as such from chapter 5 apply for general material behavior. However, these conclusions may be different if material specific behavior is present. Take, for instance, the low-temperature allotropic martensitic transformation in H13 tool steel and 18Ni300 maraging steel. The associated displacive strains reduce the tensile residual stresses, and may even reverse the sign of the stress to compressive. This auto-stress reducing effect would be diminished if actions are taken to reduce thermal gradients, or to increase the overall temperature. In a recent master thesis [317], SLM of H13 tool steel without preheating resulted in a mainly martensitic material, with a hardness of 630HV. By using a 200°C preheating, the amount of retained austenite increased, and the hardness dropped to 580HV, but rises to 650HV again by using a 400°C preheating. At holding temperatures of 400°C, a bainitic transformation to ferrite and cementite is expected to take place, which leads to a harder material, but which is a diffusive transformation with a smaller effect on RS. This is reflected in the stress measured via XRD on the top surface. Initially compressive without preheating, it turns tensile with increasing preheating temperature. Higher preheating temperatures are therefore not always stress-reducing. Neither is using a slow scan speed, illustrated by the example of M2 tool steel described in the literature study, and shown in Figure 3.14. Slower scan speeds led to an increasing amount of cracking. In this case, the higher heat input increased the amount of retained austenite, much like in H13 tool steel. But due to the high carbon content, it also led to an increased formation of carbides that strengthened the material, but embrittled it to the point that it is no longer capable of handling the residual stresses.

6.3.2 Microstructure modification

Metal AM processes that create localized melt pools, in specific SLM, lead to two possible microstructures. The first is a columnar microstructure, with grains capable of growing in excess of 100 layer thicknesses high. The second is

a cellular microstructure, in which the grains have a cellular substructure that is oriented towards the center of the melt pool.

This work recapitulates the link between the material and the final microstructure, with most investigated alloys exhibiting a cellular structure, with the exception of Ti6Al4V. However, other authors have shown that working with a certain material does not necessarily dictate the microstructure that will be obtained. Although an alloy will favor a certain solidification mode, using different process parameters allows variation of the thermal gradient \vec{G} and cooling rate \vec{R} . This creates possibilities to change the solidification structure for one alloy. Moreover, by using different process parameter sets in different locations, the microstructure can be tailored locally which would lead to a subtle gradient in mechanical or other properties. For now, this has been exploited in Inconel718 [53, 142] and 316L [112], but preliminary, unpublished results show that this is also possible when using Al7075 [318].

A solidification map can be made for each alloy, in which the solidification microstructure is given as a function of the thermal gradient \vec{G} and cooling rate \vec{R} . There are practical lower and upper limits to the \vec{G} and \vec{R} combinations that can be achieved by variation of the process parameters during AM. The microstructure can only be changed if the boundaries between the different solidification regimes pass through the region delineated by these limits. For example, the expected combinations of \vec{G} and \vec{R} for three distinctly different parameter sets in EBM are displayed on the solidification map of Inconel718 in Figure 6.16. Parameter set 1 comprised an oscillation of the parameters to cover a wide range of \vec{G} and \vec{R} combinations, and to induce a mixed microstructure. Meanwhile, set 2 was located on the boundary between a columnar and mixed solidification mode, which led to substantial misorientation of the grains with respect to the other sets. Lastly, set 3 overlapped fully with the columnar regime, and created a strongly textured, columnar zone. The three different sets were assigned to different zones of one solid part, and an EBSD plot of the resulting variation in texture is shown in Figure 6.17 [142].

6.3.3 Alloy modification

Apart from the process parameters, it is also possible to alter the *material* to infer the desired changes. In this research, the choice of Mo as additional alloying element was based on its ability to stabilize the β phase and its high melting temperature, which allowed retaining partially melted Mo particles in the Ti matrix. Additionally, it increases the corrosion resistance of Ti alloys. However, based on the specific requirements of certain applications, the alloy content can be tailored to induce a particular microstructure and meet required

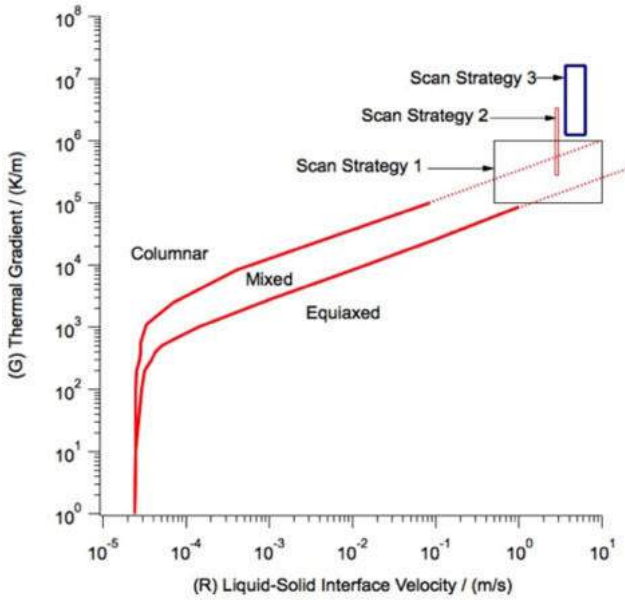


Figure 6.16: Solidification map for Inconel718, with indication of the expected combinations of \vec{G} and \vec{R} for three different parameter sets [142].

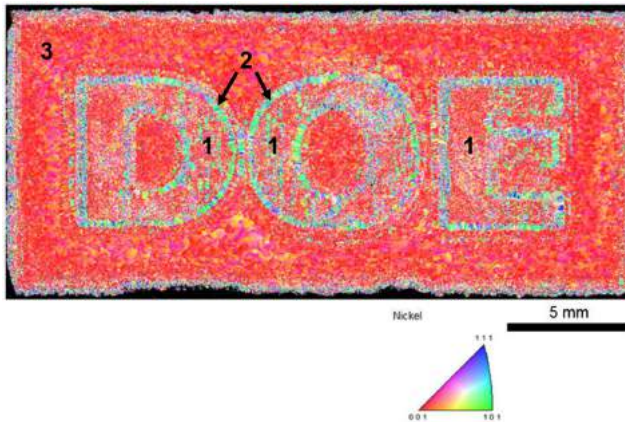


Figure 6.17: Local variation of the crystal structure in SLM Inconel718 by variation of the scan parameters and use of two different lasers (Adapted from Ref. [142]).

mechanical or physical properties. For instance, some regard the columnar prior β grains in Ti6Al4V as disadvantageous, because they lead to anisotropic properties. The planar solidification front could then potentially be destabilized by addition of a different element, that does not affect the stability of the α or β phase. As discussed in chapter 2, Sn, Zr and Hf are neutral alloy elements in Ti alloys, of which Zr is the most often used. It could therefore be that addition of Zr would change the solidification structure.

On the other hand, changing the alloy content may facilitate easier processing via SLM while still maintaining the properties of the original alloy. In this sense, alloys that are prone to solidification cracking and thermal cracking can be alloyed or de-alloyed to avoid precipitation of unwanted phases or other metallurgical phenomena, and eliminate cracks. Existing alloys were all designed to meet specific requirements, but also for a certain processing technique. Consequently, it is only logical that new alloy compositions are formulated to allow easy processing via SLM.

Concerning the presence of added, second phase particles in the material, the residual Mo particles do not seem to have a visible advantageous or disadvantageous effect on the mechanical properties in this work. In addition, they do not form a linked network and only represent 0.8 vol% of the material. Consequently, their effect on other physical properties would be small and in this particular case, use of prealloyed Ti6Al4V10Mo powder would likely have led to similar results. However, if smaller amounts of Mo are added, the matrix would not be fully β stabilized. The zones around the Mo particles would then consist of ductile β phase and would change to an $\alpha+\beta$, $\alpha+\alpha'$ or $\alpha+\alpha''$ mixture when moving away from the particle, depending on the amount of Mo in the matrix. This could lead to an increase in fracture toughness while limiting the amount of added Mo.

In general, second phase particles may lead to several advantages in other alloy combinations. For example, small and hard particles such as submicron ceramic particles are expected to increase the strength of the material. And if these particles are produced in-situ, during the SLM process, the interface with the matrix will be stronger. Another possibility is if the volume fraction of the particles is high and if the particles are soft and ductile, they can lead to stress relaxation by allowing local deformation of the matrix, thereby reducing crack formation. They would then effectively act as a pore. Care must then be taken to include particles of sufficient strength to ensure good mechanical properties. In the case of W, an alloy element that lowers the DBTT, for example Ta, would reduce the amount of cracks or even eliminate them completely.

Because of the non-equilibrium processing, elements can be mixed that normally do not mix well. Moreover, because there is only a small melt pool and rapid

cooling rates, small particles that are significantly heavier or lighter than the liquid metal will be distributed fairly homogeneously, whereas they would sink to the bottom or float to the top during normal casting. These novel materials, for which precipitates are created *in situ* or for which alien, sometimes ceramic particles are added, are called metal matrix composites or MMC's. SLM has been used to create aluminium based MMC's by mixing Al powder and Fe_2O_3 [319,320], creating a multitude of fine, distributed particles. The strength of AlSi10Mg was greatly increased by addition of TiC without compromising the ductility [321]. In order to keep the particles suspended in the liquid, a high energy input leads to a more uniform distribution of the particles in the metal matrix. A low energy input decreases Marangoni flows, which allows particles to sink and aggregate in the melt [322].

Titanium based MMC's have been produced both by *in situ* reactions as well as premixing of the reinforcing compound powder with pure Ti powder. In single track experiments, Kuhnle and Partes [323] mixed stoichiometric amounts of Ti and B_4C powder with the intent to create TiC and TiB_2 according to the reaction scheme $3Ti + B_4C \rightarrow TiC + 2TiB_2$. All of the B_4C was dissolved, but they found that Ti_2C , TiB and some Ti_3B_4 were formed, as well as maintaining pure Ti. Remelting of the (pure Ti) substrate was not taken into account in their initial reaction scheme, which caused the deviation. Guet *al.* [324] also neglected remelting of the substrate, but built cuboids measuring $8 \times 8 \times 8\text{mm}^3$, so the overall influence of remelting the substrate during the first layer or two can be neglected. They mixed Ti and SiC in an 8:3 ratio for the reaction $8Ti + 3SiC \rightarrow Ti_5Si_3 + 3TiC$, which was observed to be complete. The microstructure consisted of TiC dendrites with Ti_5Si_3 in between, and the dendrites were significantly coarser for lower scan speeds. TiC is completely dissolved/dissociated in high temperature melts, but tends to precipitate again during solidification. For a TiC+Ti mixture, this happened in the form of fine platelets less than 100nm thick for TiC contents below 20wt%, but as dendrites above 20wt% [325]. Lastly, mixing significant amounts of ZrB_2 with 30 to 70wt% Ti created a mixture of various complex phases, some of which were metastable [326].

6.4 Conclusion

Nine different, existing metals and alloys were processed via SLM, their resulting microstructures were compared. Their residual stress state was characterized by XRD and the bridge curvature method. Next, a new material was created by addition of Mo to Ti6Al4V.

- The microstructure, but more importantly also the response to residual stress development, was demonstrated to be specific for each alloy. In this work in particular, these specific phenomena were the susceptibility to solidification cracking (Hastelloy C-276), phase transformations (18Ni300 maraging steel) and an above-room temperature DBTT (W).
- The material specific behavior may even change the influence that process parameters have on the residual stresses.
- Additionally, changing the composition of existing alloys can serve two purposes during and after SLM. First, mechanical, functional or other properties can be improved. Second, the material properties can be altered to improve the processability by avoiding residual stress-related problems or by creating a larger, stable process window.

Chapter 7

Heat Treatment of SLM Ti6Al4V

Chapters 5 and 6 focused on minimizing the stresses developed during SLM by either changing the process parameters or the material properties. Residual stresses cannot be completely avoided, and a post-process stress relieve or heat treatment is nearly always performed. A second and equally important reason to apply a heat treatment is that the microstructure, and thus the mechanical properties can be changed.

This chapter has been published as:

- Vrancken, B., Thijs, L., Kruth, J., Van Humbeeck, J. (2012). Heat treatment of Ti6Al4V produced by Selective Laser Melting: Microstructure and mechanical properties. *Journal of Alloys and Compounds*, 541, 177-185.
- Vrancken, B., Kempen, K., Thijs, L., Kruth, J., Van Humbeeck, J. (2014). Adapted heat treatment of Selective Laser Melted materials. In Danninger, H. (Ed.), *Proceedings of the Euro PM 2014 Congress*. Euro PM2014 Congress. Salzburg, Austria, 21-24 September 2014 (pp. 1-6). Shrewsbury: European Powder Metallurgy Association (EPMA).

7.1 Introduction

Heat treatments of Ti6Al4V have been investigated extensively. The temperature profile to be applied during a heat treatment has been designed to optimize the mechanical properties of cast, rolled or forged material. Additionally, attempts have been made to model the kinetics [327–329] and phase morphology [330–332], to measure the alpha fraction at high temperature [333] and to create a CCT diagram [334, 335]. However, the starting material for these efforts has always been in the mill annealed condition (i.e. with equiaxed alpha grains) or material that has been subjected to some degree of previous deformation. As discussed in previous chapters, the microstructure of Ti6Al4V processed by SLM is unique and consists of columnar prior β grains with an acicular α' martensite in the interior. The response to a heat treatment will therefore differ from that of cast, forged or rolled material.

Mechanical properties of SLM produced Ti6Al4V are a high yield stress (about 1GPa), a high ultimate tensile strength but a relatively low ductility (less than 10%). To improve the ductility of Ti6Al4V products manufactured by SLM, and to achieve a variety of desired mechanical properties for particular applications, suitable post-production heat treatments must be elaborated. In this chapter, the different response of SLM parts on generally applied titanium heat treatments is studied and the influence of time, temperature and cooling rate is distinguished. It appears that standard treatments for bulk alloys are not optimal for SLM produced parts and have to be adapted for optimal mechanical properties.

7.2 Materials and methods

Extra-low interstitial Ti6Al4V (Grade 23) powder was used as a base material for the SLM process. For comparison, Ti6Al4V (Grade 5) with an equiaxed microstructure was used that was vacuum arc remelted, hot forged and mill annealed. This material will further be addressed as the reference material. All SLM parts were produced on the LM-Q machine with a scanning speed v of 1600mm/s, a laser power P of 250W, 60 μ m hatch spacing h and a 30 μ m layer thickness t . Layers were scanned using a continuous laser mode according to a zigzag pattern, which was rotated 90° between each layer.

Before heat treating, samples were enclosed in a vacuum quartz tube, with vacuum better than 10^{-6} mbar. Heat treatments were executed in a vertical tube furnace, with a heating rate of approximately 10°C/min. Three different cooling regimes were applied. Furnace cooling (FC) was attained by turning

the heating off, taking approximately two hours to cool from 800°C to 500°C, which corresponds to an average cooling rate of 0.04°C/s, and air cooling (AC) by cooling the quartz tube in a room temperature environment, leading to an approximate cooling rate of 7°C/s [332, 335]. To water quench (WQ), the tube was dropped and broken in a water reservoir, cooling the samples to room temperature in a matter of seconds.

Four tensile test samples of the SLM material were tested for each treatment to determine the mechanical properties. These samples were built as rectangular beams from which the final shape was cut by wire EDM. Tensile tests were performed according to ASTM E 8M at a strain rate of 1mm/min. Displacements were measured using an extensometer with a 25mm gauge length. Yield stress and Young's modulus were determined according to ASTM E 111. Samples were tested perpendicular to the build direction.

Examination of the microstructure occurred after grinding with SiC grinding paper up to a 1200 grit size, and polished with SiO₂ suspension. To reveal the microstructure, samples were etched with a 50ml H₂O, 25ml HNO₃ and 5ml HF solution. Micrographs were taken using an Axioskop 40 Pol/40 A Pol microscope. A Philips SEM XL30 FEG was used for the examination of fracture surfaces and higher resolution micrographs. Texture and crystallographic orientation were examined by X-ray diffraction (XRD) and electron backscattered diffraction (EBSD).

Dimensions of microstructural features are measured using the line intercept method described in ASTM E112. Circles are used instead of straight lines when measuring the size of elongated features such as needles and lamellae. Lamella size is reported as the true thickness, which is taken as half of the measured thickness, according to Ref [336]. All measurements are given with a 95% confidence interval.

7.3 Results

7.3.1 Microstructure

The microstructure of SLM Ti6Al4V has been discussed in the previous chapters. The starting microstructure of the material to which the response to heat treatment is compared is shown in Figure 7.1. This material is called the reference material from hereon and consists of equiaxed α grains with 10.7±0.9% β phase at the grain boundaries, as determined by pixel count of SEM images. A slight anisotropy exists in the reference material, with the α grains measuring

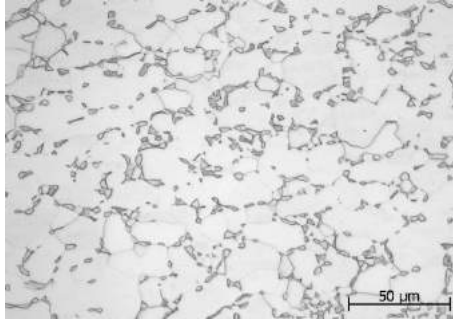


Figure 7.1: Original microstructure of the reference material. The α phase is lighter and the β phase darker.

$16.2 \pm 2.6 \mu\text{m}$ in one direction and only $11.6 \pm 1.7 \mu\text{m}$ in the perpendicular direction. This is attributed to the hot forging this material has been subjected to.

Influence of temperature

Microstructures of the SLM material after heat treating at different temperatures are shown in Figure 7.2. After two hours at 780°C , the fine martensitic structure has been transformed to a mixture of α and β , in which the α phase is present as fine platelets (Figure 7.2a). The long, columnar prior β grains remain visible in the side view of the material.

At 850°C , the β -fraction at high temperature is larger, reducing the equilibrium α -fraction from approximately 87% at 780°C to 73% at 850°C and 23% at 950°C [330, 333]. Comparing Figure 7.2a with b, it is clear that the α plates are significantly coarser for higher temperatures. This observation corresponds to the FE calculations performed by Katzarov *et al.* [330], where the α - β morphology was predicted to be coarser for higher holding temperatures beneath the β transus. The effect of temperature for subtransus treatments is further discussed in section 7.4. When heating above the β transus of 995°C , a fully homogenic, 100% β phase microstructure exists at high temperature. During furnace cooling, a lamellar α + β mixture is formed, as shown in Figure 7.2c.

Figure 7.3a shows the side view of SLM material after a heat treatment at 940°C , below the β transus. After heat treatment below the β transus and at sufficiently low cooling rates, the prior β grains are now even more visible due to the formation of a layer of $\text{GB}\alpha$ and the more aggressive etching of the α + β mixture as opposed to the original α' . On the other hand, Figure 7.3b shows

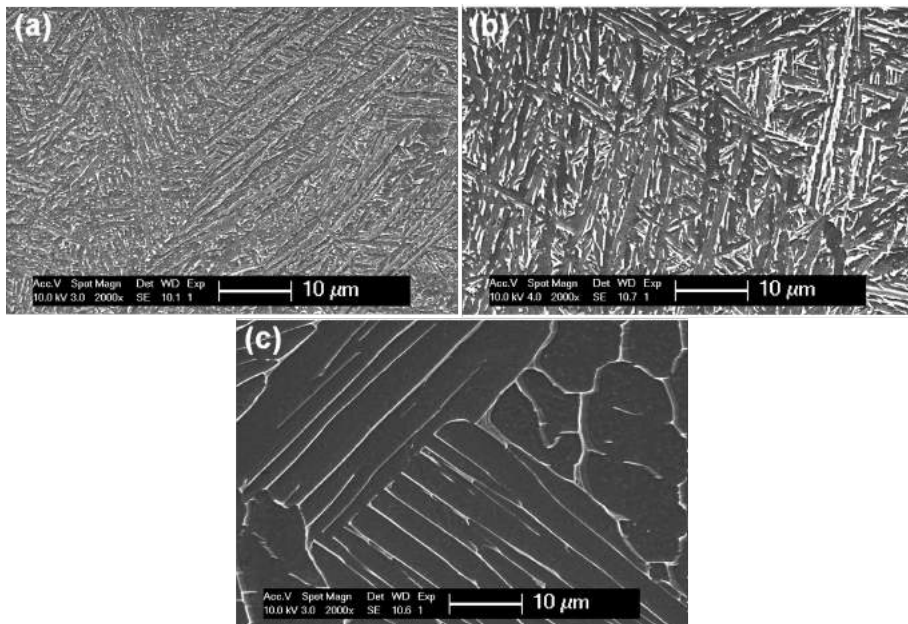


Figure 7.2: Microstructure of Ti6Al4V produced by SLM after heat treating at different temperatures for two hours, followed by FC. (a) 780°C and (b) 843°C below the β transus, (c) 1015°C above the β transus. Lighter zones are β phase, the dark phase is the α phase.

that the microstructure no longer contains long columnar prior β grains after treatment above the β transus, indicating extensive grain growth of the SLM material when heated above the β transus, up to the point of semi-equiaxed β grains. The length of the prior β grains seems unchanged but the width has increased and is now roughly 620 μm wide after 2 hours at 1015°C, compared to 50-100 μm in the as built material. A comparison of the microstructure of SLM material after sub- and super-transus treatments by Sercombe *et al.* [337] led to similar results, as did work by Vilaro *et al.* [338].

As the equilibrium fraction of β phase rises at high temperatures, the intergranular β phase in the *reference material* grows into equiaxed grains. Upon cooling, these β grains transform to lamellar $\alpha+\beta$, leading to a duplex microstructure, seen in Figure 7.4. This microstructure consists of equiaxed α grains and lamellar transformed β grains. At higher heat treatment temperatures, the equilibrium volume fraction of β phase is higher, which ultimately leads to a higher fraction of lamellar $\alpha+\beta$ at room temperature.

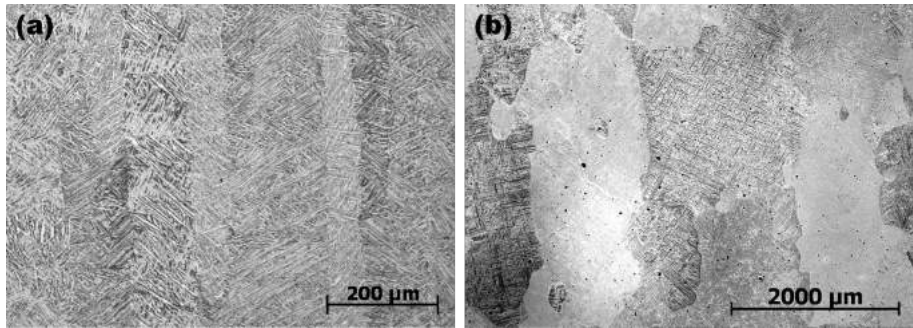


Figure 7.3: Side view of SLM material (a) after 1h at 940 °C and AC followed by 2h at 650°C and AC illustrating the long columnar prior β grains. After heat treatment, a lamellar mixture of α and β is present inside the columnar prior β grains. (b) After 1015°C, 2h, WQ, indicating the extensive growth of the columnar grains. Due to the water quench, the microstructure is fully martensitic. Notice the different scales.

When heated above the β transus, grain growth of the β phase can take place, leading to large grains.

Reference material samples treated at 1015°C still showed a duplex microstructure whereas a 100% transformed β structure was expected. This is cause to believe that the β transus of the reference material is higher than 1015°C. When treated at 1040°C, the microstructure fully consists of transformed β grains with varying degrees of grain boundary α , depending on the cooling rate.

Influence of the residence time

The residence time at high temperature affects grain growth, with longer residence times leading to larger grains. An analogous remark can be made about the heating rate. The time at high temperature and the heating rate are however of minor importance compared to the temperature for Ti6Al4V SLM parts when treated below the β transus. Both the α and the β phase will tend to coarsen but will hinder each other, hereby limiting grain growth. This effect diminishes as the temperature rises closer to the β transus and the α fraction decreases. The influence of the residence time will thus increase for higher temperatures in the $\alpha+\beta$ range.

Further evidence is provided in Figure 7.5, where the microstructure of SLM material is compared after two and twenty hours at 940°C, below the β transus.

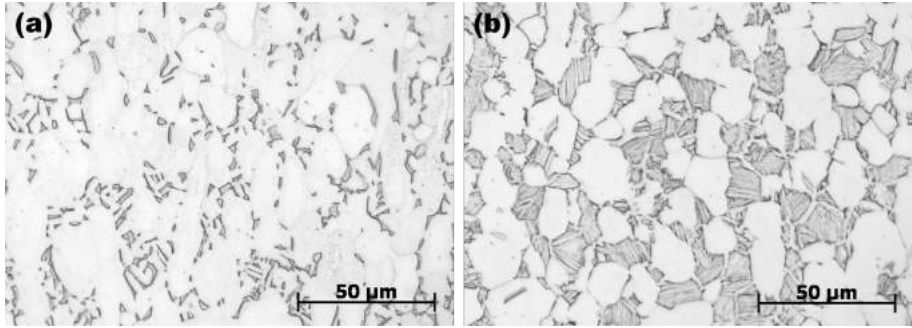


Figure 7.4: Duplex microstructure of the *reference material* consisting of equiaxed α grains and lamellar $\alpha+\beta$. (a) two hours at 780°C , followed by furnace cooling and (b) one hour at 940°C , followed by air cooling to 650°C . The α phase is light, the β phase is dark. Notice the increase in lamellar fraction when treated at a higher maximum temperature.

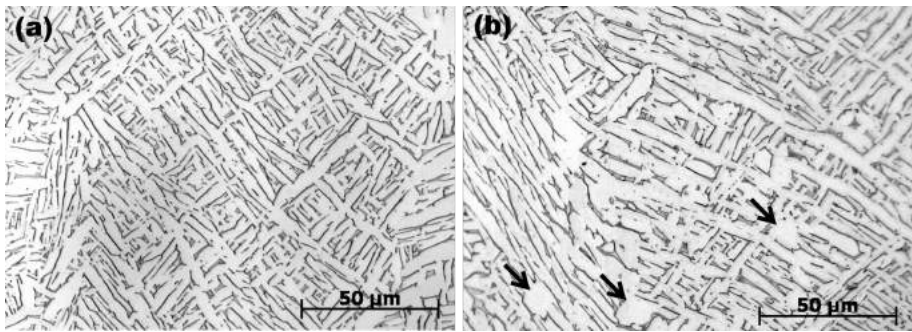


Figure 7.5: Comparison of the similarity in α plate size after (a) two hours at 940°C and (b) twenty hours at 940°C , followed by furnace cooling. The α phase is light, β is dark. The arrows in (b) indicate globularized α grains.

The α phase has started to globularize at some locations as indicated by the arrows in Figure 7.5b, whereas the majority of the section is similar to that after two hours. The α plates are $2.23\pm 0.12\mu\text{m}$ wide after two hours and have coarsened to an average width of $2.80\pm 0.16\mu\text{m}$ after twenty hours.

Previous research suggests that to achieve 50% globularization of the α phase at 955°C , a residence time of approximately 8 hours is necessary [327]. However, the starting material was originally equiaxed and deformed to local strains of 0.49, with a microstructure resembling elongated α grains rather than a lamellar

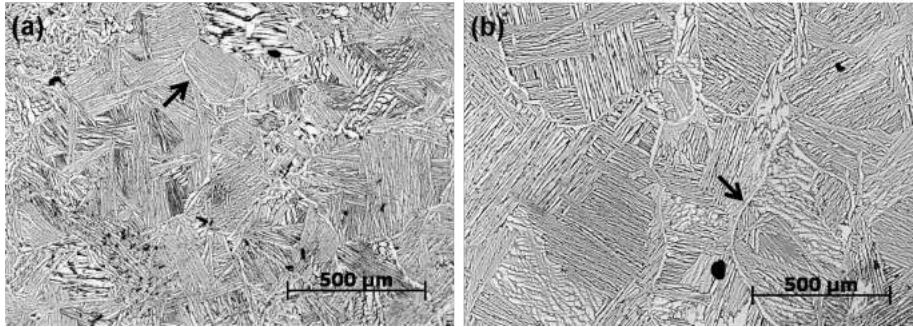


Figure 7.6: Illustration of the smaller α colony size after (a) two hours at 1020°C compared to after (b) twenty hours at 1040°C, followed by furnace cooling. The α phase is light, β is dark. The arrows indicate grain boundary α .

structure. For finer, lamellar or platelike structures, it is expected that the time for globularization is drastically increased.

The residence time is more important when heat treating above the β transus. Consisting of a single phase, grain growth can now take place unhindered and fast, considering the high temperatures. As the size of α colonies is limited to the β grain size, larger colonies are possible for longer residence times. From Figure 7.6, it is clear that the α colonies are larger after prolonged residence times. Lütjering [47] showed that the α colony size is a determining factor for the mechanical properties. As such, the residence time is an important parameter during β annealing.

Influence of the cooling rate

In Figure 7.7, the microstructure of SLM produced parts after two hours at 850°C is compared for different cooling rates. These structures all look alike, and the α needle width is similar for all three, measuring $1.27 \pm 0.13 \mu\text{m}$ after furnace cooling, $1.22 \pm 0.09 \mu\text{m}$ after air cooling and $1.16 \pm 0.13 \mu\text{m}$ after water quenching. Since the α fraction at 850°C is fairly large (73%, Ref [330,333]), the influence of the cooling rate is minimal. With rising maximum temperature, the amount of primary α that is still present at high temperature decreases and the influence of the cooling rate increases. This is apparent from needle size measurements after treatment at 950°C with different cooling rates. At this temperature, the α phase volume fraction is reduced to 23% and single α plates can now grow to a larger extent. The effect of cooling rate is now larger, leading to needle sizes of $1.48 \pm 0.14 \mu\text{m}$ after water quenching, $1.57 \pm 0.21 \mu\text{m}$ after air

Table 7.1: Mechanical properties of as built SLM and reference material.

	E [GPa]	σ_y [MPa]	UTS [MPa]	ϵ_{frac} [%]
<i>SLM</i>	109.2±3.1	1110±9	1267±5	7.28±1.12
<i>Reference</i>	120.2±1.9	960±10	1006±10	18.37±0.88

cooling and $2.23 \pm 0.12 \mu\text{m}$ after furnace cooling. During both air cooling and water quenching the cooling rate is too high for significant grain growth to occur. Low cooling rates, such as during furnace cooling, allow the grains to grow during cooling.

When treated above the β transus, the cooling rate is the most important parameter that determines the final dimensions of the α phase and even the morphology [47, 332]. At high cooling rates, the large undercooling leads to the formation of many α nuclei resulting in smaller α colony size and a finer spacing between individual α plates. Furnace cooling results in lamellar $\alpha+\beta$ and air cooling results in an α -Widmanstätten microstructure or basket weave structure. The cooling rate during water quenching is higher than 410°C/s , leading to α' martensite [334].

The microstructure of the *reference material* displays a predictable dependency on the cooling rate: upon cooling, the transformation of equiaxed β grains that exist at high temperatures produces lamellar $\alpha+\beta$. The lamellar spacing is dependent on the cooling rate, and decreases with increasing cooling rate. The thickness of the grain boundary α is also dependent on the cooling rate, decreasing with increasing cooling rate. When cooled from above the β transus, the cooling rate determines the size of the α colonies. The maximum size of an α colony is limited by the size of the β grain in which it originates [46].

7.3.2 Mechanical Properties

The tensile curves of as built SLM material and reference material are shown in Figure 7.8 and the results are listed in Table 7.1. Three differences should be noted. First, the Young's modulus of the SLM material is slightly lower than that of the reference material. This is most likely caused by texture, which will be discussed in section 7.4. Second, the SLM material is much stronger than the reference material. Third, because of the fine lamellar structure, the fracture strain is much lower compared to the equiaxed reference material. Note that the yield stress and ultimate strength of the reference material differ by only 50 MPa, indicating low strengthening by deformation.

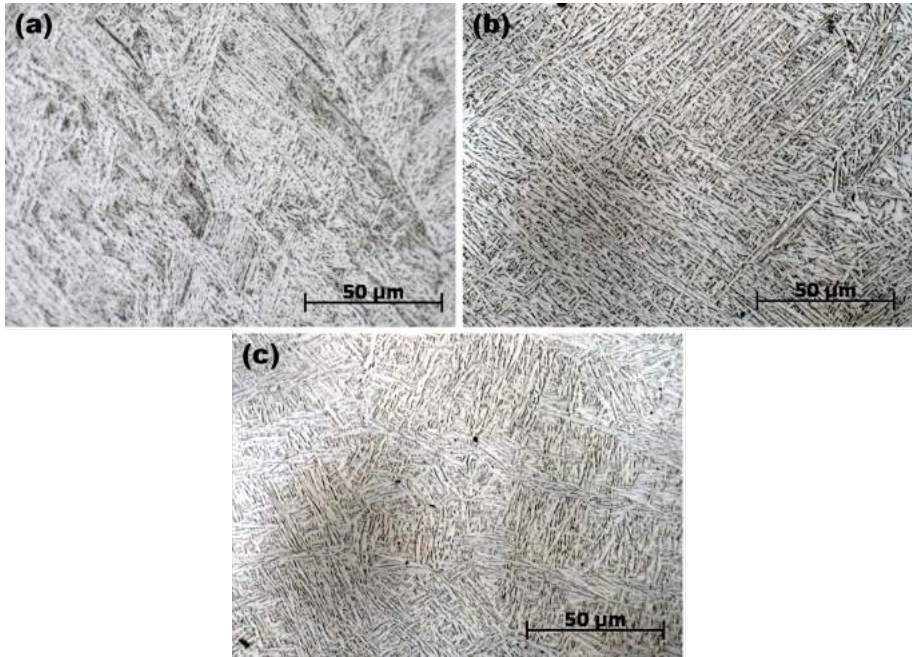


Figure 7.7: Microstructure of the SLM material after two hours at 850°C, followed by (a) furnace cooling, (b) air cooling and (c) water quenching. The α needle size is very similar for all three microstructures, illustrating the minor effect of cooling rate when treated below the β transus.

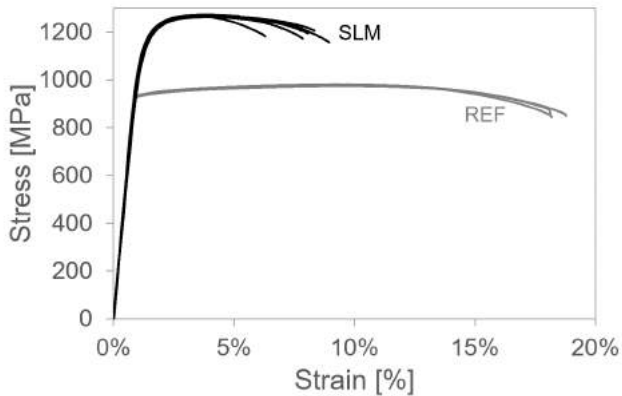


Figure 7.8: Stress-strain curves for as built SLM material and reference material.

Table 7.2: Mechanical properties of the SLM material after different heat treatments. Treatment six to eight are well known titanium heat treatments [46]. Samples for treatment three were built in a different batch in which building errors are present, which led to premature failure of the components.

Nr.	T [°C]	t [h]	Cooling		E [GPa]	σ_y [MPa]	UTS [MPa]	ϵ_{frac} [%]
			Rate					
1	540	5	WQ		113±30	1118±39	1223±52	5.4±2.0
2	850	2	FC		115±4	955±6	1004±6	12.8±1.4
3	850	5	FC		112±3	909±24	965±20	-
4	1015	0.5	AC		115±2	801±20	874±23	13.5±1.2
		followed by						
5	1020	2	FC		115±1	760±19	840±27	14.1±2.5
		2	FC					
6	705	3	AC		115±2	1026±35	1082±34	9.0±2.0
7	940	1	AC		116±2	899±27	948±27	13.6±0.3
		followed by						
		2	AC					
8	1015	0.5	AC		113±3	822±25	902±19	12.7±0.6
		followed by						
	730	2	AC					

An overview of results after heat treatments of the SLM material is given in Table 7.2. From these results, treatment two (2h at 850°C, followed by furnace cooling) and seven (1h at 940°C, followed by air cooling and tempering for 2h at 650°C and air cooling) seem to produce the best overall results. Both of these treatments reach temperatures relatively high in the $\alpha+\beta$ zone and maintain some α at high temperature. A previous study on increasing the ductility of Ti6Al4V produced by SLM [339] resulted in the same mechanical properties as were obtained after treatment two, but did not state the heat treatment parameters that were used. The microstructure, however, differed to some extent, with some globular α being reported.

The mechanical properties differ greatly after the various heat treatments. When plotting the maximum strain and yield stress as a function of the maximum heat treating temperature, as in Figure 7.9, certain tendencies can be noticed, regardless of the cooling rate. First, the fracture strain of the SLM material (hollow markers) goes up with rising maximum temperature, from 9.04±2.03% after heat treatment six (max. 705°C) to 14.06±2.53% after heat treatment five (max. 1020°C). The low fracture strain after treatment one could be due to the formation of very fine Ti₃Al precipitates, although these were not visible by SEM. These precipitates are known to occur for holding temperatures below 550°C [47].

In contrast to the results in Ref. [339] and [338], where yield stress and UTS values are reported to increase, the yield stress and UTS decrease after heat

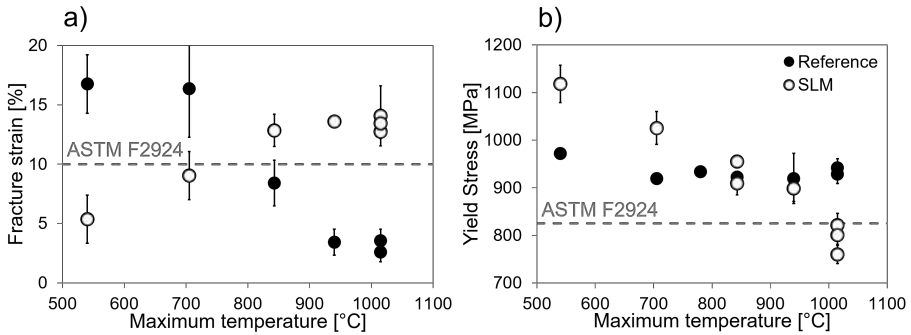


Figure 7.9: a) Fracture strain, and b) yield stress of the reference (full markers) and SLM material (hollow markers) in function of the maximum heat treating temperature. Results of all heat treatments are shown, regardless of cooling rate. All super-transus treatments used either AC or FC from the β range. The dashed line indicates minimum values required to meet ASTM standard F2924 for Ti6Al4V-ELI produced by powder bed fusion.

treatment, as was expected due to coarsening of the microstructure compared to the original fine α' martensite. The yield stress decreases from 1026 ± 35 MPa after heat treatment six to 760 ± 19 MPa after heat treatment five. The difference between the yield stress and the ultimate tensile strength, which is more than 200 MPa for as built SLM parts remains stable at about 60 MPa after heat treatment. This means that after heat treatment, the SLM material partially loses the ability to strengthen by deformation.

The response of the *reference material* to the heat treatments is completely different, indicated by the full markers in 7.9. It is clear that the yield stress does not change significantly after the different heat treatments. This is due to the competitive growth of both the α and β grains at high temperature, thus effectively hindering each other to grow. This leads to similar grain sizes after each treatment. Following the Hall-Petch relation, the yield stresses after the treatments do not differ largely. As illustrated in Figure 7.9a, the fracture strain of the reference material decreases drastically with rising heat treatment temperature. This is attributed to the development of a duplex microstructure, as will be discussed in section 7.4.

Standard heat treatments for Ti6Al4V were also performed on SLM produced parts, including the regular ‘mill anneal’ for cold deformed Ti6Al4V (treatment six, Table 7.2), duplex anneal (treatment seven) and a β anneal (treatment eight) [46]. β annealing normally leads to improved fracture toughness but a

lower ductility.

From the results in Table 7.2 and Figure 7.9, it can be seen that these treatments did not produce the expected results, neither for the SLM material nor for the equiaxed reference material. This is because these treatments are designed for specific purposes, starting from a specific microstructure, for example the heavily deformed structure before mill annealing. The reference material already consists of the equiaxed microstructure desired after treatment six, and the SLM material consists of a very fine, plate-like martensite rather than a heavily deformed mixture of α and β . The maximum temperature of treatment six is too low to lead to any significant changes. Treatment seven however is executed at high temperature below the β transus. As debated earlier in subsection 7.3.1, temperature is of major importance when treated below the β transus, which is why this treatment led to favorable results for SLM produced parts.

Considering the β anneal, the ductility of the SLM material is increased rather than decreased. β annealing an equiaxed microstructure transforms it to a lamellar $\alpha+\beta$, Widmanstätten α or martensitic α' microstructure, depending on the cooling rate. All of these structures have a lower ductility and because of the lamellar structure, the crack path is deviated during fracture. This leads to an increased fracture toughness [45]. However, during β annealing of SLM material, the α' structure transforms into a coarser lamellar structure, increasing rather than decreasing the ductility.

7.4 Discussion

Comparing the ductility of the reference material and the SLM material after heat treatment as in Figure 7.9a, the fracture strain of the SLM material increases with rising maximum temperature, whereas the reference material loses up to 86% of its ability to deform. This is most likely caused by the formation of a duplex structure in the reference material, in which the α stabilizing alloying elements are mostly located in the primary α grains. The α phase in the lamellar section is then relatively poor in alloying elements, causing a great difference in strength between the α and β lamellae. This causes rapid formation of cracks and early failure of the material [47, 49]. Because there are no equiaxed α grains, this segregation effect does not occur in the SLM material.

For the *reference material*, the maximum heat treating temperature determines only the final lamellar $\alpha+\beta$ fraction when treated below the β transus. Since the equilibrium β fraction is higher at temperatures closer to the β transus, and these equiaxed β grains transform to lamellar $\alpha+\beta$ upon cooling, a higher

heat treating temperature will result in a larger lamellar fraction at room temperature. The lamellar spacing is determined by the cooling rate, with higher cooling rates resulting in a finer lamellar spacing.

The final spacing of the microstructural features in the *SLM material* is not primarily dependent on the cooling rate, but on the maximum temperature for heat treatments in the intermediate $\alpha+\beta$ range. The SLM material originally consists of fine α' needles. When heated, α phase is nucleated along the α' boundaries and vanadium atoms are expelled, leading to the formation of β at the α phase boundaries [340]. At high temperatures, only a fraction of the original amount of nuclei is still present, since the equilibrium α fraction is lower, but still considerable (e.g. 73% at 850°C, 23% at 950°C [330,333]). Originating from a fine α' microstructure, these α phase nuclei are scattered at high temperature. For higher temperatures, less nuclei are present and they can coarsen to a greater extent before interaction with other plates will occur.

Thus, for intermediate temperatures in the $\alpha+\beta$ range, the size of the α needles at room temperature is mostly determined by the number of α needles at high temperature, which in turn is closely related to the temperature. At high temperatures in the $\alpha+\beta$ range, the effect of cooling rate becomes more distinct, with furnace cooling leading to a coarser microstructure.

From comparison between the microstructure of the *SLM material* treated below and above the β transus it is clear that the SLM footprint is erased for temperatures above the β transus. During heating, the SLM material gradually transforms back to the original columnar β grains. However, these columnar grains are no longer present after cooling from above the β transus. Instead, the microstructure consists of α colonies inside large, semi-equiaxed, previous β grains. Following the Burgers relation, a Widmanstätten structure is formed due to the preferential growth of the α phase parallel to the (110) family of crystallographic planes of the β phase [332,334] for intermediate cooling rates between air cooling and furnace cooling [46].

Because growth along these planes is faster, the α phase is formed as flat plates. The large difference in size and shape of the transformed β grains after treatment above 1000°C compared to the original columnar β grains present in as built SLM parts indicates extensive grain growth at temperatures above the β transus, up to the point where the columnar grains resemble a coarse equiaxed microstructure with large grains several millimeters long and approximately 620 μm wide. This is illustrated by Figure 7.10, where EBSD orientation maps of the microstructure after treatments below (a) and above (b) the β transus are shown. The black lines are intensified drawings of the prior β grain boundaries. Notice that the scales of both images are different as well.

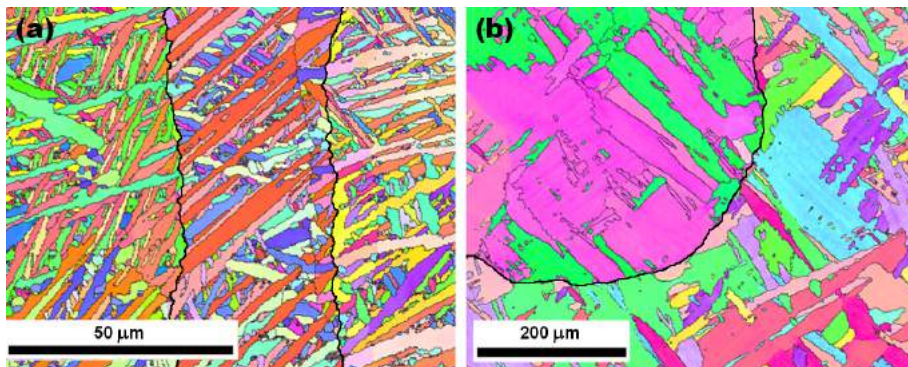


Figure 7.10: EBSD orientation maps of a) SLM material after two hours at 850°C, followed by furnace cooling. b) SLM material after half an hour at 1020°C, followed by two hours at 730°C and air cooling. Contrast is provided by the different orientations of the α phase, while the β phase is present as a thin layer between the α phase. Notice the different scale. The build direction for both images is vertical.

During solidification, the bcc β phase preferentially grows in the $\langle 100 \rangle$ direction, giving rise to the long, columnar prior β grains as described by Thijs *et al.* [341] and Kobryn *et al.* [342]. The $\langle 100 \rangle$ direction of each of these columnar grains is thus oriented quasi parallel to the build direction, and the rotation of the grain around this direction is considered to be random, causing the presence of a fiber-like texture. Due to the fast cooling, the β phase then transforms to the α' phase according to the Burgers relation. The texture of the parent β phase is transmitted to a texture of the α phase, as can be seen in the $\{10\bar{1}2\}$ pole figure of the top view of as built SLM material in Figure 7.11a.

When treated above the β transus, the β grains in the SLM material will grow and the texture is maintained, as seen in the pole figure in Figure 7.11b. The texture after homogenization in the β field is not as distinguished because of the extremely large grain sizes after prolonged treatment above the β transus, causing large intensity peaks for one individual grain.

7.5 Conclusion

Several heat treatments were performed on Ti6Al4V produced by SLM with an original α' microstructure. The influence of temperature, time and cooling rate were distinguished. At temperatures below the β transus, the mixture of α

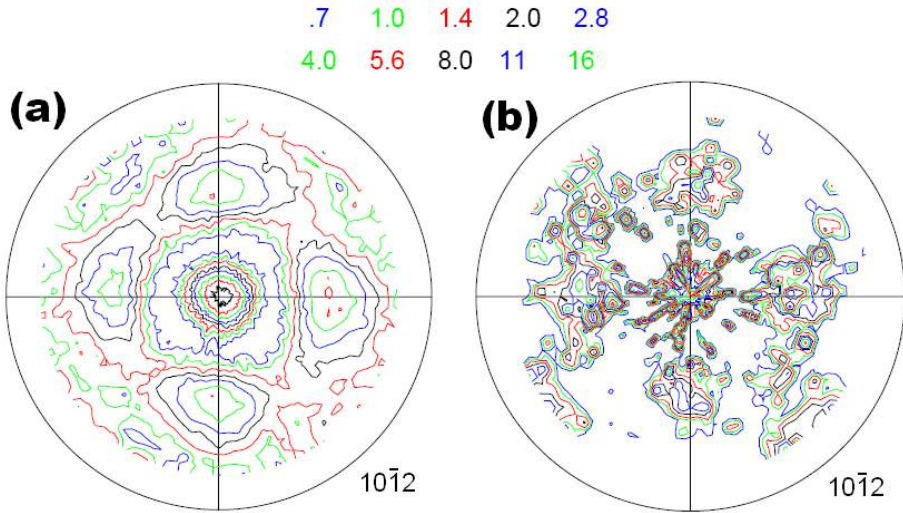


Figure 7.11: $\{10\bar{1}2\}$ pole figures of the hexagonal phase in (a) the as built SLM material and (b) the SLM material heat treated above the β transus, for 20 hours at 1040°C , followed by furnace cooling. In (a), the texture is present in the α' phase which has a similar crystal lattice as the α phase. In (b) the texture in the α phase is shown.

and β phase prevents grain growth and the original, columnar prior β grains remain visible after cooling. The width of the α plates after heat treatment is mainly dependent on the maximum temperature for sub-transus treatments, and primarily dependent on the cooling rate for super-transus treatments. The residence time and cooling rate have a smaller influence for sub-transus treatments, although their influence increases when temperatures are closer to the β transus. When treated above the β transus, the columnar β grains grow extensively to form large, semi-equiaxed β grains. For FC, AC and WQ samples, the β grains then transform to lamellar $\alpha+\beta$, α -Widmanstätten colonies or α' martensite, respectively. The residence time influences the final dimensions of the transformed β grains.

Mechanical properties are very much dependent on the maximum heat treatment temperature. With rising maximum temperature, σ_y and UTS decline and the fracture strain rises because of the transformation of the fine α' plates to a more coarse mixture of α and β . Overall best results are obtained after two hours at 850°C , followed by furnace cooling, or one hour at 940°C , air cooling and tempering for two hours at 650°C followed by air cooling. For these heat treatments, the results for all properties are well above those required

to meet ASTM standard F2924. The importance of the initial microstructure cannot be stressed enough. Due to the very fine martensite, the kinetics are completely different as compared to treatment of equiaxed or heavily deformed microstructures. Consequently, application of standard heat treatments shows that these treatments do not lead to the usual or expected results. Due to the specific process conditions and hence specific microstructure, SLM produced parts need to be treated differently than bulk alloy parts.

For SLM produced Ti6Al4V parts, heat treating at intermediate to high temperatures below the β transus, followed by furnace cooling proved to be optimal for an overall optimization of tensile properties, with fracture strains safely above the prescribed standards and yield stress and UTS levels close to 1GPa.

Chapter 8

Effect of residual stress on mechanical behavior

This intention of this work was not only to characterize the RS build up during the SLM process, but also to study the effect that it can have. Apart from the macroscopic deformations it causes, which have been used in previous chapters to study the stresses, mechanical properties are also affected by the RS. The residual stresses are superposed on applied loads. This chapter investigates the effect on dynamic properties, in particular the fatigue crack growth rate (FCGR).

The samples for this chapter were produced by 3D Systems Layerwise, and the FCGR and fracture toughness (FT) were determined by V. Cain. A summarized version of this chapter has been published in the journal article below:

- Vrancken, B., Cain, V., Knutsen, R., Van Humbeeck, J. (2014). Residual stress via the contour method in compact tension specimens produced via Selective Laser Melting. *Scripta Materialia*, 87, 29-32.

8.1 Introduction

Chapter 3, subsection 3.1.4 discusses the influence of residual stress on the FCGR. Superposition of residual stresses onto the applied dynamic loads does not change ΔK values, but does change the mean applied stress, and the stress ratio R [184]. Residual stresses therefore, are thought to have little influence on

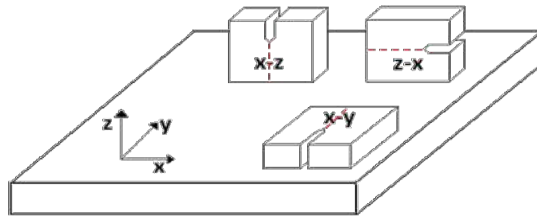


Figure 8.1: Sample orientations of the XZ, ZX and XY compact tension specimens. The dashed lines indicate the direction in which the crack would normally propagate, but also indicate the plane along which the samples were cut for the contour method.

the Paris regime, except when the residual stresses lead to crack closure, and therefore introduce compressive effects at the crack tip. On the other hand, the threshold and rupture values are greatly affected by the mean stress [180], and thus also by residual stresses.

In addition, the FCGR behavior of Ti6Al4V produced by SLM was described in detail in chapter 2, subsection 2.3.1. In summary, the FCGR of AM produced Ti6Al4V has a lower threshold value at which crack growth becomes detectable, and a lower maximum ΔK_{max} at which part failure occurs when compared to conventional material [71, 72, 76]. The Paris regime, on the other hand, exhibits a more gradual slope, meaning the FCGR does not increase as quick as in conventional material. In testing the fatigue properties, Leuders *et al.* [76] also hypothesized that while crack initiation is governed by local defects in the material, crack propagation was highly dependent on residual stresses. The evidence provided, however was scarce, and the residual stress measurements were performed at a different location than the crack growth.

8.2 Materials and Methods

Nomenclature of ASTM Standard E399 was used in labeling the specimens described below, which were made of Grade 5 Ti6Al4V. The XZ and ZX oriented samples were produced individually. The XY oriented samples were produced in a stack, after which individual samples were sliced using EDM. The XY sample used in this paper came from the center of the stack, thus not from the bottom nor the top. Sample orientations are shown in Figure 8.1. Compact tension specimen dimensions are according ASTM Standard E399.

A detailed review of the contour method and its application are given in chapter 4. For this chapter, duration of the cutting was about 15 minutes, resulting in a cut plane of 20mm by 12.5mm. The deformation of both cut planes was measured four times and averaged before further data processing. Each surface was measured using a 0.4mm point spacing, resulting in a 49 by 31 grid of 1519 data points.

8.3 Results

The average surface profiles are shown in Figure 8.2a-c. The peak-to-valley distance for the XY and XZ specimens is around $15\mu\text{m}$, while it is over $40\mu\text{m}$ for the ZX specimen. Positive (red) deformations indicate the cut surface has moved outwards, while negative (blue) values are a recession of the cut surface. Outward movements of the cut surface are caused by the relaxation of compressive stresses that push the material outwards, while tensile stresses pull the material back. The sign of the deformations are therefore opposite to the sign of the stresses that caused them.

These surfaces, although already interpolated to a common grid, are still rough and would lead to sharp and unrealistic stress jumps if applied to a stress model. The quadratic spline shown in Figure 8.2d smooths the data in Figure 8.2c enough to remove local variations, but without oversmoothing that would result in an overall loss in accuracy regarding the magnitude of the RS and the shape of the RS distribution.

In Figure 8.3a, both halves of the fracture surfaces of a representative XY oriented sample after fracture toughness testing are shown. The bottom part of the surface consists of the notch that was made using EDM, and is not an actual part of the fracture surface. Above, a pre-crack is grown to approximately 7 mm in length using cyclic fatigue cracking, as dictated by ASTM standard E399. Afterwards, the sample is loaded statically with increasing force until fracture occurs. The pre-crack front is indicated by the red dashed line in the left fracture surface for clarity. The front is relatively straight. Additionally, Figure 8.3a also shows the residual stress map of the stresses perpendicular to the fracture surface. Peculiarly, the stresses are tensile in the center, balanced by compression at the top and bottom edge. The maximum stress values are well below the yield stress, which equals 1100 MPa or higher for Grade 5 Ti6Al4V produced via SLM. Furthermore, the stress distribution appears to be slightly elongated in the building direction.

The fracture surface and stress plot for the XZ sample are shown in Figure 8.3b. As with the XY sample, stresses are low compared to the yield stress, and the

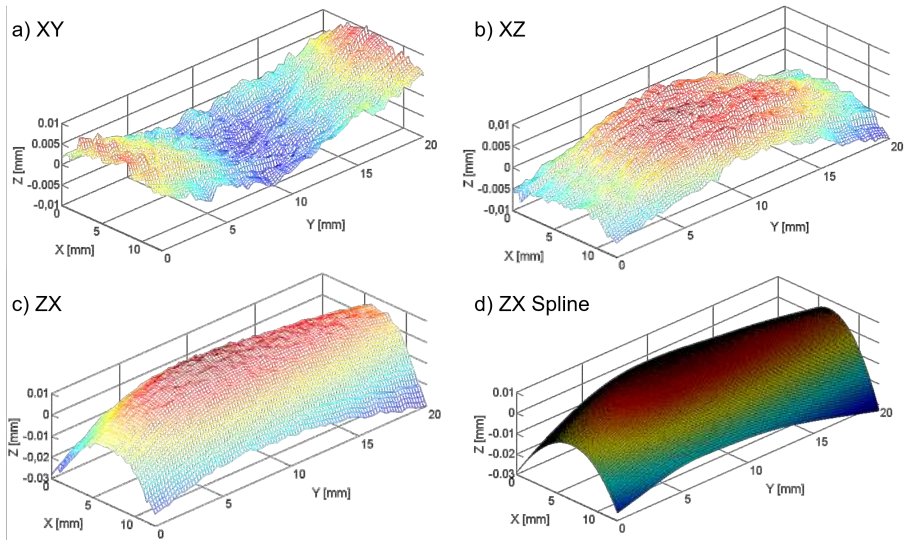


Figure 8.2: (a-c) Averaged surface contour for the three samples. d) Fitted quadratic spline of the contour data shown in (c).

stress distribution appears elongated along the building direction. Furthermore, the pre-crack front is again relatively straight. One major difference compared to the XY sample is that the stresses are compressive in the center, balanced by tensile stresses at the edges, as was expected.

The results for the ZX sample, shown in Figure 8.3c, are remarkable. The fracture surfaces clearly show that the pre-crack is not straight but curved, with the crack extending the furthest along the edges of the specimen. Moreover, the stress measurement revealed that large residual stresses are present, oriented along the building (vertical) direction, which is out of plane in the image. These stresses are much larger than those in the XY and XZ sample, where the measured stresses are in the horizontal plane. This is in agreement with the previous measurements performed by Rangaswamy [219], who indicated that the vertical stresses are dominant over the horizontal stresses. The stress distribution shows compressive stresses in the center of the specimen. The zone of compressive stresses occupies the majority of the surface area and extends outwards towards the middle of the edge where the notch was made. Large tensile stresses at the other edges balance the compressive stresses. While caution is advised in using stress values at the edges when using the contour method, it is clear that these stresses are close to the yield stress, specifically at the left and right ends of the notch edge at the bottom.

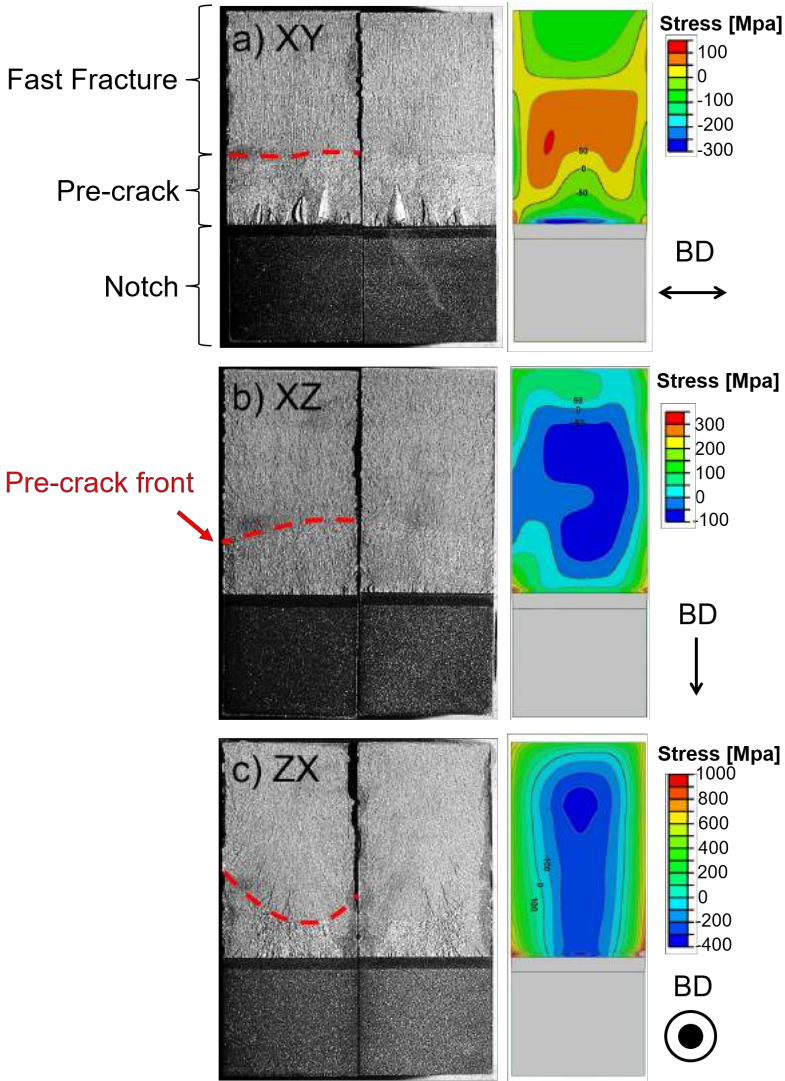


Figure 8.3: Representative fracture surfaces for all three orientations. The surface can be divided in three parts: The notch that was precut using wire EDM and is not an actual part of the fracture surface, the pre-crack (front indicated by dashed red line), and the fast fracture zone. On the right: 2D residual stress plots obtained using the contour method, for a) the XY specimen, b) the XZ specimen and c) the ZX specimen.

8.4 Discussion

The residual stress distributions and magnitudes provide a surprisingly clear insight in the behavior of the material during fabrication of the pre-crack and during fatigue crack growth rate (FCGR) testing. First, the pre-crack fronts of the XY and XZ sample are both relatively straight. The residual stresses inside those samples are fairly low compared to the yield stress. Moreover, at the notch where the pre-crack is initiated, the maximum and minimum stresses only differ by roughly 300MPa. As the pre-crack grows, the residual stress distribution will be readjusted, and the difference will only decrease. This means that, when applying load to grow the pre-crack, the whole crack front will experience a relatively uniform stress and the crack will grow more or less straight. Because of the compressive stresses in the XY sample, higher maximum loads were needed to avoid crack closure phenomena and to grow the pre-crack, with initial loads of 8, 9 and 9kN for the three XY samples versus 6, 7 and 7kN for the XZ samples.

For the ZX sample, however, the maximum and minimum stress at the notch edge differ by more than 1GPa. This means that one part of the crack front could be experiencing tensile stresses high enough to cause crack growth, while other parts experience almost no stress, or even compressive stresses that cause crack closure. This will cause the crack to grow faster along the sides and leads to the curved shape of the pre-crack, visible in Figure 8.3c. Overall, at 5kN, the initial maximum stress level to grow the pre-crack is lower than that for the XY and XZ samples.

Second, the effect of the stresses at the crack front are also clearly visible in results obtained during FCGR testing. Samples for FCGR tests are only half as thick as fracture toughness samples (6.25mm versus 12.5mm), but the stress distribution is likely to be similar. While the ZX sample clearly stands out from the other two regarding magnitude of the stresses, the XY sample is distinguished by the sign of the stresses. The XZ and ZX sample both have compressive stresses in the center and tensile stresses along the edges. In the XY sample, the stresses at the notch are compressive. The stress the material experiences at the notch or crack tip will therefore be lower than the applied stress, causing the crack to grow slower because of crack closure. This is visible in Figure 8.4 [72], where the FCGR of the as built (AB) XY sample (Figure 8.4a) can be compared to that of as built XZ (Figure 8.4b) and ZX (Figure 8.4c) samples. Further evidence of the influence of the residual stress on crack growth rates is found in the FCGR of stress relieved (SR) samples. In the XY sample, this relieves the compressive stresses that would slow down crack growth, and therefore, the FCGR is worse after stress relieving. On the other hand, relief of the tensile stresses in the ZX and XZ sample lowers the FCGR.

A further improvement compared to the stress relieved state is obtained by heat treatment (HT) by altering the microstructure. However, this is the topic of a different investigation and is discussed elsewhere [72].

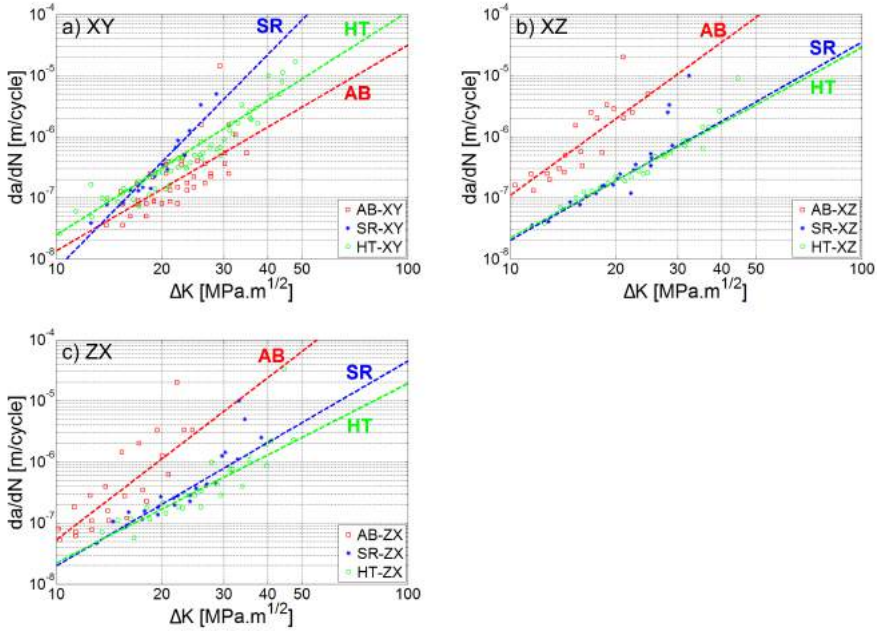


Figure 8.4: FCGR curves for all three orientations in the as built (AB) condition, after stress relief at 650°C (SR) and after heat treatment (HT) at 890°C . Note that in a), the XY orientation shows an increased FCGR after stress relieving, while the XZ and ZX orientation experience a decrease in FCGR after stress relief [72].

8.5 Conclusion

Three, differently oriented Ti6Al4V compact tension specimens destined for fracture toughness testing were sectioned along the plane in which the crack would normally grow. The deformations of the cut planes were used to determine the residual stresses acting perpendicular to this plane.

The residual stress was mainly oriented along the building direction. Furthermore, the influence of the residual stress on the fracture behavior during fracture

toughness testing and FCGR testing is evident. The shape of the pre-crack is clearly influenced by the internal stress configuration, as is the FCGR. Further corroboration of the influence of the residual stresses is found in the distinct effect of a stress relief treatment in the FCGR behavior.

Chapter 9

Conclusions and future work

In Selective Laser Melting, a high power laser is used to melt and fuse powder in a localized, moving melt pool. This melt pool is surrounded by a large volume of previously solidified material or a base plate which act as a heat sink, thereby leading to high solidification rates and large, directional thermal gradients. The thermal shrinkage of the hot, recently solidified material is restricted by the cold substrate on which they are deposited, which introduces thermal residual stress. Geometrically complex structures are thus built up from 1D scan vectors, to 2D thin layers, to a 3D part, as are the residual stresses. They limit the number of materials that are readily processed by SLM, as well as limit the size of producible parts.

This research attempted to understand how the process parameters and material properties affect residual stress. Furthermore, the residual stresses in compact tension specimens were linked with the anisotropic fatigue crack growth behavior of the material. Two methods to optimize the properties of SLM produced parts were investigated, namely application of post-process heat treatments, as well as tailoring the alloy composition. Ti6Al4V served as the research material for most of this work, but eight other materials were also investigated to study the influence of the material properties.

If there is anything to take away from this work, it is that the material, process and properties are inextricably linked with each other. It is difficult to discern clear correlations between the residual stress and any variable, be it a material property or process parameter. Nevertheless, this resulted in a number of conclusions, listed below.

- During SLM, residual stress is introduced by the restricted, horizontal

thermal shrinkage of the last deposited layer, which is anisotropic due to the difference in thermal contraction in the direction of the scan vectors and the contraction perpendicular to it. This leads to a horizontal tensile stress in the upper layer. Addition of more layers on top with their own horizontal tensile stresses slightly compresses the now buried layers and lowers the magnitude of the tensile stress therein. Addition of each new layer therefore tends to decrease the horizontal stress in the material below. Each layer, however, contributes to the build up of vertical tensile stresses along the side surfaces as the horizontal tensile stresses induce a curl-up effect that is restricted by fixation to the base plate. If enough layers are added, this eventually causes the vertical stress to become bigger than the horizontal stress. Removal from the base plate results in significant deformation of the part, unless the geometry is stiff enough to withstand the curl-up effect. Stress redistribution creates a part with tensile stresses along all outer surfaces, and compressive stresses within.

- Fluctuating laser powers, Plateau-Rayleigh instabilities and a heterogeneous powder bed cause stochastic variations in the melt pool size and dimensions. As a result, there is a large spread on the local stresses and correlations between the residual stress and the process parameter values are weak, but are summarized as follows in ranking order of importance:
 1. The effect of preheating is twofold. First, it reduces overall thermal gradients, which allows more time for the material in the HAZ to undergo metallurgical changes. Examples are the decomposition of α' martensite in Ti6Al4V to an $\alpha+\alpha'+\beta$ structure, or the increased formation of carbides in M2 high speed steel. Generally, lowering the thermal gradients also acts to lower the residual stress, but the main stress-reducing effect of preheating is attributed to the lower yield stress at higher temperatures.
 2. Apart from preheating, the layer thickness had the strongest influence on residual stress in this work, but with mixed results. There were differences between different batches of parts, and anomalous behavior for one layer thickness per batch. Overall, there is an indication that thicker layers increase the residual stress, which is attributed to the lack of heat accumulation. Allowing heat to accumulate and temperatures to rise during the process is equivalent to using preheating.
 3. Increasing the scan speed elongates the melt pool, which increases the magnitude and anisotropy of the residual stress in one layer. However, this effect is only present when increasing from low to moderate scan speeds. Above a threshold scan speed, the anisotropy and magnitude of the residual stress are no longer increased. Furthermore, high scan

speeds increase the solidification rate, increases thermal gradients and decreases the overall heat input.

4. The higher heat input by using high laser powers slightly lowers thermal gradients and allows for a higher temperature increase during the process, but this effect is subordinate to the effects described above.
- Material specific phenomena override the influence of general material properties, which makes it hard or even impossible to find correlations between the general material properties and residual stress. Examples that have been encountered in this research, and in literature are:
 1. Formation of precipitates: Generally, precipitates strengthen, but embrittle the material, but plastic yielding is an inevitable and necessary coping mechanism to handle the residual stresses developed during SLM. In M2 high speed steel, an increasing amount of carbides with slower scan speeds increased the amount of macrocracks. In some nickel based superalloys, such as Inconel738LC, γ' precipitates will contribute to the formation of microcracks, and should thus be avoided as much as possible.
 2. Ductile-to-Brittle Transition: Thought to be the main reason for microcracks in W parts, the stress built up above the DBTT cannot be accommodated in the brittle state. relative to its melting point, the DBTT in W is close to room temperature, and residual stress developed below the DBTT is limited, and would also lead to further microcracking.
 3. Low temperature allotropic transformations: These types of (displacive) transformations are often accompanied by a volume expansion of the crystal structure, as in 18Ni300 maraging steel and H13 tool steel. This reduces the tensile residual stresses. Because they occur at a low temperature, any new build-up of stresses during further cooling is limited.
 4. Solidification Cracking: Some materials, such as Hastelloy C-276, Hastelloy X and Al7075, are susceptible to solidification cracking. Because these cracks are already formed during solidification, extensive residual stress can still be developed in the solid state. It is possible that the solidification cracks grow under the influence of the residual stress.

The result is that it is hard to transfer knowledge attained on SLM of one material to another. Moreover, these phenomena also change the effect of stress-reducing parameter sets discussed in the paragraph above.

- Post process heat treatments can help to improve the mechanical properties of parts produced by SLM. Coming of the base plate, these parts are often strong, but are riddled with residual stress-induced dislocations and in general, have a metastable microstructure and lower ductility than is desired. Because the microstructure obtained after SLM is unique, existing heat treatments must be adapted or even completely redesigned for SLM to create the desired response. For Ti6Al4V, this work showed that a heat treatment moderately high in the $\alpha+\beta$ range, combined with moderate cooling rates, leads to a significant improvement in static mechanical properties.
- The presented results highlight the capabilities of SLM to process powder mixtures of different materials. This allows tailoring of the microstructure or producing material with superior properties, or can facilitate easier processing of certain materials via AM, for instance by adding alloying elements that toughen the material, avoid unwanted metallurgical phenomena and reduce problems with thermal stresses. Just as alloys were previously designed for other processing techniques such as casting or forging, purposeful formulation of alloys for AM may greatly increase the AM material pallet.
- Anisotropy of the residual stresses is a strong contributor to the anisotropy of the mechanical behavior, in addition to the morphological and crystallographic texture. This may be used to optimize designs for AM and in choosing a suitable part build orientation. This was illustrated in this work by the correlation between 2D residual stress maps and crack growth behavior of compact tension specimens.

Suggestions for future work

Despite all the research that has already been conducted, SLM is still production technique in development. It is hard for research into the correlation between process parameters and material properties to keep up with the technological advances of the process itself. As the process capabilities expand, opportunities for conducting research are therefore only expanding.

The process parameters that were varied in this work are limited to the laser power, scan speed and layer thickness. Even though the sample set consisted of more than 100 samples, variability of the residual stress meant that the correlations found in this work cannot be supported by strong, quantitative relations. Moreover, there are numerous other tunable parameters of which the influence remains unknown. One example is the offset of the focal point of the laser with the powder bed, which was used by Xu *et al.* [41] to induce martensite decomposition in Ti6Al4V, which leads to the belief that it may

also have a beneficial effect on reducing residual stress. The search for optimal RS-reducing parameters is not over.

Apart from an overall stress-reducing effect, preheating has already shown to be an interesting parameter to shape the microstructure. It adds another dimension to the process window that has only recently been opened up for exploration. Not only can it assist in obtaining fully dense parts, it can also help to change the microstructure developed during the process, for example via precipitation, decomposition of metastable phase or by avoiding the formation of metastable phases all together.

The geometry of samples produced in this work was limited to simple, cuboid shapes or specific designs to incur measurable deformations. One of the major advantages of SLM is that it allows production of complex or intricate geometric shapes. An example are thin walls, which are known to warp or buckle due to residual stresses. Additionally, abrupt changes in cross section, internal cavities or geometries with a high aspect ratio are other examples of geometrical features that are suspected to be affected.

A powerful tool in answering the questions above is modeling. In an ideal world, one step of the AM process preparation would be that the designer imports the sliced and hatched model of the part to be built, and that a coupled thermo-mechanical model would predict the stress distribution that would be generated. As this work has shown, RS is built up track by track, layer by layer. This model should therefore span multiple scales, from the micro-scale of the melt pool to capture the influence of process parameters as the scan speed and laser power, to the meso-scale of the individual layers (influence of the scan strategy), to the macro-scale of the part. Unfortunately, a model of such complexity is far from reach and it may take decades before it is feasible to run within acceptable time spans. For now, modeling should focus on one dimensional magnitude and try to predict effects that occur at that scale.

The process is not the only variable in the process-material interactions. The material itself largely dictates if, and how residual stresses cause problems. This work has shown that this response is very material-specific, and transfer of knowledge from one material to another is limited. Moreover, the composition of some alloys is not suitable for processing by SLM. The composition of existing alloys can either be changed, or new alloys can be designed based on a fundamental approach.

On a related note, powders used in SLM are usually pre-alloyed, but it could be interesting if powder blends of elemental powders could be used as well. Powder blends, however, are inherently heterogeneous and only a handful of particles are melted at a given time. Therefore, the homogeneity of material processed

by powder blends is questionable, but worthy of extra attention.

Lastly, the microstructure after SLM is the result of local rapid solidification and cooling, and is therefore metastable and unique. This microstructure reacts differently to high temperatures than that of the same material processed via another technique. For example, a stress relieve at 650°C will cause decomposition of the martensite in Ti6Al4V, while it does not affect a mixture of $\alpha+\beta$. A large amount of work is to be performed to design bespoke heat treatments for material processed by SLM to obtain the desired properties.

Appendix A

Appendices

A.1 Static mechanical properties of AM Ti6Al4V

Table A.1: Static tensile properties of Ti6Al4V reported in literature, for different AM techniques, heat treatments and build orientations. * =flat. ° =polished

	Process	Cond.	Orient.	σ_y MPa	UTS MPa	ϵ_{frac} %
ASTM F2924				>825	>895	>10
Equiaxed [316]				960±10	1006±10	18.4±0.9
Brandl [49]	Wire LMD	AB		820	895	4
		SR600	Hor.	875	940	7.5
		HT843		820	900	12.5
		AB		790	870	11
		SR600	Ver.	845	940	11
		HT843		810	880	11
Brandl [49]	Wire Arc MD	AB		890	965	8
		SR600	Hor.	915	980	7
		HT843		900	965	13.5
		AB		860	940	16.5
		SR600	Ver.	890	975	12
		HT843		855	930	20.5
Carroll [51]	LMD	AB	Hor.	959	1064	11
			Ver.	959	1064	14
Yu [343]	LMD	AB	Hor.	976±24	1099±2	4.9±0.1
Murr [344]	EBM	AB	Ver.	1150	1200	25
			Ver.	1100	1150	16
Svensson [345]	EBM	AB	Hor.	910	997	13.1
			Ver.	912	986	14.2
Hrabe [52]	EBM	AB	Hor.	975±5	1024±5	12.2±1.4
			Ver.	972±8	1020±14	8.0±3.1

Table A.1 - continued from previous page

	Process	Cond.	Orient.	σ_y MPa	UTS MPa	ϵ_{frac} %
Koike [346]	EBM	AB	Ver.	720	780	2.2
	SLM			850	920	7
Facchini [339]	EBM	AB	Ver.	830±5	915±10	13.1±0.4
		AB		990±5	1095±10	8.1±0.3
	SLM	AB	Hor.	1040±10	1140±10	8.2±0.3
		HT	Ver.	835±5	915±5	10.6±0.6
		HT		870±15	990±15	11.0±0.5
Edwards [66]	SLM	AB	Hor.	910±10	1035±39	3.3±0.8
		AB	Hor.	1093±94	1279±13	6±0.7
Cain [72]	SLM	SR650	Ver.	1125±22	1216±8	6±0.4
			Hor.	1145±17	1187±10	7±2.7
	HT890	Ver.	Hor.	1132±13	1156±13	8±0.4
			Hor.	973±8	996±10	3±0.4
		Hor.	Ver.	964±7	998±14	6±2
			Ver.	900	1020	7.5
Wycisk [68]	SLM	AB	45°	1075±75	1199±49	7.6±0.5
		AB	Hor.*	978±5	1143±6	11.8±0.5
Simonelli [63]	SLM	HT730	Ver.	967±10	1117±3	8.9±0.4
			Hor.*	974±7	1065±21	7.0±0.5
	Ver.	Hor.	958±6	1057±8	9.6±0.9	
		Ver.	937±9	1052±11	7.6±0.5	

Table A.1 - continued from previous page

Process	Cond.	Orient.	σ_y MPa	UTS MPa	ϵ_{frac} %
Kasperovich [61]	AB		664-802	1040-1062	11.3-12.7
	AB°		984-988	1151-1157	10.2-11.3
	HT700°	Ver.	1045-1054	1115-1116	9.5-12.3
	HT900°		905-911	987-989	7.4-12.5
Leuders [64]	HIP°		883-888	973-974	18.5-19.4
	AB			1315±16	4±1.2
	HT800			1228±32	8±1.5
	HT1050	Ver.		986±45	13.8±0.8
Qiu [65]	HIP920			1089±26	13.8±1.3
	HIP1050			1007±15	13.5±0.7
	AB	Hor.	1000-1100	1200-1300	4-6
	HIP	Ver.	1000-1100	1150-1200	7-10
Becker [73]	HIP	Hor.	925-1000	1000-1100	12-13
	AB	Ver.	900	1000	15-18
	HIP	Hor.		1155	4.1
	AB	Ver.		960	8.5
Vilaro [347]	AB	Hor.	1137±20	1206±8	7.6±2
	HT700FC	Ver.	962±47	1166±25	1.7±0.3
	HT950FC	Hor.	965±16	1046±6	9.5±1
	HT1050WQ	Ver.	900±101	1000±53	1.9±0.8
Vilaro [347]	HIP	Hor.	944±8	1036±30	8.5±1
	HT950FC	Ver.	925±14	1040±4	7.5±2
	HT1050WQ	Hor.	913±7	1019±11	8.9±1
	HIP	Ver.	836±64	951±55	7.9±2

Table A.1 - continued from previous page

Process	Cond.	Orient.	σ_y MPa	UTS MPa	ϵ_{frac} %
Thone [348]	AB			1080	1.6
	HT750			1062	3.7
	HT800	Ver.		1040	5.1
	HT850			1009	5.2
	HT950			972	10.1
Xu [41]	HT1050			945	11.6
	AB°		1106±6	1240	11.4±0.4

A.2 $\text{Sin}^2\psi$ -curves for the XRD results discussed in subsection 5.1.2

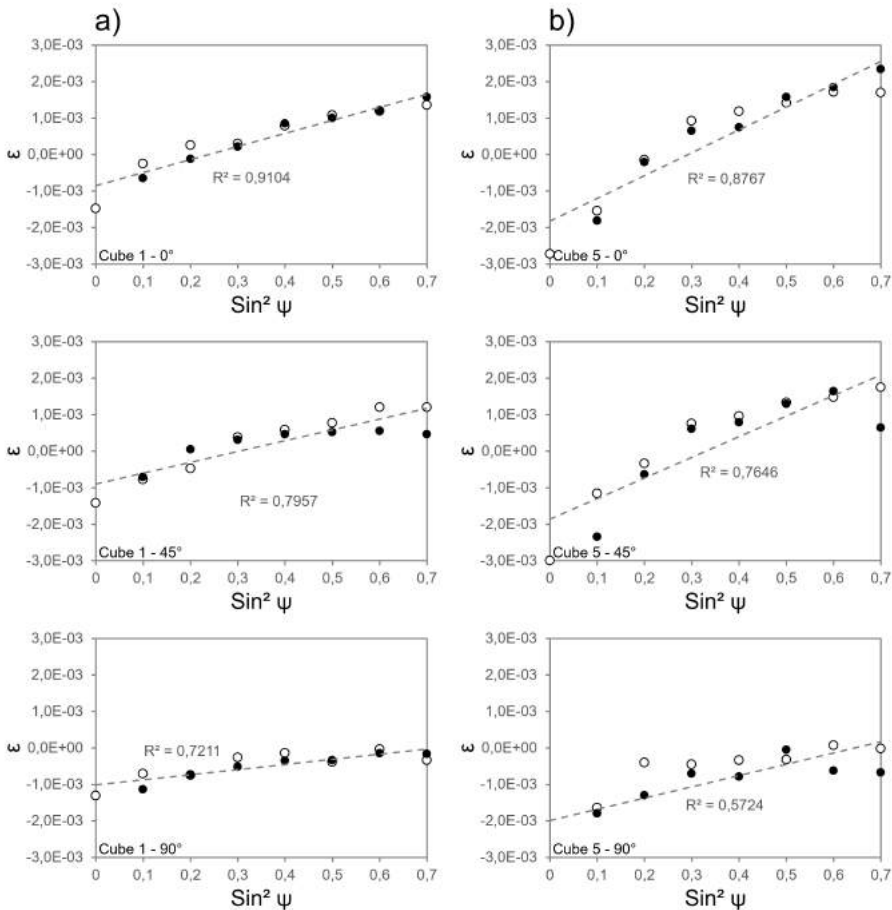


Figure A.1: $\text{Sin}^2\psi$ -curves as measured on the Ti6Al4V cubes a) 1 and b) 5, for $\phi=0^\circ$ (top graph), $\phi=45^\circ$ (middle graph) and $\phi=90^\circ$ (bottom graph). Measurement points for negative ψ values are indicated by hollow markers, and those for positive ψ values with full markers. These curves are representative for all curves obtained on Ti6Al4V samples in this work.

A.3 $Sin^2\psi$ -curves for the XRD results reported in Table 6.4

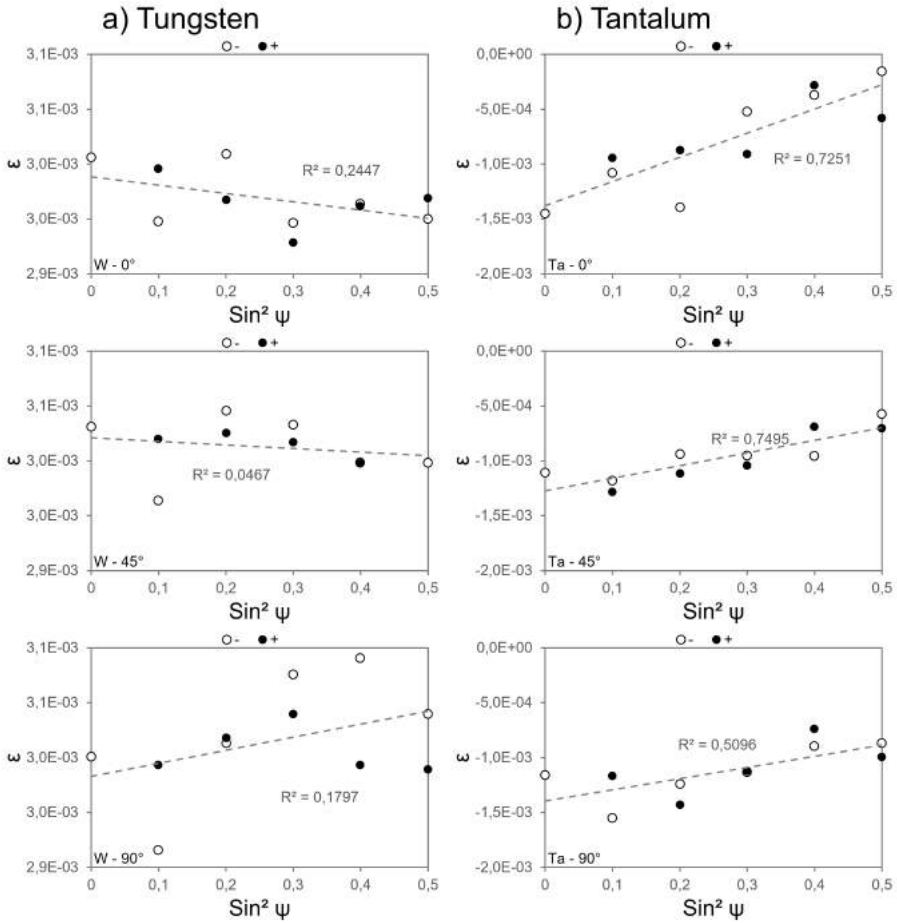


Figure A.2: $Sin^2\psi$ -curves for $\phi=0^\circ$ (top graph), $\phi=45^\circ$ (middle graph) and $\phi=90^\circ$ (bottom graph), as measured on the cubes made of (a) tungsten, (b) tantalum, (c) Inconel 718, (d) Hastelloy C-276, (e) 316L, (f) Ti Grade 1, (g) 18Ni300 maraging steel and (h) AlSi10Mg. Measurement points for negative ψ values are indicated by hollow markers, and those for positive ψ values with full markers.

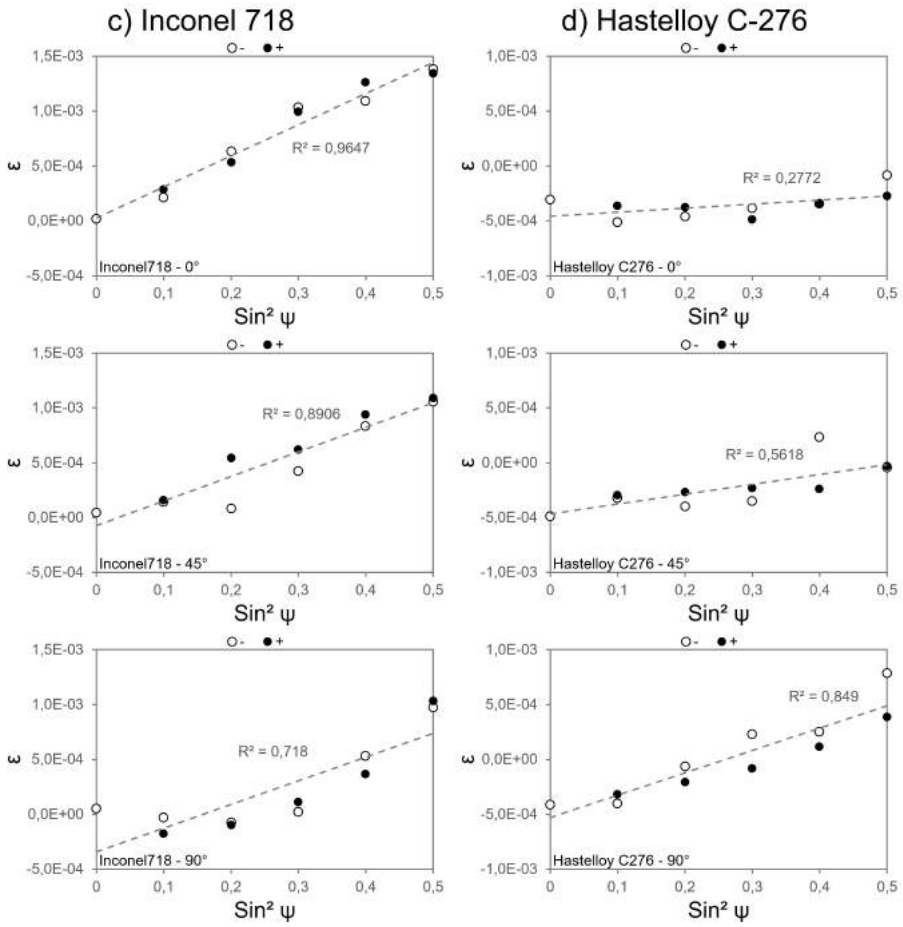


Figure A.2 (continued).

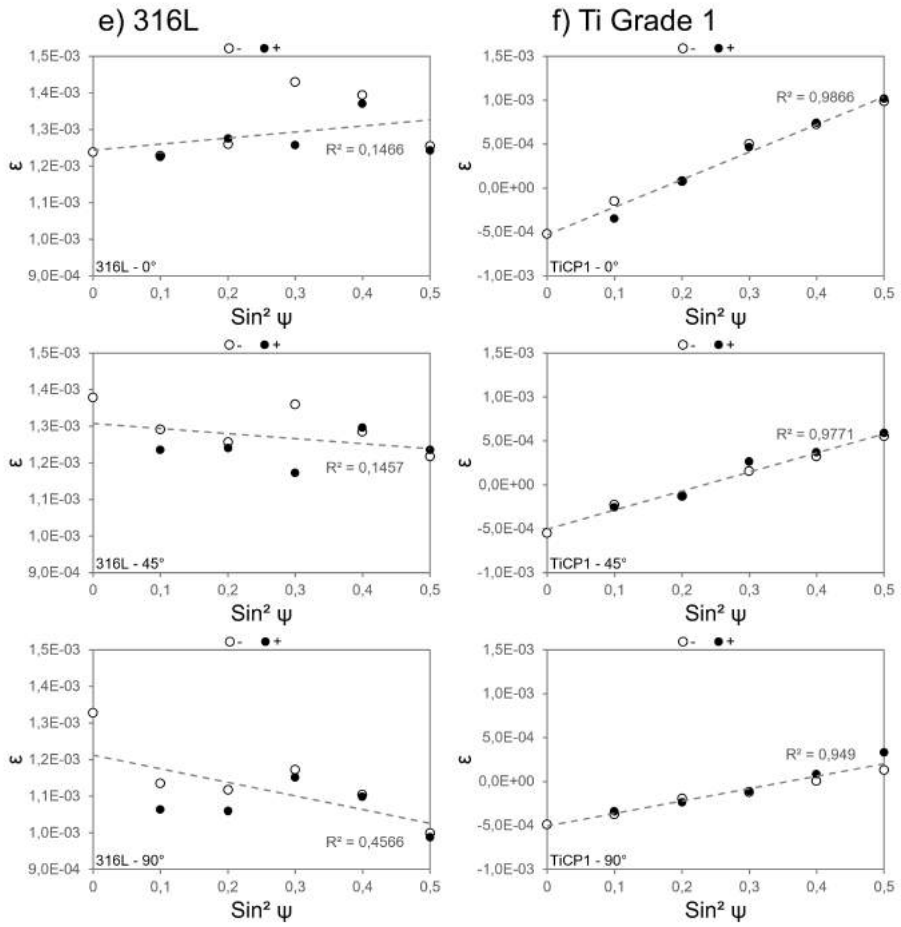


Figure A.2 (continued).

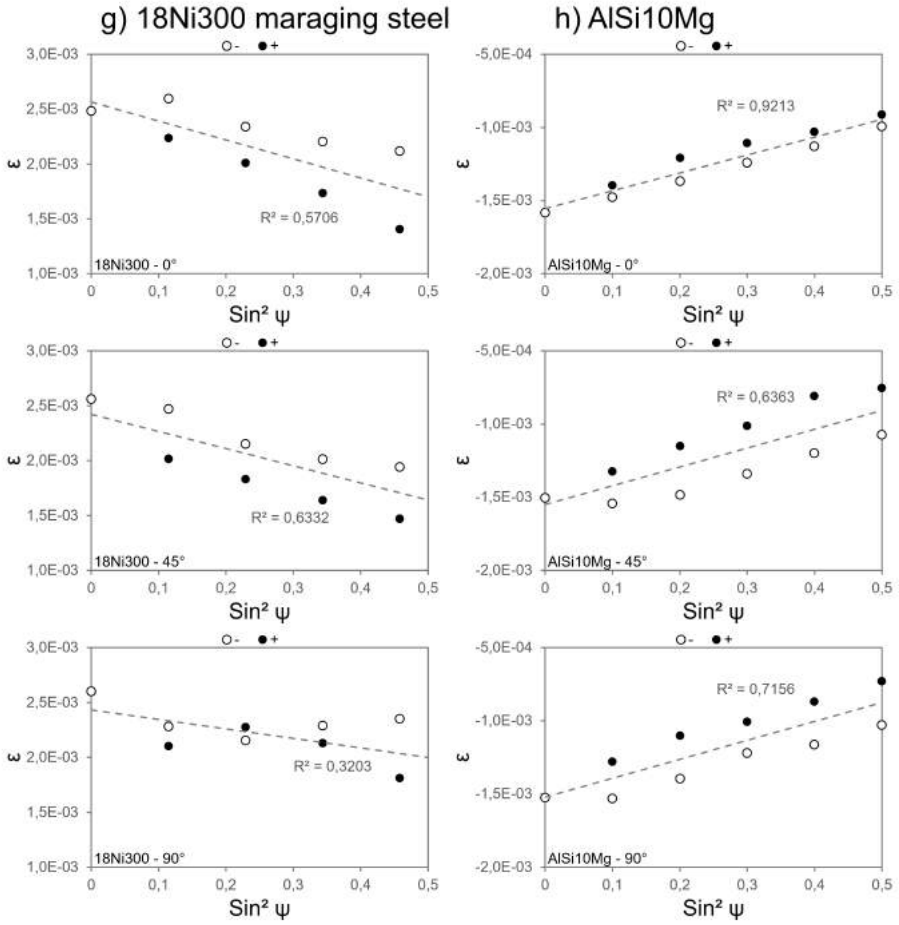


Figure A.2 (continued).

Bibliography

- [1] ASTM International. ISO/ASTM Standard 52921 - 13: Standard Terminology for Additive Manufacturing-Coordinate Systems and Test Methodologies, 2013.
- [2] J.-P. Kruth, M.C. Leu, and T. Nakagawa. Progress in Additive Manufacturing and Rapid Prototyping. In *CIRP Annals - Manufacturing Technology*, volume 47, pages 525–540, 1998.
- [3] Charles Hull. Apparatus for production of three-dimensional objects by stereolithography, 1986.
- [4] International Standards Organisation. ISO Standard 17296-2:2015 : Additive manufacturing – General principles – Part 2: Overview of process categories and feedstock, 2015.
- [5] Gartner, Inc. <http://www.gartner.com>. [Accessed 2016-02-06].
- [6] Inc Wohlers Associates. Wohlers Report 2015. Technical report, Wohlers Associates, 2015.
- [7] Materialise. Materialise Contributes to Pininfarina Sintesi Concept Car. <http://www.materialise.com/cases/materialise-contributes-to-pininfarina-sintesi-concept-car>, 2008. [Accessed 2015-12-18].
- [8] Rhett Allain. How Can Airlines Reduce Fuel Costs? <http://www.wired.com/2012/09/how-can-airlines-reduce-fuel-costs/>, 2012. [Accessed 2015-12-18].
- [9] Airbus. EOS and Airbus Group Innovations join forces on study for 3D printing in aerospace. <http://www.tctmagazine.com/3D-printing-news/eos-and-airbus-group-innovations-join-forces-on-study-for-3d/>, 2014. [Accessed 2015-12-19].

- [10] Airbus. Printing the future: Airbus expands its applications of the revolutionary additive layer manufacturing process. <http://www.airbus.com/presscentre/pressreleases/press-release-detail/detail/printing-the-future-airbus-expands-its-applications-of-the-revolutionary-additive-layer-manufacturi/>, 2014. [Accessed 2015-12-19].
- [11] T. Kellner. Fit To Print: New Plant Will Assemble World's First Passenger Jet Engine With 3D Printed Fuel Nozzles, Next-Gen Materials. <http://www.gereports.com/post/80701924024/fit-to-print>, 2014. [Accessed 2015-12-19].
- [12] A. Zaleski. GE's bestselling jet engine makes 3-D printing a core component. <http://fortune.com/2015/03/05/ge-engine-3d-printing/>, 2015. [Accessed 2015-12-19].
- [13] Mobelife. 3D Printed Hip by Mobelife Puts Teenager Back On Her Feet. <http://ortho.materialise.com/cases/3d-printed-hip-mobelife-puts-teenager-back-her-feet>, 2014. [Accessed 2015-12-19].
- [14] Layerwise. Layerwise AM burners increase quality and efficiency of quartz glass pinching and forming. http://www.layerwise.com/wp-content/uploads/2015/09/3DS_LayerWise_Havells-Sylvania_EN_view.pdf, 2015. [Accessed 2015-12-18].
- [15] ASTM International. ASTM Committee F42. <http://www.astm.org/COMMITTEE/F42.htm>. [Accessed 2015-12-05].
- [16] P. J. Withers and H. K. D. H. Bhadeshia. Residual stress. Part 1 : Measurement techniques. *Materials Science and Technology*, 17(4):355–365, 2001.
- [17] J. Blahovec. Stress relaxation in cherry fruit. *Biorheology*, 33(6):451–62, January 1996.
- [18] G. E. Dieter. Chapter 15: Residual Stresses. In *Mechanical Metallurgy*, chapter 15. McGraw-Hill, New York, 3rd edition, 1961.
- [19] Wikipedia. Prince Rupert's Drop. https://en.wikipedia.org/wiki/Prince_Rupert%27s_Drop. [Accessed 2015-12-15].
- [20] Layerwise. Material data sheet: Ti6Al4V Grade 5. Technical report, LayerWise, 2012.

- [21] S. Buls, S. Clijsters, and J.-P. Kruth. Homogenizing the Melt Pool Intensity Distribution in the SLM Process through System Identification and Feedback Control. In *Proceedings of the Solid Freeform Fabrication Symposium*, pages 6–11, Austin, Texas, 2014. University of Texas in Austin, Texas.
- [22] S. Clijsters, T. Craeghs, S. Buls, K. Kempen, and J.-P. Kruth. In situ quality control of the selective laser melting process using a high-speed, real-time melt pool monitoring system. *The International Journal of Advanced Manufacturing Technology*, August 2014.
- [23] E. Rodriguez, F. Medina, D. Espalin, C. Terrazas, D. Muse, C. Henry, E. Macdonald, and R. B. Wicker. Integration of a Thermal Imaging Feedback Control System in Electron Beam Melting. In *Solid Freeform Fabrication Symposium*, pages 945–961, 2012.
- [24] T. Craeghs, S. Clijsters, E. Yasa, F. Bechmann, S. Berumen, and J.-P. Kruth. Determination of geometrical factors in Layerwise Laser Melting using optical process monitoring. *Optics and Lasers in Engineering*, 49(12):1440–1446, 2011.
- [25] S. Kleszczynski, J. zur Jacobsmühlen, J.T. Sehart, and G. Witt. Error detection in Laser beam melting systems by high resolution imaging. In *Solid Freeform Fabrication Symposium*, pages 975–987, 2012.
- [26] M. Mani, B. Lane, A. Donmez, S. Feng, S. Moylan, and R. Fesperman. Measurement Science Needs for Real-time Control of Additive Manufacturing Powder Bed Fusion Processes. Technical report, US Department of Commerce, NIST, 2015.
- [27] M. Rombouts, J.-P. Kruth, L. Froyen, and P. Mercelis. Fundamentals of Selective Laser Melting of alloyed steel powders. *CIRP Annals - Manufacturing Technology*, 55(1):187–192, 2006.
- [28] L. Thijs. *Microstructure and Texture of Metal Parts Produced by Selective Laser Melting*. PhD thesis, University of Leuven, 2014.
- [29] K. Kempen. *Expanding the Materials Palette for Selective Laser Melting of Metals*. PhD thesis, University of Leuven, 2015.
- [30] W. E. King, H. D. Barth, V. M. Castillo, G. F. Gallegos, J. W. Gibbs, D. E. Hahn, C. Kamath, and A. M. Rubenchik. Observation of keyhole-mode laser melting in laser powder-bed fusion additive manufacturing. *Journal of Materials Processing Technology*, 214(12):2915–2925, December 2014.

- [31] C. Qiu, N. J. E. Adkins, H. Hassanin, M. M. Attallah, and K. Essa. In-situ shelling via selective laser melting: Modelling and microstructural characterisation. *Materials & Design*, 87:845–853, December 2015.
- [32] H. Meier and C. Haberland. Experimental studies on selective laser melting of metallic parts. *Materialwissenschaft und Werkstofftechnik*, 39(9):665–670, 2008.
- [33] E. Yasa and J-P. Kruth. Microstructural investigation of Selective Laser Melting 316L stainless steel parts exposed to laser re-melting. *Procedia Engineering*, 19(0):389–395, January 2011.
- [34] E. Yasa. *Manufacturing by Combining Selective Laser Melting and Selective Laser Erosion / Laser Re- Melting*. PhD thesis, University of Leuven, 2011.
- [35] L. Thijs, B. Vrancken, J.-P. Kruth, and J. Van Humbeeck. The Influence of Process Parameters and Scanning Strategy on the Texture in Ti6Al4V Parts Produced by Selective Laser Melting. *Proceedings of the Materials Science and Technology (MS&T) Conference*, pages 21–28, 2013.
- [36] L. Thijs, F. Verhaeghe, T. Craeghs, J. Van Humbeeck, and J.-P. Kruth. A study of the microstructural evolution during selective laser melting of Ti-6Al-4V. *Acta Materialia*, 58(9):3303–3312, May 2010.
- [37] A.H. Nickel, D.M. Barnett, and F.B. Prinz. Thermal stresses and deposition patterns in layered manufacturing. *Materials Science and Engineering: A*, 317(1-2):59–64, 2001.
- [38] D. Vanbuel. *Vermoeiingsgedrag van Ti6Al4V componenten geproduceerd door het Selectief Laser Smelten Proces*. Master thesis, Department of Mechanical Engineering, University of Leuven, 2011.
- [39] L. Thijs, M. Montero, R. Wauthle, Q. Xie, J.-P. Kruth, and J. Van Humbeeck. Strong morphological and crystallographic texture and resulting yield strength anisotropy in selective laser melted tantalum. *Acta Materialia*, 61(12):4657–4668, 2013.
- [40] L. E. Murr, E. Martinez, J. Hernandez, S. Collins, K. N. Amato, S. M. Gaytan, and P. W. Shindo. Microstructures and Properties of 17-4 PH Stainless Steel Fabricated by Selective Laser Melting. *Journal of Materials Research and Technology*, 1(3):167–177, October 2012.
- [41] W. Xu, M. Brandt, S. Sun, J. Elambasseril, Q. Liu, K. Latham, K. Xia, and M. Qian. Additive manufacturing of strong and ductile Ti-6Al-4V by selective laser melting via in situ martensite decomposition. *Acta Materialia*, 85:74–84, February 2015.

- [42] D. Kaminski. Laser marking: How to choose the best laser for your marking application. <http://www.laserfocusworld.com/articles/2011/04/laser-marking-how-to-choose-the-best-laser-for-your-marking-application.html>, 2011. [Accessed 2015-12-24].
- [43] N. K. Tolochko, Y. V. Khlopkov, S. E. Mozzharov, M. B. Ignatiev, T. Laoui, and V. I. Titov. Absorptance of powder materials suitable for laser sintering. *Rapid Prototyping Journal*, 6(3):155–161, 2000.
- [44] C. D. Boley, S. A. Khairallah, and A. M. Rubenchik. Calculation of laser absorption by metal powders in additive manufacturing. *Applied optics*, 54(9):2477–82, March 2015.
- [45] G. Lütjering, J. C. Williams, and A. Gysler. Microstructure and mechanical properties of titanium alloys. In *Titanium*, page 3540713972. Springer Science and Business Media, 2007.
- [46] R. R. Boyer, G. Welsh, and E. W. Collings. *Materials properties handbook: Titanium alloys*. ASM International, Materials Park: Ohio, 1994.
- [47] G. Lütjering. Influence of processing on microstructure and mechanical properties of $\alpha+\beta$ titanium alloys. *Materials Science and Engineering: A*, 243(1-2):32–45, 1998.
- [48] S. Lampman. Wrought Titanium and titanium alloys. In *Properties and selection: Nonferrous alloys and special-purpose alloys*, volume 2, pages 592–633. ASM International, Materials Park, OH, 1990.
- [49] E. Brandl. *Microstructural and mechanical properties of additive manufactured Ti-6Al-4V using wire*. PhD thesis, Brandenburg Technical University of Cottbus, 2010.
- [50] S. M. Kelly and S. L. Kampe. Microstructural evolution in laser-deposited multilayer Ti-6Al-4V builds: Part I. Microstructural characterization. *Metallurgical and Materials Transactions A: Physical Metallurgy and Materials Science*, 35(6):1869–1879, 2004.
- [51] B. E. Carroll, T. A. Palmer, and A. M. Beese. Anisotropic tensile behavior of Ti-6Al-4V components fabricated with directed energy deposition additive manufacturing. *Acta Materialia*, 87:309–320, April 2015.
- [52] N. Hrabe and T. Quinn. Effects of processing on microstructure and mechanical properties of a titanium alloy (Ti-6Al-4V) fabricated using electron beam melting (EBM), Part 2: Energy input, orientation, and location. *Materials Science and Engineering: A*, 573:271–277, June 2013.

- [53] L. L. Parimi, R. G. A., D. Clark, and M. M. Attallah. Microstructural and texture development in direct laser fabricated IN718. *Materials Characterization*, 89:102–111, March 2014.
- [54] F. Verhaeghe, T. Craeghs, J. Heulens, and L. Pandelaers. A pragmatic model for selective laser melting with evaporation. *Acta Materialia*, 57(20):6006–6012, 2009.
- [55] M. J. Bermingham, D. Kent, H. Zhan, D.H. StJohn, and M. S. Dargusch. Controlling the microstructure and properties of wire arc additive manufactured Ti–6Al–4V with trace boron additions. *Acta Materialia*, 91:289–303, June 2015.
- [56] L. E. Murr, E. Martinez, J. Hernandez, S. Collins, K. N. Amato, P. W. Shindo, S. M. Gaytan, and R. A. Meklus. Additive Manufacturing of Fe-17Cr-4Ni-4Cu, Comparing Build Chamber Process Gas with Mechanical Properties, 2011.
- [57] L. E. Murr. Metallurgy of Additive Manufacturing: Examples from Electron Beam Melting. *Additive Manufacturing*, 5:40–53, December 2015.
- [58] A. A. Antonysamy, J. Meyer, and P. B. Prangnell. Effect of build geometry on the β -grain structure and texture in additive manufacture of Ti6Al4V by selective electron beam melting. *Materials Characterization*, 84:153–168, October 2013.
- [59] M. Simonelli, Y. Y. Tse, and C. Tuck. Further understanding of Ti6Al4V selective laser melting using texture analysis. *Proceedings of the Solid Freeform Fabrication Symposium*, pages 480–491, 2012.
- [60] C. de Formanoir, S. Michotte, O. Rigo, L. Germain, and S. Godet. Electron beam melted Ti–6Al–4V: Microstructure, texture and mechanical behavior of the as-built and heat-treated material. *Materials Science and Engineering: A*, 652:105–119, January 2016.
- [61] G. Kasperovich and J. Hausmann. Improvement of fatigue resistance and ductility of TiAl6V4 processed by selective laser melting. *Journal of Materials Processing Technology*, 220:202–214, February 2015.
- [62] M. Simonelli, Y. Y. Tse, and C. Tuck. The formation of $\alpha + \beta$ microstructure in as-fabricated selective laser melting of Ti–6Al–4V. *Journal of Materials Research*, 29(17):2028–2035, July 2014.
- [63] M. Simonelli, Y. Y. Tse, and C. Tuck. Effect of the build orientation on the mechanical properties and fracture modes of SLM ti-6Al-4V. *Materials Science and Engineering: A*, 616:1–11, August 2014.

- [64] S. Leuders, T. Lieneke, S. Lammers, T. Tröster, and T. Niendorf. On the fatigue properties of metals manufactured by selective laser melting – The role of ductility. *Journal of Materials Research*, FirstView:1–9, 2014.
- [65] C. Qiu, N. J. E. E Adkins, and M. M. Attallah. Microstructure and tensile properties of selectively laser-melted and of HIPed laser-melted Ti-6Al-4V. *Materials Science and Engineering: A*, 578:230–239, August 2013.
- [66] P. Edwards and M. Ramulu. Fatigue performance evaluation of selective laser melted Ti-6Al-4V. *Materials Science and Engineering: A*, 598:327–337, March 2014.
- [67] H. Gong, K. Rafi, T. Starr, and B. E. Stucker. Effect of Defects on Fatigue Tests of As-Built Ti-6Al-4V Parts Fabricated by Selective Laser Melting. In *Solid Freeform Fabrication Symposium*, pages 499–506, 2012.
- [68] E. Wycisk, C. Emmelmann, S. Shafaqat, and F. Walther. High Cycle Fatigue (HCF) Performance of Ti-6Al-4V Alloy Processed by Selective Laser Melting. *Advanced Materials Research*, 2013.
- [69] B. Van Hooreweder, D. Moens, R. Boonen, J.-P. Kruth, and P. Sas. Analysis of Fracture Toughness and Crack Propagation of Ti6Al4V Produced by Selective Laser Melting. *Advanced Engineering Materials*, 14(1-2):92–97, February 2012.
- [70] M. Seifi, M. Dahar, R. Aman, O. Harrysson, J. Beuth, and J. J. Lewandowski. Evaluation of Orientation Dependence of Fracture Toughness and Fatigue Crack Propagation Behavior of As-Deposited ARCAM EBM Ti-6Al-4V. *JOM*, 67(3):597–607, February 2015.
- [71] P. Edwards and M. Ramulu. Effect of build direction on the fracture toughness and fatigue crack growth in selective laser melted Ti-6Al-4 V. *Fatigue & Fracture of Engineering Materials & Structures*, 38(10):1228–1236, March 2015.
- [72] V. Cain, L. Thijs, J. Van Humbeeck, B. Van Hooreweder, and R. Knutsen. Crack propagation and fracture toughness of Ti6Al4V alloy produced by selective laser melting. *Additive Manufacturing*, 5:68–76, December 2015.
- [73] T. H. Becker, M. Beck, and C. Scheffer. Microstructure and mechanical properties of Direct Metal Laser Sintered Ti-6Al-4V. *The South African Journal of Industrial Engineering*, 26(1):1, March 2015.
- [74] M. J. Donachie. *Titanium: A Technical Guide*. ASM International, 2000.

- [75] N. Dhansay. *Fracture Mechanics Based Fatigue and Fracture Toughness Evaluation of SLM Ti-6Al-4V*. Master thesis, University of Cape Town, 2015.
- [76] S. Leuders, M. Thöne, a. Riemer, T. Niendorf, T. Tröster, H.a. A Richard, and H.J. J Maier. On the mechanical behaviour of titanium alloy TiAl6V4 manufactured by selective laser melting: Fatigue resistance and crack growth performance. *International Journal of Fatigue*, 48(0):300–307, March 2012.
- [77] V. J. Challis, X. Xu, L. C. Zhang, A. P. Roberts, J. F. Grotowski, and T. B. Sercombe. High specific strength and stiffness structures produced using selective laser melting. *Materials & Design*, 63:783–788, November 2014.
- [78] C. Z. Yan, L. Hao, A. Hussein, and D. Raymont. Evaluations of cellular lattice structures manufactured using selective laser melting. *International Journal of Machine Tools & Manufacture*, 62:32–38, November 2012.
- [79] T. B. Kim, S. Yue, Z. Zhang, E. Jones, J. R. Jones, and P. D. Lee. Additive manufactured porous titanium structures: Through-process quantification of pore and strut networks. *Journal of Materials Processing Technology*, 214(11):2706–2715, November 2014.
- [80] C. Qiu, S. Yue, N. J. E. Adkins, M. Ward, H. Hassanin, P. D. Lee, P. J. Withers, and M. M. Attallah. Influence of processing conditions on strut structure and compressive properties of cellular lattice structures fabricated by selective laser melting. *Materials Science and Engineering: A*, 628:188–197, March 2015.
- [81] M. Speirs, J.-P. Kruth, J. Van Humbeeck, J. Schrooten, S. Buls, S. Dadbakhsh, and J. Luyten. The effect of SLM parameters on geometrical characteristic of open porous NiTi scaffolds. In *VRAP Advanced Research in Virtual and Rapid Prototyping*, Leiria, Portugal, 2013. Taylor & Francis.
- [82] A. Barbas, A. S. Bonnet, P. Lipinski, R. Pesci, and G. Dubois. Development and mechanical characterization of porous titanium bone substitutes. *Journal of the Mechanical Behavior of Biomedical Materials*, 9(0):34–44, 2012.
- [83] F. Brenne, T. Niendorf, and H.J. Maier. Additively manufactured cellular structures: Impact of microstructure and local strains on the monotonic and cyclic behavior under uniaxial and bending load. *Journal of Materials Processing Technology*, 213(9):1558–1564, September 2013.

- [84] B. Gorny, T. Niendorf, J. Lackmann, M. Thöne, T. Tröster, and H. J. Maier. In situ characterization of the deformation and failure behavior of non-stochastic porous structures processed by selective laser melting. *Materials Science and Engineering: A*, 528(27):7962–7967, 2011.
- [85] T. B. Sercombe, X. Xu, V. J. Challis, R. Green, S. Yue, Z. Zhang, and P. D. Lee. Failure modes in high strength and stiffness to weight scaffolds produced by Selective Laser Melting. *Materials & Design*, 67:501–508, February 2015.
- [86] S. Van Bael, G. Kerckhofs, M. Moesen, G. Pyka, J. Schrooten, and J.-P. Kruth. Micro-CT-based improvement of geometrical and mechanical controllability of selective laser melted Ti6Al4V porous structures. *Materials Science and Engineering: A*, 528(24):7423–7431, September 2011.
- [87] G. Pyka, G. Kerckhofs, J. Schrooten, and M. Wevers. The effect of spatial micro-CT image resolution and surface complexity on the morphological 3D analysis of open porous structures. *Materials Characterization*, 87(0):104–115, January 2014.
- [88] P. Lipinski, A. Barbas, and A. S. Bonnet. Fatigue behavior of thin-walled grade 2 titanium samples processed by selective laser melting. Application to life prediction of porous titanium implants. *Journal of the Mechanical Behavior of Biomedical Materials*, 28(0):274–290, 2013.
- [89] T. Bormann, G. Schulz, H. Deyhle, F. Beckmann, M. de Wild, J. Kuffer, C. Munch, W. Hoffmann, and B. Muller. Combining micro computed tomography and three-dimensional registration to evaluate local strains in shape memory scaffolds. *Acta Biomaterialia*, 10(2):1024–1034, 2014.
- [90] G. Pyka, A. Burakowski, G. Kerckhofs, M. Moesen, S. Van Bael, J. Schrooten, and M. Wevers. Surface Modification of Ti6Al4V Open Porous Structures Produced by Additive Manufacturing. *Advanced Engineering Materials*, 14(6):363–370, June 2012.
- [91] S. Amin Yavari, R. Wauthle, A. J. Böttger, J. Schrooten, H. Weinans, and A. A. Zadpoor. Crystal structure and nanotopographical features on the surface of heat-treated and anodized porous titanium biomaterials produced using selective laser melting. *Applied Surface Science*, 290:287–294, January 2014.
- [92] S. M. Ahmadi, G. Campoli, S. Amin Yavari, B. Sajadi, R. Wauthle, J. Schrooten, H. Weinans, and A. A. Zadpoor. Mechanical behavior of regular open-cell porous biomaterials made of diamond lattice unit cells.

- Journal of the mechanical behavior of biomedical materials*, 34:106–15, June 2014.
- [93] E. Sallica-Leva, A. L. Jardini, and J. B. Fogagnolo. Microstructure and mechanical behavior of porous Ti–6Al–4V parts obtained by selective laser melting. *Journal of the Mechanical Behavior of Biomedical Materials*, 26(0):98–108, 2013.
- [94] S. Amin Yavari, R. Wauthle, J. van der Stok, A. C. Riemsdag, M. Janssen, M. Mulier, J.-P. Kruth, J. Schrooten, H. Weinans, and A. A. Zadpoor. Fatigue behavior of porous biomaterials manufactured using selective laser melting. *Materials Science and Engineering: C (Materials for Biological Applications)*, 33(8):4849–4858, December 2013.
- [95] E. Sallica-Leva, R. Caram, A. L. Jardini, and J. B. Fogagnolo. Ductility improvement due to martensite α' decomposition in porous Ti–6Al–4V parts produced by selective laser melting for orthopedic implants. *Journal of the mechanical behavior of biomedical materials*, 54:149–58, February 2016.
- [96] M. Speirs, J.-P. Kruth, J. Schrooten, J. Van Humbeeck, and J. Luyten. The effect of pore geometry on the mechanical properties of selective laser melted Ti–13Nb–13Zr scaffolds. In *CIRP First Conference On Biomanufacturing: Vol. 5*, Tokyo, 2013. Elsevier.
- [97] L. Yang, O. Harrysson, H. West, and D. Cormier. Compressive properties of Ti–6Al–4V auxetic mesh structures made by electron beam melting. *Acta Materialia*, 60(8):3370–3379, May 2012.
- [98] R. Wauthle, J. van der Stok, S. Amin Yavari, J. Van Humbeeck, J.-P. Kruth, A. A. Zadpoor, H. Weinans, M. Mulier, and J. Schrooten. Additively manufactured porous tantalum implants. *Acta biomaterialia*, 14:217–25, March 2015.
- [99] E. C. Santos, K. Osakada, M. Shiomi, Y. Kitamura, and F. Abe. Microstructure and mechanical properties of pure titanium models fabricated by selective laser melting. *Proceedings of the Institution of Mechanical Engineers, Part C: Journal of Mechanical Engineering Science*, 218(7):711–719, 2004.
- [100] C. M. Liu, X. J. Tian, H. B. Tang, and H. M. Wang. Microstructural characterization of laser melting deposited Ti–5Al–5Mo–5V–1Cr–1Fe near β titanium alloy. *Journal of Alloys and Compounds*, 572(0):17–24, 2013.
- [101] C. Qiu, G. A. Ravi, and M. M. Attallah. Microstructural control during direct laser deposition of a β -titanium alloy. *Materials & Design*, 81:21–30, September 2015.

- [102] L. C. Zhang, D. Klemm, J. Eckert, Y.L. Hao, and T. B. Sercombe. Manufacture by selective laser melting and mechanical behavior of a biomedical Ti-24Nb-4Zr-8Sn alloy. *Scripta Materialia*, 65(1):21–24, June 2011.
- [103] H. Schwab, K. Prashanth, L. Löber, U. Kühn, and J. Eckert. Selective Laser Melting of Ti-45Nb Alloy, April 2015.
- [104] T. Bormann, R. Schumacher, B. Müller, Bert, M. Mertmann, and M. de Wild. Tailoring Selective Laser Melting Process Parameters for NiTi Implants. *Journal of Materials Engineering and Performance*, 21(12):2519–2524, July 2012.
- [105] S. Dadbakhsh, M. Speirs, J.-P. Kruth, J. Schrooten, J. Luyten, and J. Van Humbeeck. Effect of SLM Parameters on Transformation Temperatures of Shape Memory Nickel Titanium Parts. *Advanced Engineering Materials*, 16(9):1140–1146, September 2014.
- [106] S. Dadbakhsh, B. Vrancken, J.-P. Kruth, J. Luyten, and J. Van Humbeeck. Texture and anisotropy in selective laser melting of NiTi alloy. *Materials Science and Engineering A*, 650:225–232, 2016.
- [107] M. de Wild, F. Meier, T. Bormann, C. B. Howald, and B. Müller. Damping of Selective-Laser-Melted NiTi for Medical Implants. *Journal of Materials Engineering and Performance*, 23(7):2614–2619, February 2014.
- [108] T. Habijan, C. Haberland, H. Meier, J. Frenzel, J. Wittsiepe, C. Wuwer, C. Greulich, T. A. Schildhauer, and M. Koumlller. The biocompatibility of dense and porous Nickel-Titanium produced by selective laser melting. *Materials Science & Engineering: C (Materials for Biological Applications)*, 33(1):419–426, 2012.
- [109] B. C. Zhang, J. Chen, and C. Coddet. Microstructure and Transformation Behavior of in-situ Shape Memory Alloys by Selective Laser Melting Ti-Ni Mixed Powder. *Journal of Materials Science & Technology*, 29(9):863–867, 2013.
- [110] E. Bassoli, A. Gatto, N. Sewell, and D. Johnston. On the effect of build orientation in powder ALM of 316L. In P Bartolo, editor, *Innovative Developments in Design and Manufacturing*, pages 263–268. Taylor & Francis Group, 2010.
- [111] R. Morgan, C. J. Sutcliffe, and W. O’Neill. Density analysis of direct metal laser re-melted 316L stainless steel cubic primitives. *Journal of Materials Science*, 39(4):1195–1205, 2004.

- [112] T. Niendorf, S. Leuders, A. Riemer, H. A. Richard, T. Tröster, and D. Schwarze. Highly Anisotropic Steel Processed by Selective Laser Melting. *Metallurgical and Materials Transactions B*, 44(4):794–796, 2013.
- [113] I. Yadroitsev, M. Pavlov, P. Bertrand, and I. Smurov. Mechanical properties of samples fabricated by selective laser melting. In *14emes Assises Européennes du Prototypage & Fabrication Rapide*, 2009.
- [114] E. Yasa, J. Deckers, and J.-P. Kruth. The investigation of the influence of laser re-melting on density, surface quality and microstructure of selective laser melting parts. *Rapid Prototyping Journal*, 17(5):312–327, 2011.
- [115] E. Yasa, J. Deckers, J.-P. Kruth, M. Rombouts, and J. Luyten. Charpy impact testing of metallic selective laser melting parts. *Virtual and Physical Prototyping*, 5(2):89–98, June 2010.
- [116] S. L. Campanelli, N. Contuzzi, and A. D. Ludovico. Manufacturing of 18 Ni Marage 300 steel samples by selective laser melting. *Advanced Materials Research*, 83-86:850–857, December 2010.
- [117] E. Jäggle, P.-P. Choi, J. Van Humbeeck, and D. Raabe. Precipitation and austenite reversion behaviour of a maraging steel produced by selective laser melting. *Journal of Materials Research*, Submitted., 2014.
- [118] K. Kempen, E. Yasa, L. Thijs, J.-P. Kruth, and J. Van Humbeeck. Microstructure and mechanical properties of Selective Laser Melted 18Ni-300 steel. *Physics Procedia*, 12, Part A(0):255–263, January 2011.
- [119] E. Yasa, K. Kempen, J.-P. Kruth, L. Thijs, and J. Van Humbeeck. Microstructure and mechanical properties of 18Ni300 maraging steel after Selective Laser Melting. *Proceedings of the Solid Freeform Fabrication Symposium*, pages 383–396, 2010.
- [120] G. Casalino, S. L. Campanelli, N. Contuzzi, and A. D. Ludovico. Experimental investigation and statistical optimisation of the selective laser melting process of a maraging steel. *Optics & Laser Technology*, 65:151–158, January 2015.
- [121] J.H. Ouyang, H. Mei, M. Valant, and R. Kovacevic. Application of laser based additive manufacturing to production of tools for friction stir welding. In *Proceedings of the Solid Freeform Fabrication Symposium*, pages 65–72, Austin, Texas, 2002. University of Texas in Austin, Texas.
- [122] A. J. Pinkerton and L. Li. Direct additive laser manufacturing using gas- and water-atomised H13 tool steel powders. *The International Journal of Advanced Manufacturing Technology*, 25(5-6):471–479, June 2005.

- [123] R. Nair, We. Jiang, and P. Molian. Nanoparticle Additive Manufacturing of Ni-H13 Steel Injection Molds. *Journal of Manufacturing Science and Engineering*, 126(3):637, August 2004.
- [124] J. Mazumder, A. Schifferer, and J. Choi. Direct materials deposition: designed macro and microstructure. *Materials Research Innovations*, 3(3):118–131, October 1999.
- [125] D. Cormier, O. Harrysson, and H. West. Characterization of H13 steel produced via electron beam melting. *Rapid Prototyping Journal*, 10(1), 2004.
- [126] J. Mazumder, J. Choi, K. Nagarathnam, J. Koch, and D. Hetzner. The direct metal deposition of H13 tool steel for 3-D components. *JOM*, 1997.
- [127] R. R. Unocic and J. N. DuPont. Composition control in the direct laser-deposition process. *Metallurgical and Materials Transactions B*, 34(4):439–445, 2003.
- [128] S. Pogson, P. Fox, W. O'Neill, and C. J. Sutcliffe. The direct metal laser remelting of copper and tool steel powders. *Materials Science and Engineering A*, 386(1-2):453–459, November 2004.
- [129] V. E. Beal, P. Erasenthiran, N. Hopkinson, P. Dickens, and C. H. Ahrens. Fabrication of x-graded H13 and Cu powder mix using high power pulsed Nd: YAG laser. In *Solid Freeform Fabrication Symposium*, pages 187–197, 2004.
- [130] V. E. Beal, P. Erasenthiran, C. H. Ahrens, and P. Dickens. Evaluating the use of functionally graded materials inserts produced by selective laser melting on the injection moulding of plastics parts. *Proceedings of the Institution of Mechanical Engineers Part B-Journal of Engineering Manufacture*, 221(6):945–954, 2007.
- [131] G. Telasang, J. Dutta Majumdar, N. Wasekar, G. Padmanabham, and I. Manna. Microstructure and Mechanical Properties of Laser Clad and Post-cladding Tempered AISI H13 Tool Steel. *Metallurgical and Materials Transactions A*, 46(5):2309–2321, February 2015.
- [132] K. Kempen, L. Thijs, J. Van Humbeeck, and J.-P. Kruth. Mechanical Properties of AlSi10Mg Produced by Selective Laser Melting. *Physics Procedia*, 39(0):439–446, 2012.
- [133] Z. H. Liu, D. Q. Zhang, C. K. Chua, and K. F. Leong. Crystal structure analysis of M2 high speed steel parts produced by selective laser melting. *Materials Characterization*, 84(0):72–80, 2013.

- [134] T. Mahale, D. Cormier, O. Harrysson, and K. Ervin. Advances in Electron Beam Melting of Aluminum alloys. In *Proceedings of the Solid Freeform Fabrication Symposium*, pages 312–323, Austin, Texas, 2007. University of Texas in Austin, Texas.
- [135] C. Weingarten, D. Buchbinder, N. Pirch, W. Meiners, K. Wissenbach, and R. Poprawe. Formation and reduction of hydrogen porosity during selective laser melting of AlSi10Mg. *Journal of Materials Processing Technology*, 221:112–120, July 2015.
- [136] D. Buchbinder, W. Meiners, N. Pirch, K. Wissenbach, and J. Schrage. Investigation on reducing distortion by preheating during manufacture of aluminum components using selective laser melting. *Journal of Laser Applications*, 26(1):012004 (10 pp.)–012004 (10 pp.), 2014.
- [137] X. P. Li, M. Roberts, Y. J. Liu, C. W. Kang, H. Huang, and T. B. Sercombe. Effect of substrate temperature on the interface bond between support and substrate during selective laser melting of Al–Ni–Y–Co–La metallic glass. *Materials & Design*, 65:1–6, January 2015.
- [138] A. Verwimp. *Onderzoek naar een optimale warmtebehandeling voor AlSi10Mg stukken vervaardigd via Selectief Laser Smelten*. Bachelor thesis, Department of Materials Engineering, University of Leuven, 2012.
- [139] E. Brandl, U. Heckenberger, V. Holzinger, and D. Buchbinder. Additive manufactured AlSi10Mg samples using Selective Laser Melting (SLM): Microstructure, high cycle fatigue, and fracture behavior. *Materials & Design*, 34(0):159–169, 2012.
- [140] M. J. Donachie and S. J. Donachie. *Superalloys: A Technical Guide, 2nd Edition*. ASM International, 2002.
- [141] R. C. Reed. *The Superalloys: Fundamentals and Applications*. Cambridge University Press, 2006.
- [142] R. R. Dehoff, M. M. Kirka, W. J. Sames, H. Bilheux, A. S. Tremsin, L. E. Lowe, and S. S. Babu. Site specific control of crystallographic grain orientation through electron beam additive manufacturing. *Materials Science and Technology*, 31(8):931–938, May 2015.
- [143] K. N. Amato, S. M. Gaytan, L. E. Murr, E. Martinez, P. W. Shindo, J. Hernandez, S. Collins, and F. Medina. Microstructures and mechanical behavior of Inconel 718 fabricated by selective laser melting. *Acta Materialia*, 60(5):2229–2239, 2012.

- [144] E. Chlebus, K. Gruber, B. Kuźnicka, J. Kurzac, and T. Kurzynowski. Effect of heat treatment on microstructure and mechanical properties of Inconel 718 processed by selective laser melting. *Materials Science and Engineering: A*, May 2015.
- [145] Z. Wang, K. Guan, M. Gao, X. Li, X. Chen, and X. Zeng. The microstructure and mechanical properties of deposited-IN718 by selective laser melting. *Journal of Alloys and Compounds*, 513(0):518–523, 2012.
- [146] L. M. Sochalski-Kolbus, E. A. Payzant, P. A. Cornwell, T. R. Watkins, S. S. Babu, R. R. Dehoff, M. Lorenz, O. Ovchinnikova, and C. Duty. Comparison of Residual Stresses in Inconel 718 Simple Parts Made by Electron Beam Melting and Direct Laser Metal Sintering. *Metallurgical and Materials Transactions A*, 46(3):1419–1432, January 2015.
- [147] P.L. Blackwell. The mechanical and microstructural characteristics of laser-deposited IN718. *Journal of Materials Processing Technology*, 170(1-2):240–246, December 2005.
- [148] F. Wang, X. H. Wu, and D. Clark. On direct laser deposited Hastelloy X: dimension, surface finish, microstructure and mechanical properties. *Materials Science and Technology*, 27(1):344–356, January 2011.
- [149] D. Tomus, T. Jarvis, X. Wu, J. Mei, P. Rometsch, E. HERNY, J. F. Rideau, and S. Vaillant. Controlling the Microstructure of Hastelloy-X Components Manufactured by Selective Laser Melting. *Physics Procedia*, 41(0):816–820, 2013.
- [150] N. J. Harrison, I. Todd, and K. Mumtaz. Reduction of micro-cracking in nickel superalloys processed by Selective Laser Melting: A fundamental alloy design approach. *Acta Materialia*, 94:59–68, August 2015.
- [151] J. Ramos-Grez and D. L. Bourell. Solidification Morphology Analysis of SLM of Cu Powder 203. In *Proceedings of the Solid Freeform Fabrication Symposium*, pages 203–213, Austin, Texas, 2004. University of Texas in Austin, Texas.
- [152] S. R. Pogson, P. Fox, C. J. Sutcliffe, and W. O’Neill. The production of copper parts using DMLR. *Rapid Prototyping Journal*, 9(5):334–343, 2003.
- [153] Y. Tang, H.T. Loh, Y.S. Wong, J.Y.H. Fuh, L. Lu, and X. Wang. Direct laser sintering of a copper-based alloy for creating three-dimensional metal parts. *Journal of Materials Processing Technology*, 140(1-3):368–372, September 2003.

- [154] H.H. Zhu, L. Lu, and J.Y.H. Fuh. Development and characterisation of direct laser sintering Cu-based metal powder. *Journal of Materials Processing Technology*, 140(1-3):314–317, September 2003.
- [155] D. A. Ramirez, L. E. Murr, E. Martinez, D. H. Hernandez, J. L. Martinez, B. I. Machado, F. Medina, P. Frigola, and R. B. Wicker. Novel precipitate–microstructural architecture developed in the fabrication of solid copper components by additive manufacturing using electron beam melting. *Acta Materialia*, 59(10):4088–4099, June 2011.
- [156] P. Frigola, O. Harrysson, T. J. Horn, H. West, R. Aman, J. M. Rigsbee, D. A. Ramirez, L. E. Murr, F. R. Medina, R. B. Wicker, and E. Rodriguez. Fabricating Copper Components with Electron Beam Melting - ASM International. *Advanced Materials and Processes*, July, 2014.
- [157] 3tRPD. 3T announces success with Pure Copper production – and an open invitation. <http://www.3trpd.co.uk/3t-success-with-pure-copper-am-production/>, 2014. [Accessed 2016-01-26].
- [158] Fraunhofer ILT. Additive Manufacturing of copper components with Selective Laser Melting. http://www.ilt.fraunhofer.de/content/dam/ilt/en/documents/product_and_services/laser_material_processing/HO_Additive_Manufacturing_of_Copper_Components_with_SLM_2011.pdf, 2011. [Accessed 2016-01-26].
- [159] A. Weisheit, D. Dobrzanski, M. Valentin, S. Ocylok, K. Wissenbach, and I. Kelbassa. Laser Additive Manufacturing - A New Manufacturing Technology for Parts of Composites with Refractory Metals ? In *18th Plansee Seminar*, pages 1–12, 2013.
- [160] R. Gehm. Aerojet Rocketdyne pursues copper alloy additive manufacturing for thrust chamber assembly. <http://articles.sae.org/13665/>, 2014. [Accessed 2016-01-26].
- [161] C. C. Ng, M. M. Savalani, H. C. Man, and I. Gibson. Layer manufacturing of magnesium and its alloy structures for future applications. *Virtual and Physical Prototyping*, 5(1):13–19, March 2010.
- [162] C. C. Ng, M. M. Savalani, M. L. Lau, and H. C. Man. Microstructure and mechanical properties of selective laser melted magnesium. *Applied Surface Science*, 257(17):7447–7454, June 2011.
- [163] B. Zhang, H. Liao, and C. Coddet. Effects of processing parameters on properties of selective laser melting Mg–9%Al powder mixture. *Materials & Design*, 34(0):753–758, 2012.

- [164] K. Wei, M. Gao, Z. Wang, and X. Zeng. Effect of energy input on formability, microstructure and mechanical properties of selective laser melted AZ91D magnesium alloy. *Materials Science and Engineering: A*, 611:212–222, August 2014.
- [165] M. Gieseke, C. Nölke, S. Kaierle, H. J. Maier, and H. Haferkamp. Selective Laser Melting of Magnesium Alloys for Manufacturing Individual Implants. In *Fraunhofer Direct Digital Manufacturing Conference*, pages 1–6, 2014.
- [166] H. Rieper. *Systematic parameter analysis for Selective Laser Melting of (SLM) of Silver based materials*. Phd, Aachen University of Applied Sciences, 2013.
- [167] M. Khan and P. Dickens. Processing parameters for Selective Laser Melting (SLM) of gold. In *Proceedings of the Solid Freeform Fabrication Symposium*, pages 278–289, Austin, Texas, 2008. University of Texas in Austin, Texas.
- [168] M. Khan and P. Dickens. Selective laser melting (SLM) of gold (Au). *Rapid Prototyping Journal*, 18(1):81–9494, 2012.
- [169] D. Zito, M. Fockele, and A. Molinari. Optimisation of the Main Selective Laser Melting Technology Parameters in the Production of Gold and Platinum Jewellery. In *Proceedings of the Santa Fe Symposium*, 2014.
- [170] P. Fox, S. Pogson, C. J. Sutcliffe, and E. Jones. Interface interactions between porous titanium/tantalum coatings, produced by Selective Laser Melting (SLM), on a cobalt–chromium alloy. *Surface and Coatings Technology*, 202(20):5001–5007, July 2008.
- [171] X. Zhou, X. Liu, D. Zhang, Z. Shen, and W. Liu. Balling phenomena in selective laser melted tungsten. *Journal of Materials Processing Technology*, 222:33–42, August 2015.
- [172] K. Deprez, S. Vandenbergh, K. Van Audenhaege, J. Van Vaerenbergh, and R. Van Holen. Rapid additive manufacturing of MR compatible multipinhole collimators with selective laser melting of tungsten powder. *Medical Physics*, 40(1), 2013.
- [173] K. Van Caekenbergh, P. Bleys, T. Craeghs, S. Van Bael, and M. Pelk. A W-band waveguide fabricated using selective laser melting. *Microwave and Optical Technology Letters*, 54(11):2572–2575, 2012.
- [174] Y. Brif, M. Thomas, and I. Todd. The use of high-entropy alloys in additive manufacturing. *Scripta Materialia*, 99:93–96, December 2015.

- [175] S. Pauly, L. Löber, R. Petters, M. Stoica, S. Scudino, U. Kühn, and J. Eckert. Processing metallic glasses by selective laser melting. *Materials Today*, 16(1–2):37–41, 2013.
- [176] K.G. Prashanth, H. Shakur Shahabi, H. Attar, V.C. Srivastava, N. Ellendt, V. Uhlenwinkel, J. Eckert, and S. Scudino. Production of high strength Al85Nd8Ni5Co2 alloy by selective laser melting. *Additive Manufacturing*, 6:1–5, April 2015.
- [177] J. Luo, H. Pan, and E. C. Kinzel. Additive Manufacturing of Glass. *Journal of Manufacturing Science and Engineering*, 136(6), 2014.
- [178] M. Kayser. Solar Sinter. <http://www.markuskayser.com/work/solarsinter/>, 2011. [Accessed 2016-01-26].
- [179] J. Klein, M. Stern, G. Franchin, M. Kayser, C. Inamura, DaveShreya, W. J. C., P. Houk, P. Colombo, M. Yang, and N. Oxman. Additive Manufacturing of Optically Transparent Glass. *3D Printing and Additive Manufacturing*, September 2015.
- [180] P. J. Withers and H. K. D. H. Bhadeshia. Residual stress. Part 2 : Nature and origins. *Materials Science and Technology*, 17(4):366–375, 2001.
- [181] P.J. Withers. Residual stress and its role in failure. *Reports on Progress in Physics*, 70(12):2211–2264, December 2007.
- [182] T.J. Lu and N.A. Fleck. The thermal shock resistance of solids. *Acta Materialia*, 46(13):4755–4768, August 1998.
- [183] H. K. D. H. Bhadeshia. Material Factors. In *Handbook of residual stress and deformation of steel*. ASM International, Materials Park, OH, 2002.
- [184] G. A. Webster and A. N. Ezeilo. Residual stress distributions and their influence on fatigue lifetimes. *International Journal of Fatigue*, 23:S375–S383, 2001.
- [185] R.R. Ambriz and D. Jaramillo. Mechanical Behavior of Precipitation Hardened Aluminum Alloys Welds. In Waldemar Alfredo Monteiro, editor, *Light Metal Alloys Applications*. InTech, June 2014.
- [186] K. Kempen, L. Thijs, B. Vrancken, S. Bols, J. Van Humbeeck, and J.-P. Kruth. Producing crack-free, high density M2 HSS parts by Selective Laser Melting: Pre-heating the baseplate. In *Proceedings of the Solid Freeform Fabrication Symposium*, pages 131–139, 2013.
- [187] Z. H. Liu, C. K. Chua, K. F. Leong, K. Kempen, L. Thijs, E. Yasa, and J.-P. Kruth. A Preliminary Investigation on Selective Laser Melting of M2 High Speed Steel. In *Virtual and Physical Prototyping*, 2011.

- [188] L. N. Carter, M. M. Attallah, and R. C. Reed. Laser Powder Bed Fabrication of Nickel-Base Superalloys: Influence of Parameters; Characterisation, Quantification and Mitigation of Cracking. In *Superalloys 2012*, pages 577–586. John Wiley & Sons, Inc., 2012.
- [189] K. Kunze, T. Etter, J. Grässlin, and V. Shklover. Texture, anisotropy in microstructure and mechanical properties of IN738LC alloy processed by selective laser melting (SLM). *Materials Science and Engineering: A*, 620:213–222, January 2015.
- [190] C. Amon, J. Beuth, H. Kirchner, R. Merz, F. B. Prinz, K. Schmaltz, and L. Weiss. Material Issues in Layered Forming. In *Proceedings of the Solid Freeform Fabrication Symposium*, Austin, Texas, 1993. University of Texas in Austin, Texas.
- [191] A. V. Gusarov, I. Yadroitsev, P. Bertrand, and I. Smurov. Heat transfer modelling and stability analysis of selective laser melting. *Applied Surface Science*, 254(4):975–979, 2007.
- [192] W. King, A. T. Anderson, R. M. Ferencz, N. E. Hodge, C. Kamath, and S. A. Khairallah. Overview of modelling and simulation of metal powder bed fusion process at Lawrence Livermore National Laboratory. *Materials Science and Technology*, 31(8):957–968, June 2015.
- [193] I. Yadroitsev, P. Krakhmalev, and I. Yadroitsava. Selective laser melting of Ti6Al4V alloy for biomedical applications: Temperature monitoring and microstructural evolution. *Journal of Alloys and Compounds*, 583(0):404–409, 2014.
- [194] X.P. Li, C.W. Kang, H. Huang, and T.B. Sercombe. The role of a low-energy-density re-scan in fabricating crack-free Al85Ni5Y6Co2Fe2 bulk metallic glass composites via selective laser melting. *Materials & Design*, 63:407–411, November 2014.
- [195] Y. Li and D. Gu. Parametric analysis of thermal behavior during selective laser melting additive manufacturing of aluminum alloy powder. *Materials & Design*, 63:856–867, November 2014.
- [196] C.H. Fu and Y.B. Guo. 3-Dimensional Temperature Gradient Mechanism in Selective Laser Melting of Ti-6Al-4V. *Journal of Manufacturing Science and Engineering*, September 2014.
- [197] L.-E. Loh, C.-K. Chua, W.-Y. Yeong, J. Song, M. Mapar, S.-L. Sing, Z.-H. Liu, and D.-Q. Zhang. Numerical investigation and an effective modelling on the Selective Laser Melting (SLM) process with aluminium alloy 6061. *International Journal of Heat and Mass Transfer*, 80:288–300, January 2015.

- [198] A. Hussein, L. Hao, C. Z. Yan, and R. Everson. Finite element simulation of the temperature and stress fields in single layers built without-support in selective laser melting. *Materials & Design*, 52:638–647, 2013.
- [199] S. A. Khairallah and A. Anderson. Mesoscopic simulation model of selective laser melting of stainless steel powder. *Journal of Materials Processing Technology*, 214(11):2627–2636, November 2014.
- [200] S. Price, K. Cooper, and K. Chou. Evaluations of temperature measurements by near-infrared thermography in powder-based electron beam additive manufacturing. In *Solid Freeform Fabrication Symposium*, pages 761–773, 2012.
- [201] A. V. Gusarov, M. Pavlov, and I. Smurov. Residual Stresses at Laser Surface Remelting and Additive Manufacturing. *Physics Procedia*, 12, Part A(0):248–254, 2011.
- [202] J. Ding, P. Colegrove, J. Mehnen, S. Ganguly, P. M. Sequeira Almeida, F. Wang, and S. Williams. Thermo-mechanical analysis of Wire and Arc Additive Layer Manufacturing process on large multi-layer parts. *Computational Materials Science*, 50(12):3315–3322, 2011.
- [203] F. Brückner, D. Lepski, and E. Beyer. Modeling the Influence of Process Parameters and Additional Heat Sources on Residual Stresses in Laser Cladding. *Journal of Thermal Spray Technology*, 16(3):355–373, 2007.
- [204] P. Aggarangsi, J. L. Beuth, and M. L. Griffith. Melt Pool Size and Stress Control for Laser-Based Deposition Near a Free Edge. In *Proceedings of the Solid Freeform Fabrication Symposium*, pages 196–207, Austin, Texas, 2003. University of Texas in Austin, Texas.
- [205] P. Aggarangsi and J. Beuth. Localized Preheating Approaches for Reducing Residual Stress in Additive Manufacturing. *Proceedings of the Solid Freeform Fabrication Symposium*, pages 709–720, 2006.
- [206] A. Vasinonta, J. Beuth, and M. L. Griffith. Process Maps for Controlling Residual Stress and Melt Pool Size in Laser-Based SFF Processes. *Proceedings of the Solid Freeform Fabrication Symposium*, pages 200–208, 2000.
- [207] A. Vasinonta, J. Beuth, and M. L. Griffith. Process Maps for Predicting Residual Stress and Melt Pool Size in the Laser-Based Fabrication of Thin-Walled Structures. *Journal of Manufacturing Science and Engineering*, 129(1):101–109, 2007.

- [208] J. Beuth and N. Klingbeil. The role of process variables in laser-based direct metal solid freeform fabrication. *JOM Journal of the Minerals Metals and Materials Society*, 53(9):36–39, 2001.
- [209] J. Gockel and J. Beuth. Understanding Ti-6Al-4V Microstructure Control in Additive Manufacturing via Process Maps. In *Solid Freeform Fabrication Symposium*, pages 666–674, 2013.
- [210] J. Gockel, J. Fox, J. Beuth, and R. Hafley. Integrated melt pool and microstructure control for Ti-6Al-4V thin wall additive manufacturing. *Materials Science and Technology*, 31(8):912–916, June 2015.
- [211] L. Costa, R. Vilar, T. Reti, and A. M. Deus. Rapid tooling by laser powder deposition: Process simulation using finite element analysis. *Acta Materialia*, 53(14):3987–3999, 2005.
- [212] A. Crespo, A. Deus, and R. Vilar. Modeling of Phase Transformations and Internal Stresses in Laser Powder Deposition. In *Xvii International Symposium on Gas Flow, Chemical Lasers, and High-Power Lasers*, volume 7131. Spie-Int Soc Optical Engineering, Bellingham, 2009.
- [213] R. J. Moat, A. J. Pinkerton, L. Li, P. J. Withers, and M. Preuss. Residual stresses in laser direct metal deposited Waspaloy. *Materials Science and Engineering: A*, 528(6):2288–2298, 2011.
- [214] P. Rangaswamy, T. M. Holden, R. B. Rogge, and M. L. Griffith. Residual stresses in components formed by the laserengineered net shaping (LENS®) process. *The Journal of Strain Analysis for Engineering Design*, 38(6):519–527, January 2003.
- [215] P. Pratt, S. D. Felicelli, L. Wang, and C. R. Hubbard. Residual Stress Measurement of Laser-Engineered Net Shaping AISI 410 Thin Plates Using Neutron Diffraction. *Metallurgical and Materials Transactions A*, 39(13):3155–3163, 2008.
- [216] S. Zekovic, R. Dwivedi, and R. Kovacevic. Thermo-structural Finite Element Analysis of Direct Laser Metal Deposited Thin-Walled Structures. *Proceedings of the Solid Freeform Fabrication Symposium*, pages 338–355, 2005.
- [217] M. L. Griffith, M. E. Schlienger, L. D. Harwell, M. S. Oliver, M. D. Baldwin, M. T. Ensz, M. Essien, J. Brooks, C. V. Robino, J. E. Smugeresky, W. H. Hofmeister, M. J. Wert, and D. V. Nelson. Understanding thermal behavior in the LENS process. *Materials & Design*, 20(2-3):107–113, 1999.

- [218] W. E. King, A. T. Anderson, R. M. Ferencz, N. E. Hodge, C. Kamath, S. A. Khairallah, and A. M. Rubenchik. Laser powder bed fusion additive manufacturing of metals; physics, computational, and materials challenges. *Applied Physics Reviews*, 2(4):041304, December 2015.
- [219] P. Rangaswamy, M. L. Griffith, M. B. Prime, T. M. Holden, R. B. Rogge, J. M. Edwards, and R. J. Sebring. Residual stresses in LENS (R) components using neutron diffraction and contour method. *Materials Science and Engineering a-Structural Materials Properties Microstructure and Processing*, 399(1-2):72–83, 2005.
- [220] Laurent Van Belle, Guillaume Vansteenkiste, and Jean Claude Boyer. Comparisons of Numerical Modelling of the Selective Laser Melting. *Key Engineering Materials*, 504-506:1067–1072, 2012.
- [221] A. Royakkers. *Selectief Laser Smelten van AISI M2 Snelstaal poeder*. Master thesis, 2011.
- [222] M. Zaeh and G. Branner. Investigations on residual stresses and deformations in selective laser melting. *Production Engineering*, 4(1):35–45, 2010.
- [223] J. Elambasseril, S. Feih, M. Bringezu, and M. Brandt. Influence of process parameters on residual stresses in Selective Laser Melting of Ti6Al4V components. Technical report, School of Aerospace, Mechanical and Manufacturing Engineering, RMIT, 2012.
- [224] A. S. Wu, D. W. Brown, M. Kumar, G. F. Gallegos, and W. E. King. An Experimental Investigation into Additive Manufacturing-Induced Residual Stresses in 316L Stainless Steel. *Metallurgical and Materials Transactions A*, September 2014.
- [225] R. Cottam, J. Wang, and V. Luzin. Characterization of microstructure and residual stress in a 3D H13 tool steel component produced by additive manufacturing. *Journal of Materials Research*, 29(17):1978–1986, August 2014.
- [226] S. Ghosh and J. Choi. Deposition Pattern Based Thermal Stresses in Single-Layer Laser Aided Direct Material Deposition Process. *Journal of Manufacturing Science and Engineering*, 129(2):319–332, 2007.
- [227] P. Van Puyvelde. *Involed van voorverwarming op Selectief Laser Smelten van M2 snelstaal*. Master thesis, Department of Mechanical Engineering, University of Leuven, 2013.

- [228] S. M. Kelly and S. L. Kampe. Microstructural evolution in laser-deposited multilayer Ti-6Al-4V builds: Part II. Thermal modeling. *Metallurgical and Materials Transactions A*, 35(6):1869–1879, June 2004.
- [229] C. R. Knowles. *Residual Stress Measurement and Structural Integrity Evaluation of SLM Ti-6Al-4V*. Master thesis, University of Cape Town, 2012.
- [230] M. Shiomi, K. Osakada, K. Nakamura, T. Yamashita, and F. Abe. Residual Stress within Metallic Model Made by Selective Laser Melting Process. *CIRP Annals - Manufacturing Technology*, 53(1):195–198, 2004.
- [231] P. Mercelis and J.-P. Kruth. Residual stresses in selective laser sintering and selective laser melting. *Rapid Prototyping Journal*, 12(5):254–265, 2006.
- [232] V. Manvatkar, A. De, and T. DebRoy. Spatial variation of melt pool geometry, peak temperature and solidification parameters during laser assisted additive manufacturing process. *Materials Science and Technology*, 31(8):924–930, June 2015.
- [233] R. Wauthle. *Verminderen van thermische spanningen bij selectief laser smelten*. Master thesis, Department of Mechanical Engineering, University of Leuven, 2010.
- [234] M. A. Taha, A. F. Yousef, K. A. Gany, and H. A. Sabour. On selective laser melting of ultra high carbon steel: Effect of scan speed and post heat treatment. *Selektives Laserschmelzen von hoch kohlenstoffhaltigen Stählen: Einfluss der Abtastgeschwindigkeit und der Wärmenachbehandlung. Materialwissenschaft und Werkstofftechnik*, 43(11):913–923, 2012.
- [235] H. Pohl, A. Simchi, M. Issa, and H. Calefi Dias. Thermal Stresses in Direct Metal Laser Sintering. *Proceedings of the Solid Freeform Fabrication Symposium*, pages 366–372, 2001.
- [236] M. Alimardani, E. Toyserkani, J. P. Huissoon, and C. P. Paul. On the delamination and crack formation in a thin wall fabricated using laser solid freeform fabrication process: An experimental and numerical investigation. *Optics and Lasers in Engineering*, 47(11):1160–1168, 2009.
- [237] J.-P. Kruth, J. Deckers, E. Yasa, and R. Wauthle. Assessing and comparing influencing factors of residual stresses in selective laser melting using a novel analysis method. *Proceedings of the Institution of Mechanical Engineers Part B-Journal of Engineering Manufacture*, 226(B6):980–991, 2012.

- [238] L. van Belle, G. Vansteenkiste, and J. C. Boyer. Investigation of Residual Stresses Induced during the Selective Laser Melting Process. *Key Engineering Materials*, 554-557:1828–1834, June 2013.
- [239] E. R. Denlinger, J. C. Heigel, P. Michaleris, and T. A. Palmer. Effect of inter-layer dwell time on distortion and residual stress in additive manufacturing of titanium and nickel alloys. *Journal of Materials Processing Technology*, 215:123–131, January 2015.
- [240] J. McIntosh, S. Danforth, and V. Jamalabad. shrinkage and deformation in components manufactured by fused deposition of ceramics. *Proceedings of the Solid Freeform Fabrication Symposium*, pages 159–166, 1997.
- [241] P. Mercelis. *Control of selective laser sintering and selective laser melting processes*. PhD thesis, KU Leuven, Leuven, 2007.
- [242] B. Qian, Y. S. Shi, Q. S. Wei, and H. B. Wang. The helix scan strategy applied to the selective laser melting. *International Journal of Advanced Manufacturing Technology*, 63(5-8):631–640, January 2012.
- [243] J Yang, H Bin, X Zhang, and Z Liu. Fractal scanning path generation and control system for selective laser sintering (SLS). *International Journal of Machine Tools and Manufacture*, 43(3):293–300, 2003.
- [244] L. Ma and H. Bin. Temperature and stress analysis and simulation in fractal scanning-based laser sintering. *The International Journal of Advanced Manufacturing Technology*, 34(9-10):898–903, August 2006.
- [245] H.P. Tang, G.Y. Yang, W.P. Jia, W.W. He, S.L. Lu, and M. Qian. Additive manufacturing of a high niobium-containing titanium aluminide alloy by selective electron beam melting. *Materials Science and Engineering: A*, 636:103–107, June 2015.
- [246] H. Wang. *The influence of process parameters on the residual stress in Selective Laser Melting*. Master thesis, University of Leuven, 2014.
- [247] N. W. Klingbeil, J. L. Beuth, R. K. Chin, and C. H. Amon. measurement and modeling of residual stress-induced warpage in direct metal deposition processes. *Proceedings of the Solid Freeform Fabrication Symposium*, pages 367–374, 1998.
- [248] F. Abe, K. Osakada, M. Shiomi, K. Uematsu, and M. Matsumoto. The manufacturing of hard tools from metallic powders by selective laser melting. *Journal of Materials Processing Technology*, 111(1-3):210–213, April 2001.

- [249] P. Vora, K. Mumtaz, I. Todd, and N. Hopkinson. AlSi12 In-Situ Alloy Formation and Residual Stress Reduction using Anchorless Selective Laser Melting. *Additive Manufacturing*, 7:12–19, June 2015.
- [250] P. Prabhakar, W.J. Sames, R. Dehoff, and S.S. Babu. Computational modeling of residual stress formation during the electron beam melting process for Inconel 718. *Additive Manufacturing*, 7:83–91, July 2015.
- [251] K. Dai, X-X. Li, and L. L. Shaw. Comparisons between thermal modeling and experiments: effects of substrate preheating. *Rapid Prototyping Journal*, 10(1):24–34, 2004.
- [252] B. Vrancken, S. Buls, J.-P. Kruth, and J. Van Humbeeck. Preheating of Selective Laser Melted Ti6Al4V : Microstructure and mechanical properties. In *Proceedings of the World Conference on Titanium*, San Diego, 2015. TMS.
- [253] Department of Physics and Astronomy - Georgia State University. Experimental K-alpha x ray energies. <http://hyperphysics.phy-astr.gsu.edu/hbase/tables/kxray.html>. [Accessed 2016-03-14].
- [254] J. H. Hubbell and S. M. Seltzer. NIST: X-Ray Mass Attenuation Coefficients. <http://www.nist.gov/pml/data/xraycoef/index.cfm>, 1996. [Accessed 2016-03-14].
- [255] P. S. Prevey. The use of Pearson VII distribution functions in X-ray diffraction residual stress measurement. *Advances in X-Ray Analysis*, 29:103–111, 1986.
- [256] I.C. Noyan and J.B. Cohen. Residual stress. January 1986.
- [257] P. Van Houtte and L. De Buyser. The influence of crystallographic texture on diffraction measurements of residual stress. *Acta Metallurgica Et Materialia*, 41(2):323–336, 1993.
- [258] G. Bruno and B. D. Dunn. The precise measurement of Ti6Al4V microscopic elastic constants by means of neutron diffraction. *Measurement Science and Technology*, 8(11):1244, 1997.
- [259] M. B. Prime. Cross-sectional mapping of residual stresses by measuring the surface contour after a cut. *Journal of Engineering Materials and Technology-Transactions of the Asme*, 123(2):162–168, 2001.
- [260] P. Pagliaro, M. B. Prime, H. Swenson, and B. Zuccarello. Measuring Multiple Residual-Stress Components using the Contour Method and Multiple Cuts. *Experimental Mechanics*, 50(2):187–194, 2010.

- [261] A. DeWald and M. Hill. Multi-Axial Contour Method for Mapping Residual Stresses in Continuously Processed Bodies. *Experimental Mechanics*, 46(4):473–490, 2006.
- [262] P. Pagliaro. *Mapping multiple residual stress components using the contour method and superposition*. PhD thesis, University of Study of Palermo, 2008.
- [263] P. Pagliaro, M. B. Prime, J. S. Robinson, B. Clausen, H. Swenson, M. Steinzig, and B. Zuccarello. Measuring Inaccessible Residual Stresses Using Multiple Methods and Superposition. *Experimental Mechanics*, 51(7):1123–1134, 2011.
- [264] F. Hosseinzadeh and P. J. Bouchard. Mapping Multiple Components of the Residual Stress Tensor in a Large P91 Steel Pipe Girth Weld Using a Single Contour Cut. *Experimental Mechanics*, 53(2):171–181, May 2012.
- [265] F. De Paolis, C. Caroselli, and S. Riscifuli. Mechanical Treatments Evaluation on Ti-6Al-4V Alloy by Means of XRD Residual Stress Measurement Technique. In *RTO AVT Specialists Meeting on 'Cost Effective Application of Titanium Alloys in Military Platforms'*, pages 7–11, Loen, Norway, 2001.
- [266] E. S. Fisher and C. J. Renken. Single-Crystal Elastic Moduli and the hcp to bcc Transformation in Ti, Zr, and Hf. *Physical Review*, 135(2A):A482–A494, 1964.
- [267] Y. D. Wang, R. L. Peng, and R. McGreevy. High anisotropy of orientation dependent residual stress in austenite of cold rolled stainless steel. *Scripta Materialia*, 41(9):995–1000, 1999.
- [268] J. A. Rayne and B. S. Chandrasekhar. Elastic Constants of Iron from 4.2 to 300°K. *Physical Review*, 122(6):1714–1716, 1961.
- [269] C. E. Anderson. The single crystal elastic constants of the tantalum tungsten alloy system from 4 to 300 K. Technical report, Rice University, 1980.
- [270] F. H. Featherston. The elastic constants of Tantalum and Molybdenum. Technical report, Monterey, California. Naval Postgraduate School, 1963.
- [271] F. F. Schmitt and H. R. Ogden. The Engineering Properties of Tantalum and Tantalum Alloys. Technical report, Defense Metals Information Center, 1963.

- [272] E. Lassner and W. D. Schubert. *Tungsten: properties, chemistry, technology of the elements, alloys, and chemical compounds*. Springer Science+Business Media, LLC, 1999.
- [273] R. B. Parker, D. W. Brown, and P. Rangaswamy. Residual Stresses in an Inconel-718-Clad Tungsten Tube Processed by Hot Iso-static Pressing. *Materials Science Forum*, 347-349:229–234, 2000.
- [274] U. Bayerlein and H.-G. Sockel. Measurements and calculations of the elastic moduli of ODS and cast Ni-based superalloys. *Materials Science and Engineering: A*, 141(2):179–187, 1991.
- [275] M. Eckhardt and H. Ruppertsberg. Influence of Texture on \sin^2 Curves Obtained From a Cold Rolled Nickel Sheet using Synchrotron Radiation. *Textures and Microstructures*, 8(2):679–691, 1988.
- [276] A. S. Gill, Z. Zhou, U. Lienert, J. Almer, D. F. Lahrman, S. R. Mannava, D. Qian, and V. K. Vasudevan. High spatial resolution, high energy synchrotron x-ray diffraction characterization of residual strains and stresses in laser shock peened Inconel 718SPF alloy. *Journal of Applied Physics*, 111(8):84904–84912, 2012.
- [277] V. Stelmukh, L. Edwards, and S. Ganguly. Full Stress Tensor Determination in A textured Aerospace Aluminium Alloy Plate Using synchrotron X-Ray Diffraction. *Textures and Microstructures*, 35(3-4):175–183, 2003.
- [278] J.L. Tallon and A. Wolfenden. Temperature dependence of the elastic constants of aluminum. *Journal of Physics and Chemistry of Solids*, 40(11):831–837, 1979.
- [279] S. J. Wei and K. Liao. Surface Stress Measurement of Aluminum Alloy by X-Ray Diffraction Method. *Advanced Materials Research*, 393-395:343–348, November 2012.
- [280] Howard A Canistraro, Eric H Jordan, Shi Shixiang, Leroy H Favrow, and Francis A Reed. Elastic Constants of Single Crystal Hastelloy X at Elevated Temperatures. *J Eng Mater Technol*, 120(3):242–247, 1998.
- [281] M. B. Prime. The Contour Method: A New Approach in Experimental Mechanics. *Proceedings of the SEM Annual Conference*, 2009.
- [282] M. B. Prime. Plasticity effects in incremental slitting measurement of residual stresses. *Engineering Fracture Mechanics*, 77(10):1552–1566, 2010.

- [283] M. B. Prime, R. J. Sebring, J. M. Edwards, D. J. Hughes, and P. J. Webster. Laser surface-contouring and spline data-smoothing for residual stress measurement. *Experimental Mechanics*, 44(2):176–184, 2004.
- [284] Y. Zhang, S. Ganguly, L. Edwards, and M. E. Fitzpatrick. Cross-sectional mapping of residual stresses in a VPPA weld using the contour method. *Acta Materialia*, 52(17):5225–5232, 2004.
- [285] M. B. Prime. Residual Stress Measurement by Successive Extension of a Slot: The Crack Compliance Method. *Applied Mechanics Reviews*, 52(2):75–96, 1999.
- [286] L. Papadakis, A. Loizou, J. Risse, S. Bremen, and J. Schrage. A computational reduction model for appraising structural effects in selective laser melting manufacturing: a methodical model reduction proposed for time-efficient finite element analysis of larger components in Selective Laser Melting. *Virtual and Physical Prototyping*, 9(1):17–25, 2014.
- [287] Neugebauer, Keller, Ploshikhin, Feuerhahn, and Köhler. Multi Scale FEM Simulation for Distortion Calculation in Additive Manufacturing of Hardening Stainless Steel. In *International Workshop on Thermal Forming and Welding Distortion, IWOTE 14*, April 2014.
- [288] S. Jayanthi, M. Keefe, and E. Gargiulo. studies in stereolithography: influence of process parameters on curl distortion in photopolymer models. *Proceedings of the Solid Freeform Fabrication Symposium*, pages 250–258, 1994.
- [289] S. Har’el. Curvature of curves and surfaces - a parabolic approach. <http://www.math.technion.ac.il/S/rl/docs/parabola.pdf>.
- [290] J. Van Vaerenbergh. *Process optimisation in Selective Laser Melting*. PhD thesis, University of Twente, Twente, 2008.
- [291] S. A. Khairallah, A. T. Anderson, A. Rubenchik, and W. E. King. Laser powder-bed fusion additive manufacturing: Physics of complex melt flow and formation mechanisms of pores, spatter, and denudation zones. *Acta Materialia*, 108:36–45, April 2016.
- [292] M. B. Prime and A. L. Kastengren. The Contour Method Cutting Assumption: Error Minimization and Correction. *Proceedings of the SEM Annual Conference & Exposition on Experimental and Applied Mechanics Indianapolis*, 6:233–250, 2010.
- [293] O. Raeymaekers. *Analyse van scheurpropagatie en breuktaaiheid bij selectief laser gesmolten proefstukken in titanium*. Master thesis, Lessius College, Mechelen, 2011.

- [294] S. Timoshenko. Analysis of bi-metal thermostats. *Journal of the Optical Society of America*, 11(3):233, September 1925.
- [295] Z. Zhu, V. Dhokia, A. Nassehi, and S. T. Newman. Investigation of part distortions as a result of hybrid manufacturing. *Robotics and Computer-Integrated Manufacturing*, 37:23–32, February 2016.
- [296] A. H. Nickel. *Analysis of thermal stresses in shape deposition manufacturing of metal parts*. PhD thesis, Stanford University, 1999.
- [297] L.-P. Lefebvre, E. Baril, and L. de Camaret. The effect of oxygen, nitrogen and carbon on the microstructure and compression properties of titanium foams. *Journal of Materials Research*, 28(17):2453–2460, May 2013.
- [298] H. Conrad. Effect of interstitial solutes on the strength and ductility of titanium. *Progress in Materials Science*, 26(2-4):123–403, January 1981.
- [299] Q. Yu, L. Qi, T. Tsuru, R. Traylor, D. Rugg, J. W. Morris, M. Asta, D. C. Chrzan, and A. M. Minor. Metallurgy. Origin of dramatic oxygen solute strengthening effect in titanium. *Science (New York, N. Y.)*, 347(6222):635–9, February 2015.
- [300] D. L. Bourell, M. C. Leu, and D. W. Rosen. Roadmap for Additive Manufacturing: Identifying the future of freeform fabrication. Technical report, University of Texas at Austin, Austin, 2009.
- [301] Inc Wohlers Associates. Additive Manufacturing Technology roadmap for Australia. Technical report, Wohlers Associates Inc, 2011.
- [302] LayerWise. Internal database.
- [303] EOS. Material data sheet: EOS Aluminium AlSi10Mg for EOSINT M 270 Material data sheet. 2011.
- [304] Hastelloy C-276 alloy information. <http://www.haynesintl.com/C276HASTELLOYALLOY.htm>. [Accessed 2015-12-19].
- [305] N. C. Cole, R. G. Gilliland, and G. M. Slaughter. *Weldability of tungsten and its alloys*. Defense Technical Information Center., 1968.
- [306] M. Cloots, P. J. Uggowitzer, and K. Wegener. Investigations on the microstructure and crack formation of IN738LC samples processed by selective laser melting using Gaussian and doughnut profiles. *Materials & Design*, 89:770–784, January 2016.

- [307] T. Hua, C. Jing, Z. Fengying, L. Xin, and H. Weidong. Microstructure and Mechanical Properties of Laser Solid Formed Ti-6Al-4V from Blended Elemental Powders. *Rare Metal Materials and Engineering*, 38(4):574–578, 2009.
- [308] P. Stenlund, S. Kurosu, Y. Koizumi, F. Suska, H. Matsumoto, A. Chiba, and A. Palmquist. Osseointegration Enhancement by Zr doping of Co-Cr-Mo Implants Fabricated by Electron Beam Melting. *Additive Manufacturing*, 6:6–15, April 2015.
- [309] P. C. Collins, R. Banerjee, S. Banerjee, and H.L. Fraser. Laser deposition of compositionally graded titanium–vanadium and titanium–molybdenum alloys. *Materials Science and Engineering: A*, 352(1–2):118–128, July 2003.
- [310] A. Almeida, D. Gupta, C. Loable, and R. Vilar. Laser-assisted synthesis of Ti–Mo alloys for biomedical applications. *Materials Science and Engineering: C*, 32(5):1190–1195, 2012.
- [311] E W Collings. The physical metallurgy of titanium alloys. *American Society for Metals, 1984*, page 261, 1984.
- [312] P. J. Bania. Beta titanium alloys and their role in the titanium industry. *JOM Journal of the Minerals Metals and Materials Society*, 46(7):16–19, 1994.
- [313] W. F. Ho, C. P. Ju, and J. H. Chern Lin. Structure and properties of cast binary Ti–Mo alloys. *Biomaterials*, 20(22):2115–2122, 1999.
- [314] J. L. Murray. The Molybdenum-Titanium system. *Bulletin of Alloy Phase Diagrams*, 2(2):185–192, 1981.
- [315] M. E. Glicksman. Constitutional Undercooling. In *Principles of Solidification*, chapter 9. Springer New York, New York, NY, 2011.
- [316] Bey Vrancken, Lore Thijs, Jean-Pierre Kruth, and Jan Van Humbeeck. Heat treatment of Ti6Al4V produced by Selective Laser Melting: Microstructure and mechanical properties. *Journal of Alloys and Compounds*, 541(0):177–185, 2012.
- [317] Y. Kinds and N. Holmstock. *De invloed van voorverwarming op de productie en eigenschappen van Hastelloy-X en H13 gereedschapsstaal bij Selectief Laser Smelten*. Master thesis, Department of Mechanical Engineering, University of Leuven, 2015.
- [318] R. Mertens. Unpublished results. Technical report, Department of Mechanical Engineering, University of Leuven, 2015.

- [319] S. Dadbakhsh and L. Hao. Effect of Al alloys on selective laser melting behaviour and microstructure of in situ formed particle reinforced composites. *Journal of Alloys and Compounds*, 541:328–334, 2012.
- [320] S. Dadbakhsh and L. Hao. Effect of hot isostatic pressing (HIP) on Al composite parts made from laser consolidated Al/Fe₂O₃ powder mixtures. *Journal of Materials Processing Technology*, 212(11):2474–2483, November 2012.
- [321] D. Gu, H. Wang, D. Dai, P. Yuan, W. Meiners, and R. Poprawe. Rapid fabrication of Al-based bulk-form nanocomposites with novel reinforcement and enhanced performance by selective laser melting. *Scripta Materialia*, 96:25–28, February 2015.
- [322] P. Yuan, D. Gu, and D. Dai. Particulate migration behavior and its mechanism during selective laser melting of TiC reinforced Al matrix nanocomposites. *Materials & Design*, May 2015.
- [323] T. Kühnle and K. Partes. In-Situ Formation of Titanium Boride and Titanium Carbide by Selective Laser Melting. *Physics Procedia*, 39:432–438, 2012.
- [324] D. Gu, Y.-C. Hagedorn, W. Meiners, K. Wissenbach, and R. Poprawe. Selective Laser Melting of in-situ TiC/Ti₅Si₃ composites with novel reinforcement architecture and elevated performance. *Surface and Coatings Technology*, 205(10):3285–3292, 2011.
- [325] D D Gu, G B Meng, C Li, W Meiners, and R Poprawe. Selective laser melting of TiC/Ti bulk nanocomposites: Influence of nanoscale reinforcement. *Scripta Materialia*, 67(2):185–188, 2012.
- [326] C.-N. Sun, M. C. Gupta, and E. A. Payzant. Effect of Laser Sintering on Ti-ZrB₂ Mixtures. *Journal of the American Ceramic Society*, 94(10):3282–3285, October 2011.
- [327] N. Stefansson, S. Semiatin, and D. Eylon. The kinetics of static globularization of Ti-6Al-4V. *Metallurgical and Materials Transactions A*, 33(11):3527–3534, 2002.
- [328] S Semiatin, N Stefansson, and R Doherty. Prediction of the kinetics of static globularization of Ti-6Al-4V. *Metallurgical and Materials Transactions A*, 36(5):1372–1376, 2005.
- [329] S. Malinov, Z. Guo, W. Sha, and A. Wilson. Differential scanning calorimetry study and computer modeling of beta double right arrow alpha phase transformation in a Ti-6Al-4V alloy. *Metallurgical and Materials*

- Transactions a-Physical Metallurgy and Materials Science*, 32(4):879–887, 2001.
- [330] I. Katarov, S. Malinov, and W. Sha. Finite element modeling of the morphology of beta to alpha phase transformation in Ti-6Al-4V alloy. *Metallurgical and Materials Transactions a-Physical Metallurgy and Materials Science*, 33(4):1027–1040, 2002.
- [331] S. L. Semiatin, S. L. Knisley, P. N. Fagin, D. R. Barker, and F. Zhang. Microstructure evolution during alpha-beta heat treatment of Ti-6Al-4V. *Metallurgical and Materials Transactions A*, 34(10):2377–2386, 2003.
- [332] F. J. Gil, M. P. Ginebra, J. M. Manero, and J. A. Planell. Formation of alpha-Widmanstätten structure: effects of grain size and cooling rate on the Widmanstätten morphologies and on the mechanical properties in Ti6Al4V alloy. *Journal of Alloys and Compounds*, 329(1):142–152, 2001.
- [333] R. Pederson, O. Babushkin, F. Skystedt, and R. Warren. Use of high temperature X-ray diffractometry to study phase transitions and thermal expansion properties in Ti-6Al-4V. *Materials Science and Technology*, 19(11):1533–1538, 2003.
- [334] T. Ahmed and H. J. Rack. Phase transformations during cooling in $\alpha+\beta$ titanium alloys. *Materials Science and Engineering: A*, 243(1-2):206–211, 1998.
- [335] R. Dabrowski. The Kinetics of Phase Transformations During Continuous Cooling of Ti6Al4V Alloy from the Diphase $\alpha + \beta$ Range. *Archives of metallurgy and materials*, 56(2):217–221, January 2011.
- [336] E. Underwood. *Quantitative stereology*. Addison-Wesley Educational Publishers Inc, 1970.
- [337] T. Sercombe, N. Jones, R. Day, and A. Kop. Heat treatment of Ti-6Al-7Nb components produced by selective laser melting. *Rapid Prototyping Journal*, 14(5):300–304, 2008.
- [338] T. Vilaro, C. Colin, and J. D. Bartout. As-Fabricated and Heat-Treated Microstructures of the Ti-6Al-4V Alloy Processed by Selective Laser Melting. *Metallurgical and Materials Transactions A: Physical Metallurgy and Materials Science*, 42A(10):3190–3199, 2011.
- [339] L. Facchini, E. Magalini, P. Robotti, A. Molinari, S. Hoges, and K. Wissenbach. Ductility of a Ti-6Al-4V alloy produced by selective laser melting of prealloyed powders. *Rapid Prototyping Journal*, 16(6):450–459, 2010.

- [340] F. X. Gil Mur, D. Rodriguez, and J. A. Planell. Influence of tempering temperature and time on the Ti6Al4V martensite. *Journal of Alloys and Compounds*, 234(2):287–289, 1996.
- [341] L Thijs. *Influence of Selective Laser Melting on the microstructure of titanium alloys*. PhD thesis, Leuven, 2009.
- [342] P. A. Kobryn and S. L. Semiatin. Microstructure and texture evolution during solidification processing of Ti6Al4V. *Journal of Materials Processing Technology*, 135(2–3):330–339, 2003.
- [343] J. Yu, M. Rombouts, G. Maes, and F. Motmans. Material Properties of Ti6Al4V Parts Produced by Laser Metal Deposition. *Physics Procedia*, 39:416–424, January 2012.
- [344] L. E. Murr, S. A. Quinones, S. M. Gaytan, M. I. Lopez, A. Rodela, E. Y. Martinez, D. H. Hernandez, E. Martinez, F. Medina, and R. B. Wicker. Microstructure and mechanical behavior of Ti-6Al-4V produced by rapid-layer manufacturing, for biomedical applications. *Journal of the Mechanical Behavior of Biomedical Materials*, 2(1):20–32, 2009.
- [345] Svensson (ARCAM). Influence of interstitials on material properties of Ti6Al4V fabricatde with electron beam melting. pages 1–19, 2011.
- [346] M. Koike, P. Greer, K. Owen, G. Lilly, L. E. Murr, S. M. Gaytan, E. Martinez, and T. Okabe. Evaluation of Titanium Alloys Fabricated Using Rapid Prototyping Technologies-Electron Beam Melting and Laser Beam Melting. *Materials*, 4(10):1776–1792, October 2011.
- [347] T. Vilaro, C. Colin, J. D. Bartout, L. Nazé, and M. Sennour. Microstructural and mechanical approaches of the selective laser melting process applied to a nickel-base superalloy. *Materials Science and Engineering: A*, 534(0):446–451, 2012.
- [348] M. Thöne, S. Leuders, A. Riemer, T. Tröster, and H. A. Richard. Influence of heat-treatment on Selective Laser Melting products – e.g. Ti6Al4V. In *Proceedings of the Solid Freeform Fabrication Symposium*, Austin, Texas, 2012. University of Texas in Austin, Texas.

Curriculum Vitae

Bey Vrancken

bey.vrancken@gmail.com

19 November 1988, Leuven, Belgium

Education

- | | |
|-----------|--|
| 2011-2016 | Doctoral training program
Arenberg Doctoral School (ADS), Faculty of Engineering Sciences, KU Leuven. |
| 2006-2011 | Master of Materials Engineering (Polymer composites)
Department of Materials Engineering, KU Leuven.
<i>Magna Cum Laude</i> |

Professional experience

Research assistant

- | | |
|-----------|--|
| 2011-2016 | PhD at Department of Materials Engineering, KU Leuven. |
|-----------|--|

Teaching assistant

2011-2014	Ombuds person.
2011-2012	P&O Materiaalkunde: Module 2: Ternary Phase Diagrams (H09Z2A, later H0T31a): Exercise sessions.
2011-2012	P&O Materiaalkunde: Reverse Engineering (H01Q1C, later H0T32A): Practical sessions.
2012-2016	P&O Materiaalkunde: Reverse Engineering (H01Q1C, later H0T32A): Senior assistant, practical sessions.
2013-2014	Structuurgenese van Materialen: Microstructurele Karakterisatie (H01I9a): Exercise sessions.

Bachelor thesis daily supervisor

B. Beynaerts	(2014) <i>Invloed van bouworiëntatie en geometrie op de microstructuur en mechanische eigenschappen van lichtgewicht scaffold structuren vervaardigd via Selectief Laser Smelten.</i>
--------------	---

Master thesis daily supervisor

P. Van Puyvelde	(2013) <i>Invloed van voorverwarming op Selectief Laser Smelten van M2 snelstaal.</i>
C. Heymans	(2014) <i>Effect van warmtebehandelingen op de microstructuur en interne spanningen in selectief laser gesmolten Inconel 738LC.</i> In cooperation with Fraunhofer ILT, Aachen.
H. Wang	(2014) <i>The Influence of Process Parameters on The Residual Stress in Selective Laser Melting.</i>
M. Montero	(2015) <i>The influence of process parameters and silicon content on the reduction of cracks in Al7075 processed by Selective Laser Melting.</i>
W. Xiong	(2015) <i>Density and residual stress of SLM produced Ti6Al4V.</i>
N. Holmstock & Y. Kinds	(2015) <i>De invloed van voorverwarming op de productie en eigenschappen van Hastelloy-X en H13 gereedschapsstaal bij Selectief Laser Smelten.</i>
N. Omnidvari	(Planned June 2016) <i>Selective Laser Melting of Tungsten.</i>

List of Publications

Articles in internationally reviewed academic journals

- Strantza, M., Vafadari, R., de Baere, D., **Vrancken, B.**, van Paepegem, W., Vandendael, I., Terryn, H., Guillaume, P., van Hemelrijck, D. (2016). Fatigue of Ti6Al4V Structural Health Monitoring Systems Produced by Selective Laser Melting. *Materials*, 9 (2), 106.
- Dadbakhsh, S., **Vrancken, B.**, Kruth, J., Luyten, J., Van Humbeeck, J. (2016). Texture and anisotropy in selective laser melting of NiTi alloy. *Materials Science and Engineering A, Structural Materials: Properties, Microstructure and Processing*, 650, 225-232.
- Kempen, K., **Vrancken, B.**, Buls, S., Thijs, L., Van Humbeeck, J., Kruth, J. (2014). Selective Laser Melting of crack-free high density M2 HSS parts by baseplate pre-heating. *Journal of Manufacturing Science and Engineering*, 136 (6), 1-6.
- **Vrancken, B.**, Cain, V., Knutsen, R., Van Humbeeck, J. (2014). Residual stress via the contour method in compact tension specimens produced via Selective Laser Melting. *Scripta Materialia*, 87, 29-32.
- **Vrancken, B.**, Thijs, L., Kruth, J., Van Humbeeck, J. (2014). Microstructure and mechanical properties of a novel β titanium metallic composite by selective laser melting. *Acta Materialia*, 68, 150-158.
- Wauthle, R., Kruth, J., **Vrancken, B.**, Beynaerts, B., Jorissen, K., Schrooten, J., Van Humbeeck, J. (2014). Effects of build orientation and heat treatment on the microstructure and mechanical properties of selective laser melted Ti6Al4V lattice structures. *Additive Manufacturing*, 5 (March 2015), 77-84.

- **Vrancken, B.**, Thijs, L., Kruth, J., Van Humbeeck, J. (2012). Heat treatment of Ti6Al4V produced by Selective Laser Melting: Microstructure and mechanical properties. *Journal of Alloys and Compounds*, 541, 177-185.

Article in academic book, internationally recognized scientific publisher

- Kruth, J., Dadbakhsh, S., **Vrancken, B.**, Kempen, K., Vleugels, J., Van Humbeeck, J. (2015). Additive manufacturing of metals via Selective Laser Melting: Process aspects and material developments. In: Srivatsan T., Sudarshan T. (Eds.), *Additive Manufacturing, Innovations, Advances, and Applications*, Chapt. 3 CRC Press, 69-99.

Papers at international scientific conferences and symposia, published in full in proceedings

- **Vrancken, B.**, Buls, S., Kruth, J., Van Humbeeck, J. (2015). Preheating of Selective Laser Melted Ti6Al4V - Microstructure and mechanical properties. *Proceedings of the World Conference on Titanium. World Conference on Titanium. San Diego, CA, US, 16-20 August 2015 TMS.*
- **Vrancken, B.**, Buls, S., Kruth, J., Van Humbeeck, J. (2015). Influence of preheating and oxygen content on Selective Laser Melting of Ti6Al4V. *Proceedings of the 16th RAPDASA Conference. RAPDASA, Annual International Conference on Rapid Product Development Association of South Africa. Pretoria, South Africa, 4-6 November 2015.*
- **Vrancken, B.**, Kempen, K., Thijs, L., Kruth, J., Van Humbeeck, J. (2014). Adapted heat treatment of Selective Laser Melted materials. In Danninger, H. (Ed.), *Proceedings of the Euro PM 2014 Congress. Euro PM2014 Congress. Salzburg, Austria, 21-24 September 2014 (pp. 1-6).* Shrewsbury: European Powder Metallurgy Association (EPMA).
- Thijs, L., **Vrancken, B.**, Kruth, J., Van Humbeeck, J. (2013). The influence of process parameters and scanning strategy on the texture in Ti6Al4V part produced by selective laser melting. *Advanced Materials, Processes and Applications for Additive Manufacturing. Materials Science & Technology. Montreal, Canada, 27-31 October 2013.*

- **Vrancken, B.**, Wauthle, R., Kruth, J., Van Humbeeck, J. (2013). Study of the influence of material properties on residual stress in selective laser melting. Proceedings of the Solid Freeform Fabrication Symposium. Solid Freeform Fabrication Symposium. Austin, Texas, USA, 12-14 August 2013 (pp. 1-15).
- Kempen, K., **Vrancken, B.**, Thijs, L., Bults, S., Van Humbeeck, J., Kruth, J. (2013). Lowering thermal gradients in Selective Laser melting by pre-heating the baseplate. Solid Freeform Fabrication Symposium Proceedings. solid freeform fabrication Symposium. Austin, Texas USA, 12-15 august 2013.

Meeting abstracts, presented at international scientific conferences and symposia, published or not published in proceedings or journals

- **Vrancken, B.**, Thijs, L., Kruth, J.-P. , Van Humbeeck, J. (2016). Process parameters and residual stress in Additive Manufacturing. International Conference on Residual Stress, ANSTO. Sydney, Australia, 3-7 July 2016.
- Van Humbeeck, J., **Vrancken, B.**, Mertens, R., Montero Sistiaga, M. (2015). Re-viewing alloy compositions for Selective Laser Melting. RAP-DASA, Annual International Conference on Rapid Product Development Association of South Africa. Pretoria, South Africa, 4-6 November 2015.
- Van Hooreweder, B., **Vrancken, B.**, Thijs, L., Dadbakhsh, S., Van Humbeeck, J., Kruth, J. (2014). On the properties of Ti-based parts produced by Selective Laser Melting. Workshop on additive manufacturing for space applications. Noordwijk, The Netherlands, 27-28 October 2014.

FACULTY OF ENGINEERING SCIENCE
DEPARTMENT OF MATERIALS ENGINEERING
ADVANCED CERAMICS AND POWDER METALLURGY, SIEM

Kasteelpark Arenberg 44 box 2450

B-3001 Heverlee

info@mtm.kuleuven.be

www.mtm.kuleuven.be

